THE UNIVERSITY *of* EDINBURGH

Search for the Higgs boson via the $H \to b\bar{b}$ decay mode, in the boosted regime on the ATLAS experiment

Brendan Joseph O'Brien

A thesis submitted in fulfilment of the requirements
for the degree of Doctor of Philosophy
to the
University of Edinburgh
January 2014

Abstract

This thesis presents details of the search for the Standard Model Higgs boson, in the low mass region ($100 \leq M_H < 150$ GeV), with the ATLAS detector at CERN. In this range, a Higgs boson may be produced in association with a W or Z-boson and decay predominantly to two b-quarks ($H \to b\bar{b}$). Specifically events having large Higgs boson transverse momentum ($p_T > 200$ GeV) and large recoiling W-boson transverse momentum ($p_T > 200$ GeV) are considered as a means to reduce the contribution from background processes. In this high p_T (boosted) regime, novel jet-substructure techniques are applied to the reconstructed jets resulting from the Higgs boson decay. In order to use these jet-substructure techniques, b-tagging efficiency scale factors in the jet-substructure regime have also been derived for the first time. Details of their derivation are presented for many b-tagging algorithms, with 14.3 fb^{-1} of ATLAS proton-proton collision data in 2012 at $\sqrt{s} = 8$ TeV. These, and their associated systematic uncertainties, are then applied to the Higgs boson search. No significant measurement of Higgs boson production was made, based on 20.4 fb^{-1} of ATLAS proton-proton collision data in 2012 at $\sqrt{s} = 8$ TeV. For a Higgs boson mass of 125 GeV, an exclusion limit of $6.12 \times \sigma_{\mathrm{SM}}$ was found at the 95% confidence level, and a signal strength of 0.93 ± 2.63 was measured, consistent with both background-only and signal (Standard Model Higgs boson) plus background hypotheses.

Declaration

Except where otherwise stated, the research undertaken in this thesis was the unaided work of the author. Where the work was done in collaboration with others, a significant contribution was made by the author.

Brendan Joseph O'Brien
January 2014

Acknowledgements

I would like to thank all those who have helped me in the course of this research, both academically and otherwise. In particular I thank Dr. Victoria Martin for her guidance, assistance and support as my principal supervisor. Professor Philip Clark as my secondary supervisor and with whom I worked closely during the first part of my PhD. All the remaining academic staff and students I have had the pleasure to work with both at the University of Edinburgh and at CERN. Particularly the members of the ATLAS collaboration who contributed to the running of the detectors, and collection of data, without whom this work would not have been possible.

I would like to thank my grandad, Peter Smith, whose natural curiosity about the world inspired me to study science. My secondary school physics teacher Richard Hannah, who shared with me his excitement for physics and was always willing to go beyond the boundaries of the course, for the sake of science!

Finally my family and friends for their continued support and encouragement, particularly my parents, those in 301-01-007 who provided many laughs and interesting discussions as a welcome distraction from work, Euan and Sarah for being great friends and Donna who helped more than I could have imagined.

Contents

List of Figures

List of Tables

Chapter 1

Introduction

The Large Hadron Collider (LHC) at CERN is a proton-proton collider with a design collision energy of 14 TeV, with 8 TeV being the highest obtained thus far. The LHC was designed to test the Standard Model of particle physics [1], explore beyond the Standard Model phenomena and to search for the Higgs boson. Prior to the start of writing this thesis, the Higgs boson had not been discovered. Its theoretical origins date back to 1964 [2, 3, 4] and fits to electroweak data predicted a most likely mass of around 120 GeV [5]. At the time of writing a new particle having properties consistent with those of the Higgs boson and a mass of $\sim$ 126 GeV has been discovered [6, 7] by the ATLAS and CMS experiments at the LHC at CERN.

In order to assist with the search for the Higgs boson and other physics analyses, an effective and efficient computer simulation of the experimental detectors is required to model the effects of particles and their experimental signatures. In addition, due to the high-energy nature of the LHC collisions, existing particle identification techniques have to be reviewed and improved. One such area is in the identification of "jets" originating from b-quarks produced in the collisions. It is found that jets often contain a substructure of multiple objects, and events that would otherwise be discarded can be analysed with new "jet-substructure" techniques.

This thesis begins by describing the underlying theory of the Standard Model of particle physics in Chapter 2, including predictions made about the existence and properties of a Higgs boson. The LHC and ATLAS experiment are then described in Chapter 3. I then detail my work starting with the development

and testing of the ATLAS simulation software and development of a new electromagnetic end cap calorimeter geometry description in Chapter 4. This is followed in Chapter 5 by studies to measure the efficiency of b-tagging events with jet-substructure. Finally the results of this jet-substructure b-tagging calibration are used with their associated systematic uncertainties to perform a search for the Higgs boson in the $q\,\bar{q} \to WH \to b\,\bar{b}\,l\,\bar{\nu}$ decay channel, in the regime with Higgs boson $p_T > 200$ GeV, detailed in Chapter 6.

The Higgs boson search resulted in no significant measurement of Higgs boson production, and set an exclusion limit of $6.12 \times \sigma_{\mathrm{SM}}$ at the 95% confidence level. A signal strength parameter of $\mu = 0.93 \pm 2.63$ was measured, consistent with both background-only ($\mu = 0$) and signal plus background hypotheses ($\mu = 1$ for a Standard Model Higgs boson). This search channel is known to be particularly difficult for observation, dominated by large yields of hadronic backgrounds. This analysis was limited by the data statistical uncertainties and, under the 2012 LHC operating conditions ($\sqrt{s} = 8$ TeV), would require a large increase in integrated luminosity in order to provide a statistically significant result. This analysis technique will yield improved performance in the $\sqrt{s} = 14$ TeV regime due to the predicted increase in the Higgs boson production cross-section at this energy [8]. Also in this energy regime a larger proportion of jets will be produced spatially close together requiring the jet-substructure techniques applied in this analysis.

Chapter 2

Theories in Particle Physics

2.1 The Standard Model of Particle Physics

2.1.1 Introduction

The Standard Model [1] of particle physics is a highly successful theory in high energy physics. Its mathematical formalism is that of a quantum field theory, and provides a description of particles and their interactions. The interactions in the Standard Model are in the form of electromagnetic, strong and weak interactions. Each of these plays an important role, not only in high energy physics colliders, but also in daily life.

Simply stated:

- **Electromagnetic interactions** - describe the interactions between electrically charged particles, mediated by massless photons. The electromagnetic force is responsible for the binding of electrons to nuclei, and so forms the basis of the atom and its associated chemistry.

- **Strong interactions** - describe the interactions between particles having colour charge, mediated by massless gluons. The strong force is responsible for the binding of protons and neutrons within a nucleus.

- **Weak interactions** - in the broken symmetry case (described in Section 2.1.4) describe the interactions between particles having weak isospin, mediated by massive $W^{\pm}$ vector bosons, and interactions of a massive Z^0 vector boson which couples to a combination of weak isospin and weak

hypercharge. The weak force is responsible, for example, for nuclear β decay and all interactions involving neutrinos.

The Standard Model and its particle content are based both on experimental observations and theoretical insights. It has eighteen free and experimentally measurable parameters. These parameters include nine fermion masses, three angles and a phase from the CKM matrix, as in Section 2.1.4. There are also coupling constants for electromagnetic, weak and strong sectors and the Higgs boson mass and vacuum expectation values described in Section 2.2. The particle content of the Standard Model is shown in Figure 2.1.

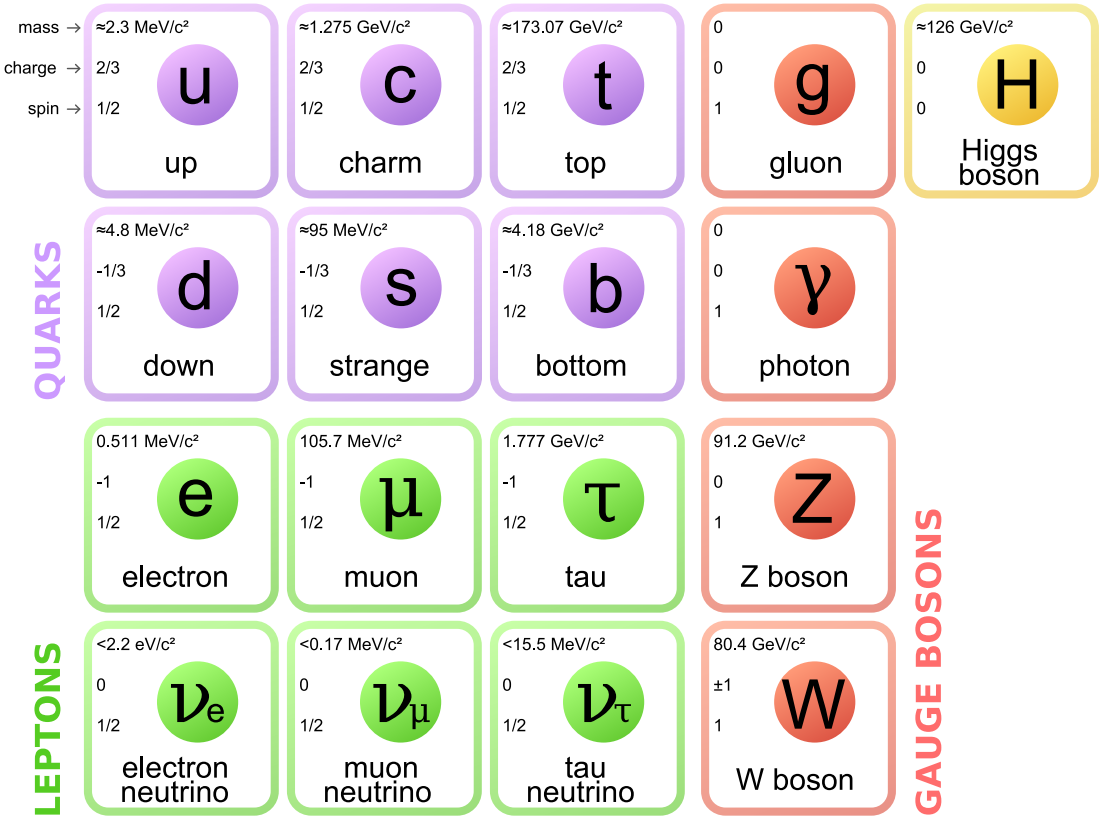

Figure 2.1: The particle content of the Standard Model [9]

There are two categories of particles: **fermions** and **bosons**. These are differentiated by their spin quantum numbers. Fermions have half-integer spin (that is half-integer multiples of $\hbar$), and follow Fermi-Dirac statistics [10]. Bosons have whole-integer spin (that is integer multiples of $\hbar$), and follow Bose-Einstein

statistics [11]. The fermions are further divided into two categories, **leptons** and **quarks**. All everyday matter is a combination of leptons and quarks, specifically up- and down-quarks (inside protons and neutrons) and electrons form the atoms. Table 2.1 summarises the physical and interaction properties of all of the fundamental Standard Model particles. The bosons act as the force mediators for each of the three interactions described above.

All charged fermions interact via the electromagnetic force, neutral fermions interact only via the weak force, and only the quarks interact via the strong force. In terms of mediator particles, the $W^{\pm}$ bosons themselves carry weak isospin and so they may couple to each other, or a Z^0 boson may couple to a $W^{\pm}$ boson. Analogously, the gluon itself carries colour charge and so may self-interact. The photon couples to particles having electric charge, but since it does not itself have electric charge, it may not couple to other photons. Every particle has a corresponding antiparticle, although some particles are their own antiparticles. Antiparticles have the same mass as their particle counterparts, but their other quantum numbers are inverted. For completeness it should be stated that there is also a gravitational interaction, but this is not formulated as part of the Standard Model, and so is not discussed here. Figure 2.2 shows the particle interactions in the Standard Model.

2.1.2 Gauge Theory Formulation

As already mentioned the Standard Model is a quantum field theory. Furthermore it is a locally gauge invariant theory, meaning that its Lagrangian density (representing the dynamics of the system, including interactions between fields) remains invariant under local gauge transformations. Local gauge invariance is the most general kind of gauge invariance, and is required to hold true as any physical phenomenon should behave in a way that is independent of any space-time dependent phase. These local gauge transformations are space-time dependent quantities. They may be simple phase factors, or more complex exponential products of matrices, depending on the theory under construction. In any case, the starting point for theory development is with a free particle Lagrangian (formally Lagrangian density, but commonly just referred to as Lagrangian). This free particle Lagrangian is typically invariant under global phase transformations, that is, phase transformations that are constant in space-

Particle	Electric change [e]	Mass [MeV]	Spin	Lifetime [s]	Colour Charge	Weak isospin (3rd comp.)	Weak hypercharge
e	-1	0.511	$\frac{1}{2}$	Stable	No	$-\frac{1}{2}$	-1
ν_e	0	$< 2 \times 10^{-6}$	$\frac{1}{2}$		No	$+\frac{1}{2}$	-1
μ	-1	105.7	$\frac{1}{2}$	2.197×10^{-6}	No	$-\frac{1}{2}$	-1
ν_μ	0	< 0.19	$\frac{1}{2}$		No	$+\frac{1}{2}$	-1
τ	-1	1776.8	$\frac{1}{2}$	290.6×10^{-15}	No	$-\frac{1}{2}$	-1
ν_τ	0	< 18.2	$\frac{1}{2}$		No	$+\frac{1}{2}$	-1
u	$+\frac{2}{3}$	2.3	$\frac{1}{2}$	Stable	Yes	$+\frac{1}{2}$	$+\frac{1}{3}$
d	$-\frac{1}{3}$	4.8	$\frac{1}{2}$	Stable	Yes	$-\frac{1}{2}$	$+\frac{1}{3}$
c	$+\frac{2}{3}$	1275	$\frac{1}{2}$	10^{-13}	Yes	$+\frac{1}{2}$	$+\frac{1}{3}$
s	$-\frac{1}{3}$	95	$\frac{1}{2}$	10^{-9}	Yes	$-\frac{1}{2}$	$+\frac{1}{3}$
t	$+\frac{2}{3}$	173500	$\frac{1}{2}$	10^{-24}	Yes	$+\frac{1}{2}$	$+\frac{1}{3}$
b	$-\frac{1}{3}$	4180	$\frac{1}{2}$	10^{-12}	Yes	$-\frac{1}{2}$	$+\frac{1}{3}$
γ	0	0	1	Stable	No	0	0
$W^\pm$	± 1	80385	1	10^{-25}	No	$\pm\frac{1}{2}$	± 1
Z^0	0	91188	1	10^{-25}	No	0	0
g	0	0	1	Stable	Yes	0	0
H	0	125500	0	?	No	$-\frac{1}{2}$	$+1$

Table 2.1: Table of particle properties. For the purposes of the weak interaction, all particles are listed with their left-handed values. The Higgs boson listing includes the current best measurement obtained by the ATLAS collaboration in the search for the Standard Model Higgs boson, and the other parameters are predicted.

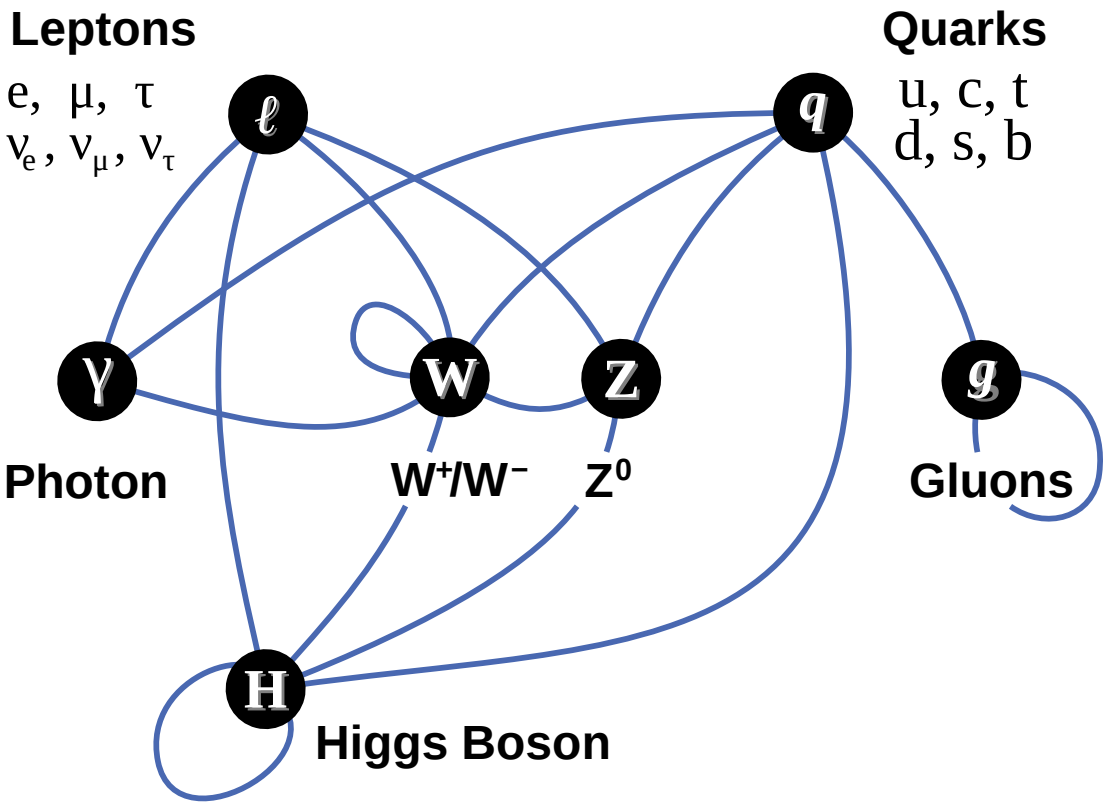

Figure 2.2: The particle interactions of the Standard Model [12]

time, and so do not depend on space-time co-ordinates. However, in order make the Lagrangians invariant under local phase transformations, extra terms must be added. The extra term added typically results in a new vector field (called a "gauge" field) that interacts with the existing fields in the Lagrangian. This gauge field must also have the ability to propagate freely without a coupling to other fields, and so an additional term is added representing this free gauge field. The final Lagrangian represents a physical system that is locally gauge invariant.

I will describe this process in detail for the simplest case of a $U(1)$ symmetry representing a lepton and an electromagnetic field. Leptons are spin-half particles and therefore described by the Dirac Lagrangian (Equation 2.1) which represents free fermions with mass m. The ψ terms are four component column vectors (known as spinors) containing four fermion wavefunctions representing spin up and down states for both particle and antiparticle. $\bar{\psi}$ is known as the adjoint spinor, and is given by $\psi^{\dagger}\gamma^{0}$. Where γ^{0} is one of the γ matrices [13].

$$\mathcal{L} = i\hbar c\, \overline{\psi}\gamma^{\mu}\partial_{\mu}\psi - mc^2\, \overline{\psi}\psi \tag{2.1}$$

This equation needs to be extended so that it is invariant under local gauge transformations, that is, transformations of the form in Equation 2.2. Where $\theta(x)$ is any function of the space-time variable x.

$$\psi \rightarrow e^{i\theta(x)}\psi \tag{2.2}$$

Applying this to the Dirac Lagrangian results in an extra term, as shown in Equation 2.3, meaning that original Lagrangian is not locally gauge invariant.

$$\mathcal{L} \rightarrow i\hbar c\, \overline{\psi}\gamma^{\mu}\partial_{\mu}\psi - mc^2\, \overline{\psi}\psi - \hbar c\, \overline{\psi}\gamma^{\mu}\psi\partial_{\mu}\theta(x) \tag{2.3}$$

The local invariance is only broken because of the derivative term, $\partial_{\mu}\theta$, and so the common approach is to replace this derivative with a more complex one known as a "covariant derivative", $\mathcal{D}_{\mu}$. The appropriate choice of which will permit the original Lagrangian to be locally gauge invariant. For this case the choice is given in Equation 2.4,

$$\mathcal{D}_{\mu} = \partial_{\mu} + i\frac{q}{\hbar c}A_{\mu}, \tag{2.4}$$

where q is electric charge and A_{μ} is the photon field. This results in Equation 2.5 for the Dirac Lagrangian:

$$\mathcal{L} = i\hbar c\, \overline{\psi}\gamma^{\mu}\mathcal{D}_{\mu}\psi - mc^2\, \overline{\psi}\psi \tag{2.5}$$

The gauge field A_{μ} introduced by the covariant derivative transforms under local gauge transformations as in Equation 2.6.

$$A_{\mu} \rightarrow A_{\mu} - \frac{\hbar c}{q}\partial_{\mu}\theta \tag{2.6}$$

After applying all of the above, the result is the locally gauge invariant Dirac Lagrangian in Equation 2.7.

$$\mathcal{L} = i\hbar c\, \overline{\psi}\gamma^{\mu}\partial_{\mu}\psi - q\overline{\psi}\gamma^{\mu}A_{\mu}\psi - mc^2\, \overline{\psi}\psi \tag{2.7}$$

The appearance of a new gauge field in the Dirac Lagrangian is now apparent

with the presence of A_μ. This term represents a coupling of the fermion fields ψ with this new gauge field, which will turn out to be the photon. The new gauge field in principle should be able to exist freely and independently of the fermion couplings and so an additional term representing this must be added to the Lagrangian. The gauge field is a vector field and so must follow the dynamics set out by the Proca Lagrangian [14] as in Equation 2.8,

$$\mathcal{L} = \frac{-1}{16\pi} F^{\mu\nu} F_{\mu\nu} + \frac{1}{8\pi} \left(\frac{m_\gamma c}{\hbar}\right)^2 A^\nu A_\nu, \tag{2.8}$$

where m_γ represents the photon mass term, and $F^{\mu\nu}$ is the QED field tensor defined in Equation 2.9.

$$F^{\mu\nu} = \partial^\mu A^\nu - \partial^\nu A^\mu \tag{2.9}$$

The second term in Equation 2.8 is not invariant under local gauge transformations, however since the photon is massless, this is irrelevant. The full Lagrangian representing fermion fields and the associated gauge fields (that is electrons, positrons and photons, i.e. QED) is then given by Equation 2.10.

$$\mathcal{L} = i\hbar c\, \overline{\psi} \gamma^\mu \partial_\mu \psi - mc^2\, \overline{\psi}\psi - q\overline{\psi}\gamma^\mu A_\mu \psi - \frac{1}{16\pi} F^{\mu\nu} F_{\mu\nu} \tag{2.10}$$

The procedure described above is the process for applying local gauge invariance to an electromagnetic system; the procedure for weak interactions and strong interactions follows a similar path, as described in the next sections. In fact, the weak and electromagnetic theories have been unified at high energies into one so-called electroweak theory, and this is presented in Section 2.1.4. The weak sector is unique in that special treatment has to be made to account for the gauge boson ($W^\pm$ and Z^0) masses as they are non-zero. For electromagnetism and the strong force, the gauge bosons are massless photons and gluons respectively. To account for the massive vector-bosons in the weak theory, the concept of spontaneous symmetry breaking will be introduced and the associated Higgs mechanism in Section 2.2.

2.1.3 Strong Sector

The theory of strong interactions is based on an $SU(3)$ symmetry. The interactions occur between massive colour charged fermions (called quarks) and

massless colour charged gauge bosons (called gluons). The theory is developed along the same principles as for QED in Section 2.1.2, but differences occur due to the fact that each quark can exist in three colour states of equal mass, and the fact that local gauge transformations take on a different form as $SU(3)$ is somewhat more complex than $U(1)$. The local gauge transformation takes the form:

$$\psi \rightarrow e^{i\lambda \cdot \mathbf{a}(x)}\psi \tag{2.11}$$

Where the $\mathbf{a}(x)$ terms are real scalars, and the λ terms are eight matrices which are the generators of $SU(3)$, and are called the Gell-Mann matrices [15]. The matrix $e^{i\lambda \cdot \mathbf{a}(x)}$ then has determinant 1 ($SU(3)$). The covariant derivative, $\mathcal{D}_\mu$, for the strong sector (with q now representing colour charge) is shown in Equation 2.12.

$$\mathcal{D}_\mu = \partial_\mu + i\frac{q}{\hbar c}\lambda \cdot \mathbf{A}_\mu \tag{2.12}$$

And the resulting Lagrangian is shown in Equation 2.13.

$$\mathcal{L} = i\hbar c\overline{\psi}\gamma^\mu\partial_\mu\psi - q\overline{\psi}\gamma^\mu\psi\lambda \cdot \mathbf{A}_\mu - mc^2\overline{\psi}\psi \tag{2.13}$$

As can be seen the requirement for local gauge invariance led to the introduction of eight gauge fields, $\mathbf{A}_\mu$. These are coupled to the fermion fields, ψ. Additionally there is a term representing the free propagation of these gauge fields, of the form in Equation 2.14.

$$\mathcal{L} = -\frac{1}{16\pi}\mathbf{G}^{a\mu\nu} \cdot \mathbf{G}^a_{\mu\nu} \tag{2.14}$$

where:

$$\mathbf{G}^a_{\mu\nu} = \partial_\mu \mathbf{A}^a_\nu - \partial_\nu \mathbf{A}^a_\mu - \frac{2q}{\hbar c}\left(\mathbf{A}_\mu \times \mathbf{A}_\nu\right)^a \tag{2.15}$$

and since the $SU(3)$ cross-product is defined as:

$$\left(\mathbf{A}_\mu \times \mathbf{A}_\nu\right)^a = f^{abc}\mathbf{A}^b_\mu \mathbf{A}^c_\nu \tag{2.16}$$

where f^{abc} are the structure constants of $SU(3)$, then:

$$\mathbf{G}^a_{\mu\nu} = \partial_\mu \mathbf{A}^a_\nu - \partial_\nu \mathbf{A}^a_\mu - \frac{2q}{\hbar c} f^{abc} \mathbf{A}^b_\mu \mathbf{A}^c_\nu \tag{2.17}$$

This leads to the full QCD Lagrangian of strong interactions given in Equation 2.18. This Lagrangian applies for each quark flavour, and so there are six copies with different masses required to represent the full strong sector. Each Lagrangian takes account of all three possible colour charges for a given quark flavour.

$$\mathcal{L} = i\hbar c\, \overline{\psi}\gamma^\mu \partial_\mu \psi - q\, \overline{\psi}\gamma^\mu \psi \lambda \cdot \mathbf{A}_\mu - mc^2\, \overline{\psi}\psi - \frac{1}{16\pi} \mathbf{G}^{\mu\nu} \cdot \mathbf{G}_{\mu\nu} \tag{2.18}$$

This Lagrangian describes all the same kinds of interactions as we have seen for electromagnetism, with q now representing the colour charge coupling, rather than the electric charge. There is one additional component. There is a term in $F^{\mu\nu}$ related to the cross product of the gauge fields. This cross product leads to terms of the form $A^\mu A^\nu$ which are interactions between the gauge fields, or gluons, themselves. This term is responsible for the gluon self-interactions observed in the strong sector. This is consistent with the fact that gluons themselves have colour charge (or more specifically a colour and an anticolour charge), and so couple to other gluons.

2.1.4 Electroweak Sector

The theory of electroweak interactions, first postulated by Weinberg, Salam and Glashow [16, 17, 18], is an $SU(2) \otimes U(1)$ symmetry. The $SU(2)$ group representing the weak interactions, and the $U(1)$ group representing the electromagnetic ones. The theories of leptonic electroweak interactions and quark electroweak interactions are described separately below.

The starting point is the massless Dirac Lagrangian.

$$\mathcal{L} = i\hbar c\, \overline{\psi}\gamma^\mu \partial_\mu \psi \tag{2.19}$$

Also note that we anticipate some left-handed, right-handed asymmetry of the weak interaction by defining the Dirac spinors as composites of left- and right-handed components. Left-handed means a chirality of -1, and right-handed

means a chirality of +1, where chirality is the projection of the particle's spin onto its direction of motion.

The definitions of the projection operators are shown in Equations 2.20 and 2.21.

$$\psi_{\mathrm{L}} = \frac{1}{2}\left(1 - \gamma^5\right)\psi \tag{2.20}$$

$$\psi_{\mathrm{R}} = \frac{1}{2}\left(1 + \gamma^5\right)\psi \tag{2.21}$$

The Lagrangian becomes:

$$\mathcal{L} = i\hbar c\,\overline{\psi_{\mathrm{L}}}\gamma^{\mu}\partial_{\mu}\psi_{\mathrm{L}} + i\hbar c\,\overline{\psi_{\mathrm{R}}}\gamma^{\mu}\partial_{\mu}\psi_{\mathrm{R}} \tag{2.22}$$

Leptonic Electroweak Interactions

The theory of electroweak interactions with leptons is constructed assuming the neutrinos are massless, however evidence [19] shows that neutrinos in fact do have a non-zero mass. The leptons can be combined in isospin doublets, as follows:

$$\psi = \begin{pmatrix} \nu \\ e \end{pmatrix} \tag{2.23}$$

$$\psi_{\mathrm{L}} = \begin{pmatrix} \nu_{\mathrm{L}} \\ e_{\mathrm{L}} \end{pmatrix} \tag{2.24}$$

$$\psi_{\mathrm{R}} = \begin{pmatrix} 0 \\ e_{\mathrm{R}} \end{pmatrix} \tag{2.25}$$

As the neutrinos are considered massless, they must have a chirality of -1, and hence be "left-handed". There is therefore no right-handed neutrino field. Antineutrinos are "right-handed" with a chirality of +1.

There are three charges in the electroweak theory responsible for coupling of gauge bosons to particles. They are electric charge, Q, weak isospin, I, and weak hypercharge, Y. I^3 is the third component of weak isospin. They are related by the Gell-Mann Nishijima formula given in Equation 2.26. Table. 2.2 shows the values of these charges in the leptonic sector.

$$\mathrm{Q} = \mathrm{I}_3 + \frac{\mathrm{Y}}{2} \tag{2.26}$$

Particle	**Electric charge, Q [e]**	**Weak isospin (3rd comp.), I_3**	**Weak hypercharge, Y**
ν_{L}	0	$+\frac{1}{2}$	-1
e_{L}	-1	$-\frac{1}{2}$	-1
e_{R}	-1	0	-2

Table 2.2: Charges of the leptonic electroweak interaction.

These charges are more accurately known as coupling strengths. The magnitude of these coupling strengths determines how strongly a particle field may couple to (interact with) a gauge field. The types of coupling strengths represent the types of interactions. For example the electric charge represents couplings between leptons and the photon, the weak isospin charges represent couplings between the leptons and the $W^{\pm}$ bosons, and the weak hypercharge is more complicated and involves electroweak mixing, as will be discussed subsequently.

The procedure described in Section 2.1.2 by imposing local gauge invariance, generating gauge fields and introducing their non-coupled interaction terms into the Lagrangian results in the Lagrangian for the electroweak-leptonic interactions given by Equation 2.27.

$$\begin{aligned}\mathcal{L} = {} & i\hbar c\overline{\psi_{\mathrm{R}}}\gamma^{\mu}\left(\partial_{\mu} + \frac{ig_{\mathrm{B}}}{2}B_{\mu}\right)\psi_{\mathrm{R}} \\ & + i\hbar c\overline{\psi_{\mathrm{L}}}\gamma^{\mu}\left(\partial_{\mu} + \frac{ig_{\mathrm{B}}}{2}B_{\mu} + \frac{ig_{\mathrm{W}}}{2}\tau^{1}W_{\mu}^{1} + \frac{ig_{\mathrm{W}}}{2}\tau^{2}W_{\mu}^{2} + \frac{ig_{\mathrm{W}}}{2}\tau^{3}W_{\mu}^{3}\right)\psi_{\mathrm{L}} \\ & - \frac{1}{4}f^{\mu\nu}f_{\mu\nu} - \frac{1}{8}\mathrm{Tr}\left(F^{\mu\nu}F_{\mu\nu}\right)\end{aligned} \tag{2.27}$$

In this equation, g_B and g_W are the coupling strengths for the B and W fields respectively. τ^n are the Pauli matrices of $SU(2)$, given by:

$$\tau^1 = \begin{pmatrix} 0 & 1 \\ 1 & 0 \end{pmatrix} \tau^2 = \begin{pmatrix} 0 & -i \\ i & 0 \end{pmatrix} \tau^3 = \begin{pmatrix} 1 & 0 \\ 0 & -1 \end{pmatrix} \tag{2.28}$$

And:

$$f_{\mu\nu} = \partial_\mu B_\nu - \partial_\nu B_\mu \tag{2.29}$$

$$F^i_{\mu\nu} = \partial_\mu W^i_\nu - \partial_\nu W^i_\mu - g_W \epsilon^{ijk} W^j_\mu W^k_\nu \tag{2.30}$$

This Lagrangian has a few interesting features. Firstly the B_μ field is the gauge field introduced by requiring local invariance of the $U(1)$ symmetry, and the $\mathbf{W}_\mu$ gauge fields have come from the same requirement on the $SU(2)$ symmetry. $\mathbf{W}_\mu$ is a three-component object containing the fields W^1_μ, W^2_μ and W^3_μ. It can be seen from the Lagrangian that the right-handed fermion fields only interact with the B_μ field, and that the left-handed fermion fields interact with both the B_μ and $\mathbf{W}_\mu$ fields. There is an obvious asymmetry between right-handed and left-handed fermion interactions. The penultimate term represents the free propagation of the B_μ field, and the last term represents the free propagation of the $\mathbf{W}_\mu$ fields.

It turns out that these four gauge fields are not the fields representing the physical particles we observe in particle physics detectors, but rather a mixture manifest themselves as those physical particles. Specifically:

$$W^+_\mu = \frac{W^1_\mu - iW^2_\mu}{\sqrt{2}} \tag{2.31}$$

$$W^-_\mu = \frac{W^1_\mu + iW^2_\mu}{\sqrt{2}} \tag{2.32}$$

$$Z^0_\mu = -B_\mu \sin\theta_\mathrm{W} + W^3_\mu \cos\theta_\mathrm{W} \tag{2.33}$$

$$A_\mu = B_\mu \cos\theta_\mathrm{W} + W^3_\mu \sin\theta_\mathrm{W} \tag{2.34}$$

which are the familiar bosons of the electroweak force. Where A_μ is the massless photon field. The angle θ_W is known as the Weinberg angle, or weak mixing angle and is given by Equation 2.35.

$$\tan\theta_\mathrm{W} = \frac{g_\mathrm{W}}{g_\mathrm{B}} \tag{2.35}$$

Quark Electroweak Interactions

The electroweak force also couples to quarks, and the electroweak coupling strengths for the quarks have the values given in Table. 2.3.

Particle	**Electric charge, Q [e]**	**Weak isospin (3rd comp.), I_3**	**Weak hypercharge, Y**
u_{L}	$+\frac{2}{3}$	$+\frac{1}{2}$	$+\frac{1}{3}$
u_{R}	$+\frac{2}{3}$	0	$+\frac{4}{3}$
d_{L}	$-\frac{1}{3}$	$-\frac{1}{2}$	$+\frac{1}{3}$
d_{R}	$-\frac{1}{3}$	0	$-\frac{2}{3}$

Table 2.3: Charges of the quark electroweak interaction. u represents up-type quarks (u, c, t) and d represents down-type quarks (d, s, b).

Conservation of lepton numbers requires, that in the lepton sector, there is no coupling between a $W^{\pm}$ boson and fermion doublets in different generations. However in the quark sector this restriction is not present. It is more probable that coupling occurs between a $W^{\pm}$ boson and quarks of the same generation than between different generations, but both are possible. The mechanism for this was first postulated by Cabibbo in 1963 [20] explaining the couplings between the bosons and the three lightest quark flavours, up (u), down (d) and strange (s). This was later extended by Glashow, Iliopoulos and Maiani (GIM) in 1970 [21] to include the fourth lightest quark, the charm (c). Finally these principles were extended once again to include the third and final generation of quarks, the top (t) and bottom (b), by Kobayashi and Maskawa in 1973 [22].

The GIM coupling mechanism postulates that the $W^{\pm}$ bosons couple not to the "physical" quark states (e.g. d), but rather to some other complex state (d') which is a mixture of the physical quark states and given by Equation 2.36.

$$d' = d\cos\theta_C + s\sin\theta_C \tag{2.36}$$

The angle θ_C is known as the Cabibbo angle. These relationships between the weak states and physical states for the three quark generations can be written in matrix form as in Equation 2.37. This is known as the CKM (Cabibbo-Kobayashi-Maskawa) matrix. In the Standard Model with three quark generations, this matrix is unitary, meaning it has four free parameters, one of which has a complex phase.

$$\begin{pmatrix} d' \\ s' \\ b' \end{pmatrix} = \begin{pmatrix} V_{ud} & V_{us} & V_{ub} \\ V_{cd} & V_{cs} & V_{cb} \\ V_{td} & V_{ts} & V_{tb} \end{pmatrix} \begin{pmatrix} d \\ s \\ b \end{pmatrix} \tag{2.37}$$

The CKM matrix, is often represented in the Wolfenstein parameterisation with the four parameters λ, A, ρ and η as shown in Equation 2.38 [23]:

$$V_{CKM} = \begin{pmatrix} 1 - \frac{\lambda^2}{2} & \lambda & A\lambda^3(\rho - i\eta) \\ -\lambda & 1 - \frac{\lambda^2}{2} & A\lambda^2 \\ A\lambda^3(1 - \rho - i\eta) & -A\lambda^2 & 1 \end{pmatrix} + \mathcal{O}(\lambda^4) \tag{2.38}$$

The magnitudes of the elements in the CKM matrix can be obtained from a constrained fit to all data, requiring the condition that the matrix is unitary, and are given below [23]:

$$V_{CKM} = \begin{pmatrix} 0.97427 \pm 0.00015 & 0.22534 \pm 0.00065 & 0.00351^{+0.00015}_{-0.00014} \\ 0.22520 \pm 0.00065 & 0.97344 \pm 0.00016 & 0.0412^{+0.0011}_{-0.0005} \\ 0.00867^{+0.00029}_{-0.00031} & 0.0404^{+0.0011}_{-0.0005} & 0.999146^{+0.000021}_{-0.000046} \end{pmatrix} \tag{2.39}$$

The Feynman diagrams of Figure 2.3, show that there is now a vertex factor present in the matrix element which comes directly from the CKM matrix. A cross-generational coupling, as in Figure 2.3(b), includes the term V_{us} from Equation 2.37 instead of V_{ud} for the same-generational coupling of Figure 2.3(a). The resulting matrix element is scaled by this factor, and hence the probability of this process occurring would be reduced compared to the same-generational one. As discussed above and demonstrated with the Wolfenstein parameterisation of Equation 2.38 there are four free parameters in the matrix, three quark-mixing angles and one complex phase. This complex phase leads to a difference in the rates at which a process, and its antiparticle equivalent process occur, and hence is responsible for CP (Charge-Parity) violation. CP is the application of both charge-conjugation and parity transformations. Charge-conjugation inverts a particles quantum numbers, thereby replacing a particle with its antiparticle. Parity transformations invert the sign of all spatial coordinates.

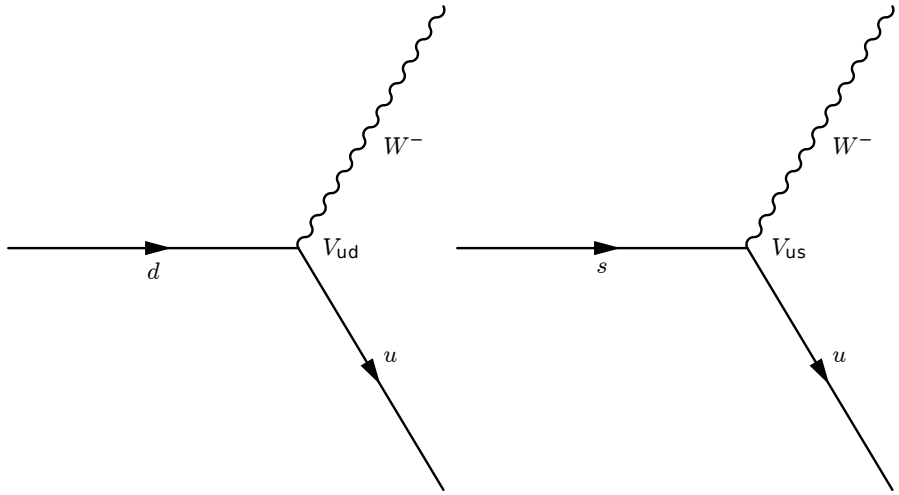

(a) $d \to u + W^-$ (b) $s \to u + W^-$

Figure 2.3: $W^{\pm}$ bosons coupling to quarks.

2.2 The Higgs Boson and Higgs Mechanism

The Lagrangians derived thus far represent massless particles, but both the fermions and the electroweak gauge vector bosons are known to be massive. The Higgs mechanism (utilising spontaneous symmetry breaking) was introduced in 1964 by Peter Higgs [2], Francois Englert and Robert Brout [3] and Gerald Guralnik, Carl Hagan and Tom Kibble [4] to explain the generation of these masses. Higgs postulated that there existed a field throughout the universe, now known as the Higgs field. He further postulated that the functional form of the potential representing this field was such that it led to symmetry breaking. The Higgs field exists in the form of a complex scalar doublet, as in Equation 2.40.

$$\phi = \begin{pmatrix} \phi_1 \\ \phi_2 \end{pmatrix} \tag{2.40}$$

As usual it is required that a Lagrangian formed from the Higgs fields be invariant under local gauge transformations. The choice of which can be exploited such that:

$$\phi = \begin{pmatrix} 0 \\ \phi_0 + \frac{h(x)}{\sqrt{2}} \end{pmatrix} \tag{2.41}$$

ϕ_0 is the ground state (also called vacuum expectation value) of the Higgs field and a non-zero value permits the symmetry to be broken. $h(x)$ is a fluctuation of the Higgs field around this ground state. From the scalar doublet configuration, it is clear that the Higgs field has weak isospin $= \frac{1}{2}$ and the lower component of the doublet has a third component of weak isospin of $-\frac{1}{2}$. Since it is not electrically charged, its weak hypercharge is $+1$.

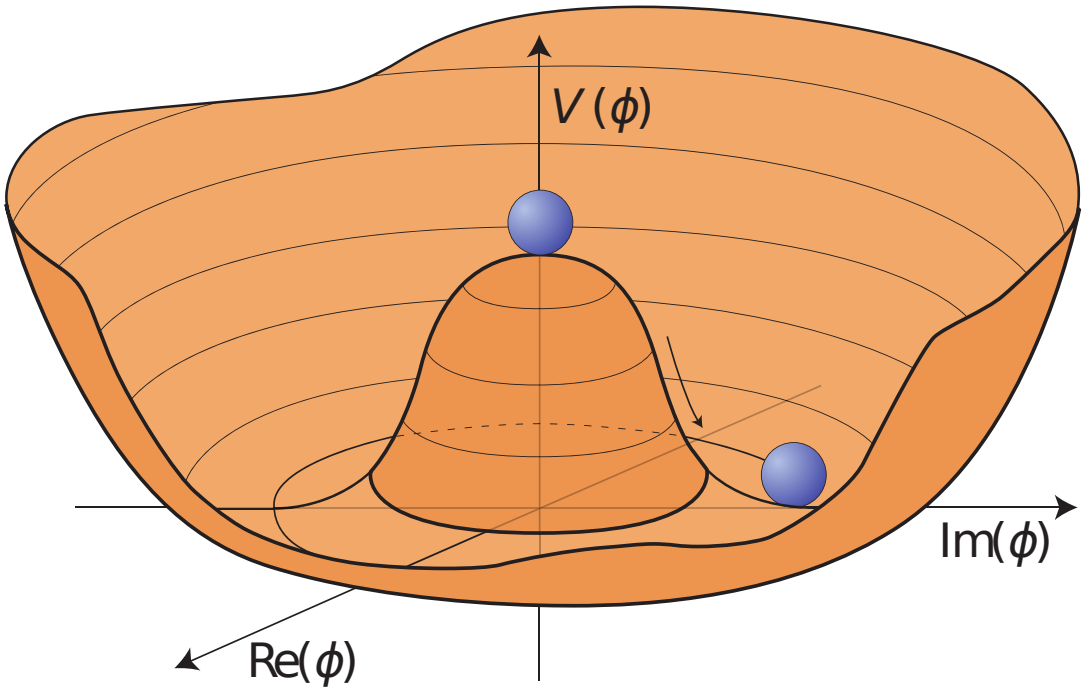

Figure 2.4: The shape of the Higgs potential. [24]

The form of the potential is as in Equation 2.42, and in Figure 2.4.

$$\mathcal{U} = \mu^2\phi^\dagger\phi + \lambda\left(\phi^\dagger\phi\right)^2 \tag{2.42}$$

The sign of μ^2 determines the shape of the potential and whether it can provide symmetry breaking or not. For symmetry breaking it is required that $\mu^2 < 0$. λ accounts for a quartic Higgs self-interaction, it is required that $\lambda > 0$. This is the simplest form of potential for which symmetry breaking can occur, but not the only one. In fully expanded form (around the minimum):

$$\begin{aligned}\mathcal{U} = &\left(\mu^2\phi_0^2 + \lambda\phi_0^4\right) + \left(\sqrt{2}\,\mu^2\phi_0 + 2\sqrt{2}\,\lambda\phi_0^3\right) h \\ &+ \left(\frac{\mu^2}{2} + 3\lambda\phi_0^2\right) h^2 + \sqrt{2}\,\lambda\phi_0\, h^3 + \frac{\lambda}{4}h^4\end{aligned} \tag{2.43}$$

The minimum of this function occurs at:

$$\phi_0 = \sqrt{-\frac{\mu^2}{2\lambda}} \tag{2.44}$$

The mass term of a scalar field follows that of the Klein-Gordon equation, and is of the form:

$$\text{Mass term} = -\frac{1}{2}M_{\text{h}}^2\,\phi^2 \tag{2.45}$$

Therefore the term in Equation 2.43 of second order in h yields the mass of the excitation. As:

$$M_{\text{h}} = \sqrt{-2\mu^2} \tag{2.46}$$

As discussed, for spontaneous symmetry breaking, $\mu^2 < 0$. Because the Higgs boson mass is a real number, there is a minus sign under the square root.

The complex scalar doublet Higgs field, and the particular form of the Higgs potential, result in an excitation of the Higgs field (a Higgs boson) of mass given by Equation 2.46. From Equation 2.43, it can be seen that there are terms in h^3 and h^4 meaning that the Higgs boson may also interact with (couple to) itself, as shown in Figure 2.5.

2.2.1 Giving Mass to the Gauge Bosons

The Higgs mechanism not only is responsible for the generation of a massive self-interacting scalar boson, but also in giving mass to the weak bosons and fermions. In this section we shall consider how the gauge bosons acquire their mass, and in Section 2.2.2, we consider how the fermion masses are acquired via the Higgs mechanism.

This is achieved by applying the electroweak covariant derivative to the Higgs field, ϕ. The electroweak covariant derivative, from Equation 2.27 applied to the

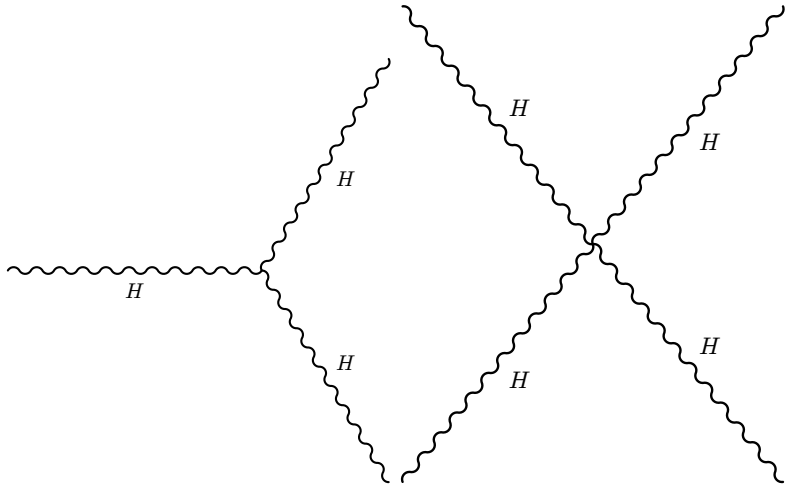

(a) Tri Higgs boson coupling (b) Quad Higgs boson coupling

Figure 2.5: Higgs boson self coupling Feynman diagrams.

Higgs field is given by Equation 2.47.

$$\mathcal{D}_\mu\phi = \partial_\mu\phi + \frac{ig_\mathrm{B}}{2}B_\mu\phi + \frac{ig_\mathrm{W}}{2}\tau^1 W_\mu^1\phi + \frac{ig_\mathrm{W}}{2}\tau^2 W_\mu^2\phi + \frac{ig_\mathrm{W}}{2}\tau^3 W_\mu^3\phi \tag{2.47}$$

Computing $(\mathcal{D}_\mu\phi)^\dagger(\mathcal{D}_\mu\phi)$, and using the substitutions given in Equations 2.31 - 2.34. The following terms are present in the Lagrangian:

$$\left(\frac{g_\mathrm{B}^2 + g_\mathrm{W}^2}{4}\right)\phi_0^2\, Z_\mu Z^\mu \tag{2.48}$$

$$\frac{g_\mathrm{W}^2}{2}\phi_0^2\, W_\mu^- W^{+\mu} \tag{2.49}$$

There is no term in $A^\mu A_\mu$, indicating the photon does indeed have zero mass. The masses then are:

$$M_\mathrm{Z} = \frac{\sqrt{g_\mathrm{B}^2 + g_\mathrm{W}^2}}{2}\phi_0 \tag{2.50}$$

$$M_\mathrm{W} = \frac{g_\mathrm{W}\phi_0}{2} \tag{2.51}$$

which can be related to the $\sin^2\theta_\mathrm{W}$ parameter by Equation 2.52.

$$\sin^2\theta_{\mathrm{W}} = 1 - \left(\frac{M_{\mathrm{W}}}{M_{\mathrm{Z}}}\right)^2 \approx 0.222 \tag{2.52}$$

2.2.2 Giving Mass to the Fermions

The masses acquired by the fermions occur through the addition of a Yukawa term into the Lagrangian, as given in Equation 2.53. g is the Yukawa coupling strength and represents the strength of the interaction.

$$\mathcal{L}_{\mathrm{Yukawa}} = -g\left(\overline{\psi_{\mathrm{L}}}\phi\psi_{\mathrm{R}} + \overline{\psi_{\mathrm{R}}}\phi^{\dagger}\psi_{\mathrm{L}}\right) \tag{2.53}$$

Which ultimately results in a term of the form:

$$\mathcal{L}_{\mathrm{Mass}} = -g\phi_0\left(\overline{e_{\mathrm{L}}}e_{\mathrm{R}} + \overline{e_{\mathrm{R}}}e_{\mathrm{L}}\right) \tag{2.54}$$

and in the mass for each fermion flavour, f:

$$M_{\mathrm{f}} = -g_{\mathrm{f}}\phi_0 \tag{2.55}$$

2.3 Higgs Boson Production, Decays and Electroweak Measurements

2.3.1 Higgs Boson Production at Hadron Colliders

At a proton-proton (pp) collider such as the LHC, Higgs bosons may be produced by interactions between the partons (valence or sea) of both of the incident protons. This means that both quark-quark (qq) and gluon-gluon (gg) interactions can lead to the production of Higgs bosons at the LHC.

The most common methods of production are shown in Figure 2.6 and their cross-sections, as a function of Higgs boson mass, are shown in Figure 2.7. The process with the highest cross-section is that of gluon-gluon fusion, where incident gluons couple to a top-quark loop which emits a Higgs boson, as shown in Figure 2.6(a), and as is the case with all hadron collider processes, additional hadronic activity, hadrons showers etc, will be produced. The second most common process is the vector-boson fusion mechanism, whereby two incident quarks emit vector bosons which annihilate to form a Higgs boson and a pair

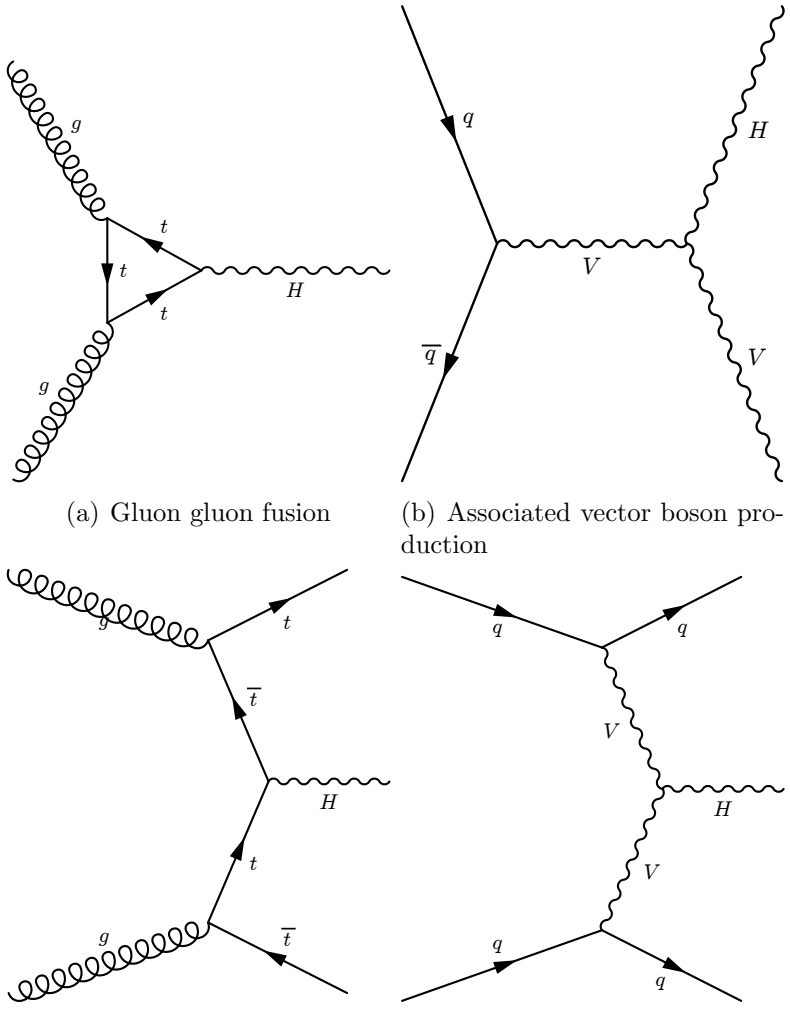

(a) Gluon gluon fusion

(b) Associated vector boson production

(c) Associated quark production

(d) Vector boson fusion

Figure 2.6: Higgs production process Feynman diagrams.

of forward jets, as shown in Figure 2.6(d). The third most common production process is that of production in association with a vector boson. This proceeds from the annihilation of a quark-antiquark pair to produce a virtual vector boson, which then emits a Higgs boson, leaving a Higgs boson and a vector boson, as shown in Figure 2.6(b). Finally there is also an associated production mechanism leading to the production of a Higgs boson with heavy quarks, such as $t\bar{t}$. This process involves gluons interacting with top quark pairs, which then emit a Higgs boson, and a $t\bar{t}$ pair remains also, as shown in Figure 2.6(c). The total Higgs boson production cross-section is dependent upon the centre-of-mass energy of

the collider, and increases with energy as shown in Figure 2.8. Increasing the centre-of-mass energy from 8 TeV to 14 TeV, would result in an increase in the Higgs boson production cross-section of $\sim$ 2.5 times at low Higgs boson mass, and $\sim$ 5 times at higher mass [25].

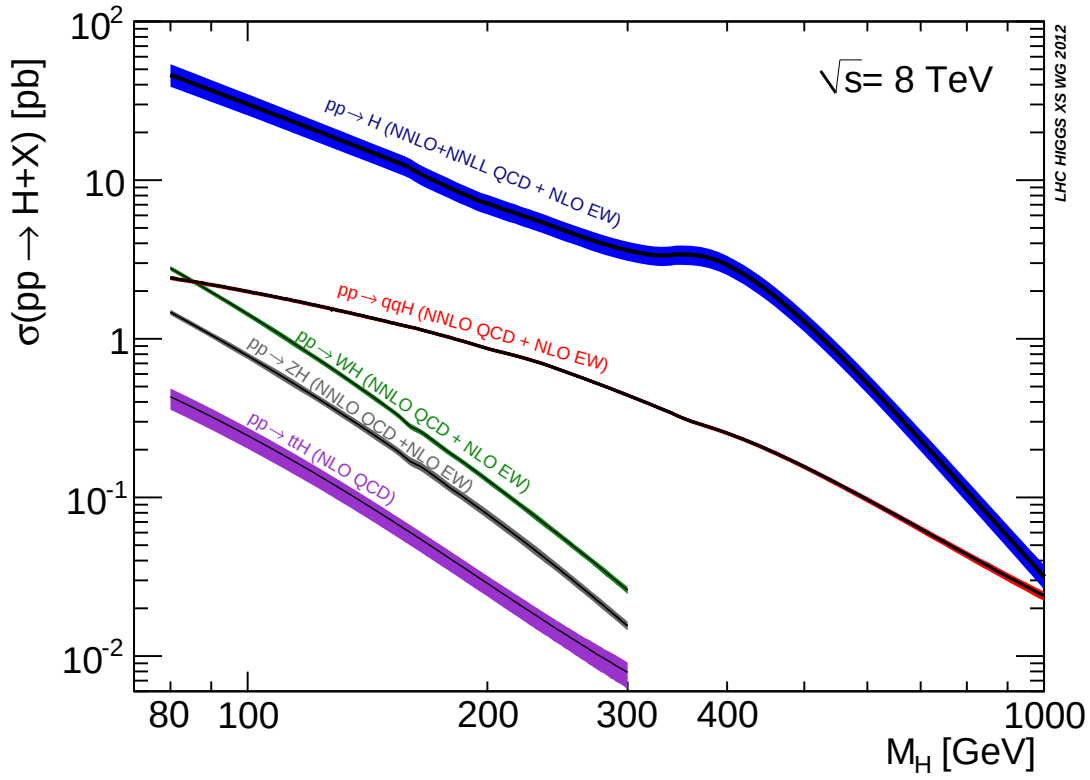

Figure 2.7: Theoretical predictions [25] for the production cross-section of a Standard Model Higgs boson at 8 TeV.

2.3.2 Higgs Boson Decay Channels

The possible decay mechanisms for a Standard Model Higgs boson are shown in Figure 2.9 as a function of Higgs boson mass. As can be seen from the figure, there are many possible Higgs boson decays that dominate different regions of the Higgs boson mass spectrum. This is due to there being some decays which are energetically forbidden for certain Higgs boson masses, and also the fact that the Higgs boson coupling strength is greater for higher mass particles. For a Higgs boson mass, $M_H \leq 140$ GeV, a so-called "low-mass Higgs boson", the

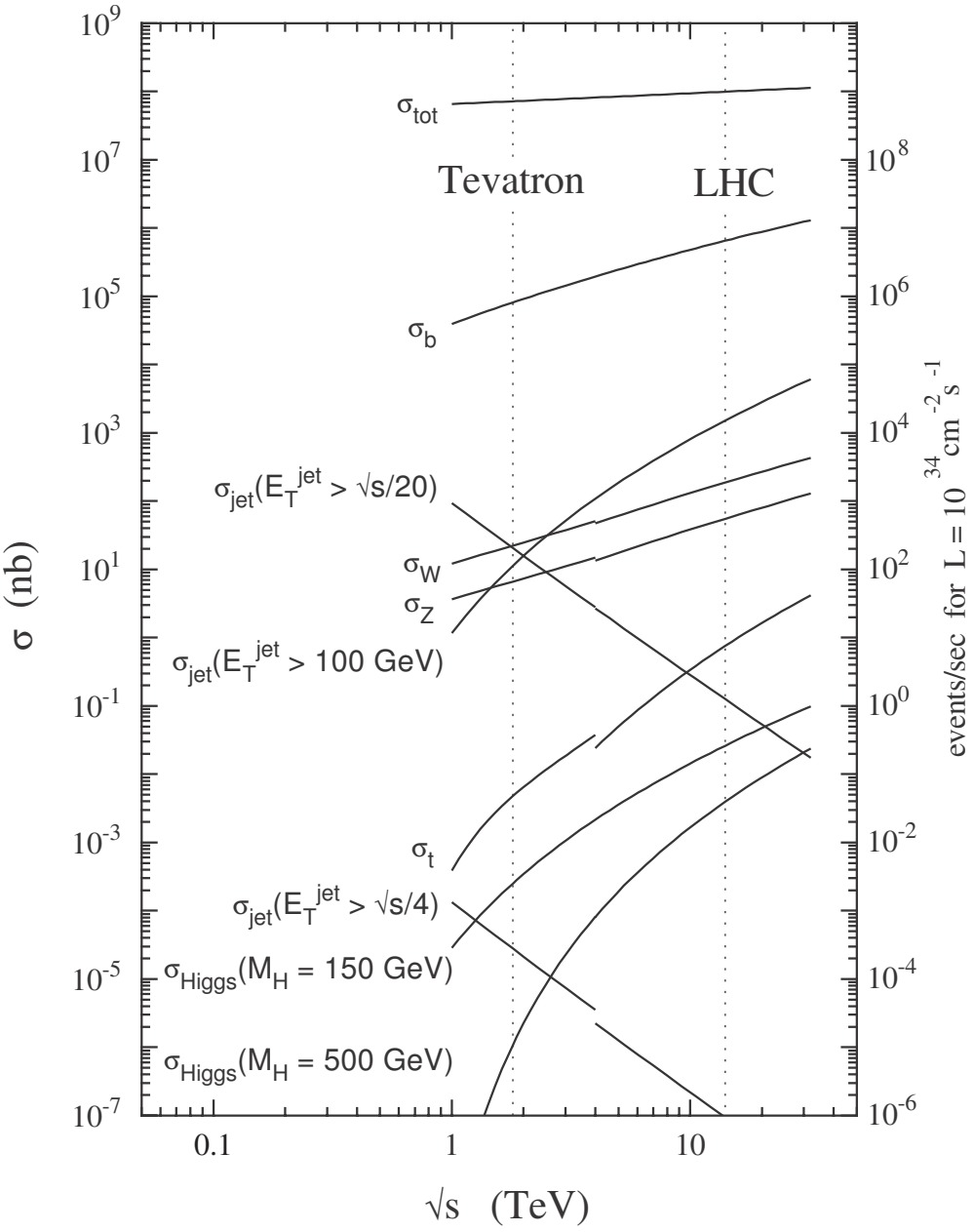

Figure 2.8: Standard Model cross-sections for LHC (proton-proton collisions) and Tevatron (proton-antiproton collisions) and event rates based on a luminosity of $10^{34}\mathrm{cm}^{-2}\mathrm{s}^{-1}$ [8].

$H \to b\bar{b}$ process dominates, being an order of magnitude more probable than the $H \to \tau^+\tau^-$, $H \to gg$, and $H \to c\bar{c}$ processes. In the high mass regime where $M_H > 140$ GeV, the $H \to W^+W^-$ and $H \to ZZ$ processes begin to dominate. For $M_H > 350$ GeV the $H \to t\bar{t}$ process may occur.

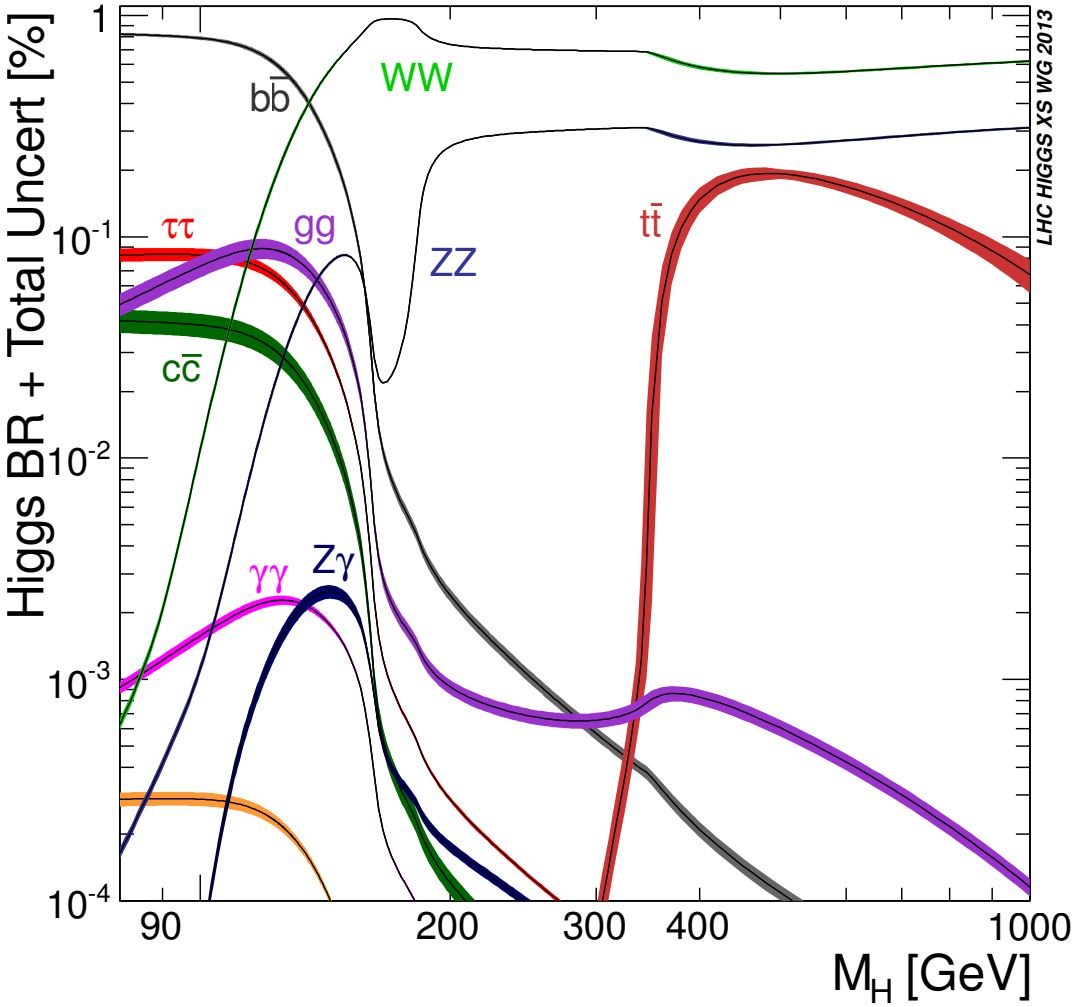

Figure 2.9: Theoretical predictions [26] for the branching ratios of a Standard Model Higgs boson as a function of Higgs boson mass.

Many of the final state decay products will result in clusters of strongly interacting particles known as "jets". These objects are described in detail in Section 5.1.

2.3.3 Electroweak Physics Results on the Higgs Boson Mass

Direct Higgs boson exclusions have been found from the LEP [27] (Large Electron Positron collider, the predecessor to the LHC) and Tevatron [28] experiments. The Tevatron analyses have excluded the region $158 < M_{\mathrm{H}} < 175$ GeV [29], and LEP analyses have excluded the region below 114.4 GeV [30], both at the 95% confidence level. Global fits to electroweak data have shown a preference for a "low-mass Higgs boson" and result in predictions for the Higgs boson mass such as those in Figure 2.10. Figure 2.10(a) shows the fit result when the exclusions from direct LEP and Tevatron searches (shown in grey) are not taken into account in the fit. The precise results from this fit, done by the GFitter collaboration [5], predict the most probable Higgs boson mass to be $\sim$ 90 GeV, which is clearly excluded by LEP searches already. Figure 2.10(b) shows the results of the fit that does take into account these exclusion boundaries, and results in a most likely Higgs boson mass of $\sim$ 120 GeV [5].

2.3.4 LHC Results in the Search for the Higgs Boson

In July, 2012, results [6, 7] published by the ATLAS and CMS collaborations identified a new particle, having properties consistent with those of a predicted Standard Model Higgs boson, with a significance in excess of 5 σ and a mass of 125 - 126 GeV. The specific ATLAS result was 5.9 σ at 126 GeV, as shown in Figure 2.11. The main channels included in this analysis were $H \to ZZ^* \to l\bar{l}l\bar{l}$, $H \to WW \to l\bar{\nu}q\bar{q}$ and $H \to \gamma\gamma$. These results led to the award of the 2013 Nobel Prize in physics to François Englert and Peter Higgs.

2.4 Summary

The Standard Model theory is quantum field theory based on the principle of local gauge invariance. The matter particles are introduced into the Standard Model and represented as fields, with some coupling strength parameters defining how they may interact, and with what other particles. The local gauge invariance requirement introduces additional "gauge" fields into the theory, and it is these gauge fields that represent the mediator particles of the three Standard Model

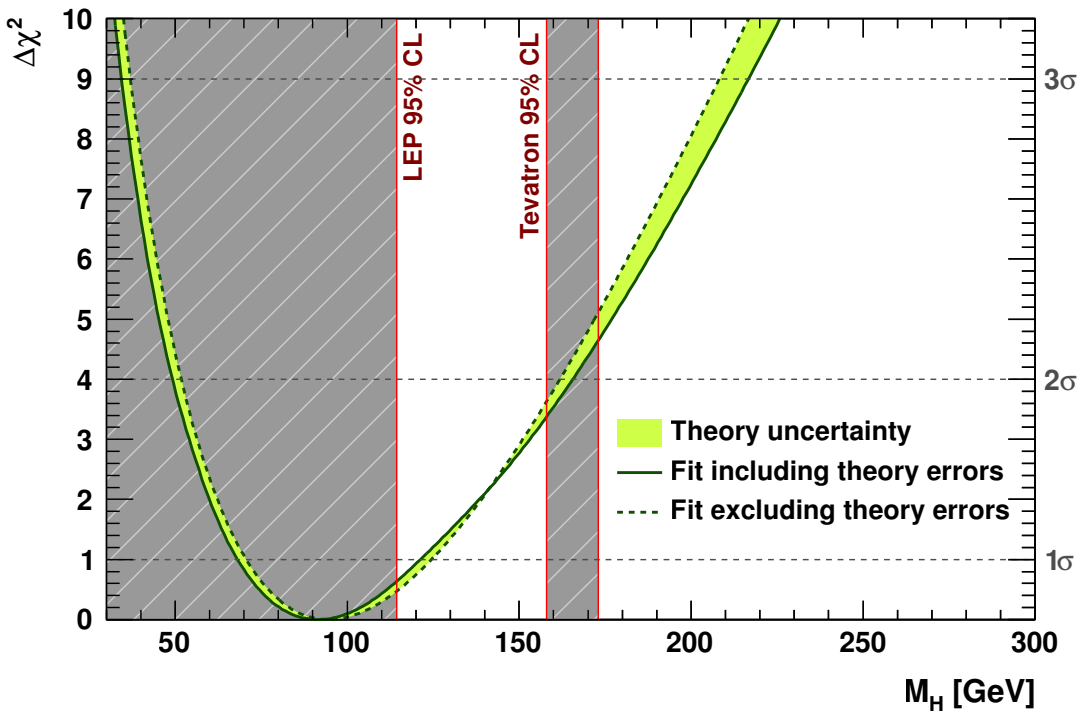

(a) Not taking account of direct Higgs boson mass constraints.

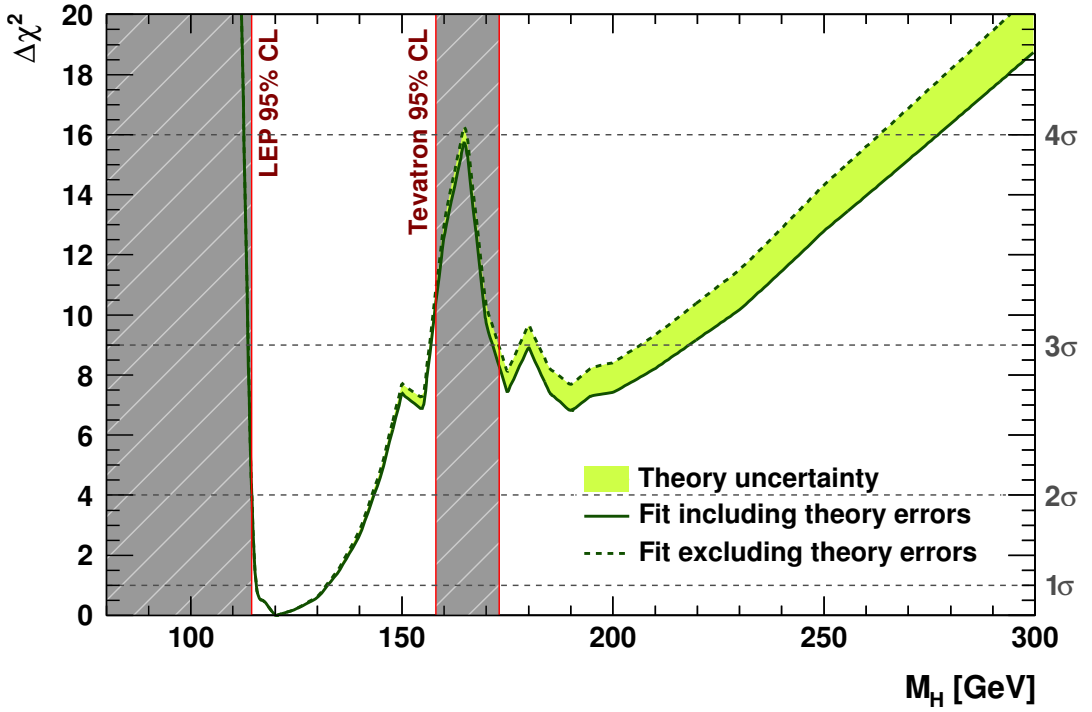

(b) Taking account of direct Higgs boson mass constraints.

Figure 2.10: Results of fits to electroweak data showing the most probable Standard Model Higgs boson mass. [5]

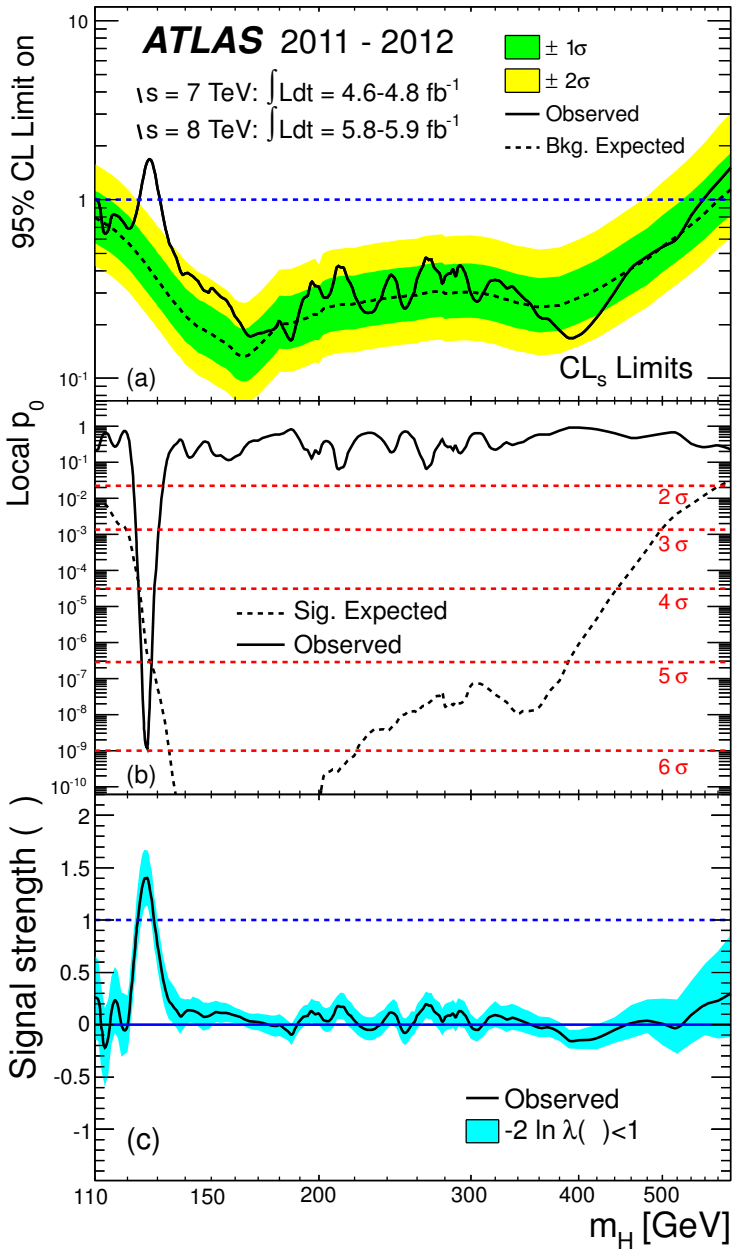

Figure 2.11: Results from the ATLAS experiment in the search for the Higgs boson [6]. (a) shows the CLs exclusion limit set at the 95% confidence level. The Standard Model Higgs boson has been excluded at the 95% confidence level at any mass where the observed value is below 1. (b) shows the p_0-value, which is the probability that an observation at least as large as the one seen could be made in the absence of a Higgs boson signal. (c) shows the best-fit signal strength, $\hat{\mu}$, as a function of Higgs boson mass. This indicates how "signal-like" the measurement is. For absence of Higgs boson in a measurement, $\mu = 0$ and for measurement of a Standard Model Higgs boson $\mu = 1$. The blue band indicates the approximate 68% confidence level around the fitted value [6]. These parameters are defined in more detail in Section 6.8.

forces. The Standard Model is built from a combination of $SU(3)$ symmetry for strong interactions, and $SU(2) \otimes U(1)$ symmetry for electroweak interactions, making it an $SU(3) \otimes SU(2) \otimes U(1)$ symmetry. The Standard Model does not introduce masses directly into these theories, but rather does so through the Higgs mechanism. Whereby interactions with a Higgs field, having a particular potential and configuration lead to the masses being generated for the weak vector bosons, and the fermions.

The expectation of a "low-mass Higgs boson", later confirmed with LHC results, provide motivation for an analysis in the low Higgs boson mass regime. In addition an analysis which can test the Higgs boson coupling properties to fermions was desired. The details of the analysis I performed in the search for Higgs boson, in the $H \to b\bar{b}$ decay channel, are presented in Chapter 6.

There are still some outstanding issues with the Standard Model and the Higgs mechanism, in particular is the question of why the Higgs boson mass is low. While the low mass was expected from fits to electroweak data, from a theoretical point of view the mass was expected to be much larger. This is due to loop corrections, which force the theoretical mass to be high. Unless there are cancellations with these loop corrections, then the theoretically predicted Higgs boson mass is much larger than the experimentally determined mass. Theories beyond the Standard Model can offer some explanations and one example is supersymmetry (SUSY). SUSY predicts that each Standard Model particle has a supersymmetric partner particle, for the fermions these partners are bosons, and for the bosons these partners are fermions. Loop corrections have different signs for bosons and fermions, meaning that in SUSY, the loop corrections to the Higgs mass predicted in the Standard Model, would be cancelled by additional loop corrections of opposite sign, thereby permitting a theoretical low Higgs boson mass.

Chapter 3

The Large Hadron Collider and the ATLAS Detector

3.1 The Large Hadron Collider

The Large Hadron Collider (LHC) at CERN (Conseil Européen pour la Recherche Nucléaire) is a 14 TeV centre-of-mass energy proton-proton collider and is also used to collide lead ions at a centre-of-mass energy of 2.76 TeV per nucleon, or 574 TeV in total. 14 TeV is the design energy of the collider but until now the LHC has had major runs at both 7 TeV and 8 TeV centre-of-mass energies. The LHC will reach instantaneous luminosity of up to 10^{34} $\mathrm{cm}^{-2}\,\mathrm{s}^{-1}$. At the time of writing the LHC is the world's most energetic and luminous hadron collider. The following sections provide more details on the separate components of the LHC design, performance and operation.

3.1.1 Machine Overview

The LHC was constructed between 2000 and 2008 in the 26.7 km tunnel formerly occupied by the LEP (Large Electron Positron) collider. The tunnel is between 45 m and 170 m below ground level, and slopes at 1.4% ($\sim 0.8°$). The tunnel consists of eight octants, consisting of arc sections and separated by straight sections. The straight sections, also called insertions, are approximately 528 m long, and are a remnant from the LEP accelerator, where the straight sections were used as RF accelerating cavities to compensate for energy lost by synchrotron radiation. The

LHC inherited all the properties of the LEP tunnel and four of these eight straight sections are now the collision points on the LHC [31]. These collision points are home to four large experimental detectors, ALICE [32] (A Large Ion Collider Experiment), ATLAS [33] (A Toroidal LHC ApparatuS), CMS [34] (Compact Muon Solonoid) and LHCb [35] (LHC beauty). The LHC is only the final part in a more complex accelerator network at CERN and the full network of accelerators and detectors is shown in Figure 3.1

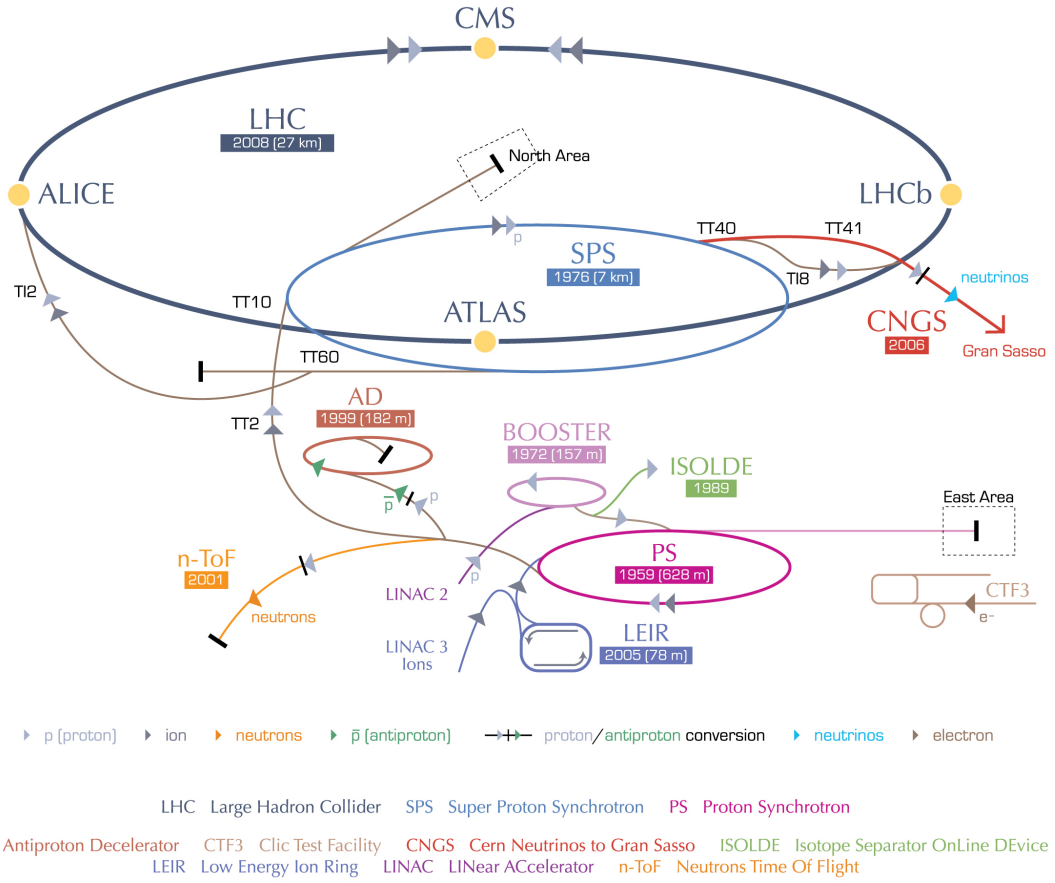

Figure 3.1: The LHC accelerator complex. [36]

3.1.2 Design Requirements

To satisfy the LHC physics outcomes, the number of events of a particular final state produced in LHC collisions must be large enough to permit data analysers to perform physics measurements with a high level of confidence. Two

parameters control the number of events produced in particle collisions, the integrated luminosity (L) and the cross-section (σ) for a particular event to occur, as explained in Equation 3.1. For events with higher mass final states, the cross-sections tend to increase with collider centre-of-mass energy [8], therefore one main LHC design requirement was to maximise the number of events produced by finding the correct balance between cost, luminosity and energy.

$$N_{\text{events}} = L\sigma_{\text{event}} \tag{3.1}$$

The instantaneous luminosity, $\mathcal{L}$, of the machine is controlled by several parameters as detailed in Equation 3.2. A comparison of these design parameters and those of the 2012 runs is listed in Table 3.1.

$$\mathcal{L} = \frac{N_p^2 n_b f_{\text{rev}} \gamma}{4\pi\epsilon_n \beta^*} F \tag{3.2}$$

- N_p is the number of particles per bunch
- n_b is the number of bunches per beam
- f_{rev} is the revolution frequency of the machine
- γ is the relativistic factor
- ϵ_n is the normalised beam emittance
- β^* is the betatron function at the collision point. It is a measure of the beam size at the interaction point.
- F is the geometric luminosity reduction factor due to the crossing angle at the collision point [31], given in Equation 3.3

$$F = \left(1 + \left(\frac{\theta_c \sigma_z}{2\sigma^*}\right)^2\right)^{-\frac{1}{2}} \tag{3.3}$$

Here θ_c is the crossing angle of the beams, which is ~ 300 μrad. A non-zero crossing angle is used to avoid "parasitic collisions" between bunches not located at the interaction point. σ_z is the RMS of the bunch length and σ^* is the RMS of the transverse beam size at the point of interaction. At full capacity the LHC will run with 10^{34} cm^{-2} s^{-1}, from $n_b = 2,808$ bunches, separated by 25 ns.

Parameter [Units]	2012 Configuration	Design Configuration
E_{CM} [TeV]	8	14
N_p [protons]	1.48×10^{11}	1.15×10^{11}
n_b [bunches]	1380	2808
f_{rev} [MHz]	20	40
γ	4260	7460
ϵ_n [μm]	2.6	3.75
β^* [m]	0.6	0.55

Table 3.1: Comparison of run parameters [37].

The β^* parameter is a measure of the distance between the interaction point, and the point at which the beam is twice the width of that at the interaction point. Typically this is 11 m for the LHC before squeezing, 2 m after squeezing with an eventual goal of 0.55 m after squeezing [38]. The smaller the β^*, the more dense the beam is in terms of particles per unit area, and the more instantaneous luminosity can be achieved.

Aside from reducing the size of β^*, the luminosity may be increased by several other methods. One could increase the number of protons per bunch, as $\mathcal{L} \propto N_p^2$. As the number of protons is increased, collisions can occur between more than two protons in the bunch. These additional interactions are known as "in-time pileup". During the second half of the 2012 *pp* run, the ATLAS experiment has recorded events with $\mathcal{O}(30)$ pileup vertices. Another way to increase the luminosity is to increase the number of bunches in the machine, as $\mathcal{L} \propto n_b$. This has the effect of reducing the time between bunches, and there can be some overlap between events measured by a detector during different bunch crossings. This effect is known as "out-of-time pileup". These effects must be taken into account in any physics analysis.

3.1.3 Magnet Systems

In order to control beams of up to 7 TeV in the LHC a powerful system of magnets is used. The maximum beam energy possible depends on the magnetic field strength of the magnets. For 7 TeV the magnetic field strength required is 8.33 T. Each of the eight LHC arcs contain twenty three regular FODO cells. A FODO cell contains six main dipole (for bending) and two main quadrupole (for

focussing) magnets [39] and a few additional multipole correcting magnets. Each cell is 106.9 m long and the structure is shown in Figure 3.2. The sixteen points of transition between arc and straight sections also use magnet configurations known as dispersion suppressors. These are designed to alter the reference orbit of the LHC beam (circular) to conform to the geometry of the existing LEP tunnel and to cancel any beam dispersion that may have arisen due to the bending of the beam, or beam crossing induced effects [40]. In each straight section, approximately 10 quadrupole magnets are used to ensure the beam dispersion remains minimal [31]. The dipole magnet structure adopted for the LHC is a twin-bore [41] design and was born out of the necessity to conserve space in the 3.7 m internal diameter LEP tunnel, while still requiring two opposite magnetic fields for the particle-particle (as opposed to particle-anti-particle) beams circulating in opposite directions around the tunnel. A cross-section of a dipole magnet, and its associated magnetic field are shown in Figures 3.3 & 3.4.

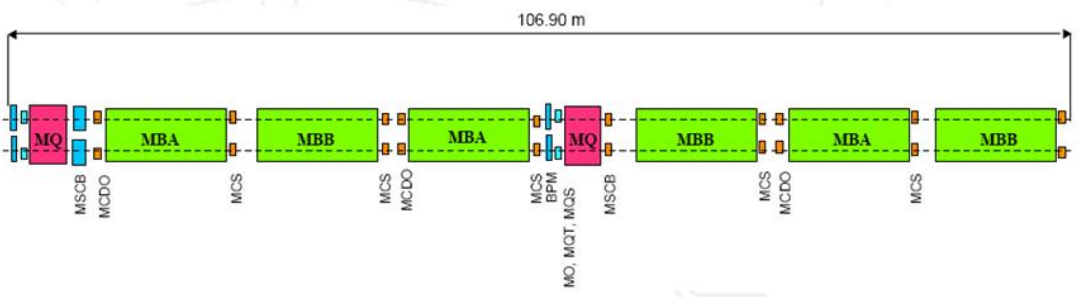

Figure 3.2: Layout of a FODO cell. [42]

The dipole magnet cold mass (yoke) is cooled with superfluid helium to 1.9 K [31].

3.1.4 Radio Frequency Systems

The LHC relies upon Radio Frequency (RF) systems for acceleration and capture (or control) of the beam. During the acceleration phase, protons (or lead-ions) pass through eight RF cavities, each with an accelerating field of 5 MVm^{-1} at a frequency of 400 MHz. Repeated cycling through these cavities is used to accelerate the LHC beams to maximum energy. The RF system is also used to replenish energy lost due to synchrotron radiation, and stabilise the bunches in

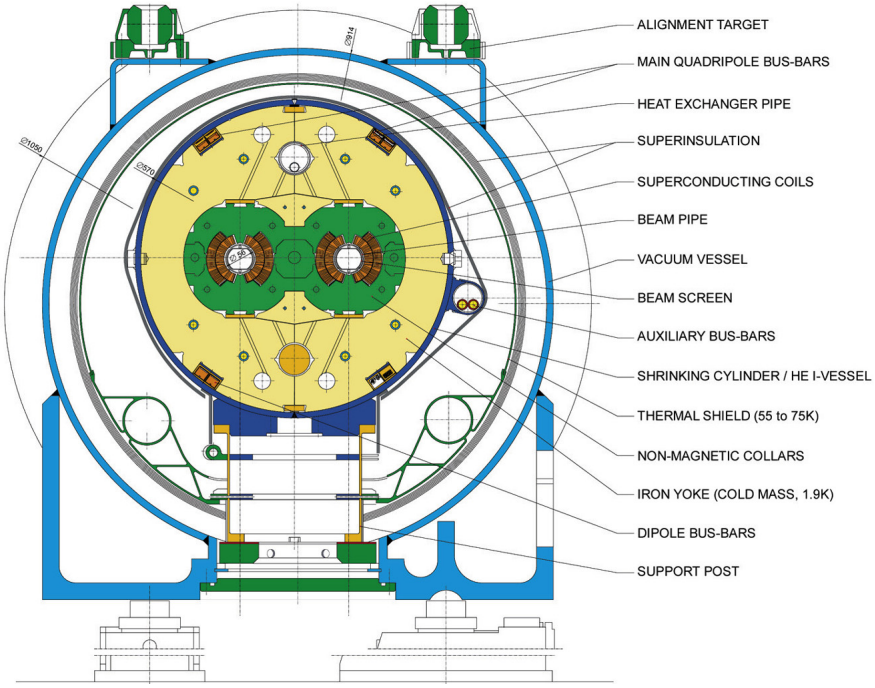

Figure 3.3: Cross-section of an LHC dipole magnet. [43]

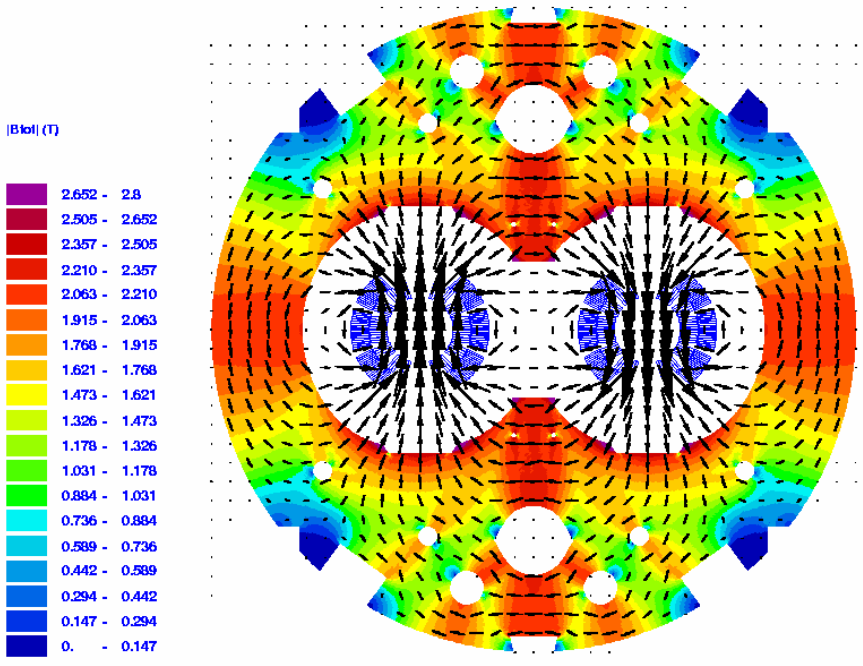

Figure 3.4: Magnetic flux distribution in an LHC dipole magnet. [44]

the beam.

3.1.5 Injection Chain

The LHC is only the final step in a complex accelerator network at CERN. Use is made of machines designed primarily for previous experiments to accelerate beams to a fraction of the final desired centre-of-mass energy. A six step acceleration process is required before beams of up to 7 TeV each can be collided in the LHC. Referring to Figure 3.1, the first step is to extract protons from a hydrogen bottle and inject them in to LINAC2 for acceleration up to 50 MeV. The proton beam is extracted from LINAC2 and injected into the PS (Proton Synchrotron) Booster where the energy of the protons in the beam are increased to 1.4 GeV. Next is injection into the PS and acceleration up to 25 GeV (4 cycles, $\sim$ 14 s), before injection into the SPS for acceleration up to 450 GeV (12 cycles, $\sim$ 259 s). The final step is then injection into the LHC and acceleration up to 7 TeV ($\sim$ 20 minutes). This is done for two beams, and including other monitoring constraints and ramp down times, results in minimum turn-around time of 1.15 hours [31]. This is summarised in the Table 3.2

Phase	**Beam exit energy**	**Time required**
Hydrogen gas	–	–
LINAC2	50 MeV	–
PS Booster	1.4 GeV	–
PS	25 GeV	14 seconds
SPS	450 GeV	259 seconds
LHC	7 TeV	20 minutes

Table 3.2: Accelerator chain information.

3.2 The ATLAS Detector

The ATLAS (A Toroidal LHC ApparatuS) detector has a variety of subsystems, each carefully designed to allow the physics programme to be explored. The ATLAS detector has the following subsystems:

- Magnet systems

- Inner detector
- Calorimeters
- Muons system
- Trigger and data acquisition systems.

In this section I shall introduce the ATLAS detector including its physics programme and the detector design to suit this programme, with particular emphasis on the physics motivation behind each detector component. The ATLAS detector was designed to search for new physics in the high energy frontier. The main searches include the search for the Higgs boson, some decays ATLAS is sensitive to are: $H \to \gamma\gamma$, $H \to b\bar{b}$, fully leptonic Higgs decays such as $H \to \tau^+\tau^-$, $H \to ZZ^* \to l\bar{l}l\bar{l}$ and $H \to ZZ \to l\bar{\nu}l\bar{\nu}$, and the semi-leptonic decay $H \to WW \to l\bar{\nu}q\bar{q}$. In addition to these Standard Model Higgs searches, there is also discovery potential for non Standard Model Higgs bosons, for example from the Minimal Supersymmetric Standard Model (MSSM), which predicts five Higgs bosons [45]. The neutral MSSM Higgs bosons may decay via similar processes to the Standard Model Higgs bosons, but in addition there is some sensitivity to decays involving the charged Higgs bosons such as $t \to bH^+$. Measurement of the top quark mass, and the $t \to bW$ branching ratio are also of interest. It is also expected that ATLAS could measure the mass of the W-boson with half the uncertainty of previous experiments [46]. Although more commonly associated to another LHC experiment, the LHCb experiment, ATLAS also has a B physics programme, including study of CP violation in B_d^0 and B_s^0 decays. ATLAS will also search for additional vector bosons, for quark compositeness, and for other Beyond the Standard Model (BSM) phenomena.

The ATLAS detector in full is illustrated in Figure 3.5

3.2.1 Co-ordinate System

The ATLAS co-ordinate system is defined in the following way, the along beam axis is defined as z, the direction from the interaction point to the center the of LHC ring is defined as x, and vertically upwards from the interaction point is defined as y. Additionally two angles are defined, ϕ is the azimuthal angle defined as the angle around the z-axis, and θ is the polar angle, defined between the z-

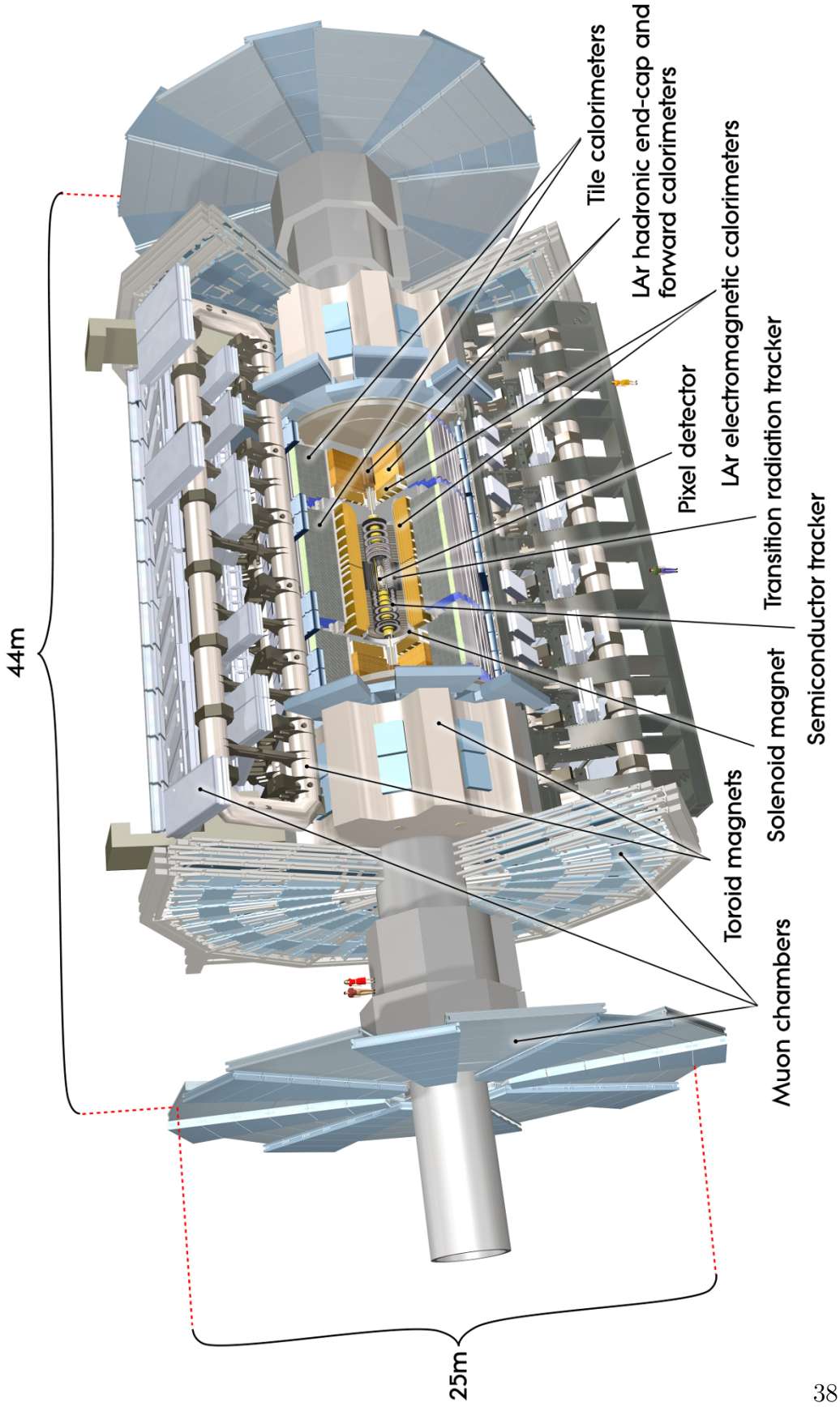

Figure 3.5: Computer generated image of the ATLAS detector [47].

and y-axes. θ is usually represented by the parameter pseudorapidity, hereafter labelled as η, which is defined in Equation 3.4.

$$\eta = -\ln\left(\tan\left(\frac{\theta}{2}\right)\right) \tag{3.4}$$

Since the beams in the LHC are oriented along the z-axis, the particles have very little momentum in the $x-y$ plane. After collision, there may exist particles with large momenta in this plane, and so it is usual to define the transverse momentum as:

$$p_T = \sqrt{p_x^2 + p_y^2} \tag{3.5}$$

3.2.2 Magnet Systems

Physics Motivation

Many processes investigated by ATLAS will involve the measurement of charged particles either in the final or intermediate states. For example a common Higgs decay channel is the $H \to ZZ^* \to l\bar{l}l\bar{l}$ channel involving four charged leptons in the final state. A magnetic field (with field strength B) causes a particle having charge q, and momentum p to be bent in a direction dependent on the sign of its charge by radius given in Equation 3.6. In this equation the 0.3 factor is for a specific set of units, namely m for r, e for q, GeV/c for p_T and T for B.

$$r = \frac{p_T}{0.3qB} \tag{3.6}$$

Hence measuring a charged particle trajectory in a magnetic field allows both the charge sign and the momentum of the particle to be determined. If the particle trajectory is not curved it implies that the particle is neutral (although very high momentum particles may have trajectories that are almost straight). The magnet systems are used in conjunction with other systems described in the next sections.

Detector Description

As can be seen from Figure 3.5 the ATLAS magnet system contains two magnet sub-systems, a solenoid and a toroidal magnet system. The solenoid magnet is

aligned around the z-axis, and has a field strength of 2 Tesla. Its purpose is to cause the bending of charged particles as they propagate through the tracking system, thereby revealing their charge and momentum information. The solenoid has been designed to be less than one radiation length (χ_0, defined as the distance travelled by a particle as its energy is reduced to $1/e$ of its original value) in dead material radial thickness, thereby minimising the effect on the energy measurements by the surrounding calorimeters (see Section 3.2.4). The toroidal magnet system is constructed in a barrel geometry surrounding the beam axis, made from eight toroidal magnets, with 9.4 m radial distance from the interaction point and a field strength of 0.5 T [48]. Additionally two toroidal end cap magnets are also used of field strength 1 T [48]. The purpose of the toroidal magnet systems is to cause the muons, which propagate through the inner detector and calorimeters with minimal interaction, to have curved trajectories for tracking and momentum determination by the muon system. The main design constraint on the magnet systems is to find a balance between maximising the value of the product BL^2 (the magnetic bending power, with L being the distance travelled by a particle in the field of strength B) in order to maximise the momentum resolution achievable in the tracking systems, while minimising the financial cost. The 2 T field value for the solenoid is less than that of the Compact Muon Solenoid (CMS) experiment at CERN, which will search for similar physics. However the extra dead material required to supply such a field could compromise accuracy in the calorimeters for example, and the extra cost is prohibitive.

3.2.3 Inner Detector

Physics Motivation

In order to make use of the curved tracks generated by the magnetic field, as discussed in Section 3.2.2, the position of a particle at several points must be measured and a track formed between all the points to form a measured particle trajectory. The components of the inner detector are designed to perform this "tracking". Considering another Higgs decay channel, $H \to b\bar{b}$, where the final state products are b-quarks, which hadronise to form B-hadrons. B-hadrons have the property that their decay length (due to a relatively long lifetime) is ~ 450 μm (with $\gamma\beta = 1$), and in ATLAS with a typical $\gamma\beta$ factor of $\sim 12 - 13$,

this decay length can be $\sim$ 6mm. A tracking detector having sufficient precision to resolve this distance, and being as close to the interaction point as possible, is required in order to properly identify these b-quarks resulting from the Higgs boson decay (a process known as b-tagging, and described in more detail in Chapter 5). It is also essential to distinguish between particle types, and ATLAS has incorporated methods to do this in the inner detector, including pion and electron identification.

Detector Description

As illustrated in Figure 3.6 the ATLAS Inner Detector (ID) system [49] consists of a barrel and an end-cap region. The barrel region contains eight layers of detectors, surrounding the beam-pipe, which itself has a radius of 31.5 mm. The innermost layer is that of a pixelated vertex detector, followed by two subsequent layers of pixelated tracking detector. Each pixel layer contains pixels of size 50 μm in ϕ by 400 μm in z, containing a total of 1456 pixel modules, with 67 million channels [50]. The next four layers are composed of silicon strip detectors, known as the SemiConductor Tracker (SCT) and the final layer is that of the Transition Radiation Tracker (TRT) extending to $\sim$ 108 cm in radius. A cutaway diagram is shown in Figure 3.7.

The pixel detectors have very high resolution in both the $R\phi$ plane ($\sim$ 14 μm), and the z plane ($\sim$ 115 μm) [52], and are predominantly used for tracking, and sagitta measurement (for the determination of momentum). The silicon strip detectors are a less costly alternative to measure the same parameters, but while they have comparable resolution in $R\phi$, they have an order of magnitude poorer resolution in z. They have poor radiation hardness and so are not a feasible alternative to the pixel detector close to the beam-pipe, due to the high radiation doses expected of $\sim$ 1 MGy [48].

The vertex detector is a replaceable pixelated layer closest to the beam pipe, providing enhanced vertexing capabilities which will be particularly useful in B-physics studies at low luminosity, and eventually in b-tagging measurements at higher luminosity. Low material path length is essential in this detector as the vertexing resolution is heavily compromised by the effects of multiple scattering, and the path length is $\sim 0.01\chi_0$.

The final layers are that of the TRT, which is constructed of 37,000 tubular

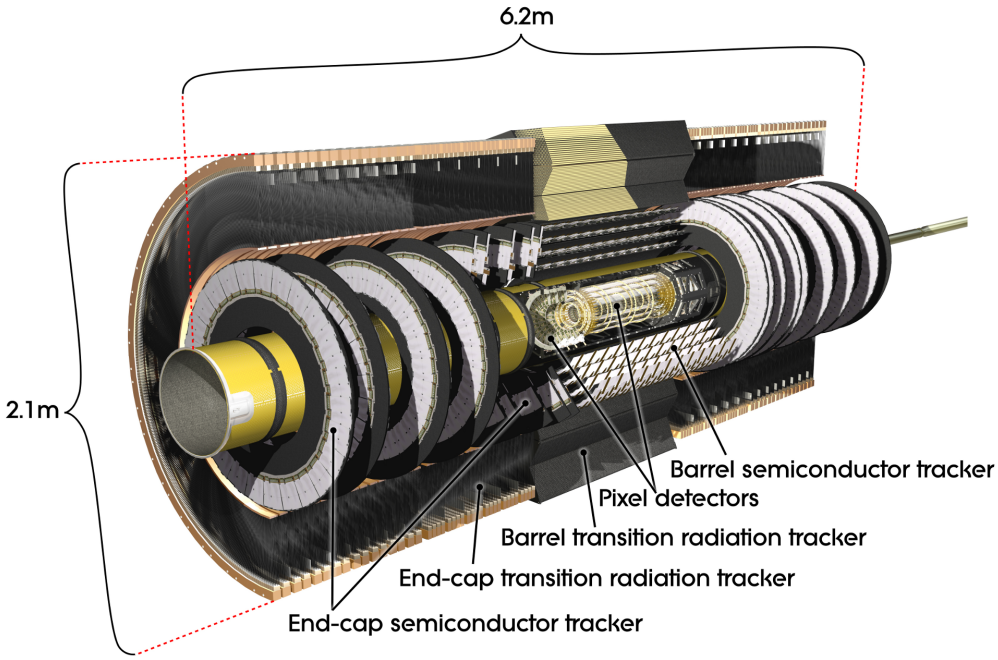

Figure 3.6: Computer generated image of the ATLAS inner detector [51].

structures filled with the gas mixture Xe-CO_2-O_2 in the proportions 70%-27%-3% [53], whose axes are parallel to the beam axis. The TRT operates by two mechanisms: firstly a charged particle passing through the gas in the drift tubes causes the gas to become ionised. The resulting electrons are repelled from the negatively charged straw tubes, onto a central anode wire, a current can be measured, allowing a space-point to be identified and therefore tracking can be performed. Additionally, as a highly relativistic particle propagates across the boundary between the straw material and the composite gas inside the straw (having two differing dielectric constants), transition radiation is emitted in the X-ray region of the spectrum. This radiation is particularly well absorbed by the Xe gas, liberating more electrons, and in any drift tube where this occurs, a stronger signal will be measured. The intensity of the signal depends on the incident energy, and when momentum information is also available, particle identification may be performed. In ATLAS the TRT is particularly useful for identification of electrons, and tests have shown an electron identification efficiency of $\sim 90\%$, leading to a factor of ~ 75 in the rejection of charged pions [53].

The design constraints on the inner detector are defined in Reference [54] and

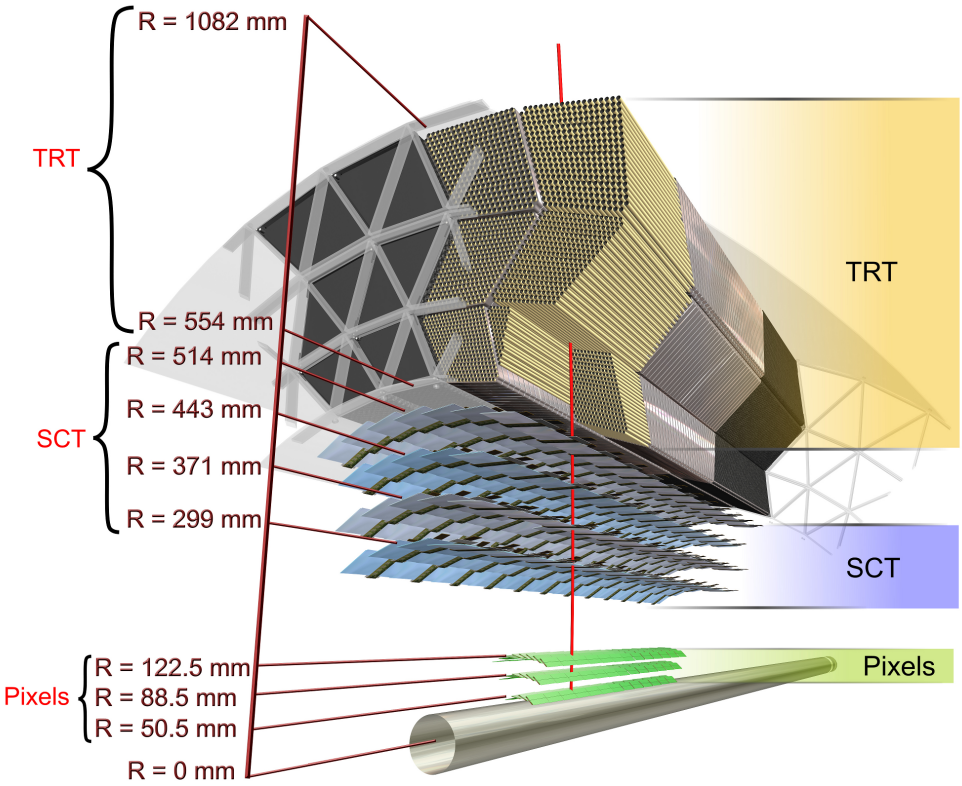

Figure 3.7: Computer generated image of the ATLAS inner detector (cutaway) [51].

include the requirement to have complete tracking coverage in the range $|\eta| \leq 2.5$, this is predominantly driven by the required acceptance of the physics processes to be studied at ATLAS. For example in the $H \rightarrow ZZ^* \rightarrow l\bar{l}l\bar{l}$ decay, an additional 20% in η would improve the acceptance by only 16%, but a 20% reduction in η would impose a 40% reduction on acceptance. The range was chosen so as to provide optimum balance of acceptance/cost. The number of tracking layers in the inner detector was chosen to provide at least 5 tracking points in the $R\phi$ plane, allowing for a fine momentum resolution, as the momentum resolution is inversely proportional to the square root of the number of measured points. The solenoid magnet system, and tracking detectors are designed to provide a momentum

resolution, $\frac{\sigma(p_T)}{p_T}$, of 0.03 in the most central region, and this is compromised to 0.05 for the highest η regions of the inner detector.

A b-tagging requirement was also built into the design. As I will discuss b-tagging in Chapter 5 in more detail, I will just present the constraints here. b-tagging is to be accomplished by the inner detector with an efficiency of ∼30%, in the central $|\eta| < 1.5$ range, with a rejection of hadronic jets not originating from b-quark decays to be greater than 10 for high luminosity, and greater than 50 for low luminosity. Another important task of the inner detector is a contribution to photon identification, particularly for $H \to \gamma\gamma$ processes in the identification of photons with 90% efficiency, while rejecting photons which originate from π^0 decays with a rejection factor of > 3, which is not thought to be possible with calorimetry alone when a photon conversion takes place before the calorimeter [55]. This is due to the fact that if a photon converts, the electron-positron pair produced will be bent in the magnetic field, and potentially deposit their energy in the calorimeter well separated from each other. It is difficult to resolve this from a multiple photon event, for example. Therefore tracking information is also required. For $|\eta| \geq 1$, a photon conversion will take place in the inner detector $\sim 60\%$ of the time [33].

3.2.4 Calorimeters

Physics Motivation

Energy measurement in high energy physics experiments is vital. A measurement of energy, whether of charged particles, neutral particles, clusters of particles known as "jets", or as a means to determine "missing-energy" carried away by neutrinos, are all important in physics searches at the LHC. For example in the $WH \to l\nu b\bar{b}$ search, the b-jet energies are required to determine the invariant mass of the b-jet system and hence the rest mass of the Higgs boson, and the lepton and neutrino energies are required to reconstruct the W-boson. Neutrinos interact very weakly with all the detector components, but their presence can be inferred from the principle of missing transverse energy/momentum. The vector sum of the momentum transverse to the beam direction of all partons before a collision is zero and so it is expected to be zero after a collision. If it is non-zero then there is a momentum imbalance in the transverse plane and this is evidence

of a neutrino carrying energy and momentum out of the detector. It is important to use the transverse-plane because there may be a net momentum in the z-plane, and it is not possible to completely measure it due to areas of no acceptance at large η. Often the quantity "transverse energy", E_T, is used instead of "transverse momentum", p_T, which is defined in Equation 3.7.

$$E_T = \sqrt{m^2 + p_T^2} \tag{3.7}$$

In order to infer the presence of neutrinos, the energy and momentum measurements of all the measurable particles must be sufficiently accurate. The missing transverse energy, E_T^{miss}, is given by:

$$E_T^{\text{miss}} = -\Sigma E_T \tag{3.8}$$

In practice in ATLAS this is calculated as [56]:

$$\begin{aligned} E_T^{\text{miss}} = &-\Sigma E_T\,(\text{Calorimeter cell}) - \Sigma E_T\,(\text{Muon}) \\ &- \Sigma E_T\,(\text{Losses in dead material}) \end{aligned} \tag{3.9}$$

Detector Description

Calorimeters are designed to measure the energy of particles in high energy physics experiments. The principle of operation involves complete termination of a particle in the calorimeter material, normally by inducing a particle shower in the process, and the deposition of energy associated with this can then be measured. Calorimeters are classified according to the type of particle interactions they are typically used to measure the energy of, either electromagnetically interacting particles, or strongly interacting particles. In practice both types of particles interact with both types of calorimeter.

In the energy regime above 10 MeV an electron incident on a material will mainly undergo a Bremsstrahlung process ($e \rightarrow e\gamma$) and create a photon. This photon may then undergo a pair-production process ($\gamma \rightarrow e^+e^-$) and create two more electrons. This process continues, creating a shower of particles with ever decreasing energy. As the energy decreases the dominant processes change, therefore the existing particles continue to lose energy but not to the creation of other particles. At lower energies, electrons instead lose energy to the calorimeter

material by ionisation or excitation and photons by the photoelectric effect as shown in Figure 3.8 and Figure 3.9, and the shower ceases to expand.

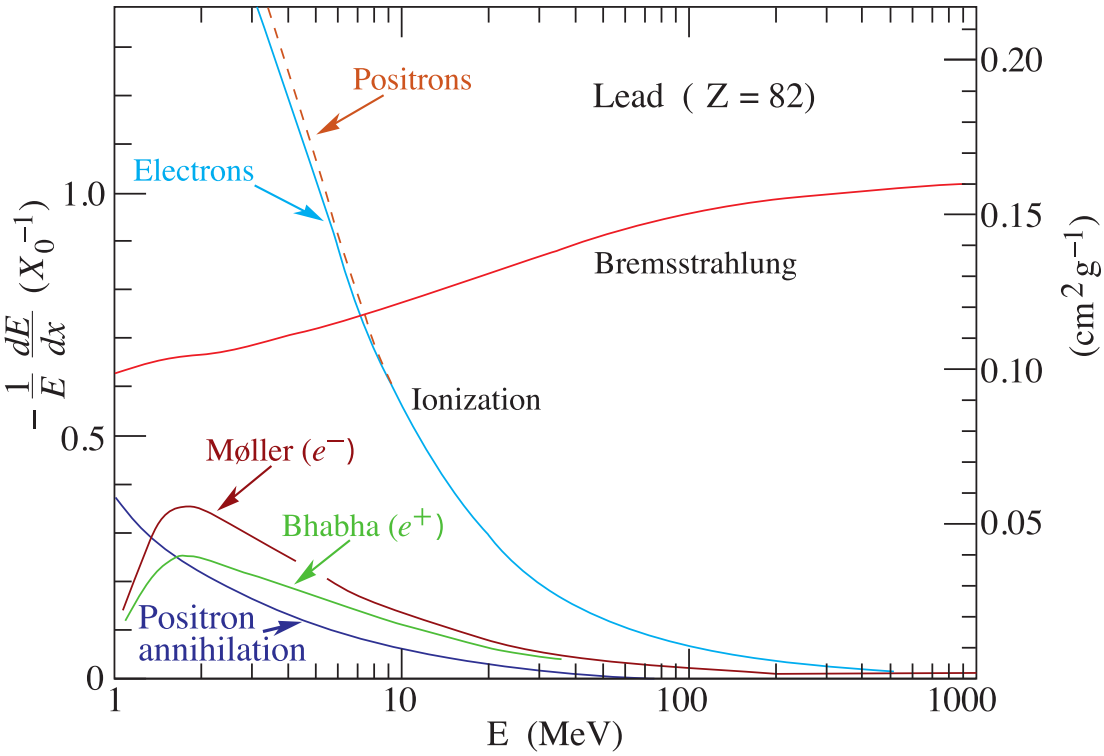

Figure 3.8: Energy loss by electrons in lead. [57]

ATLAS contains both electromagnetic and hadronic calorimeters with varying construction and granularity, as shown in Figure 3.10. In the region $|\eta| < 3.2$, are the ElectroMagnetic Barrel (EMB) calorimeter and two ElectroMagnetic End Cap (EMEC) calorimeters. These are both constructed using Liquid Argon (LAr) as the active material combined with lead (Pb) absorber plates in an accordion structure. The ATLAS hadronic calorimetry consists of a Tile Barrel (TB) calorimeter made from a scintillating tile and iron (Fe) absorber structure, oriented in a barrel shape around the beam axis, in the range $|\eta| < 1.7$. Also present is an LAr Hadronic End Cap (HEC) calorimeter in the range $1.5 < |\eta| < 3.2$. The final calorimeter component in ATLAS is the Forward CALorimeter (FCAL), covering $3.1 < |\eta| < 4.9$. The FCAL is made up of a tube/rod structure, with stainless steel tubes containing rods of different material separated by a thin layer of LAr. The materials of the rods are chosen for purpose, e.g. Cu for electromagnetic calorimetry, and Tungsten (W) alloy for hadronic calorimetry.

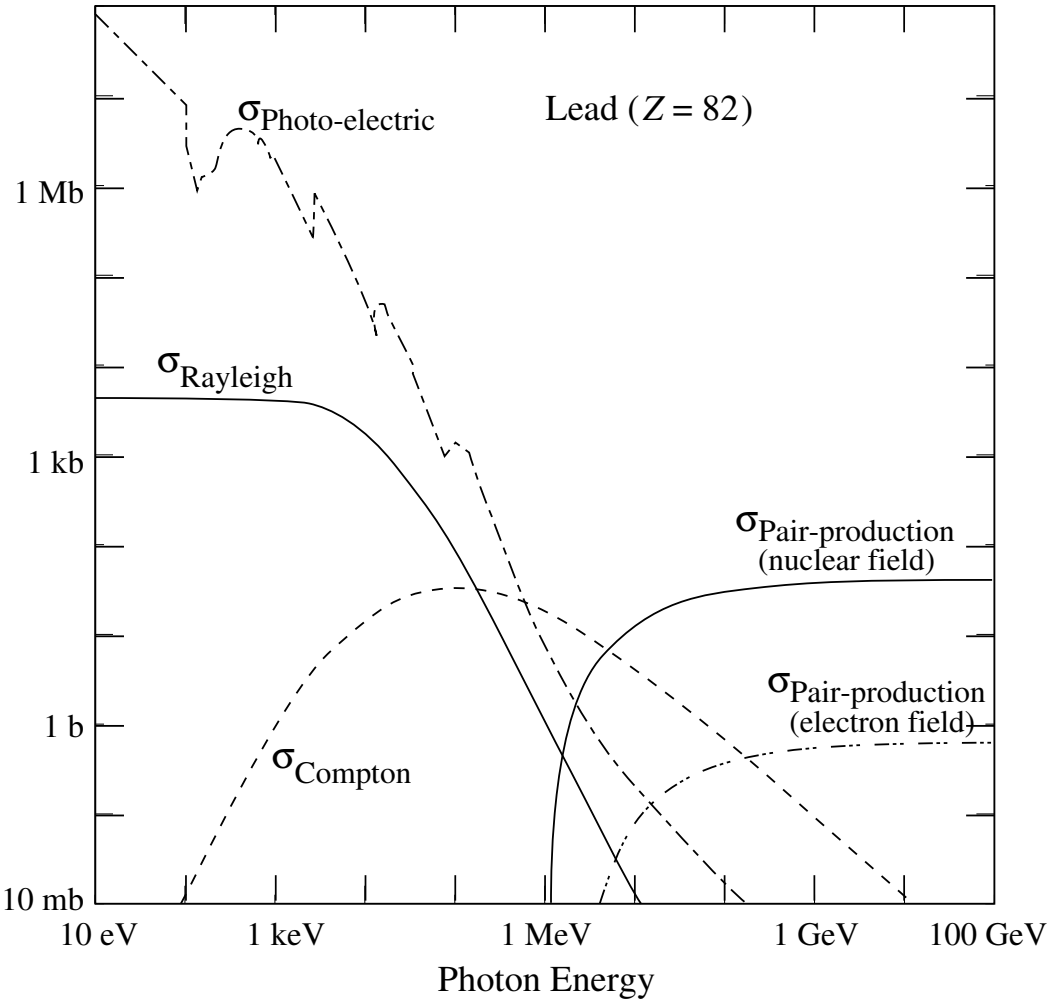

Figure 3.9: Cross-section of photon processes in lead. Modified from [57]

The ATLAS construction places the electromagnetic calorimeters closer to the interaction point than the hadronic ones. This ensures that electrons and photons encounter the electromagnetic calorimeters first, and can be completely terminated in these media leaving little leakage into the hadronic calorimeters.

It is approximately on the scale of one radiation length (χ_0) that an interaction occurs. The length of shower (shower depth) has a logarithmic dependence on the incident particle energy. The ATLAS electromagnetic calorimeters have a depth of at least 22 χ_0. The width of an electromagnetic shower is due to multiple scattering of electrons and positrons and the extent of the shower width is given by the Molière radius. For nuclear interactions a similar property to

the radiation length exists, known as the interaction length, λ. The hadronic calorimeter thickness in ATLAS is typically $> 11\ \lambda$. Both of these thickness constraints minimise punch-through of electromagnetic clusters into the hadronic calorimeter, and hadronic jets into the muon system.

Energy measurement is done by measuring the energy of all particles whose energy is deposited directly in the detector material i.e. not in the creation of new particles, but via excitations of the material for example. This can be done via scintillation, for example, where an electron loses its energy to an excitation in a scintillator material. The light produced can be measured and the energy information recovered. The energy resolution of an electromagnetic calorimeter is parameterised and has three main components:

$$\frac{\sigma}{E_0} = \sqrt{\left(\frac{a}{\sqrt{E_0}}\right)^2 + \left(\frac{b}{E_0}\right)^2 + c^2} \tag{3.10}$$

The first term in Equation (3.10) is related to fluctuations in the length of all tracks depositing energy directly in the active material. The second term is a noise contribution from the read-out processes/electronics. The third term, known as the constant term due to its independence of energy, is due to the calorimeter design, its instrumentation, and the uniformity of the material response in all directions/conditions. Clearly the contribution of the first two terms reduce with increasing energy, however the third term is independent of incident energy and therefore becomes the dominant contribution at higher energies [58] such as those achievable by the LHC. Design values for the ATLAS calorimeters are listed in Table 3.3.

Calorimeter	**Resolution**
EM Barrel & Endcap	$\frac{\sigma_{\mathrm{E}}}{\mathrm{E}} = \frac{0.1}{\sqrt{\mathrm{E}}} \oplus 0.007$
Hadronic Endcap	$\frac{\sigma_{\mathrm{E}}}{\mathrm{E}} = \frac{0.5}{\sqrt{\mathrm{E}}} \oplus 0.03$
Forward Calorimeter	$\frac{\sigma_{\mathrm{E}}}{\mathrm{E}} = \frac{1}{\sqrt{\mathrm{E}}} \oplus 0.1$

Table 3.3: ATLAS calorimeter energy resolutions [59]. E is measured in GeV.

Hadronic calorimeters have a more complicated set of interactions possible within them, but nevertheless, $\sim 20\%$ of the incident hadronic particle's energy is converted to an electromagnetic shower within the hadronic calorimeter. This

level of complexity of interactions makes hadronic calorimeters more difficult to optimise. Accurate determination of the energy of hadrons in hadronic calorimeters is more challenging than for purely electromagnetically interacting particles in electromagnetic calorimeters. A portion of nuclear interaction energy is typically lost as binding energy and is not deposited in the active material of the calorimeter. A very important parameter and characteristic of a particular hadronic calorimeter is $\frac{e_{\mathrm{EM}}}{e_{\mathrm{HAD}}}$, which is defined as the ratio of visible energies of electromagnetic to hadronic showers. Clearly $\frac{e_{\mathrm{EM}}}{e_{\mathrm{HAD}}} < 1$ in a homogeneous, hadronic calorimeter since some energy is lost to nuclear binding energy. Changes in the fraction of the shower which is electromagnetic is energy dependent, and so the total fraction of energy measured in the hadronic calorimeter is energy dependent also. The resolution has a less favourable energy dependence than for electromagnetic calorimeters.

ATLAS uses sampling calorimeters which are designed to tune this $\frac{e_{\mathrm{EM}}}{e_{\mathrm{HAD}}}$ parameter, as close to unity as possible. At this point the energy measured in the hadronic calorimeter becomes independent of the fraction of the shower which is hadronic in nature. By increasing the absorber thickness in sampling calorimeters, that is tuning the sampling fraction, and thereby altering the ratios dominant processes, the ratio can be tuned to $\frac{e_{\mathrm{EM}}}{e_{\mathrm{HAD}}} \approx 1$.

Many physics processes that will be studied at ATLAS, result in products which interact electromagnetically, in particular electrons and photons. It is the job of the EMB, EMEC, and to a lesser extent the FCAL to measure the energies, identify and permit reconstruction of these particles with a high level of accuracy. Requirements for the calorimetry included having a large acceptance, the ability to perform particle identification for some types of particles, to have a sufficiently good energy resolution and the ability to determine particle direction. Simulation work done on the electromagnetic calorimeter response to some important Higgs decays such as $H \rightarrow \gamma\gamma$ and $H \rightarrow e^+e^-e^+e^-$, shows that very good efficiency may be achieved in the reconstruction of the associated decay tracks, within the covered $|\eta|$ ranges of the electromagnetic calorimeters. To achieve a very fine energy resolution, the parameters from Equation 3.10 have to be minimised. Whilst the first two terms improve with increasing energy, the constant term is critical to accuracy in high energy measurements, and the constant term for the electromagnetic calorimetry in ATLAS has been minimised to 0.7%. Critical

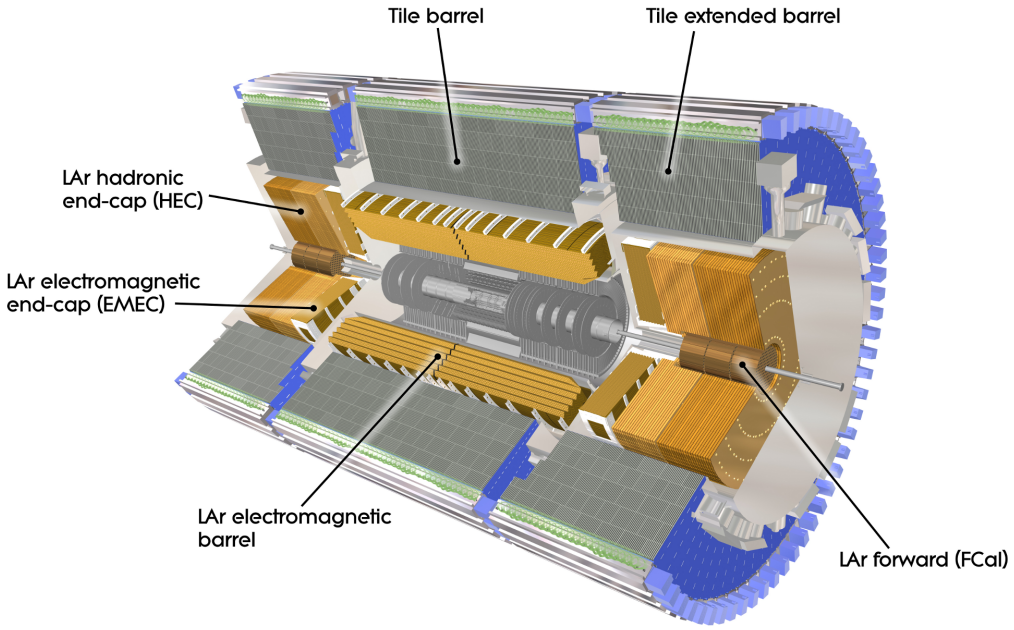

Figure 3.10: Computer generated image of the ATLAS electromagnetic and hadronic calorimeters.

to this achievement were a sufficiently thick material depth, $\sim 28\ \chi_0$ to prevent leakage out of the calorimeters, and homogeneous sampling in ϕ, which is achieved by virtue of the novel accordion structure in the EMB and EMEC. The angular resolution is also important to determine shower direction in order to accurately reconstruct invariant masses. More on the specific geometry of the EMEC will be discussed in section 4.3.

The ATLAS hadronic calorimetry system is mainly used to measure jet energy, direction, identification, and also to determine any missing transverse energy E_T^{miss}. The prospective physics searches for top quark mass via $t \rightarrow 3$ jets, and quark compositeness via an excess in the jet cross-section compared to the Standard Model , lead to a required energy resolution of $\frac{\sigma(E)}{E} = \frac{0.5}{\sqrt{E}} \oplus 0.03$ [49], where E is measured in GeV.

3.2.5 Muon System

Physics Motivation

Muons, although interacting electromagnetically, interact very little with the calorimetry in ATLAS. For this reason they are one of only a small number of particles that propagate to the outermost parts of the ATLAS detector. Detection of muons is important to identify many particle physics decays, for example the Higgs decay $H \rightarrow \mu^+\mu^-\mu^+\mu^-$, and $Z' \rightarrow \mu^+\mu^-$. It is vital that not only the muons be detected, but also that their momentum be measured with a high level of accuracy. Muons resulting from decays provide a very clear signature for experimentalists to search for, and for this reason it often makes sense to judge the potential interest of an event based on whether it contains muons or not (this is known as triggering and is decribed in Section 3.2.6).

Detector Description

The outermost detector system in ATLAS is the Muon Spectrometer (MS). The decays mentioned above, and other processes have naturally dictated the design of the MS. The MS must be able to provide fine momentum resolution for signals from processes which can have large backgrounds. The toroidal magnet system in ATLAS (which has already been discussed in Section 3.2.2) has a large bending power that contributes to the good momentum resolution in the MS. Triggering performance is also a critical feature to optimise in the ATLAS physics programme, and this can be done in the muon trigger system which also provides timing data which can be used to resolve events during pile up. The muon system consists of three separate subsystems, the barrel region covering $|\eta| < 1.4$, the transition region covering $1.4 < |\eta| < 1.6$, and the end-cap region covering $1.6 < |\eta| < 2.7$.

The barrel muon system is constructed from three layers of Monitored Drift Tubes (MDTs), each containing two sets, around the beam axis, at 4.5, 7 and 10 m radially from the interaction point. MDTs are metal tubes containing a charged wire through their gas-filled centre. An incident particle causing ionisation in the gas will cause electrons to drift towards these wires, thereby creating a measurable signal. A segment of three overlapping layers of the barrel muon system is illustrated in Figure 3.11. These segments are replicated along the z

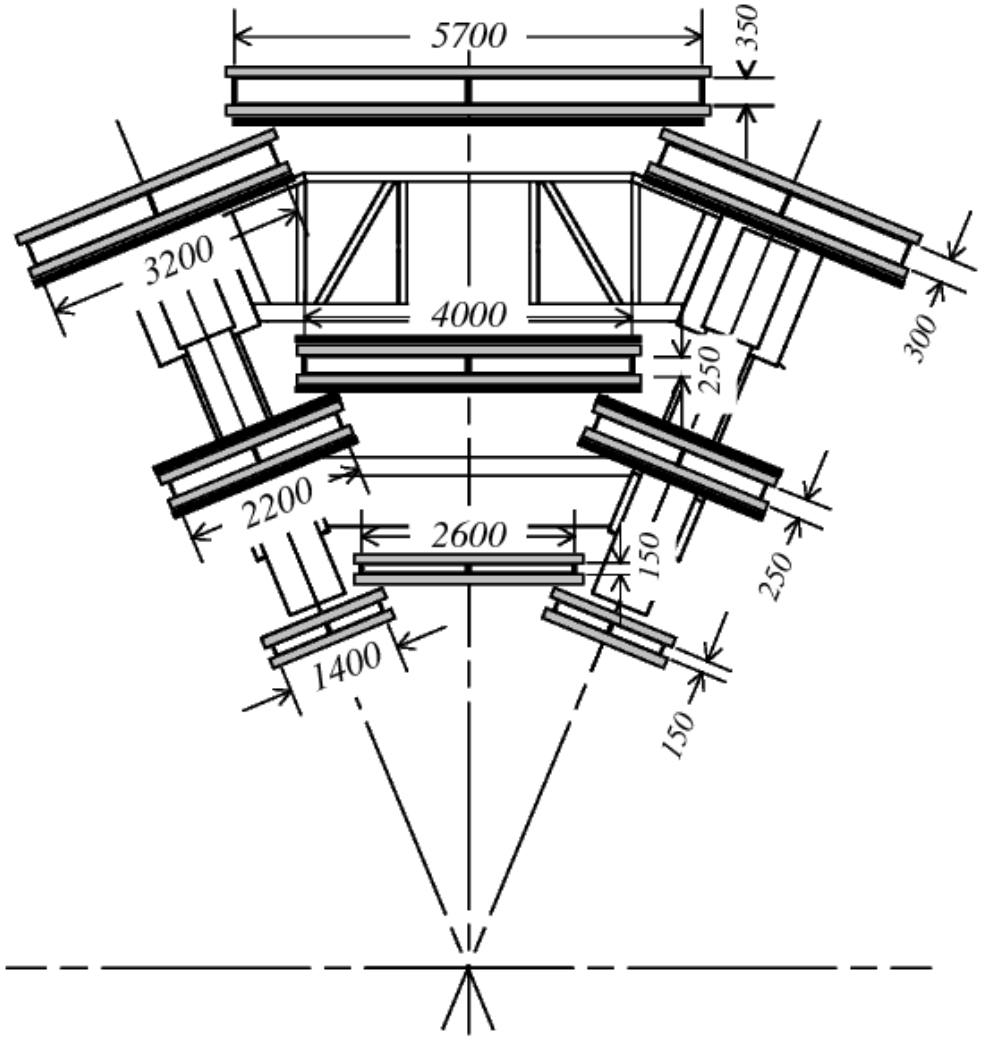

Figure 3.11: Barrel muon system in the ATLAS detector. The grey rectangles represent the monitored drift tubes for tracking in the muon system, and the black rectangles represent the resistive plate chambers used for triggering [49]. z axis is into the page. Distances are in mm.

axis with lengths up to 2.6 m in z. The trigger system is required to be able select muons with $p_T > 6$ GeV and $p_T > 20$ GeV in different luminosity regimes and this is implemented using Resistive Plate Chambers (RPCs) in the middle and outer layers of the barrel, also shown in Figure 3.11. RPCs have charged parallel plates, separated by a gas. An incident particle can ionise the gas, and the resulting electrons drift to the positively charged plate, creating a signal.

In the transition and end cap muon systems, the MDTs are aligned to perform tracking for forward travelling particles, and the triggering is done with Thin Gap Chambers (TGCs). TGCs have parallel grounded plates, with multiple charged wires in the gas filled chamber between. Any electrons liberated in the ionisation process will drift to these wires, thereby creating a signal. The triggering in the muon system checks for coincidence between hits in different RPCs, and can make an approximate standalone measurement of the transverse momentum of muons to as little as $\sim 25\%$ uncertainty in some η ranges [60].

3.2.6 Trigger and Data Acquisition Systems

Physics Motivation

In any collision between two or more particles, there are many processes that can occur, each having a particular probability to occur (cross-section, σ). The Standard Model cross-sections for proton-proton collisions are shown in Figure 2.8. The cross-section for anything to happen in a collision at the LHC is $\mathcal{O}$ (10^8 nb) and the cross-section for the production of a Z-boson, for example, is $\mathcal{O}$ (10^2 nb). For a physics analysis wishing to observe a Z-boson, it makes little sense to record the factor of 10^6 of superfluous data. In order to filter potentially interesting events from the vast amounts of collision data produced, a trigger system must be implemented. Not only is it impractical to record superfluous data, but it is also costly, and the trigger system must be optimised accordingly. In fact, it is not always necessary to record every interesting event. For events that are produced copiously, and where an analysis is limited by systematic uncertainties rather than statistical uncertainties, it is useful to be able to accept only one in N interesting events. A trigger system must also be designed with this consideration.

Detector Description

The final major system in ATLAS is the triggering system. This makes use of information from many systems. ATLAS is divided into three levels of trigger. The first Level 1 trigger system generally makes use of data from the calorimetry and muon systems, with sub-optimal resolution, to identify whether an event is potentially interesting and in what regions of the detector the next trigger should be deployed. An interesting event may typically be high p_T jets in the calorimeters, or presence of muons above a given p_T, or presence of missing energy after the collision (neutrinos).

The Level 1 trigger, provides a decision in under 2.5 μs [33] (latency) and the event processing rate is reduced by a factor of 400 compared to the case if no trigger was used. This latency has to be short, but it is not short enough to make decisions before a subsequent bunch crossing occurs (every 25 ns). This means that the Level 1 trigger must be capable of resolving the relevant event from the pile up, and as discussed in Section 3.2.5 for the muon triggers, they record the timing information to make this possible. In addition to these decisions, the Level 1 trigger system also identified "Regions-Of-Interest" (ROIs), the regions of the detector which contain the potentially interesting information.

The Level 2 trigger uses fully optimal resolution, but only in the interesting detector regions (ROIs) identified by trigger Level 1. The Level 2 trigger further reduces the event processing rate by a factor of 100, and the latency is $\mathcal{O}$ (10 ms). The operation of the Level 2 trigger is to extract the interesting information from each of the systems individually, i.e. the inner detector, calorimetry and muon system, and then search for interesting combinations of this information.

The Level 3 trigger (also known as the Event Filter) acts when Level 1 and Level 2 triggers have identified an event of interest. The Event Filter acts upon all data, at full resolution, in order to refine the data, and eliminate non interesting areas of the data before storage, thereby minimising the required storage. The decisions of the Event Filter are made on the order of a second, and the data rate is typically reduced by a factor of 10, with a final event size of $\mathcal{O}$(1 MB), but this depends on what fraction of the total event data is to be stored. A flow diagram of the trigger system is shown in Figure 3.12.

A trigger prescale requirement was built into the ATLAS trigger, so that the trigger decisions may be prescaled. This means accepting only one in N of the

events the trigger deemed to be interesting. Here N is known as the "prescale factor", or simply the prescale.

Figure 3.12: Flow diagram of the ATLAS trigger and DAQ systems [61].

3.3 Particle Identification

In order to perform particle identification in ATLAS, information from many subsystems is combined. Figure 3.13 illustrates this. In the ideal case the following features may be used to distinguish between particle types, and identify particles:

- **Electron** - Electrons are charged and therefore leave a curved track in the inner detector tracking systems. They are then terminated in the electromagnetic calorimeter (ideally completely terminated, but sometimes they punch through into the hadronic calorimeter).

- **Muon** - Like electrons, muons are charged and therfore leave curved tracks in the inner detector. Muons are minimum ionizing particles and will interact only slightly with both the electromagnetic and hadronic calorimeters, but usually will not be terminated in either. Therefore they propagate to the outermost regions of the detector and are bent once again by the toroid magnets to leave a curved track in the muon system.

- **Photon** - Photons are neutral and so leave no tracks in the inner detector, but will usually be completely terminated in the electromagnetic calorimeter.

- **Proton** - Protons will leave a curved track in the inner detector, deposit some energy in the electromagnetic calorimeter and then usually be fully terminated in the hadronic calorimeter.

- **Neutron** - Neutrons will leave no track in the inner detector and not interact electromagnetically (neutral charge) with the electromagnetic calorimeter, and then usually be fully terminated in the hadronic calorimeter.

- **Neutrino** - Neutrinos will leave no track in the inner detector, deposit no energy in either calorimeter, and leave no track in the muon system. Its presence may be inferred only from an imbalance in the transverse energy between that measured before and after the collision.

Example 2D and 3D event displays for a $H \rightarrow e^+e^-e^+e^-$ event are shown in Figure 3.14 and Figure 3.15 respectively.

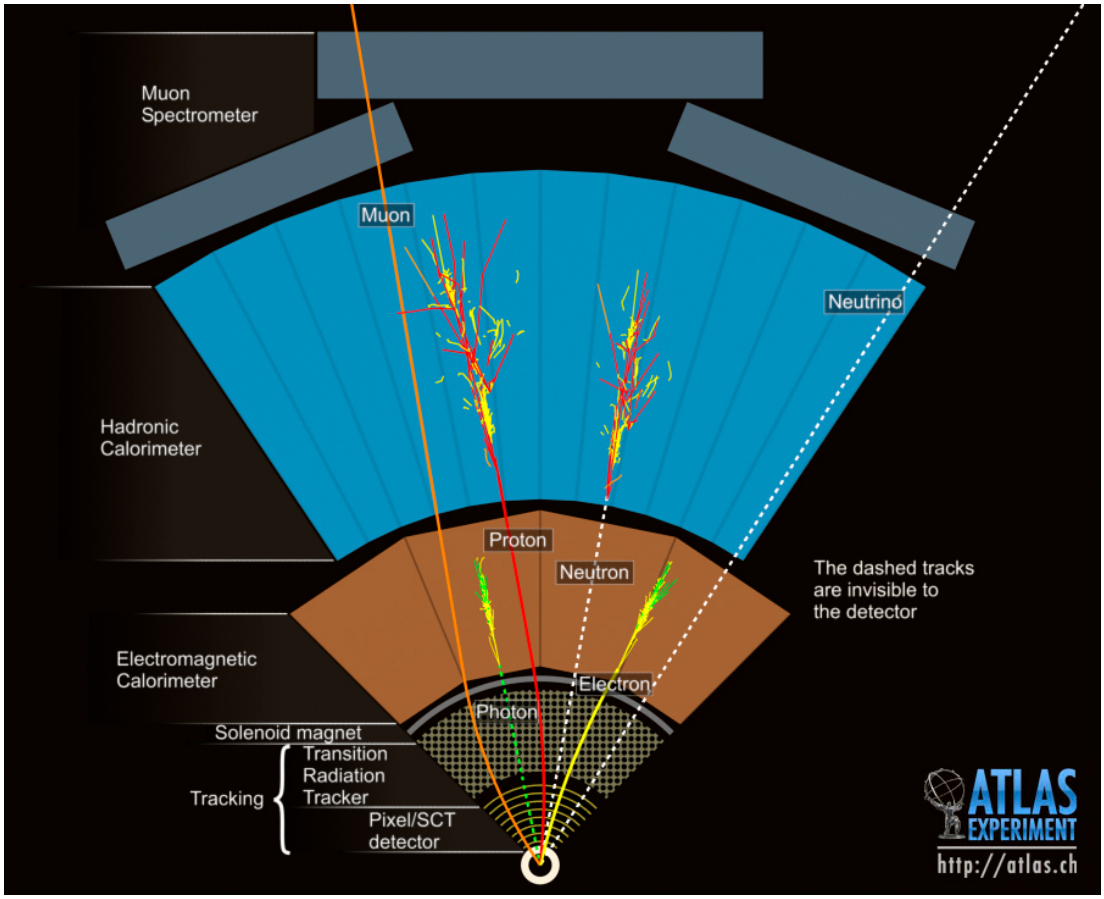

Figure 3.13: Particle identification in the ATLAS detector [62].

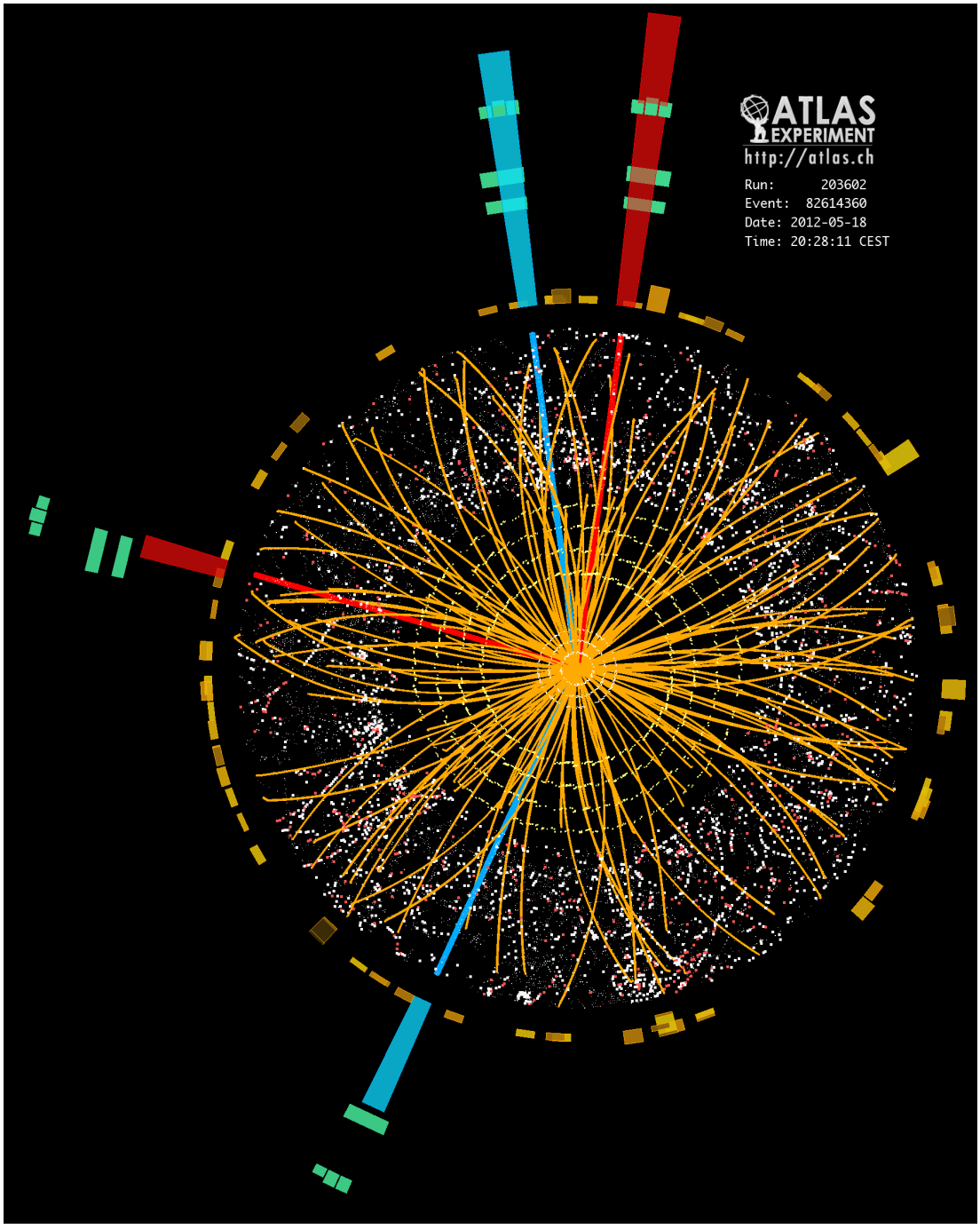

Figure 3.14: $H \rightarrow e^+e^-e^+e^-$ 2D event display [63]. z-axis runs into the page. The red clusters represent electrons and the blue clusters represent positrons.

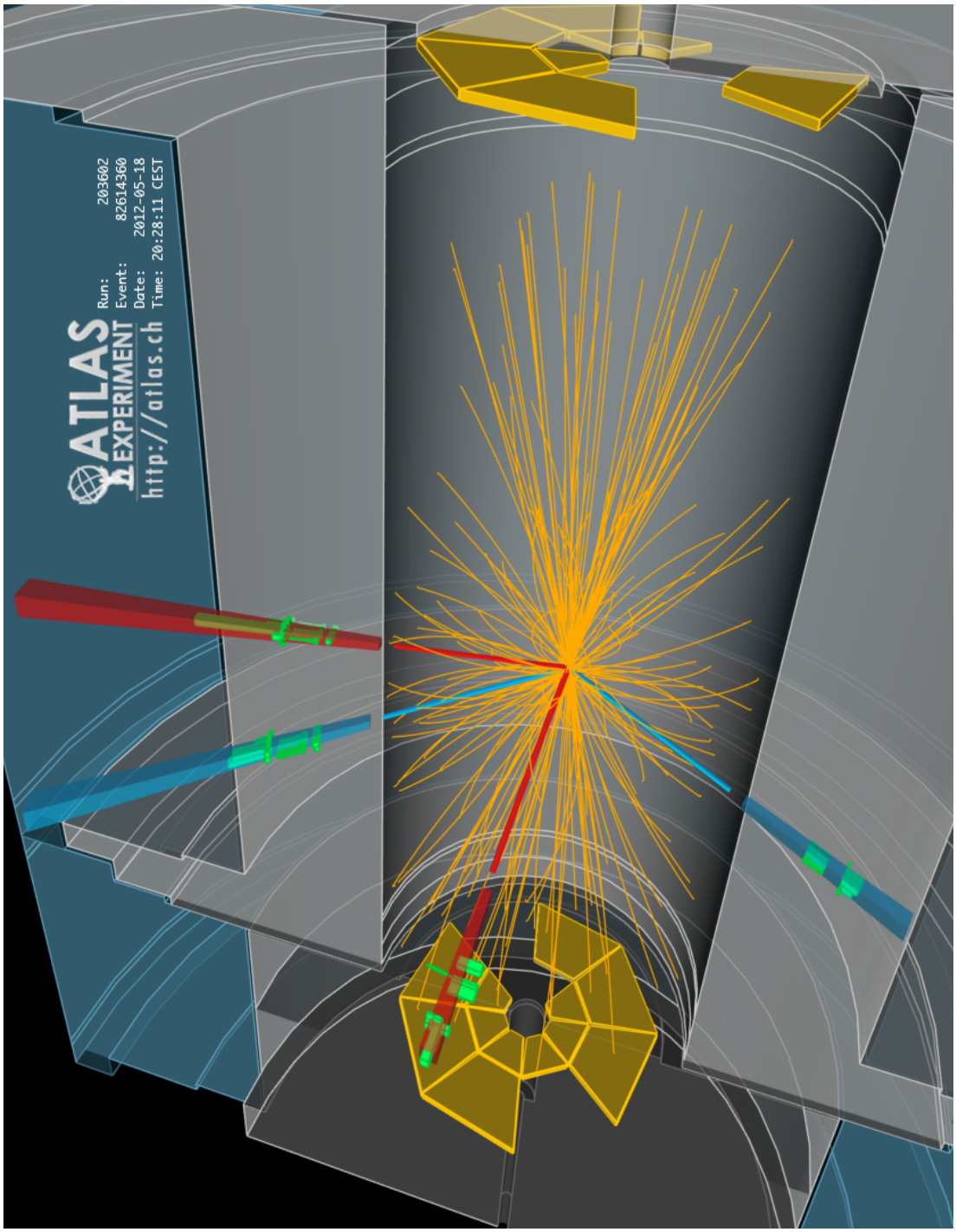

Figure 3.15: $H \to e^+e^-e^+e^-$ 3D event display [64]. The red clusters represent electrons and the blue clusters represent positrons.

Chapter 4

Simulation of the ATLAS Detector

In this chapter I will introduce the ATLAS simulation project, the GEANT4 detector simulation toolkit, and the development of the ATLAS ElectroMagnetic End Cap calorimeter (EMEC) simulated geometry.

4.1 ATLAS Simulation and GEANT4

The ATLAS simulation software [65] is embedded within a framework known as Athena [66] which was developed from the Gaudi framework [67] originally developed for the LHCb experimental software. Athena uses a collection of C++ algorithms and objects, which are configured via Python object oriented scripting. Athena relies heavily on the CLHEP [68] (Class Library for High Energy Physics) library that contains many utility classes useful in particle physics. A typical Athena simulation job comprises four stages - generation, simulation, digitisation and reconstruction, while Athena is also used in the reconstruction stage for data.

1. **Generation** - The generation stage involves the production of particle four-vectors via Monte Carlo (MC) based algorithms. Modelling of subsequent decays is done for short lived particles (particles that would decay before reaching any detector component), and their stable products are retained in a HepMC [69] record.

2. **Simulation** - The simulation is based on the GEANT4 (GEometry ANd Tracking) software package, where particles are propagated through a predefined detector geometry. Interactions of these particles with the detector materials are modelled, and hits are recorded in any defined sensitive detector regions (regions equivalent to active regions in the real detector). Hits are snapshots of a physical interaction of a track in a sensitive region of the detector. The hit object typically contains information about position, time, momentum and energy of the track [70].

3. **Digitisation** - The digitisation process is used to convert the data in the hit collection into a data form representing the equivalent signals which would be measured by the detector in a real collision. After digitisation, the simulated data is in identical format to the real data collected by the data acquisition system (DAQ).

4. **Reconstruction** - The reconstruction process is then run on the digitisation output to convert it into a collection of tracks and particles, as would be done for real events using output from the DAQ. This reconstructed information is what is typically used as part of a physics analysis.

Simulation is a valuable tool in particle physics and allows some knowledge to be gained about the type of events that occur and the rates at which they occur. It is also useful in planning new detectors, for use in optimising analysis strategies on current detectors and estimating detector induced effects that may be present on experimentally measured data. Finally comparison between existing theories and observed phenomena is also done using simulations [71].

Modelling of a particle physics process not only involves understanding of the hard scattering process itself, but also relies on the understanding and modelling of additional components. These include Bremsstrahlung type processes where a photon may be radiated from an electromagnetic process in the initial or final state, or radiation of gluons through strong processes. Gluon radiation can be especially prolific. These types of processes are typically event type independent, and rather depend on event properties like the momentum transfer. Techniques may therefore be applied to deal with these processes in the form of universal corrections. A second additional component is in the modelling of higher-order corrections introduced through loop Feynman diagrams. A third additional

component is in the modelling of the quarks and gluons themselves. In order to properly model them, details of the incoming hadrons are necessary, and models to deal with hadronisation, fragmentation and decay are required. The result is typically hundreds of final state particles that have to be accurately modelled in order to compare theory and experiment [71].

The steps are described in detail below, and Figure 4.1 shows a flow diagram of the procedure.

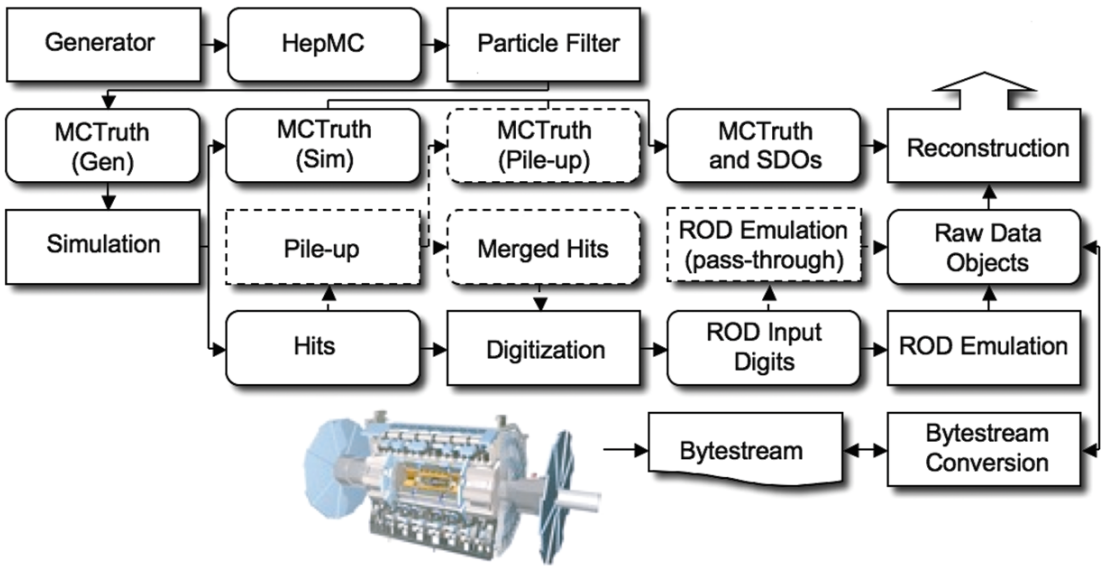

Figure 4.1: Flow diagram representing the process from event generation, through simulation, and finally reconstruction [65]. ROD stands for Read Out Driver, and SDO stands for Simulated Data Objects. MCTruth is a detailed record of the what occurred at the generator level. The record persists through generation, simulation and reconstruction. It can be useful for comparison of what was simulated and reconstructed, with what was really generated.

4.1.1 Generation

The objective of event generators is to use computers to generate particle event information comparable to that available through experimental measurement. In addition to the modelling of the hard scattering process of interest, corrections may be applied, and there are several additional factorised steps to provide these. The first of these is to determine Bremsstrahlung-type corrections for the process, next is to determine higher-order loop corrections, and finally

confinement is applied to the quarks and gluons. The repetitive nature of generation is perfect for the utilisation of computers. The result of the generation stage is in the production of events, which have the same average behaviour as the real data. In reality fluctuations exist due to the quantum mechanics of the underlying theory, and in generators Monte Carlo techniques are used to sample relevant variables from the probability distributions and ensure randomness in the generated events [71].

ATLAS uses a set of C++ classes to hold the event information produced by the generator [65], known as the HepMC [69] event record. ATLAS typically makes use of the following event generators:

- **PYTHIA** [71], **HERWIG** [72] and **SHERPA** [73] are general purpose leading order event generators. Although SHERPA uses leading order to generate the kinematic spectra, it uses weightings for the events to bring the cross sections more in line with the next-to-leading order cross sections.
- **PYTHIAB** [74] is a variant of PYTHIA (leading order) used for production of events with B-hadrons.
- **HIJING** [75] is a generator designed for parton and particle production processes in proton-proton, proton-nucleus and nucleus-nucleus collisions.
- **ALPGEN** [76] is a leading order event generator used to study hard multi parton interactions in hadron collisions.
- **MC@NLO** [77] and **POWHEG** [78] are methods of matching NLO (Next-to-Leading-Order) QCD calculations with parton shower Monte Carlo.
- **AcerMC** [79] is a leading order generator dedicated to the study of Standard Model background processes in pp LHC collisions. Including but not limited to $q\bar{q}/gg \rightarrow Z/W/\gamma \rightarrow b\bar{b}$, $q\bar{q}/gg \rightarrow Z/W/\gamma \rightarrow t\bar{t}$, and $q\bar{q}/gg \rightarrow Z/W/\gamma \rightarrow t\bar{t}b\bar{b}$.
- **ISAJET** [80] is a leading order generator used for the generation of supersymmetric events.
- **MadGraph** [81] is a leading order generator also used on ATLAS with PYTHIA for some production featuring vector boson scattering, and some production of $t\bar{t}H$ events.

- **JIMMY** [82] is a leading order model of multiple parton interactions that can be combined with HERWIG to better model the underlying event.
- **CHARYBDIS** [83] for generation of black hole events.
- **CompHEP** [84] may also be used for generation of exotic processes, defining it a leading order, or above, depends on the inputs.

In addition to the fully fledged generators described above, some generators exist which model only one specific part of the process, and these may be used in conjunction with the above generators. These are:

- **TAUOLA** [85] is used to simulate decays of τ-leptons.
- **Photos** [86] is used to model QED single photon radiative corrections in decays.
- **EvtGen** [87] provides a more detailed and precise modelling of B-hadron decays.

After the generation stage the final "stable" particles are fed into the simulation stage of the Athena framework. The entire HepMC record detailing the decays that led to those final particles is retained and known as Monte Carlo truth.

4.1.2 Simulation

The GEANT4 detector simulation toolkit is used to provide an entire simulation of the ATLAS detector. Starting with particle information provided by the generation stage (Section 4.1.1) each particle is propagated through a virtual ATLAS detector. GEANT4 provides many built-in geometries and material definitions that can be used, and combined together with a variety of techniques to build up a geometry that models the real ATLAS detector very well. In addition custom geometries may be constructed whereby the user must write the algorithms defining the boundaries of the solids. These algorithms must return information to the GEANT4 tracking algorithms including the distance to the next solid interface. In actuality the ATLAS simulated detector model is constructed from both these built-in and custom geometries. The most notable

custom geometry in ATLAS is in the Liquid-Argon calorimeter, see Section 4.3. The full simulated ATLAS detector is shown in Figure 3.5.

As the particle is tracked within GEANT4, it moves within a virtual material. There are built-in libraries (known as a physics lists) of particle physics processes that can occur in each material (e.g. Bremsstrahlung, pair-production etc), for a given particle type, with a known cross-section and GEANT4 relies on these for the modelling of such processes. Physics process modelling may also be constructed by the user, and this was done within ATLAS to model transition radiation processes in the ATLAS TRT, prior to the inclusion of these physics processes as part of the default GEANT4 physics modelling [66].

In addition to the full simulation process described above, faster and less precise options are available. Sometimes the speed of these fast algorithms make them useful when requiring high numbers of statistics in the simulation that wouldn't be feasible with full simulation procedures. As an example a $H \rightarrow ZZ^* \rightarrow l\bar{l}l\bar{l}$ decay takes approximately 1000 seconds per event (on a 1 GHz processor) to simulate.

Since 80% of the full simulation time is spent simulating particle showers in the calorimetry, the "Fast G4" approach was created. With this approach, instead of fully simulating each electromagnetic shower, several approaches are implemented depending on the energy of the incident particles. For low energy electrons (< 10 MeV) a single hit can be deposited to recreate detector response. For mid energy electrons and photons (10 MeV to 1 GeV) a library of fully pre-simulated showers is drawn upon. For high energy electrons (> 10 GeV) a tuned shower parameterisation is available. A factor of three reduction in CPU time can be achieved using this Fast G4 method [65].

Additionally two ATLFAST [65] models exist. ATLFAST-I uses no explicit realistic detector description, and is the least realistic algorithm. Instead parameterisations of the detector response and reconstruction effects are used to smear truth particle distributions to simulate detector effects. ATLFAST-I has shown CPU improvements of the order of 1000 times compared to full simulation. ATLFAST-II uses various fast algorithms to simulate the various subdetectors in a level of detail greater than that of ATLFAST-I but less than full simulation. ATLFAST-II also permits the use of full GEANT4 simulation for any subdetector if so desired. Commonly ATLFAST-II uses a fast calorimeter simulation which

uses parameterisations of the longitudinal and lateral energy profile of showers, which can be tuned to provide good agreement with data, as shown in Figure 4.2. ATLFAST-II has been found to be a factor of 100 faster than full simulation [65], but this number is heavily dependent on the particular configuration of simulated detectors and algorithms that the user choses.

4.1.3 Digitisation

The digitisation process converts the hits produced in the GEANT4 sensitive detectors into detector responses (digits). These digits are equivalent to the readout of the real detector in real collisions, and written out as RDOs (Raw Data Objects). A digit is produced when a voltage or current in a particular readout channel reaches a defined threshold. Each subdetector definition varies and seperate digitisation algorithms are used for each subdetector that take account of all the necessary effects, including cross-talk and noise [65].

Digitisation has to take account of not only the hard-scattering process, but also the underlying event, beam gas and beam halo effects and in-time and out-of-time pile up effects. Each is treated seperately and overlaid.

4.1.4 Reconstruction

Reconstruction is the process whereby the detector responses are converted into higher level objects useful for data analysis. For example, deposits of energy in the calorimeter spatially matched with a curved track in the tracking detectors could be reconstructed as an electron object with its relevant properties such as p_T, energy, charge etc. Similarly for other particles or jets. This high level information forms the basis of any physics analysis.

4.2 Performance of the ATLAS Simulation Software

This section details the work I did to develop performance tests for the ATLAS simulation software.

A testing suite for the ATLAS simulation software was developed to benchmark the performance of the software. Some basic testing was already in place

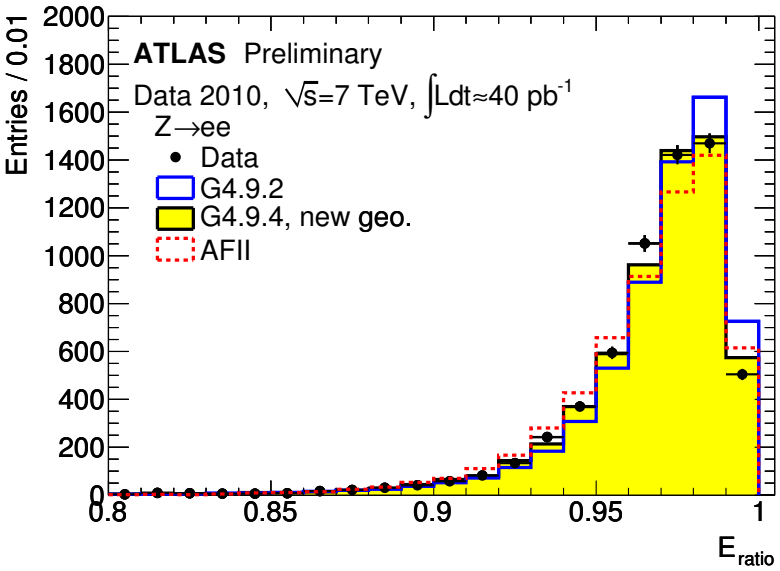

(a) E_{ratio}

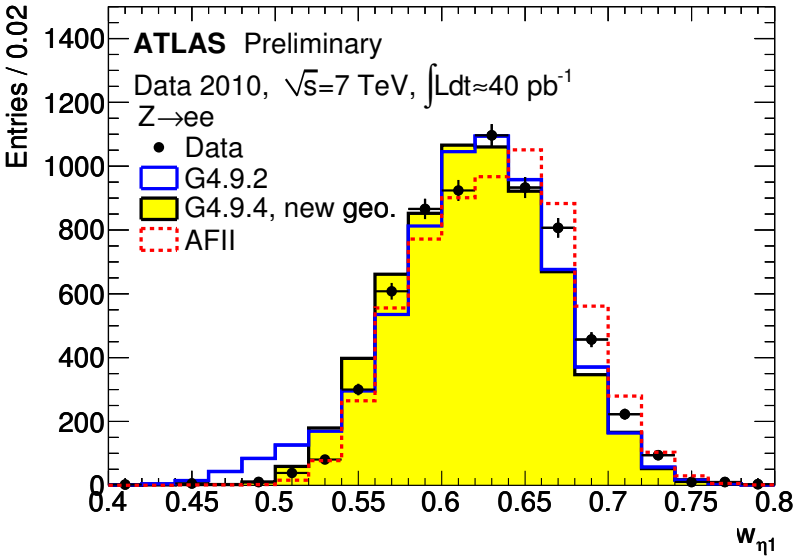

(b) W_{η_1}

Figure 4.2: Comparison of full simulation with GEANT4, ATLFAST-II and data. (a) shows the difference in energy between the calorimeter strips of highest and second highest energy divided by the sum of them, and (b) shows the core shower width measured over ± 1 calorimeter strip around the calorimeter strip with the maximum energy.

and this was modified, extended and enhanced to make it more robust and to cover a wider range of tests. For every stable release of the ATLAS simulation software, a set of tests are run which cover a variety of physics scenarios and record performance characteristics. The tests include single particles such as electrons, muons, and taus at different energies and full physics events such as minimum bias, supersymmetry, $Z \to e^- e^+$, $Z \to \mu^- \mu^+$, $Z \to \tau^- \tau^+$, fully leptonic Higgs decays, and di-jet events. Typically the single particle tests are averaged over 300 events and the full-physics over 50 events.

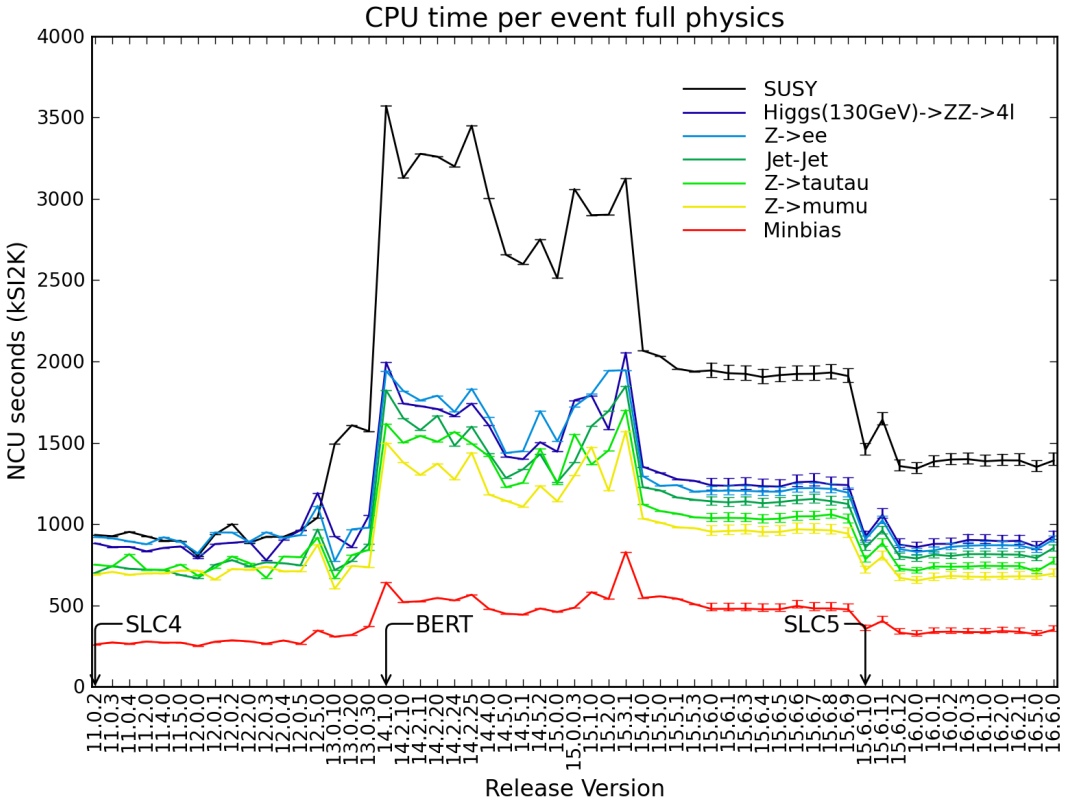

Figure 4.3: Average CPU time per event for full physics events, normalised to time taken to run on a 1 GHz processor. Tests done on 32 bit builds of Athena. Increase in simulation time at the start of the 14 series was due to the implementation of a more detailed and improved physics list, known as QGSP_BERTINI.

For each test job the following performance indicators are recorded: CPU time required per event, VMEM (Virtual MEMory) required per job, RSS (Resident Set Size) memory required per job, disk space required to store each event (event size), disk space required to store each container in the digitised hits file (container

size), and the memory used by the GEANT4 simulation package for various simulation domains. Resident Set Size contains the portion of a processes memory that is held in RAM, VMEM contains the memory in RAM and also the amount held in SWAP memory and in the file system. The CPU time plot for all full physics events is shown in Figure 4.3, and for VMEM in Figure. 4.4. SLC4 and SLC5 are versions of the Scientific Linux for CERN operating system.

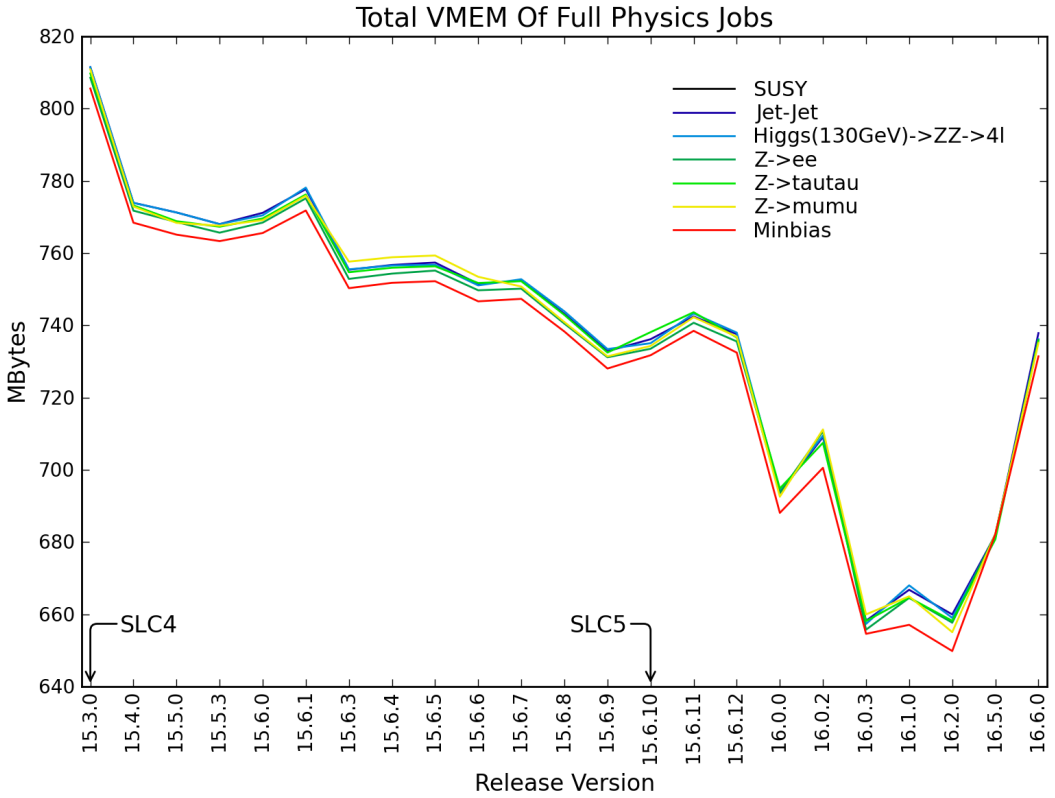

Figure 4.4: Virtual Memory (VMEM) required by full physics simulations. y-axis is zero-suppressed.

A new set of tests specifically designed to measure the memory used by particular detector components during the GEANT4 simulation were implemented. These were designed to address issues with an existing method that had been found to be an unreliable measure. These new tests run a small number of particles through the simulation of the detector, with different detector configurations each time. This allows the calculation of the contribution of a particular detector component to the memory use. These tests were backdated

through the 15.X.X series of releases to have a historical measure of the evolution of this memory use, as shown in Figure. 4.5.

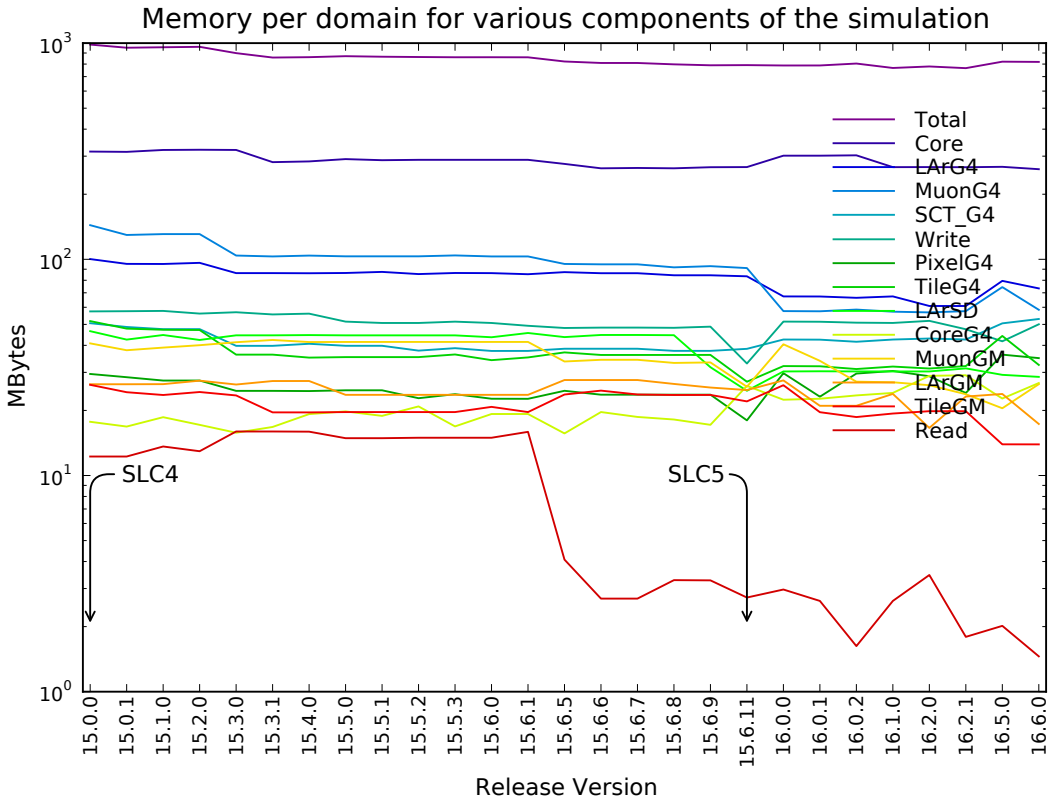

Figure 4.5: Memory used by various components of the GEANT4 simulation.

The system was inherited with minimal automation, and part of the work involved making the system fully automated. The steps are: running of the jobs, checking whether jobs completed successfully or failed, downloading the output, extracting and formatting the ouput, plotting of the data, and publication of plots and data to the validation web pages. Initially the process took around 5 days to complete a set of testing assuming fully successful job completion. The majority of time consumed was in the data processing steps. The work done ensured the whole process was automated, with several checkpoints to ensure sensibility of results and error checking. The testing process now completes in around 1.5 days where the majority of the time taken is simply in the job run-time.

As well as automating the testing, and adding new tests, some problems were highlighted in the testing processes that already existed. It was noted that the

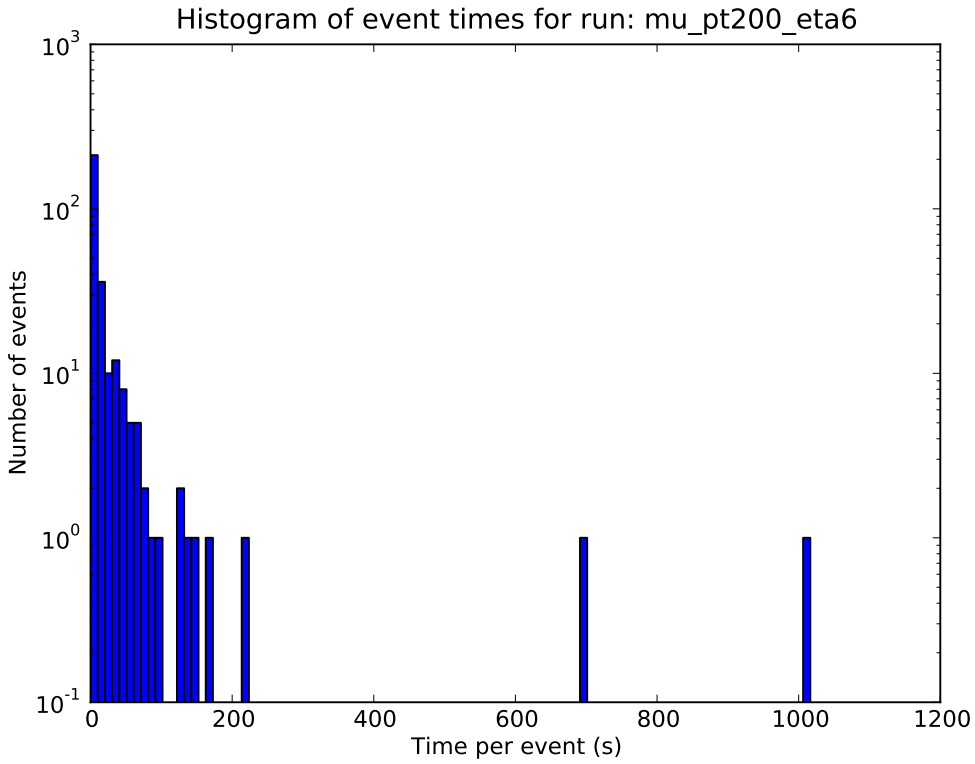

Figure 4.6: Histogram showing the distribution of event times for the 200 GeV p_T single muons in the range $-6 \leq \eta \leq 6$.

history of the CPU time evolution of the single muons (at 200 GeV) was quite erratic. During testing it was found that the average measured time increased by $\sim 40\%$ between releases when it was expected to stay relatively constant. It was found that the average time was being inflated by only a very small number ($\sim 1\%$) of events having simulation times of order 50-75 times greater than the average. Investigation of this issue led to the discovery that these long events were muons of energy ~ 20 TeV, which had undergone a Bremsstrahlung interaction, and created approximately 500,000 secondary particles. The secondary particles led to approximately a million tracking steps, leading to higher CPU time. Typically a muon would be simulated with < 100 steps. Figure 4.6 shows a distribution of event times with two very long events. The events were generated with constant p_T of 200 GeV and varying η (e.g. -6 $\leq \eta \leq$ 6) which meant that some particles were generated with very high energies, ~ 20 TeV. A particular

combination of Athena and GEANT4 resulted in a particular random seed being used when a decision was made about a particle decay. If, randomly, a Bremsstrahlung process occured with a high energy muon, then the effects on simulation time were large.

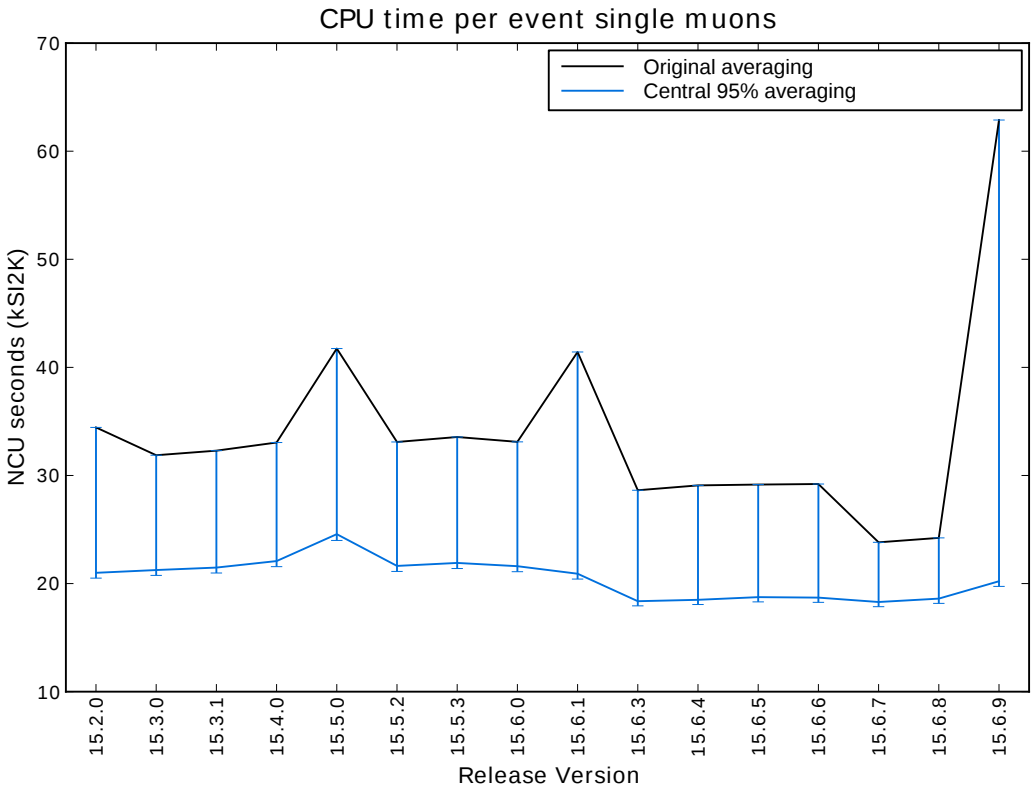

Figure 4.7: Effect of averaging over the central 95% of the full distribution of event times.

A more robust averaging system was implemented, where an average over the central 95% of events times was done, thereby eliminating the longest and shortest 2.5% of events. The result with each 2.5% included is taken as the error bars on the measurement. The procedure was backdated historically and it was found that the increased average CPU time being measured as a result of these few long events, had masked several performance improvements in the software. The effect of this new averaging method on the single muons CPU time can be seen in Figure 4.7.

In Figure 4.7 it can be seen that the transition from 15.2.0 to 15.3.0 appears to

be a performance improvement when the average is done over the full distribution, but when the outliers are eliminated, it is masking a small performance reduction. The peak at 15.6.1, which appears to be a large performance deterioration when averaged over the full distribution, is actually masking a small performance improvement. The very large peak in release 15.6.9 is clearly not indicative of the degradation in simulation performance which is suggested by averaging over the full distribution.

Additionally, it was decided that the generation of particles with constant p_T in a specified η range was not the optimal or most physically realistic method for generation. A transition was therefore made to use a new set of physics input files, generated with constant energy rather than p_T.

4.3 Simulation of the EMEC

As discussed in Section 3.2.4, the ATLAS ElectroMagnetic End Cap calorimeter (EMEC) is a lead-liquid argon (Pb-LAr) sampling calorimeter. The structure of the absorbers and electrodes in the EMEC is novel and complex. The calorimeter has a two wheel arrangement, where an inner and an outer wheel covering the ranges $2.5 < |\eta| < 3.2$ and $1.5 < |\eta| < 2.5$ respectively make up an EMEC section, and there is an EMEC section on both sides of the detector. Both wheels contain LAr as the active material and an accordion/fan shape for their absorbers and electrodes. This is illustrated in Figure 4.8, which shows only 3 of the 256 inner wheel panels and 712 outer wheel panels, and the photograph in Figure 4.9. A more complete picture of the each endcap section can be seen in the simulated geometry shown in Figure 4.14. The accordion shape provides complete coverage in ϕ [49] to maximise the detector performance.

The absorber, which is formed in a wave-like shape, must have increasing wave amplitude with increasing radius to maintain a constant combined thickness of LAr and absorber/electrode material for all ϕ. The electrodes and absorbers are of identical shapes and only differ by their material composition and thickness. The absorbers are Pb, and the electrodes are a Cu (Copper) and Kapton mixture. The absorber thickness is also increased with radius in order to maintain a constant Pb to LAr ratio. The total thickness of the EMEC is in excess of 28 χ_0 for all η values. Since each wave section has increasing amplitude along the radial axis,

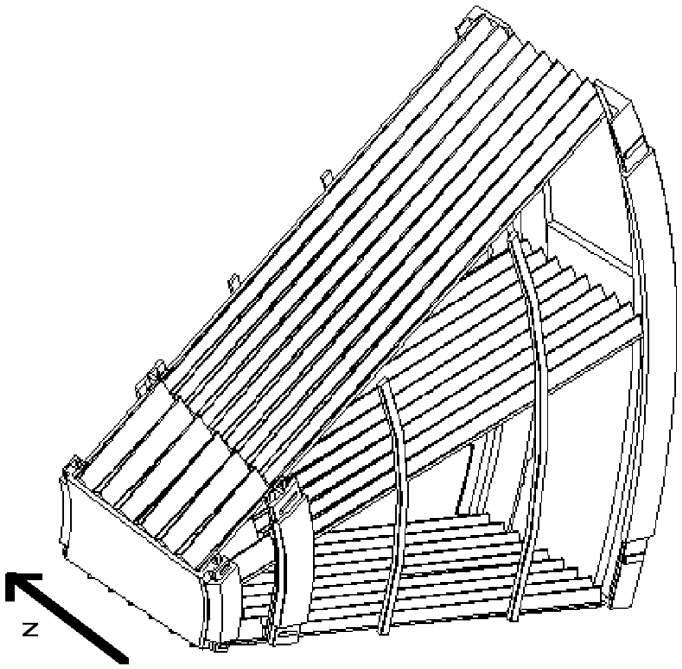

Figure 4.8: Structure of the EMEC showing both the inner and outer wheels, showing the accordion structure of the absorbers/electrodes. [49] The wavelength of the folds of the inner and outer wheel respectively are 83 mm and 55 mm. The amplitude of each wave is approximately 30 mm. This figure shows only 3 of the 712 outer panels of the EMEC.

but constant wavelength is maintained, the geometry of each absorber is similar to a planar surface that has undergone a twist along the radial axis.

The complicated nature of this geometry creates difficulties in developing a realistic but efficient simulation of this detector component. There is no accordion shape within the GEANT4 standard geometry shapes, and so for simulation this accordion structure is defined as a "custom solid" geometry. A custom solid is a user defined geometry not constructed from standard GEANT4 shapes, as discussed in Section 4.1.2. The geometry of the EMEC custom solid is defined according to a "neutral fibre", which is a wave shaped structure representing the central points in each fold of the fan. Figure 4.10 illustrates the cross-sectional structure of the neutral fibre (over a distance of 1/4 wavelength). The slant angle α varies as a function of radius, since the wave amplitude must do so, but the wavelength remains constant. The custom solid calculations are done relative to

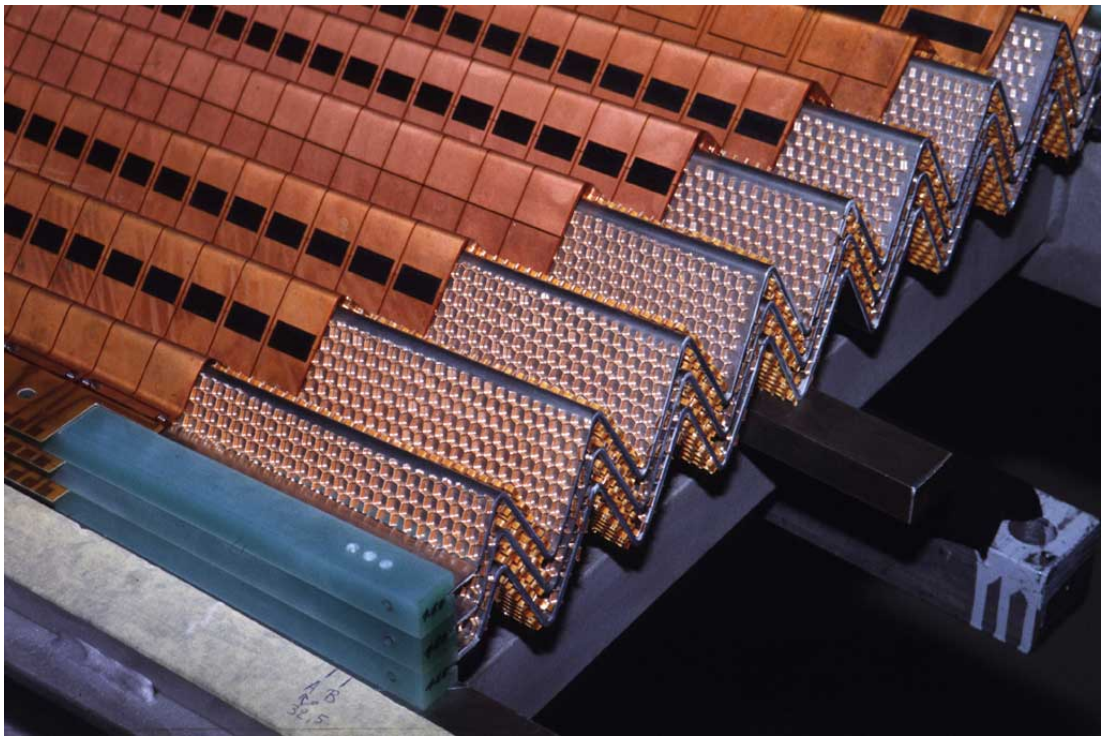

Figure 4.9: Photograph of an EMEC outer wheel section [88].

this neutral fibre, and other solids are defined and positioned with reference to it. The linear portion of the fibre is defined by $x = z\tan(\alpha)$, and the radius of the fold section, ρ is constant for all folds in each wheel, but varies between wheels.

While being three separate materials in reality, the absorber, electrode, and glue materials are represented as one average material for the purposes of the current simulation. Also implemented in the simulated geometry is an absorber sagging algorithm, which models the deformation of the geometry under the action of gravity over time.

The custom solid used for representation of the EMEC absorber/electrode structure is the only geometry in the ATLAS simulation project that is not represented by GEANT4 standard solids. It is the twist in the geometry that makes it problematic to represent, the barrel calorimeter, for example, does not require a custom solid representation because of the absence of a twist. Prior to 2001, a simulated EMEC geometry did make use of GEANT standard shapes but this was with an older version of GEANT3 which permitted the use of a "twisted trapezoid" shape that was removed in GEANT4. Due to GEANT4's

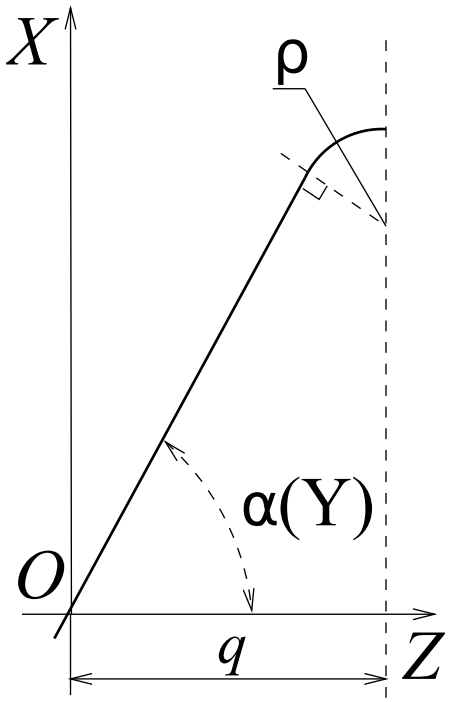

Figure 4.10: The EMEC neutral fibre profile (1/4 wave), the slant angle α varies as a function of radial distance (Y) [89]. Z is the beam axis, Y is out of the page.

improved handling of the tracking and physics, it was decided to update the EMEC geometry description to be compatible with GEANT4, thereby requiring the definition of the custom solid. As this custom solid is complex and GEANT4's voxelisation for tracking optimisation cannot be applied to custom solids, the result was a significant performance reduction, as indicated in Table 4.1 [89].

Region	**CPU time (s) for** **GEANT3**	**GEANT4**	
EMB (Barrel)	0.34	0.64	+ 88 %
EMEC Outer Wheel (at $\|\eta\| = 1.9$)	0.56	1.11	+118 %
EMEC Inner Wheel (at $\|\eta\| = 2.8$)	0.53	0.82	+ 55 %

Table 4.1: Comparison of EMEC CPU time requirements between GEANT3 and GEANT4 geometries. Tests done on Pentium III, 0.8GHz, for 10 GeV electrons [89].

The performance degradation due to the use of the custom solid is clearly very high. A detailed performance study [90] of the ATLAS simulation software

identified that the key methods associated with the EMEC simulation account for $\sim 15\%$ of the whole ATLAS simulation CPU time. In comparison, the CPU time used by the key methods for all other internally defined solids, combined, was found to account for only $\sim 2\%$ of the whole ATLAS simulation CPU time. The remaining $\sim 83\%$ of CPU time taken by the whole ATLAS simulation is used on tasks that are not geometry shape specific. GEANT4 has now re-introduced the twisted trapezoid solid, in addition to many similar complex solids.

GEANT4 also uses an optimisation scheme known as voxelisation. Voxelisation is designed to optimise the tracking of particles through the user defined volumes. It works by dividing a user defined geometry into simple virtual volumes (voxels). Where possible, tracking calculations are done on these voxels rather than on the user defined volumes. The best distribution of these voxels has to be calculated based on the user defined geometry in a process known as voxelisation. The user can control the granularity of the voxelisation via a tunable parameter known as the "smartless" parameter. This parameter represents the average number density of user defined volumes contained within any single voxel. Typically a voxel will contain around 2 user defined volumes.

The remainder of this chapter presents the efforts that I made to improve the simulation time performance by making use of a new series of shapes available within the GEANT4 library, and making use of GEANT4's optimisation algorithms.

4.3.1 Twisted Trapezoid Approach

The first approach relied on inspiration from the former GEANT3 twisted trapezoid geometry, written in MORTRAN [91], an extension of FORTRAN. This method was used with the twisted trapezoid solid recently introduced into GEANT4. This shape, shown in Figures 4.11 and 4.12 is capable of modelling the absorber shape well, permitting the definition of a shape with varying thickness and width along any axis, and also providing a detailed modelling of the surfaces that result from a twist along one axis. These surfaces are modelled by 7th order polynomials. Testing of this geometry with 20 GeV electrons produced the results shown in Table 4.2.

After development of this twisted trapezoid based geometry, the performance was found to be 194% slower in the inner wheel and 140% slower

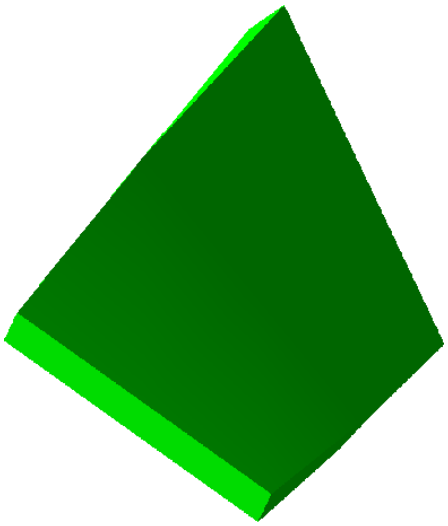

Figure 4.11: Twisted trapezoid representation of an absorber section.

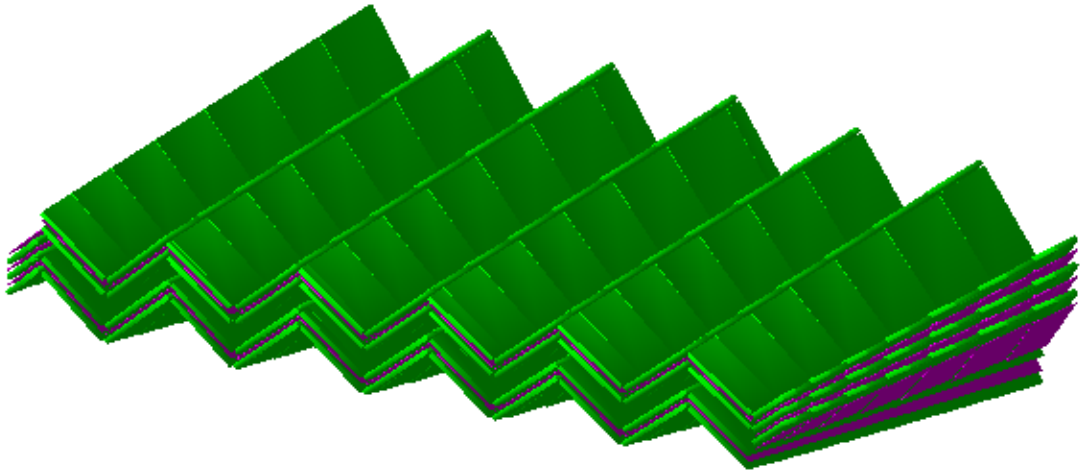

Figure 4.12: Layers of absorbers formed from twisted trapezoids.

in the outer wheel. The agreement between number of tracks simulated was within 3% between both implementations. A typical simulation will use approximately 25% of its simulation time in a GEANT4 tracking method known as `ComputeStep()`. This method contains two sub-methods known as `DistanceToIn()` and `DistanceToOut()`. These methods perform calculations to determine how far along the direction of a particle's travel it will enounter a new solid and exit the current solid, respectively.

Wheel	CPU time (s) for Custom solid	Twisted trapezoid	Increase
Inner	13.4	39.5	+194 %
Outer	11.9	28.6	+140 %

Table 4.2: Comparison of CPU time requirements between the custom solid and twisted trapezoid implementations of the EMEC.

The twisted trapezoid implementation used approximately 93% of its simulation time in the `ComputeStep()` method, almost all of which came from the `DistanceToIn()` and `DistanceToOut()` methods, thus a factor of ~ 4 greater than for typical simulations. These methods require the equation governing the surface of the solids to be solved, and in the case of the twisted trapezoid, $\sim 57\%$ of the time spent in these methods was on solving the 7th order polynomial.

4.3.2 Standard Trapezoid Approach

As a response to results obtained from the performance testing of the twisted trapezoid implementation of the geometry, it was decided to test the geometry with a standard trapezoid implementation. The standard trapezoid cannot model a twist, and so 50% more radial sections with relative rotations along the radial axis were used to construct each absorber wave segment, as shown in Figure 4.13.

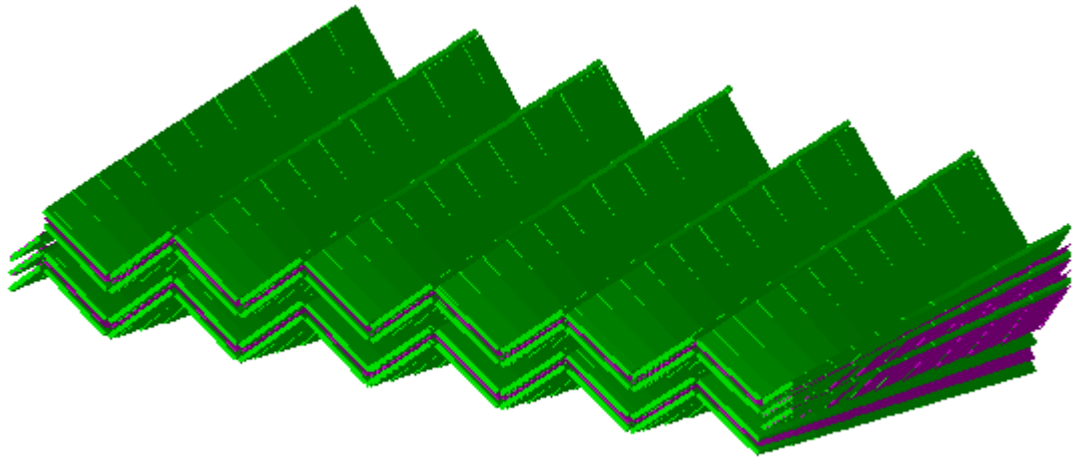

Figure 4.13: Layers of absorbers formed from standard trapezoids.

The performance of the standard trapezoid implementation was tested, and the results are shown in Table 4.3.

Wheel	CPU time (s) for Custom solid	Standard trapezoid	Increase
Inner	13.4	13.6	+ 2 %
Outer	11.9	9.8	−18 %

Table 4.3: Comparison of CPU time requirements between the custom solid and standard trapezoid implementations of the EMEC.

For the standard trapezoid implementation, an improvement of $\sim$ 18% was measured in the outer wheel, while the inner wheel had comparable performance to the custom solid implementation. In this case again, better than 3% agreement was found in the number of simulated tracks. The `ComputeStep()` method reduced significantly to $\sim$ 19%, and only a quarter of this was due to the `DistanceToIn()` and `DistanceToOut()` methods.

4.3.3 Generic Trapezoid Approach

Finally an alternative geometry was implemented using another newly introduced GEANT4 shape, known as the generic trapezoid. The generic trapezoid has eight vertices identical to those of the twisted trapezoid, but the surfaces formed by the twist are simplified considerably. Rather than a 7th order polynomial, the surfaces are constructed from many planar sections.

The performance of the generic trapezoid implementation was tested, and the results are shown in Table 4.4.

Wheel	CPU time (s) for Custom solid	Generic trapezoid	Increase
Inner	13.4	14.2	+6 %
Outer	11.9	11.3	−5 %

Table 4.4: Comparison of CPU time requirements between the custom solid and generic trapezoid implementations of the EMEC.

For the generic trapezoid implementation, an improvement of $\sim$ 5% was measured in the outer wheel, while the inner wheel had slightly degraded

performance compared to the custom solid implementation with a CPU increase of $\sim 6\%$.

4.3.4 Overlap Avoidance and Voxelisation

Having successfully obtained some performance improvements using the standard and generic trapezoid solids, without any exploration of the optimisation possibilities. The next step was to determine the best method of aligning these solids in layers to form the calorimeter's cylindrical shape, as shown in Figure 4.14, and to explore the optimisation possibilities.

One of the principles of GEANT4's tracking algorithms, is that for optimal tracking performance, a series of nested shapes should be used where the outermost shape should be the simplest. Calculations required to be performed by the tracking algorithms to determine a distance to the nearest solid can then be done, for the most part, on the simplest outer solid. Thereby removing a significant portion of CPU intensive calculations that would otherwise be required with the more complex inner solids.

The complex nature of the EMEC geometry means that absorber layers are interleaved with one another, see Figure 4.12, making it impossible to create simple volumes to contain the absorbers without causing unwanted overlaps in the geometry. Initially the geometry was developed with simple wedge shaped solids containing the more complex absorber and electrode shapes, that were then replicated to form the complete cylinder (inspired by an old GEANT3 implementation). This caused problems with overlaps in GEANT4 that were not necessary to consider in GEANT3, due to its different handling of overlapping volumes. As a first attempt to overcome the overlap problem, all absorber layers were placed inside one mother volume (the cylinder). This removed the problem of overlaps, but required the placement of millions of solids inside one volume which created problems for the tracking and voxelisation.

Figure 4.15 shows the performance of the GEANT4 voxelisation and tracking algorithms for only $\sim 5\%$ of the inner wheel ($\sim 1\%$ of the whole geometry) layers inserted. The memory use and CPU time used by the voxelisation algorithm is highly dependent upon the smartless parameter. The event time is also dependent the on smartless parameter, but in a less predictable manner. Even with the lowest number density possible (without significantly compromising the event

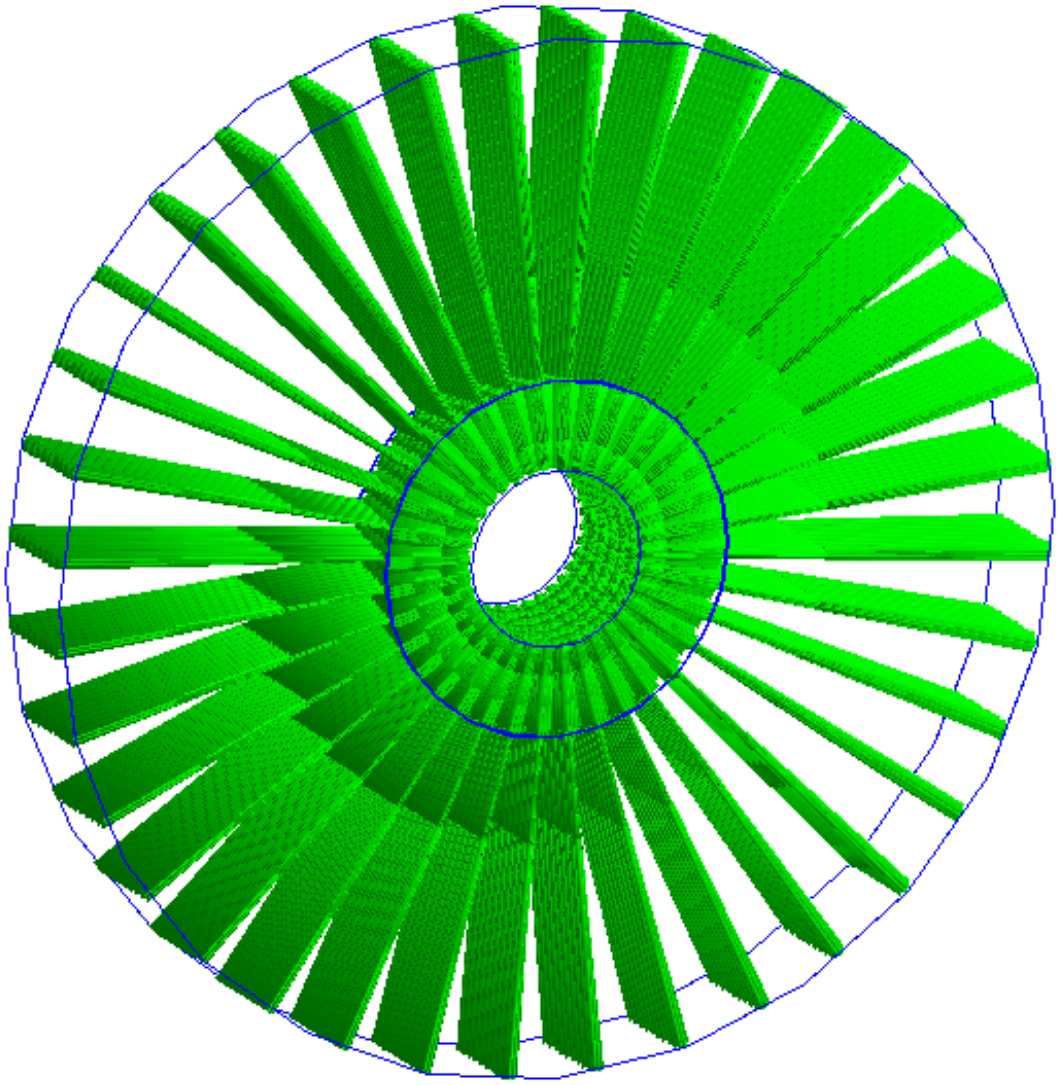

Figure 4.14: Inner and outer wheels of the EMEC, with a reduced number of absorber sections for display purposes.

time), the voxelisation algorithm required 25 Megabytes and 60 seconds to run for only 1% of the absorbers inserted. Scaling this for all absorbers would lead to over 2 Gigabytes of memory, and over 5000 seconds required to voxelise. This is not practical.

Since no suitable solids exist that can be replicated, every absorber layer is treated as an independent solid within the cylindrical wheel. This means that information about every absorber must be held in memory, and voxelisation must

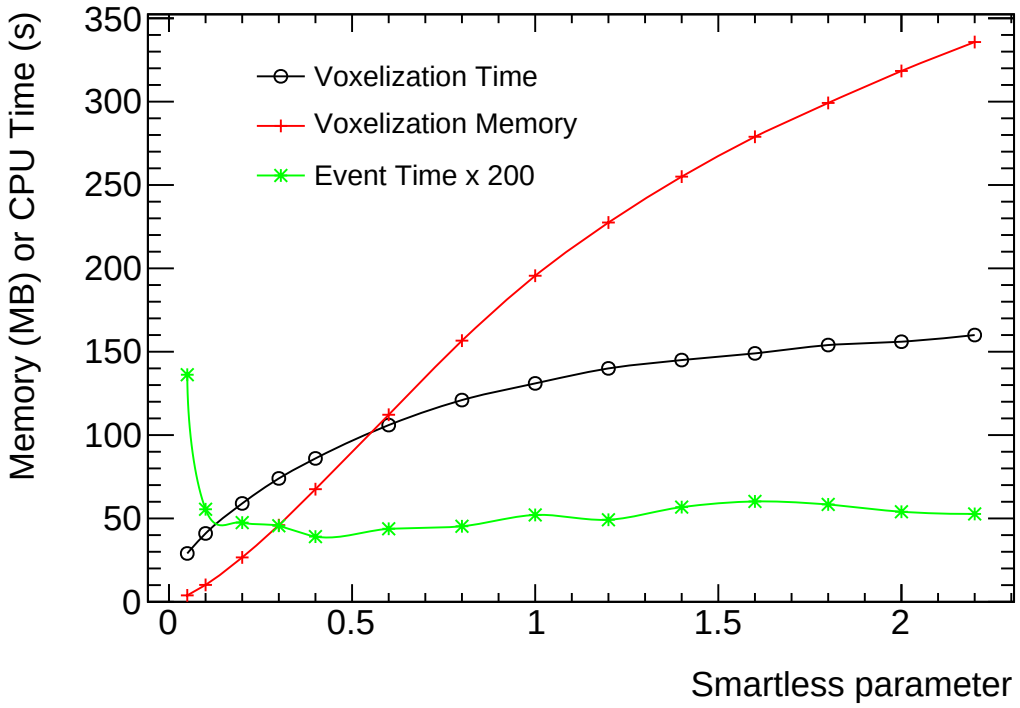

Figure 4.15: Voxelisation requirements, and event times for $\sim$ 5% of the inner wheel.

be done for every volume independently.

It is clear from the results in Section 4.3.4 that the crux of the problem with the voxelisation is the lack of straightforward replication in the geometry.

4.3.5 Summary and Status

During the re-development of the EMEC simulated geometry good progress was made, but there were several challenges that only came to light during the re-development. The first was related to how much simulation time would be required to simulate the twisted trapezoid solids in an EMEC setup. The twisted trapezoids were slower to simulate than had been expected, due to the complexity of the surface equations. This required additional implementations to be developed with standard and generic trapezoid solids which had not been anticipated.

Secondly although we anticipated being able to investigate voxelisation with a

view to obtaining the most efficient setup we could, the level of resources required by the voxelisation algorithms was much higher than expected. This is mainly due to the fact that overlap limitations prevented us from exploring a simple, nested hierarchy of volumes that would have been ideal to optimise. The result was an optimisation attempt on millions of independent volumes without a large use of nesting properties. The high voxelisation resource requirements made exploration of the voxelisation a lower priority than finding a suitable hierarchical structure in which to nest the volumes.

Both of these factors have led to additional developments being necessary and the time available to work on this task was exhausted, and not sufficient to achieve a fully implementable solution. Ideas exist for how to proceed with this development and find solutions to the latest challenges, as outlined in Section 4.3.6, and these will be passed on to future developers in this area.

In addition to the demonstration that a performance improvement is possible when using internal GEANT4 solids, much was learned about the operation of GEANT4 and the techniques required to obtain a certain outcome. Each challenge offered possibilities to learn more details of the operation of GEANT4 and find the most effective method to implement a solution where more than one method existed. The exercise provided valuable feedback to the GEANT4 experts about the performance of the voxelisation and each geometry component in real detector simulations, and challenges have been addressed alongside the GEANT4 experts.

The current status of the development is that an implementation of the EMEC now exists which can use twisted trapezoids, generic trapezoids or standard trapezoids. It is maintainable, manageable and can be visualised which is not possible with the former custom solid implementation. Studies have shown that the performance can rival or exceed that of the custom solid implementation, but a novel method of overcoming overlaps will be necessary before this implementation could be used in production as part of the full ATLAS simulation software.

Examples of 200 MeV and 200 GeV electrons incident on the inner wheel of the EMEC (with only 20 absorber sections instead of the full 256 for display purposes) are shown in Figures 4.16 and 4.17. These show the extra complexity in simulating a high energy electron shower in the calorimeter, and the extra tracks and steps present as a result. It is in this high energy regime where the new EMEC

implementation showed most performance gains. In the past visualisations like these were not possible.

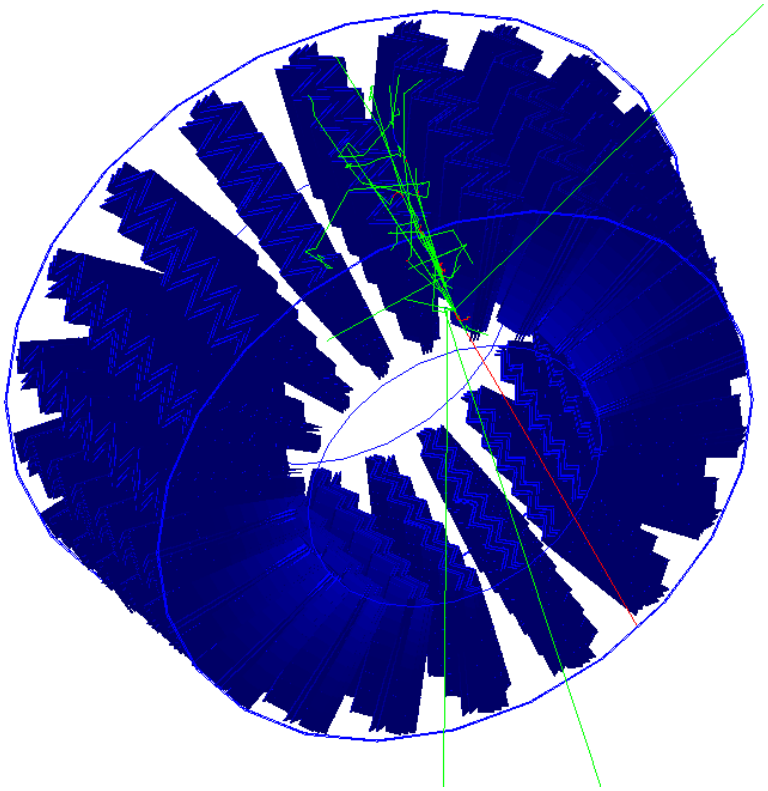

Figure 4.16: e^- incident on the EMEC inner wheel at 200 MeV. The red tracks represent negative particles, blue represent positive particles and green are neutral particles.

4.3.6 Next Steps

For further progress to be made it will be necessary to exploit some symmetry in the geometry, in order to permit nestable, repeatable volumes to be used such that GEANT4's voxelisation and tracking can run efficiently. Since the EMEC geometry is complex and depends on interleaved absorber layers, this is not a straightforward task and a novel method must be found to do this.

The objective is to find a method to divide the wheel into n sections (by use of a simpler containing volume), with the requirement that the wheel be completely filled by sub-volumes, then independent absorbers would only be required to fill

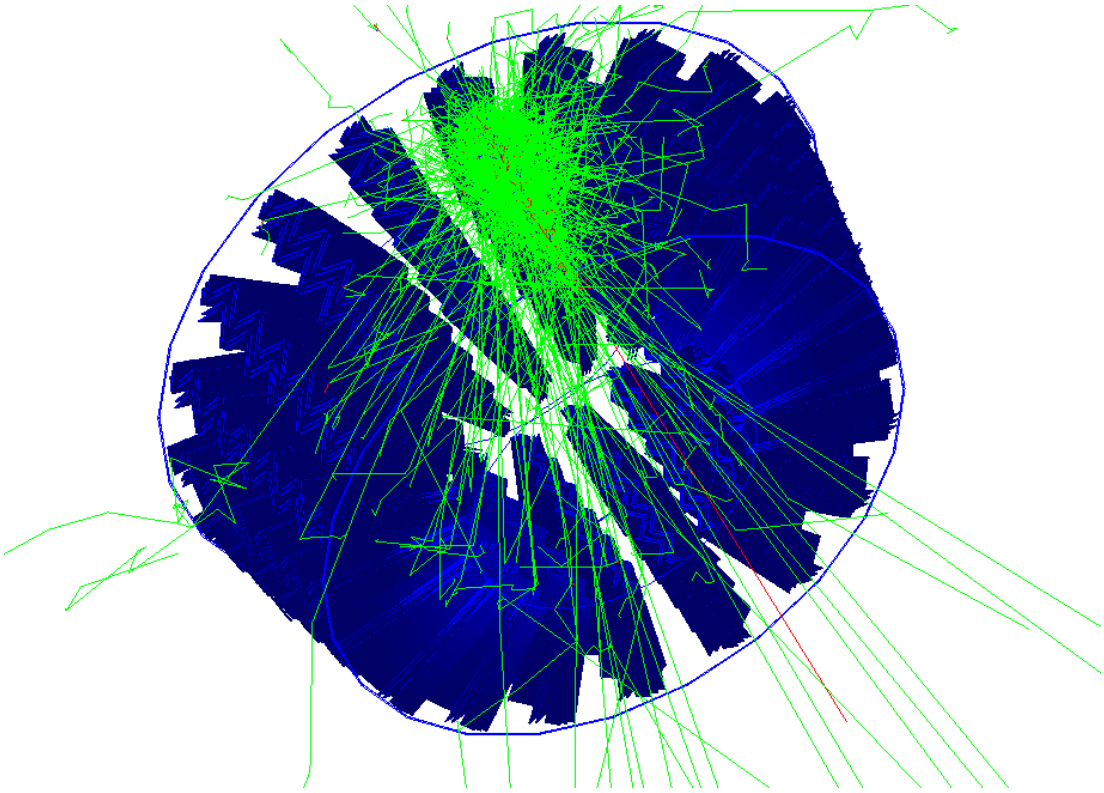

Figure 4.17: e^- incident on the EMEC inner wheel at 200 GeV. The red tracks represent negative particles, blue represent positive particles and green are neutral particles.

one section. This section could then be replicated n times, leading to a factor of n reduction in the voxelisation memory and CPU requirements. The voxelisation would effectively be done once for one section, then the results replicated n times.

One promising idea is to create a complex replicable containing volume (although simpler than the wave/fan shape) to contain a fraction of the total absorber layers, and then replicate this containing volume to form a complete cylinder. This containing volume would need to be complex enough to accommodate the wave shaped nature of the absorbers, but simple enough to allow efficient voxelisation and tracking. It is possible that this could be implemented using Boolean solid operations in GEANT4. This would involve creating a simple solid, such as a wedge shape, and then using other overlapping solids to subtract sections from the opposing surfaces of this wedge until the appropriate shape was obtained. This solution is still not ideal due to the complex

nature of the containing solid, however it would solve the problems experienced when running GEANT4's voxelisation routines, as it would reduce the memory and CPU time required to optimise the geometry for tracking purposes.

Chapter 5

b-tagging in the High p_T Regime

5.1 Introduction to jets

Since quarks and gluons carry colour charge, they interact via the strong force. After being produced they will undergo a process known as "fragmentation". Fragmentation is a result of the principle of colour-confinement, whereby colour charged particles may not exist in an isolated way, only in colourless groupings. As a quark, of a colourless quark-anti-quark pair for example, moves spatially apart from it's partner anti-quark, the force of the strong field between the quark and anti-quark (known as a colour flux-tube) does not diminish. This is contrary to the case, for example, of the electric field as the distance between electrically charged particles is increased, the force between them decreases. Eventually, as quarks are being separated, the energy in the colour flux-tube is sufficient to create a new quark-anti-quark pair and so there is an increase in the quark multiplicity. It is possible that one of the original quark or anti-quark will combine with one of the new quark or anti-quark to form a colourless bound state, known as a hadron. From what was originally a quark-anti-quark pair with the quarks having some kinetic energy, has become a process of hadron production via fragmentation and hadronisation. It proceeds to become a collection of hadrons, travelling en masse in approximately the same direction as the original quark, but with some lateral spread, and is called a "jet".

The hadrons within a jet may further decay, and their decay products may be measured in the detector. Some hadrons made from light quarks, such as the proton or neutron, have very long lifetimes and will not decay prior

to being terminated in the calorimeter. Others such as those made from b-quarks, will decay with an average lifetime long enough that they move some detectable distance before decaying, but short enough that they will decay such that their products can be observed in the detector. An example decay of a B^0 meson is $B^0 \to D^-\mu^+\nu_\mu$, with $\sim 2.2\%$ branching fraction. It is necessary to reconstruct jets from the information obtained by the detector and many methods of doing so exist. Some common algorithms for jet reconstruction are explained in Section 5.2.

The exploitation of both the decay time and the presence of muons in the decay products in order to identify, or "tag", jets containing b-quarks are explained in detail in Section 5.3.

5.2 Jet reconstruction algorithms

Typically, two types of algorithms are used: **clustering algorithms** and **cone algorithms**. Cone algorithms use a spatially constructed cone of set radius in the $\eta-\phi$-plane, R, to collect all particles lying inside it. In the cone algorithm, an initial seed is chosen, i. Then the ΔR_{ij}, given by Equation 5.1 is calculated for each particle, j. If $\Delta R_{ij} <$ R then the particle j is accepted part of that cone.

$$\Delta R_{ij} = \sqrt{(\eta_i - \eta_j)^2 + (\phi_i - \phi_j)^2} \tag{5.1}$$

If the cone is found to be stable, defined such that all particles, i, have $\Delta R_{iJ} < R$, where J is the central-axis of the jet and ΔR_{iJ} is also defined in Equation 5.1 but with J replacing j, then the process stops and this cone is considered to represent the jet. Alternatively if the cone is not found to be stable, then current central-axis of the jet, J, is taken to be the new seed, and the process is repeated until a stable cone is found.

An alternative approach is to cluster particles together to form jets. Clustering algorithms combine particles together based on some criteria, such as transverse momentum or distance between them. In the rest of this section, I shall use the word "entity" to represent a particle and also an object that has been clustered from particles already. The three main clustering algorithms used by the ATLAS reconstruction software are the K_T, AntiK_T, and Cambridge-Aachen algorithms [92]. The clustering works by calculating the distance, d_{iB}, between

an entity, i, and the beam, B. The distance, d_{ij}, between all entities i and j is also calculated. These are defined in Equations 5.2-5.3. The minimum of d_{iB} and d_{ij} is then determined. If it is a d_{iB} then this entity is accepted to be a jet, otherwise if d_{ij} is the smallest then entity i and entity j are combined (clustered) to form a new entity. The process is repeated until there are no remaining entities suitable for combination. Note that the "distance" referred to above, may have a purely spatial dependence, or it may be a transverse-momentum dependence also. It is this dependence which defines which of the three algorithms (K_T, AntiK_T, or Cambridge-Aachen) is to be used.

$$d_{iB} = k_{T_i}^{2\alpha} \tag{5.2}$$

$$d_{ij} = \min(k_{T_i}^{2\alpha}, k_{T_j}^{2\alpha}) \frac{\delta R_{ij}^2}{R^2} \tag{5.3}$$

Where:

$$\delta R_{ij} = \sqrt{\delta\phi_{ij}^2 + \delta\eta_{ij}^2} \tag{5.4}$$

Where k_T is the transverse momentum with respect to the beam axis [93], and R is a parameter defining the final width (in $\eta-\phi$-plane) of the cluster. Typically ATLAS uses $R = 0.4$ for AntiK_T jets. Often in analyses using jet-substructure, Cambridge-Aachen jets will be initially reconstructed as large jets with $R = 1.2$. This is done in the knowledge that this large jet will have some substructure. The large jet can then be split up into smaller Cambridge-Aachen jets. The large jet is often referred to as a fatjet, and it's smaller constituents subjets. The process of splitting and identification of the subjets is given in Section 5.2.1. As mentioned above, the form of the distance dependency defines the characteristics of the clustering algorithm, and this is controlled through the α parameter in Equations 5.2-5.3. α can take three values: 1 for K_T jets, -1 for AntiK_T jets and 0 for Cambridge-Aachen jets (only spatially clustered).

Due to the $1/k_T$ dependence of the AntiK_T algorithm, a key feature of the algorithm is that soft entities (small k_T) do not modify the shape of the jet, whereas the shape is defined by hard entities (large k_T) within it. This is because clustering will proceed with soft entities being clustered to hard ones first. In an event with only one hard entity (within a distance $2R$) and many soft ones, a

perfectly conical jet of radius R will be formed with the AntiK_T algorithm having clustered all the soft entities to the hard one. If another hard entity is present within R, both hard entities will ultimately be clustered together, but the cone shapes will be complex. In the case with another hard entity with $R < \delta R_{ij} < 2R$, the result will be two hard jets in intersecting cones, the exact shapes of which depend on magnitude of one entity's k_T relative to that of the other entity.

Neither the Cambridge-Aachen or K_T algorithms have this behaviour. Cambridge-Aachen has no k_T dependence and simply clusters spatially close entities first, and the K_T algorithm will tend to cluster entities which are softer and close-by first. This means that the AntiK_T algorithm generally produces the most regularly shaped jets and is the ATLAS preferred algorithm for non-substructure analyses.

Examples of jet shapes obtained with these three clustering algorithms, and a cone algorithm are shown in Figure 5.1.

5.2.1 Cambridge-Aachen jets

Due to the very high-energy nature of LHC collisions, whereby boosted objects can decay into hadrons whose spatial separation is low, there are shortcomings in using the above jet clustering algorithms alone. In these cases conventional jet clustering algorithms may cluster multiple hadrons into a single "fatjet", losing information in the process. ATLAS makes use of additional "jet-substructure" algorithms to extract additional information about the process. The jet-substructure algorithm relies upon Cambridge-Aachen jets reconstructed with a radius parameter of R = 1.2. The following steps are applied [94]:

1. The last clustering step of the Cambridge-Aachen algorithm (with R = 1.2) which identified the fatjet, J, illustrated in Figures 5.3 (a) & (b), is undone to split the jet into two jets, j_1 and j_2. This is shown in Figure 5.3 (c). If this is not possible then the object is considered to have no jet-substructure and the algorithm does not proceed.

2. If there is a large difference in mass between the original jet, J, and the heaviest of the newly split jets i.e. $\max(m_{j_1}, m_{j_2}) < \mu\, m_J$ (μ is typically $\frac{2}{3}$), then a sufficient "mass-drop" has been identified and j_1 and j_2 both share a significant fraction of the original jet mass and the algorithm proceeds. If this condition is not true because one of the split jets contains only a small

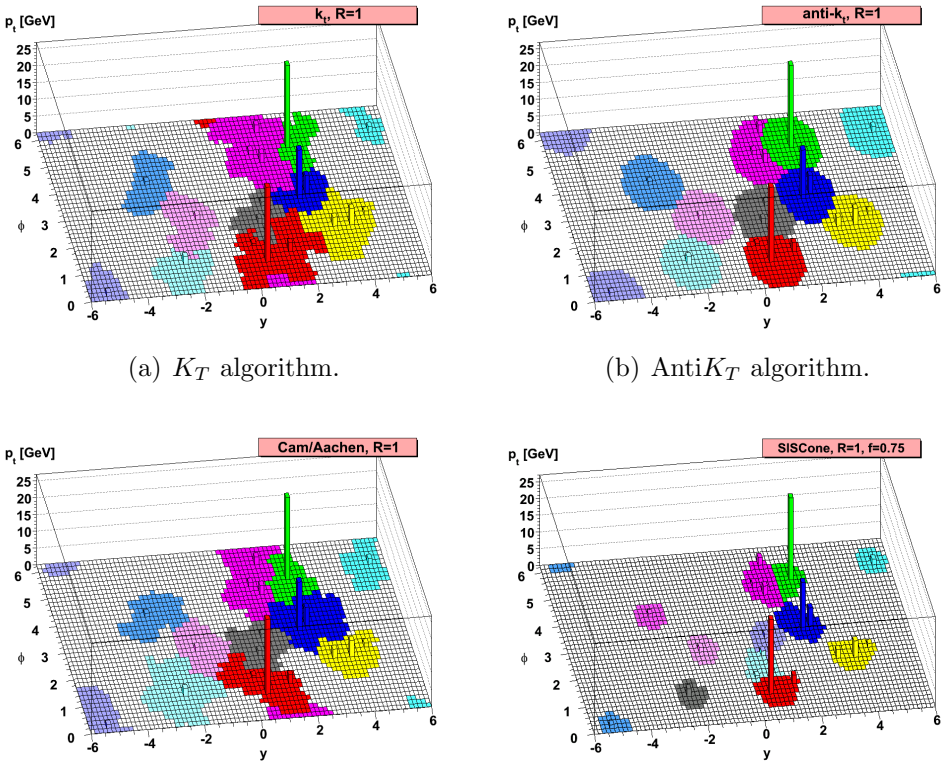

(a) K_T algorithm.

(b) AntiK_T algorithm.

(c) Cambridge-Aachen algorithm.

(d) Cone algorithm.

Figure 5.1: Jet shapes formed from various jet reconstruction algorithms, the clustering K_T, AntiK_T, and Cambridge-Aachen algorithms and a cone algorithm. For K_T and Cambridge-Aachen, in (a) and (c) it can be seen that irregular shapes are obtained by the jet shape's sensitivity to soft entities. In (b) the AntiK_T algorithm shows regularly shaped jets, but with clipping occurring where jets are overlapping. Finally the cone algorithm (d) shows regularly shaped single-entity jets, but for jets with more than one hard entity, their shapes are less regular. [92]

fraction of the original mass, then the lightest split jet is removed from the original jet, J and the algorithm is restarted from the splitting step with the re-defined jet, J. Figures 5.3 (c) & (d) show the situation where the mass drop is not sufficient, and the jet re-defined and re-split.

3. If $y_{12} > y^{\text{cut}}$ (y^{cut} is typically 0.09), where y_{12} is defined in Equation 5.5, then the algorithm proceeds. If this condition is not true then the softest split jet is removed from the original jet, J, and the algorithm is restarted from the splitting step with the re-defined jet, J.

$$y_{12} = \frac{\min(k_{T_{j1}}, k_{T_{j2}})}{m_J^2} \delta R_{j_1,j_2}^2 \tag{5.5}$$

where k_T has the same definition as for the usual Cambridge-Aachen algorithm, and $\delta R_{j_1,j_2}$ is defined in Equation 5.6.

$$\delta R_{j_1,j_2} = \sqrt{\delta\eta_{j_1,j_2}^2 + \delta\phi_{j_1,j_2}^2} \tag{5.6}$$

4. At this stage there are two jets j_1, and j_2. Next is the filtering step, where the constituents of these two jets are re-clustered using the Cambridge-Aachen algorithm, with a smaller radius parameter, now given by $R_{\text{filt}} = \min(0.3, \delta R_{j_1,j_2}/2)$. The three hardest jets clustered during this process, are accepted, and known as "subjets". The filtering and identification of subjets is illustrated in Figures 5.3 (e) & (f) respectively.

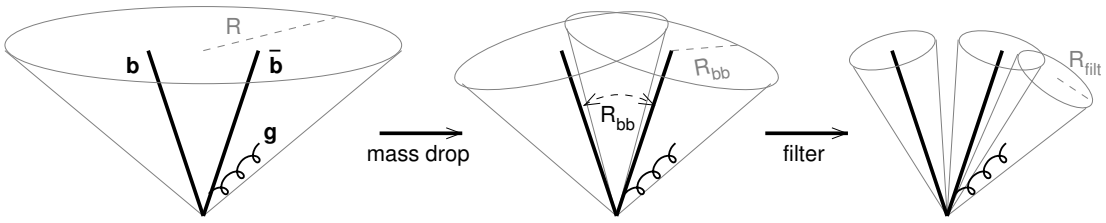

Figure 5.2: Reconstruction of "fatjets" and "subjets" with the Cambridge-Aachen algorithm [94].

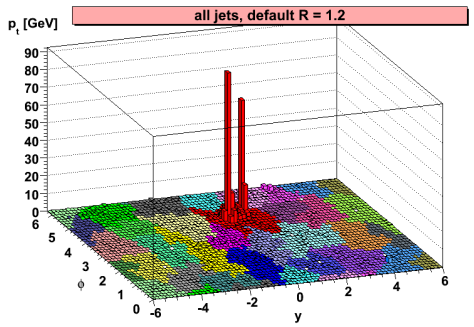

(a) Reconstruction of jets with the Cambridge-Aachen algorithm with $R = 1.2$.

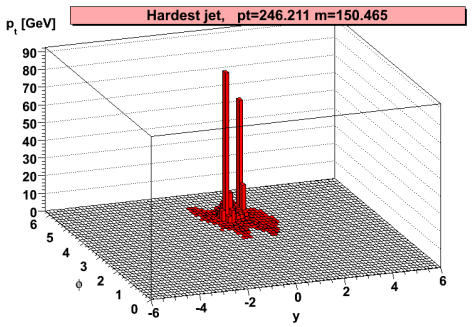

(b) The hardest of these jets is extracted, this is the "fatjet".

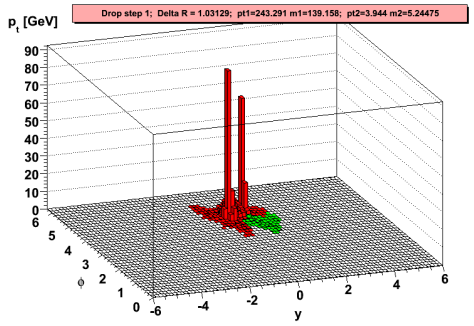

(c) The Last step of the clustering is undone to define two jets, red and green. However, the mass drop is not sufficient, and so the lighter green jet is removed.

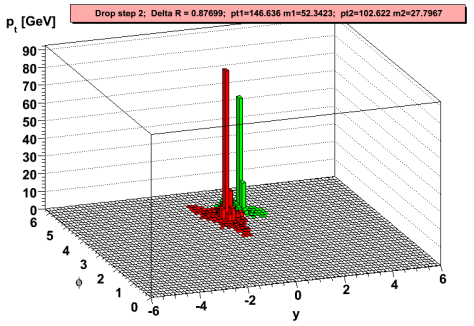

(d) The previous green jet from (c) was discarded and the splitting step was re-run on the red jet from (c). Creating two new jets. This time the mass drop is sufficient, as is the y_{12} criteria.

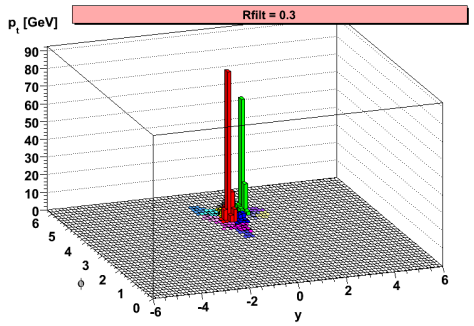

(e) The contents of the red and green jets from (d) are re-clustered with a refined radius parameter, in this case $R_{\text{filt}} = 0.3$.

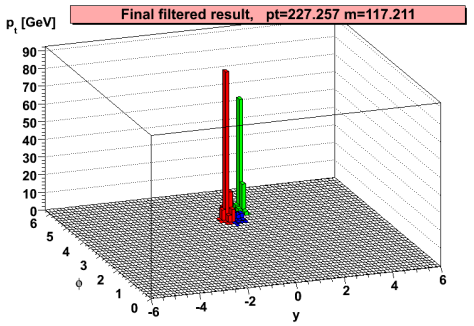

(f) Finally the three hardest jets from (e) are accepted as the "subjets".

Figure 5.3: Stages of the splitting and filtering process used to define subjets from fatjets reconstructed with the Cambridge-Aachen algorithm [95].

5.3 Introduction to b-tagging

The identification of jets originating from b-quarks is an important part of the LHC physics program. In precision measurements in the top quark sector (including the t-quark decay $t \to bW$), as well as in the search for the Higgs boson (Chapter 6) and new phenomena, the suppression of background processes containing predominantly light-flavour jets using b-tagging is of great use. It is also critical to eventually understand the flavour structure of any new physics (e.g. Supersymmetry) that may be revealed at the LHC [96]. As higher energy regimes are reached in particle physics, novel jet-substructure techniques are being utilised to improve the sensitivities of physics analyses.

The experimentally observable particles are not the b-quarks themselves, but rather B-hadrons. B-hadrons occur in both mesonic (e.g. B_s^0) and baryonic (e.g. Λ_b^0) form and typically have masses around 5 GeV. Since B-hadrons decay predominantly via the weak force, they have long life times compared to many other hadrons and this fact can be exploited to identify them.

A lifetime of approximately 1.5 ps corresponds to a $c\tau$ distance of $\sim$ 450 μm and in ATLAS with a $\gamma\beta$ factor of $\sim 12 - 13$ the decay length can be $\sim$ 6 mm. After being produced, the B-hadron will travel from the Primary Vertex (PV) and produce a Secondary Vertex (SV) spatially separated from the primary vertex. A profile of a B-hadron decay is shown in Figure 5.4.

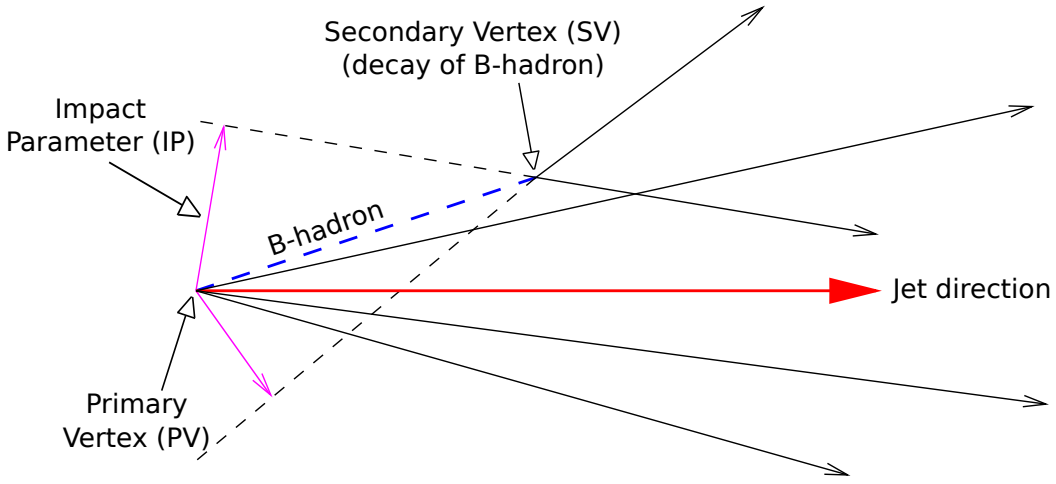

Figure 5.4: Example of a B-hadron decay. Modified from [97].

5.4 b-tagging in data and simulation

In order to make use of b-tagging in physics analyses, the efficiency of applying the b-tagging to jets must to be known in both data and simulation. The efficiency depends on the kinematics of the jet, such as the p_T and η.

The p_T^{Rel} method [98] has been used previously to perform b-tagging calibrations with AntiK_T jets. This chapter provides the results of the first b-tagging calibration where these techniques have been used to measure the efficiency of b-tagging Cambridge-Aachen subjets [92]. Results are presented for efficiencies in both data and simulation. A scale factor, derived as the ratio between the efficiencies in data and simulation, is also presented, along with associated systematic uncertainties. This analysis also is separated in terms of the ΔR between the subjets, allowing for close-by subjets ($\Delta R < 0.4$) to be calibrated for the first time. A detailed description of Cambridge-Aachen subjets is given in Section 5.2.1.

This chapter first outlines some of the common b-tagging algorithms employed by the ATLAS reconstruction software (Section 5.5), and then describes a measurement of the efficiency of several different b-tagging algorithms called SV0 [99], JetFitterCOMBNN [99] as well as a combination of the SV1, IP3D and JetFitter algorithms called MV1 [100]. This is done using the p_T^{Rel} method, as described in detail in Section 5.6.

5.5 Common ATLAS b-tagging algorithms

5.5.1 Impact Parameter (IP) based b-tagging

The impact parameter (IP) [97, 101] of tracks is calculated as illustrated in Figure 5.4. The Primary Vertex (PV) is found as the vertex that has the highest value of the sum of p_T^2 of associated tracks. The Secondary Vertex (SV) is the vertex produced by the hadron decay. The experimental resolution is taken into account by defining the impact parameter significance as the ratio of the impact parameter to the uncertainty on its measurement (σ_{IP}). By using the impact parameter significance as a discriminating variable, greater weight is given to more accurately measured tracks. A sign is applied to the IP measurement, whereby if the line joining the primary vertex and the impact parameter point is

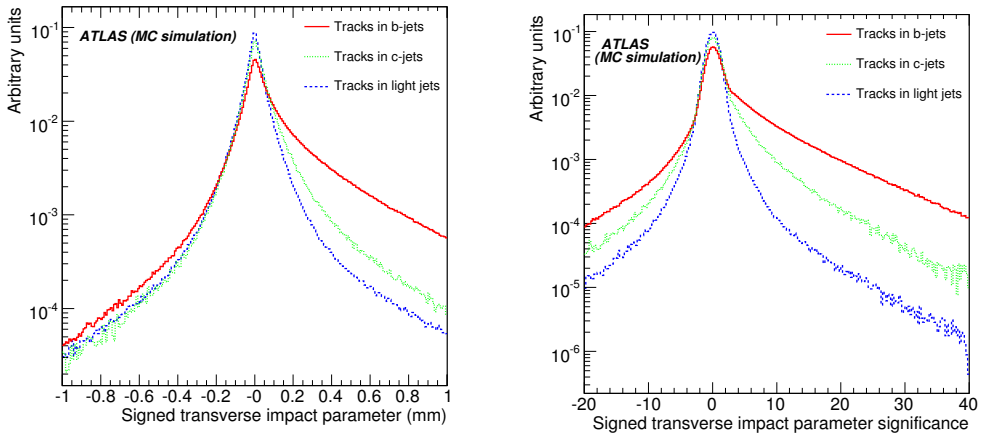

(a) Transverse impact parameter, IP

(b) Transverse impact parameter significance, $\frac{\mathrm{IP}}{\sigma_{\mathrm{IP}}}$

Figure 5.5: Distribution of the transverse impact parameter (a), and transverse impact parameter significance (b), signed with respect to the jet axis, for b-jets, c-jets and light-jets from simulated $t\bar{t}$ events at $\sqrt{s} = 14$ TeV. [101]

within 90° of the jet direction, it is signed positive, otherwise negative. Tracks originating from the primary vertex tend to have random sign (i.e. as often positive as negative), while those originating from D-hadron (containing a c-quark), or B-hadron (containing a b-quark) decays more often have a positive sign due to the longer lifetimes of these particles. Distributions of IP and $\frac{\mathrm{IP}}{\sigma_{\mathrm{IP}}}$ are shown in Figure 5.5.

The distributions have approximately Gaussian behaviour for light-jets, centred at zero, and are consistent with having originated at the primary vertex. The tails differ from a true Gaussian due to other particles in the jet having long lifetimes, and the effects of multiple scattering in the tracking system, which are not fully accounted for in the uncertainty estimation.

There are several ways that discrimination may be done to identify b-jets, based on the IP and σ_{IP} variables. One method involves track counting. This method requires a minimum number of good quality tracks to exceed some threshold in $\frac{\mathrm{IP}}{\sigma_{\mathrm{IP}}}$. Typically this works by ordering the tracks in descending values of $\frac{\mathrm{IP}}{\sigma_{\mathrm{IP}}}$, and setting the threshold at the n_{th} track, where n is chosen depending on the performance needs of the algorithm. Typically n may be 2 or 3. This is

one of the most simple b-tagging algorithms available, but requires a choice of n depending on the analysis needs.

An alternative method of discrimination involves the calculation of the probability that a given jet was a b-jet. This is done first by calculating the probability that each track originated from the primary vertex. This is calibrated against the $\frac{\mathrm{IP}}{\sigma_{\mathrm{IP}}}$ distributions for negative $\frac{\mathrm{IP}}{\sigma_{\mathrm{IP}}}$ (as this is effectively a control region for tracks originating from the primary vertex). The individual track probabilities are then combined to form a jet probability, giving the probability that the jet was a b-jet. This is a more complex algorithm but needs no choice of n.

Impact parameter based tagging may be done in two-dimensions or three-dimensions known as IP2D and IP3D respectively in the ATLAS software. A comparison of the performance of these algorithms is shown in Figure 5.6. This shows that the three-dimensional impact parameter based b-tagging can provide greater light-jet rejection compared with the two-dimensional one.

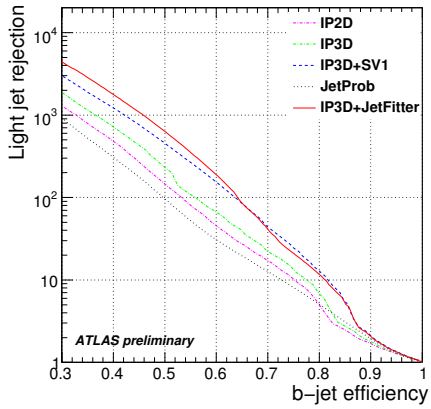

Figure 5.6: Comparison of performance of b-tagging algorithms on ATLAS[102]. It can be seen that the three-dimensional impact parameter based b-tagging, can provide greater light-jet rejection for a given b-tagging efficiency, compared to the two-dimensional algorithm.

5.5.2 Secondary Vertex (SV) based b-tagging

Secondary vertex [99, 103] based b-tagging relies upon the decay-length significance, $\frac{\mathrm{L}}{\sigma_{\mathrm{L}}}$, where L is the distance between the primary and secondary vertices and σ_{L} is the uncertainty on this measurement. It is also a signed variable having

a sign according to the projection of the decay length vector on to the jet direction vector.

The algorithm begins by constructing two-track vertices (vertices acting as the source of two tracks) whose tracks exceed the three dimensional impact parameter significance (IP3D) value of 2.3 and the sum of the impact parameter significance over the tracks exceeds 6.6. The two-track vertices must be incompatible with the primary vertex, and those having a mass consistent with a K_s^0 meson, or Λ^0 baryon, or consistent with a photon conversion are removed. Also if the two-track vertices occur spatially close to some detector material (e.g. within a pixel detector layer) then these are also removed as material interactions are likely to be the source of the vertices. The set of remaining two-track vertices are then combined, with some additional quality cuts, to form the secondary vertex representing the point of decay of the B or D-hadron.

Following this definition of the secondary vertex, a cut on the variable $\frac{\mathrm{L}}{\sigma_{\mathrm{L}}}$ can be applied. The cut can be chosen depending on the performance requirements of the analysis. This procedure forms the basis of the SV0 b-tagging algorithm.

The ATLAS reconstruction software also provides an SV1 b-tagging algorithm, which is an extension of SV0. Three additional vertex properties are considered under the SV1 algorithm. These are the invariant mass of all tracks associated to the secondary vertex, the ratio of the sum of energies of the tracks associated to the secondary vertex to those associated to the jet, and the number of two-track vertices. These parameters are combined using a likelihood ratio technique. Discrimination is also done on the ΔR between the jet direction and the direction of the line joining the primary and secondary vertices.

The SV0 algorithm is one of the algorithms calibrated in this analysis.

5.5.3 Jet Fitter based b-tagging

Jet fitter [104] based b-tagging addresses a shortcoming of the SV algorithms detailed in Section 5.5.2, when constructing a secondary vertex. SV based approaches assume that all sets of two-track vertices can be combined to form one secondary vertex that satisfies both the B-hadron decay and a D-hadron decay where the D-hadron was itself a decay product of the B-hadron. This can lead to tracks originating from the D-hadron vertex being removed in the combination procedure. Also the assumption of one secondary vertex point is

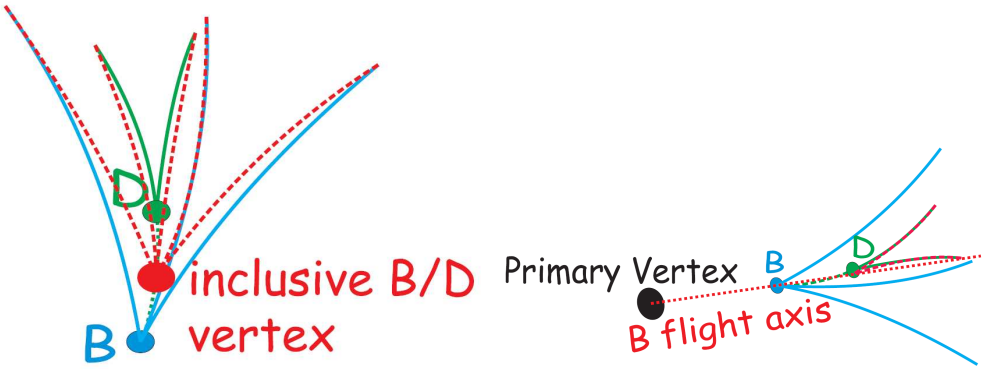

(a) SV secondary vertex finder (b) JetFitter secondary vertex finder

Figure 5.7: The reconstructed secondary vertices with (a) the default SV type secondary vertex finder, and (b) the JetFitter secondary vertex finder [104].

not valid when the distance between the B-hadron decay vertex and resulting D-hadron decay vertex is large compared to the experimental resolution. This difference in reconstructed secondary vertices is illustrated in Figure 5.7.

The JetFitter algorithm uses a different assumption than the invalid one of the SV algorithms. It assumes that both the B-hadron vertex and the D-hadron vertex are collinear along the line of the B-hadron flight path. All tracks from either vertex therefore intersect with this flight path axis. This is valid because the displacement of the D-hadron vertex from the flight path is typically very small. A Kalman filter approach is then used to reconstruct both vertices [105]. Once this is done, a likelihood function or neural network approach is used to define the b-tagging discriminator based on the following variables:

- The number of vertices having at least two tracks.
- The total number of tracks at these vertices.
- The number of additional single-track vertices on the B-hadron flight path.
- Invariant mass of all charged particles along the decay chain.
- The ratio of energies of tracks associated to the B-hadron decay chain, to those associated with the jet.
- The flight length significance for the B-hadron flight path.

A neural network approach based on the above Jet Fitter technique, is implemented in the ATLAS software and known as JetFitterCOMBNN. This is one of the algorithms calibrated in this analysis.

5.5.4 Multivariate (MV) based b-tagging

Multivariate based b-tagging [99, 106] such as the ATLAS MV1 algorithm relies upon a neural network combination that combines the output weight information from the SV1, JetFitter and IP3D taggers, and information from a $b \to c$ hadron decay chain fit. Thereby combining much of the information and discriminants already described. The MV1 tagger is now the ATLAS default tagger.

5.5.5 b-tagging efficiency working points

On ATLAS, b-tagging algorithms are provided with "efficiency working points". These working points, given in terms of b-tagging efficiency percentages, detail what cut values of the b-tagging weights are required to result in the given b-tagging efficiency. b-tagging weights are a measure of how b-jet-like a jet is. For example, Table 5.1 shows the working points for the MV1 algorithm.

Efficiency working point [%]	**b-tagging weight cut**
60	> 0.980
70	> 0.772
75	> 0.595
80	> 0.323

Table 5.1: b-tagging efficiency working points for the ATLAS MV1 algorithm [107].

5.5.6 b-tagging calibrations on data

While the b-tagging algorithms discussed in the previous sections can be utilised directly on data, they also have to be modelled in simulation, on Monte Carlo. Any mis-modelling that creates discrepancies in the performance of the algorithms between data and simulation is corrected for by the use of b-tagging scale factors. These are correction factors used to correct any efficiency modelled in Monte

Carlo to the efficiency that would have been measured in data under the same kinematic conditions. The scale factors are usually provided as a function of p_T^{jet}. The process of measuring these efficiencies in data and simulation and obtaining the scale factors is referred to as a "b-tagging calibration".

The uncertainties on the b-tagging efficiency and scale factors are typically one of the larger uncertainties in physics analyses involving b-tagging, and attempts to reduce the uncertainties in these calibrations are well motivated. In addition, while previous analyses have been dominated by use of the AntiK_T jet clustering algorithm, new analysis techniques in particular use of jet-substructure techniques are utilising other algorithms, notably the Cambridge-Aachen algorithm. There has also been movement into regions of high jet occupancy and low jet spatial separation, which require entirely new b-tagging calibrations. Several calibration methods have been used to calibrate the b-tagging efficiency on AntiK_T jets, including the p_T^{Rel} method, the System8 method and some $t\bar{t}$-based methods.

The System8 method [96] uses three selection criteria to construct a system of eight equations, based on the number of events surviving each of these selections. These are solved to obtain the number of b-jets and non-b-jets present after each selection, and the number of b-jets and non-b-jets originally present in the samples. The criteria are application of b-tagging, a requirement that the p_T of a muon, originating from a jet under study, relative to the jet axis, is greater than 700 MeV. Finally there is an "opposite-jet" requirement that another jet, with $p_T >$ 10 GeV, and b-tagged with a $L/\sigma_L > 1$, is present and travelling in the opposite direction to the jet under study, defined with the requirement $\pi - |\Delta\phi_{j_1,j_2}| < 1$.

The $t\bar{t}$-based methods rely on "tag-counting", and "kinematic-selection" and both make use of the fact that the decay $t \to bW$ occurs with almost 100% branching fraction. More details of these can be found in Reference [108].

The p_T^{Rel} method [96] builds templates of the p_T of muons originating from jets, relative to the jet axis, for b-, c- and light-jets. Due to the larger B-hadron mass, the p_T^{Rel} template for the b-jets will be harder than for c- or light-jets. These templates can then be fit to data to obtain the fractions of each jet type present in the samples before and after b-tagging with any of the b-tagging algorithms. Where results of multiple b-tagging calibrations are available, they are generally combined.

For the boosted Higgs boson analysis presented in Chapter 6, where the anal-

ysis makes use of Cambridge-Aachen subjets with spatial separation, $\Delta R_{\text{Subjets}}$, over the whole range below 1.2, a new b-tagging calibration was required. There had been no calibrations on Cambridge-Aachen subjets in the past, nor had there been calibrations in the region where subjets/jets were separated by $\Delta R < 0.4$. The remainder of this chapter describes the p_T^{Rel} method in detail, and presents details of the first full b-tagging calibration on Cambridge-Aachen subjets, including the case with spatial separation, $\Delta R_{\text{Subjets}} < 0.4$, the results of which are presented as a function of both p_T^{Subjet}, and $\Delta R_{\text{Subjets}}$.

The p_T^{Rel} method was chosen to perform the b-tagging calibration on Cambridge-Aachen subjets, for several reasons. Initially a feasibility study into how useful the p_T^{Rel} method could be in the $\Delta R_{\text{Subjets}} < 0.4$ regime was conducted, as it wasn't known how well templates could be used to discriminate between jet flavours in this regime. The results of this study found that although the discrimination wasn't as good as with the $\Delta R_{\text{Subjets}} > 0.4$ regime, it would be adequate for a full calibration. In addition the p_T^{Rel} method is less dependent on specific jet-related selections unlike, for example, the System8 method whereby selections are made on "opposite-jets". So a more like-for-like comparison could be made between a calibration on AntiK_T jets and one with Cambridge-Aachen subjets, with almost identical selections. It was therefore the recommendation of the b-tagging working group to proceed with a p_T^{Rel} calibration on Cambridge-Aachen subjets.

5.6 The p_T^{Rel} method

The p_T^{Rel} method makes use of the p_T of muons resulting from semi-leptonically decaying b-quark jets, relative to the jet + muon axis, so called p_T^{Rel}. The values of p_T^{Rel} for muons resulting from b-decays is larger than for those resulting from c- or light-decays due to the greater mass of the B-hadrons. Distributions of p_T^{Rel} for the various flavours of jet (commonly referred to as flavour templates) were built using Monte Carlo simulations, which were fit to the data distributions before and after b-tagging had been applied, allowing a measure of the b-tagging efficiency to be obtained. A schematic illustrating the definition of p_T^{Rel} is shown in Figure 5.8.

The b-tagging algorithms and working points shown in Table 5.2, applied to Cambridge-Aachen subjets, were calibrated with this analysis.

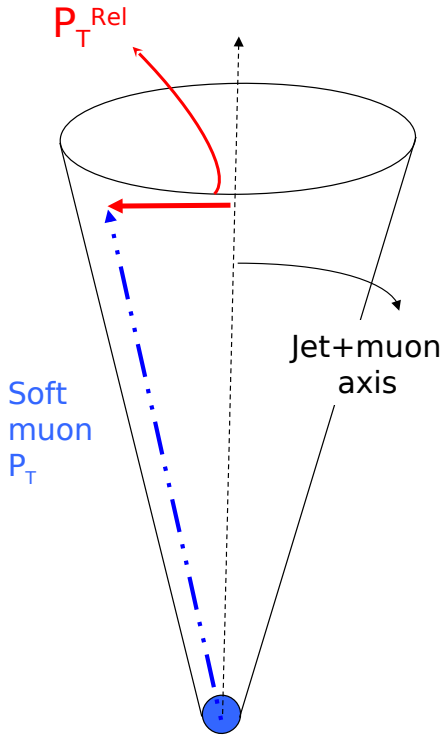

Figure 5.8: The p_T^{Rel} method. First, the vector sum of the jet and muon momenta is taken; the direction of the resulting vector gives an estimate of the direction of the b-quark in the jet. Then, the component of the muon momentum transverse to this direction, p_T^{Rel}, is calculated. Modified from [109].

b-tagging algorithm	**Efficiency working point [%]**
SV0	50
JetFitterCOMBNN	57, 60, 70, 80
MV1	60, 70, 75, 80

Table 5.2: b-tagging efficiency working points that were calibrated.

The analysis is binned in ΔR between two subjets; each bin in ΔR is further subdivided into bins in p_T^{jet}, as illustrated in Table 5.3.

dR bin	p_T^{jet} **bins [GeV]**
$\Delta R_{\text{Subjets}} < 0.4$	$20 \leq p_T^{jet} < 50$
	$50 \leq p_T^{jet} < 75$
	$75 \leq p_T^{jet} < 90$
	$90 \leq p_T^{jet} < 110$
	$110 \leq p_T^{jet} < 140$
	$140 \leq p_T^{jet}$
$\Delta R_{\text{Subjets}} \geq 0.4$	$20 \leq p_T^{jet} < 30$
	$30 \leq p_T^{jet} < 40$
	$40 \leq p_T^{jet} < 50$
	$50 \leq p_T^{jet} < 60$
	$60 \leq p_T^{jet} < 75$
	$75 \leq p_T^{jet} < 90$
	$90 \leq p_T^{jet} < 110$
	$110 \leq p_T^{jet} < 140$
	$140 \leq p_T^{jet}$

Table 5.3: Binning used in the analysis.

5.7 Analysis procedure

5.7.1 Data and Monte Carlo samples

The data sample used in this analysis corresponds to approximately 14.3 fb^{-1} of 8 TeV proton-proton collision data gathered by the ATLAS experiment during 2012. The analysis uses simulated samples produced by the ATLAS b-tagging group which from 2012 include information relating to Cambridge-Aachen "fatjets" and "subjets". The samples contain a reduced amount of information compared to the full amount recorded by ATLAS and typically only the information relevant for a specific analysis. The events were collected with five jet-muon triggers, each used in a different p_T^{jet} range. These triggers require a muon reconstructed from hits in the muon system, to be matched to a at least a 10 GeV calorimeter jet. Table 5.4 show details of the choice of triggers. The run selection was based on the official standard physics analysis good runs list.

Trigger jet energy threshold [GeV]	p_T^{jet} **range [GeV]**
15	$20 \leq p_T^{jet} < 40$
25	$40 \leq p_T^{jet} < 50$
35	$50 \leq p_T^{jet} < 75$
55	$75 \leq p_T^{jet} < 110$
80	$110 \leq p_T^{jet}$

Table 5.4: Triggers used in analysis. p_T^{jet} is the subjet p_T which caused the trigger to fire.

The Monte Carlo samples used in the analysis are listed in Table 5.5. These are dijet samples generated with PYTHIA 8, at 8 TeV, with the EvtGen shower model. To simulate the detector response the generated events are processed through the GEANT4 [110] simulation of the ATLAS detector, then reconstructed and analysed as if they were data. The Monte Carlo is split into two categories, standard and muon filtered. The muon filtered samples (referred to as JX_μ) have a 3 GeV muon p_T cut at the generator level, ensuring high statistics for events containing muons originating from b- and c-decays, but they have too few muons originating from other decays. Therefore the modelling of hadrons faking muons is not accurate in this sample and so the standard samples (referred to as JX) are used for some studies. Each sample contains information in a specific truth jet p_T range. The p_T^{jet} spectrum in Monte Carlo was re-weighted to reflect that in data. The sample number, represented by X, refers to slices of truth p_T^{jet}.

5.7.2 Procedure

As discussed already, in order to measure the b-tagging efficiency, the fraction of b-jets before and after b-tagging must be known. This information is extracted using the p_T^{Rel} method with the following procedure.

The muon selection required a reconstructed muon matched to a jet by the Equation 5.7. Where $\Delta R_{\text{Muon,Subjet}}$ may not exceed 0.4. p_T^{jet} is the p_T of the jet (in GeV) relative to the beam axis. The jet from which the muon originated is the one which is calibrated.

$$\Delta R_{\text{Muon,Subjet}} = 0.239 + e^{(-1.22-1.64\times10^{-5}\times p_T^{\text{jet}})} \tag{5.7}$$

Sample	Events	σ (nb)	Filter eff.	Truth p_T^{jet} range [GeV]
J0 (μ filtered)	2305472	7.29×10^7	3.80×10^{-4}	$17 \leq p_T^{jet} < 25$
J1 (μ filtered)	1765392	4.14×10^6	3.42×10^{-5}	$35 \leq p_T^{jet} < 70$
J2 (μ filtered)	9244822	5.01×10^3	7.97×10^{-4}	$70 \leq p_T^{jet} < 140$
J3 (μ filtered)	3735374	5.44×10^2	7.45×10^{-5}	$140 \leq p_T^{jet} < 280$
J0 (standard)	34728	7.29×10^7	9.85×10^{-1}	$17 \leq p_T^{jet} < 25$
J1 (standard)	520455	7.29×10^7	1.29×10^{-4}	$35 \leq p_T^{jet} < 70$
J2 (standard)	379361	2.64×10^4	3.98×10^{-3}	$70 \leq p_T^{jet} < 140$
J3 (standard)	486973	5.44×10^2	1.23×10^{-3}	$140 \leq p_T^{jet} < 280$
J4 (standard)	862034	6.44×10^0	7.08×10^{-4}	$280 \leq p_T^{jet} < 560$

Table 5.5: Monte Carlo samples used in the analysis. The μ filtered samples have a generator level minimum cut on muon p_T of 3 GeV to ensure high statistics for events containing muons originating from b- and c-decays.

This equation is used instead of the usual $\Delta R_{\text{Muon,Jet}} < 0.4$ definition for AntiK_T jets because where subjets may be within $\Delta R_{\text{Subjets}}$ of 0.4 of each other, muon-subjet matching would be ambiguous without applying a tighter $\Delta R_{\text{Muon,Subjet}}$ cut. p_T is in units of GeV in Equation 5.7. This equation was obtained from private communication with the inclusive p_T^{Rel} analysis team, and presented by them in unpublished documentation.

A muon p_T cut dependent on the jet p_T (both relative to beam axis) is then applied. 4 GeV for $p_T^{jet} \leq 60$ GeV, 6 GeV for $60 < p_T^{jet} \leq 90$ GeV, and 8 GeV for $p_T^{jet} > 90$ GeV. This is done to reduce the amount of fake muons in the higher p_T^{jet} ranges. Muons are required to be within $|\eta| < 2.5$, have more than one hit in the pixel system, greater than three hits in the semi-conductor tracker system, and greater than six hits in the entire silicon system. The primary vertex [111] must contain at least two tracks. The χ^2/N_{DOF} of the track fit must be less than 3. Also $|d_0| < 2$ mm, and $|z_0 \sin(\theta_0)| < 2$ mm are required. d_0 is the signed distance from the point of closest approach of a track to the global ATLAS z-axis, while z_0 is the z-coordinate of the track, also at the point of closest approach to the z-axis. θ_0 is the angle with the z-axis in the R-Z plane [112].

Jets are reconstructed using the Cambridge-Aachen clustering algorithm. This algorithm depends only on spatial parameters and not on p_T . The reconstructed object is a "fatjet" with radius 1.2. The clustering is reversed a few steps until two or three subjets are found following standard jet-substructure criteria listed

in Section 5.2.1 and illustrated in Figure 5.2. These subjets are corrected to account for the missing energy deposition from the muon and neutrino. The subjets are required to have $p_T^{jet} > 20$ GeV and $|\eta| < 2.5$. The percentage of events passing all the selection, is approximately 0.5%. The tightest selection cuts are those involving the kinematic selection of muons and fatjets, removing $\sim 90\%$ of events. The subjet-muon association, muon tracking quality cuts and subjet kinematic selection account for the remainder.

Jet flavour labelling is done by matching truth information for quarks (referred to as "truth quarks") from a Monte Carlo record to reconstructed subjets with the ΔR parameter as follows:

$$\Delta R = \sqrt{\Delta\eta^2 + \Delta\phi^2} \tag{5.8}$$

- b**-jet** - If a truth b-quark is found within 0.3 in ΔR of the subjet or within the cone of the jet (whichever is smallest), then the subjet is labelled a b-jet.
- c**-jet** - If the subjet has not yet been labelled, and a truth c-quark is found within 0.3 in ΔR of the subjet or within the cone of the subjet (whichever is smallest), then the subjet is labelled a c-jet.
- τ**-lepton** - If the subjet has not yet been labelled, and a τ-lepton is found within 0.3 in ΔR of the subjet or within the cone of the subjet (whichever is smallest), then the subjet is labelled a τ-lepton.
- **light-jet** - If the subjet has not yet been labelled, it is deemed to be a light-jet.

The b- and c-template shapes were obtained from the muon filtered Monte Carlo (JX_μ) samples with a loose b-tagging requirement used to enhance the heavy-flavour fraction. This requirement is that at least one subjet in the event must have an SV0 b-tagging weight > 1. This subjet is not used in the p_T^{Rel} calculation in order to not bias the measurement. In an event with multiple subjets passing this loose b-tagging requirement, a subjet not containing a muon will be discarded so as to maximise the number of muons-in-jets retained. The light-template shape was obtained from data with a tag veto applied. This allowed the template shapes to be built from larger statistics than were available with Monte Carlo. Events were only accepted if no jet in the event had a COMB

b-tagging weight greater than -0.85. This resulted in a sample dominated by light- and c-jets, but with a small b-jet contamination which was accounted for later, as discussed in Section 5.8.3.

5.7.3 Measuring the b-tagging efficiency with p_T^{Rel}

The b-tagging efficiency is defined as the fraction of reconstructed jets originating from b-quarks that are tagged by the b-tagging algorithm under consideration [98]. In order to extract this quantity from data, the number of b-jets before and after tagging needs to be known. This can be obtained for a subset of all b-jets, namely those containing a muon, using the p_T^{Rel} method. Muons originating from b-decays have a harder p_T^{Rel} spectrum than those in c- and light-jets. Templates of p_T^{Rel} are constructed for b-, c- and light-jets separately, and these are fit to the data in order to obtain the fraction of b-jets in the pre- and post-tagged data samples.

The p_T^{Rel} method does not separate well between c- and light-jets. To account for this the fit is instead performed on a b-template and a non-b-template. Where the non-b-template is made from the combination of light- and c-templates in fractions measured from simulations with the unfiltered Monte Carlo samples. Figure 5.9 shows an example of the p_T^{Rel} templates obtained. The fractions are listed in Tables 5.6 and 5.7, and a systematic due to the modelling of these ratios was assigned and explained in Section 5.8.2.

Both the untagged sample and tagged sample are fit with templates obtained from untagged Monte Carlo simulations. Untagged sampled are used because there is very good agreement between the template shapes for pre- and post-b-tagged cases. The fit is performed using a binned maximum likelihood, where each bin is treated as an independent Poisson variable. The fit does not take into account the statistical fluctuations on the templates, so an additional systematic (as discussed in Section 5.8.1) has been evaluated to take account of this.

Once the pre- and post-b-tagged fractions of b-jets were obtained from the p_T^{Rel} fits, the b-tagging efficiency was defined as

$$\epsilon_b = \frac{f_b^{\text{tag}} N^{\text{tag}}}{f_b N} \tag{5.9}$$

where f_b and f_b^{tag} are the fractions of b-jets before and after b-tagging respectively. N and N^{tag} are the total numbers of events before and after b-

tagging respectively. The efficiency, measured on semi-leptonically decaying b-jets in data, was then compared to the efficiency measured on semi-leptonically decaying b-jets in Monte Carlo and data-to-simulation scale factors are calculated as defined in Equation 5.10.

$$\kappa_{\epsilon}^{\text{data/sim}} = \frac{\epsilon_b^{\text{data}}}{\epsilon_b^{\text{sim}}} \tag{5.10}$$

As the b-tagging efficiency for hadronically decaying b-jets cannot be determined on data with the p_T^{Rel} method, the $\kappa_{\epsilon}^{\text{data/sim}}$ derived from semi-leptonically decaying b-jets is assumed to be valid for all b-jets. See Section 5.8.9 for more information.

5.7.4 Measurement in Data

To obtain the number of b-jets in the untagged and tagged samples, the p_T^{Rel} templates are fit to the p_T^{Rel} distribution before and after tagging according to the description in Section 5.7.3. The fits are performed in two bins of $\Delta R_{\text{Subjets}}$, each of which is sub-divided into bins of p_T^{jet}.

Knowing the fraction of b-jets in the pre- and post-b-tagged samples and the number of events in each, the b-tagging efficiency can be estimated using Equation 5.9. The efficiency and scale factor measurements are corrected for the contamination of b-jets in the light template, as described in Section 5.8.3. Example templates and fit results are shown in Figures 5.9 and 5.10 respectively.

5.8 Systematic Uncertainties

Systematic errors affecting the p_T^{Rel} analysis, may enter by affecting the shape of the flavour templates derived, or by affecting the efficiency of the simulated b-tagging algorithm. Below is a list of systematic uncertainties evaluated in the analysis:

5.8.1 Monte Carlo Statistics

The Monte Carlo statistics available can have an effect on the shapes of the p_T^{Rel} templates. The systematic effect of this is evaluated by taking the baseline template and randomly varying the bin content up or down by a Gaussian of

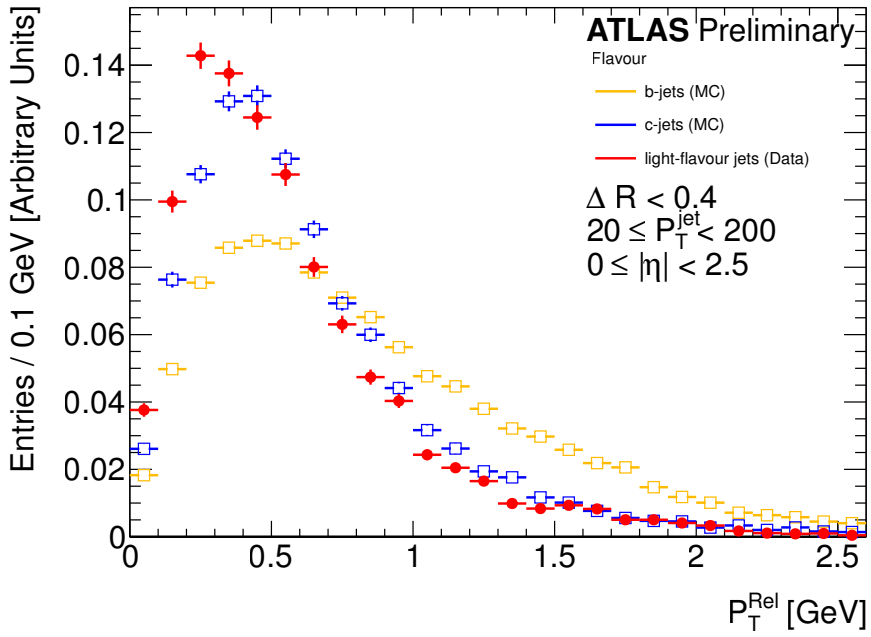

(a) $\Delta R < 0.4$

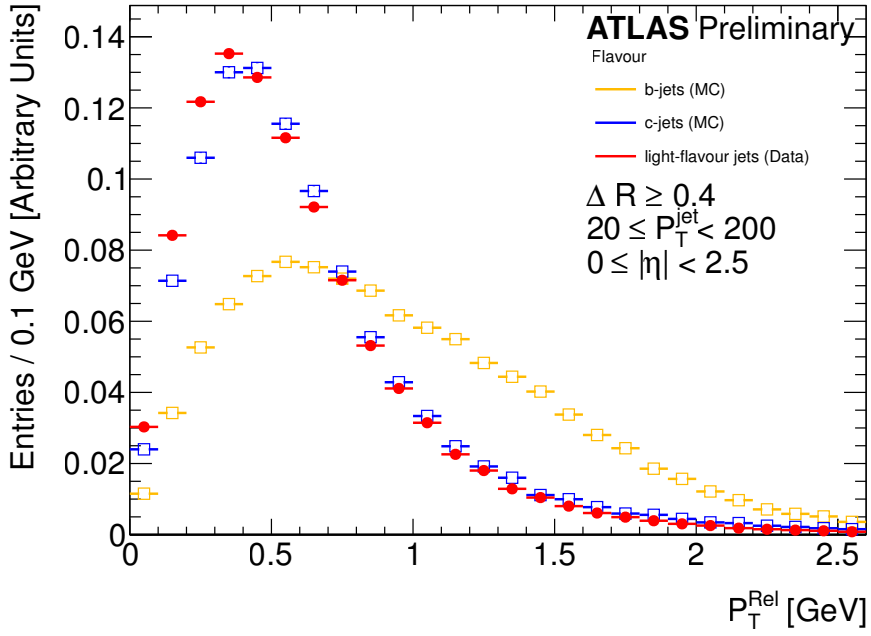

(b) $\Delta R \geq 0.4$

Figure 5.9: Example p_T^{Rel} templates show the template shapes for b- and c-jets (taken from filtered Monte Carlo), and for light-jets taken from data. The templates are normalised to unit area. It can be seen that for the $\Delta R_{\text{Subjets}} < 0.4$ region (a), there is less shape difference between the b and non-b templates, compared to the $\Delta R_{\text{Subjets}} > 0.4$ region shown in (b). There is therefore less discriminating power for the $\Delta R_{\text{Subjets}} < 0.4$ region.

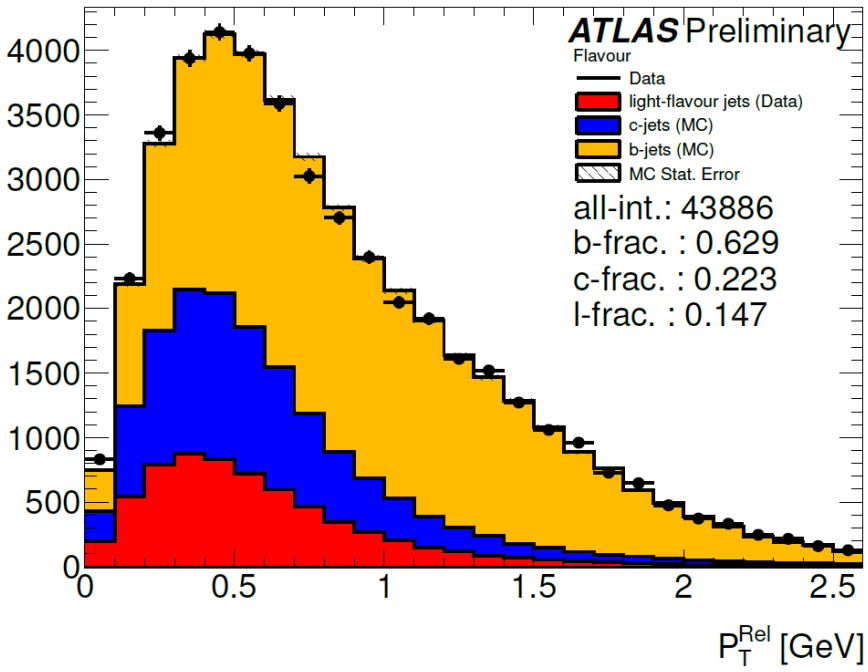

(a) Pre-b-tagging

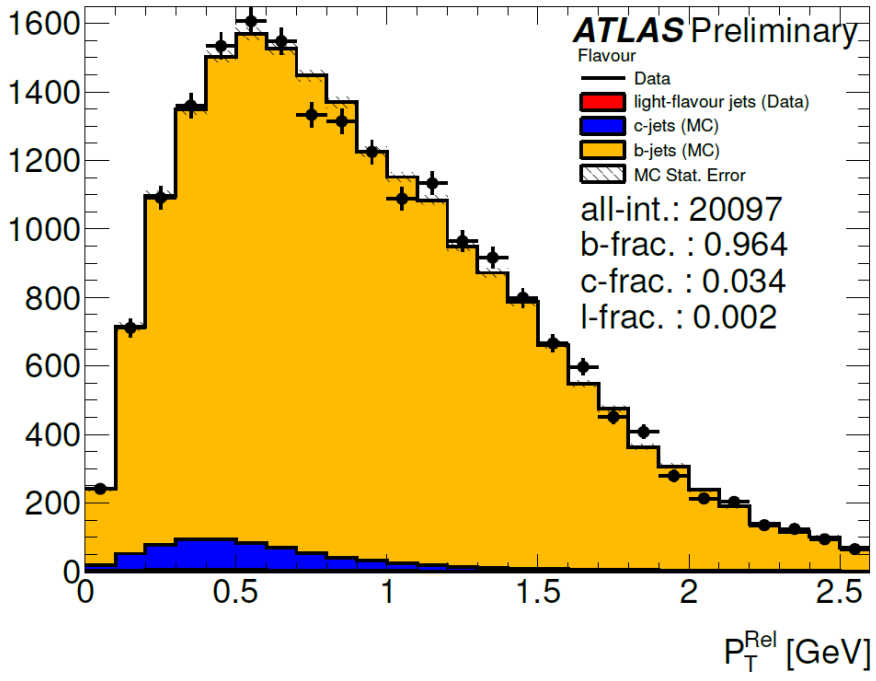

(b) Post-b-tagging with MV1 at (70%).

Figure 5.10: Example p_T^{Rel} fits before and after b-tagging with MV1 (70%). Fits done in $20 \leq p_T^{jet} < 200$ GeV bin and for $\Delta R \geq 0.4$.

width equal to the statistical uncertainy on the bin. This is done to create 10,000 randomly varying templates, which are then fit to the data. The mean value of these 10,000 fits is taken as the fit result, and the RMS of these fits is taken as the systematic error.

5.8.2 Light-to-Charm Ratio

The fits are performed with a b-template and a non-b-template, where the non-b-template is built from the c-template and the light-template in proportions taken from unfiltered Monte Carlo (the light-to-charm ratio). A mismodelling of this ratio in Monte Carlo would affect the final fit results. Tables 5.6 and 5.7 show the light-charm ratios measured from Monte Carlo . To determine the systematic effect of this, fits are performed with modified non-b-templates. These modified templates contain double and half the amount of light-jets compared to the default templates. The difference in the fit results is taken as the systematic error.

5.8.3 Light Template Contamination

As discussed in Section 5.7.2, the light template derived from the anti-tag procedure on data is not a pure light-jet sample. Tables 5.6 and 5.7 list the percentage contamination of b-jets in the light-template, as a function of p_T and for both $\Delta R_{\text{Subjets}}$ ranges. This effect is corrected for, by inflating the fitted b-fractions by the quantity of jets in the fitted light-fraction, that are actually b-jets. Even though this correction is applied, a mismodelling of the b contamination of the light-template would lead to an error on the efficiency calculation, so the following procedure was used to evaluate the systematic uncertainties. The b and c fractions in the light-template were scaled up by 100% and the effect on the efficiency is taken as the systematic uncertainty.

5.8.4 Pileup Re-weighting

The μ variable reflecting the average number of interactions per bunch crossing is varied up and down by around 9% (0.0904) [96]. In 2012 data taking the μ value was in average 21, ranging between 5 and 40 [113]. Fits are repeated with the inflated and reduced μ values and the difference is taken as the systematic error.

p_T^{jet} **bin [GeV]**	**Light-charm ratio**	b**-Fraction [%]**
$20 \leq p_T^{jet} < 50$	0.39	3.3
$50 \leq p_T^{jet} < 75$	0.52	2.1
$75 \leq p_T^{jet} < 90$	0.47	1.2
$90 \leq p_T^{jet} < 110$	0.36	1.1
$110 \leq p_T^{jet} < 140$	0.38	2.6
$140 \leq p_T^{jet}$	0.50	9.7

Table 5.6: Light-charm ratios, and percentage of b-jets in the anti-tagged light templates for $\Delta R < 0.4$. The statistical uncertainties are all below 3% on the light-charm ratios (evaluated from Monte Carlo) and all below 15% on the b-fraction (evaluated from data) which are less than the scaling applied to these quantities when evaluating the systematic uncertainties.

p_T^{jet} **bin [GeV]**	**Light-charm ratio**	b**-Fraction [%]**
$20 \leq p_T^{jet} < 30$	0.39	5.5
$30 \leq p_T^{jet} < 40$	0.37	5.8
$40 \leq p_T^{jet} < 50$	0.43	4.5
$50 \leq p_T^{jet} < 60$	0.43	4.6
$60 \leq p_T^{jet} < 75$	0.35	3.3
$75 \leq p_T^{jet} < 90$	0.41	2.2
$90 \leq p_T^{jet} < 110$	0.35	3.4
$110 \leq p_T^{jet} < 140$	0.43	2.8
$140 \leq p_T^{jet}$	0.47	2.0

Table 5.7: Light-charm ratios, and percentage of b-jets in the anti-tagged light templates for $\Delta R \geq 0.4$. The statistical uncertainties are all below 1% on the light-charm ratios (evaluated from Monte Carlo) and all below 5% on the b-fraction (evaluated from data) which are less than the scaling applied to these quantities when evaluating the systematic uncertainties.

5.8.5 Jet Energy Scale

The study of the jet energy scale in Cambridge-Aachen subjets is preliminary, and final results have not been published on this. On the advice of the jet energy scale working group on the ATLAS experiment, a value of ±5% was used as the jet energy scale uncertainty. To evaluate the systematic effect this would have on the p_T^{Rel} analysis, the following procedure was used. Fits were performed where the jet energy scale had been inflated by 5% and then reduced by 5%. The difference between these fit results was taken as the systematic uncertainty on the jet energy scale.

5.8.6 Modelling of b-Production

b-jets may be produced by many mechanisms: flavour creation, flavour excitation and gluon splitting. In the gluon splitting case two b-quarks may be produced where the angle between them is so small they are clustered into the same jet, a double b-jet. It has been shown [98] that the b-tagging efficiency for these double b-jets can be 10-25% higher than for single b-jets. A mismodelling of the ratio of double to single b-jets in Monte Carlo could affect the final efficiency results obtained from the fits. To account for this a systematic was evaluated by modifying this ratio and refitting. Fits were performed with twice the ratio of double to single b-jets and again with zero double b-jets, and the systematic was taken as the difference between these. In the high occupancy regime of a boosted analysis where the purpose of the jet-substructure techniques is to resolve two close b-jets (where the jets are separated by $\Delta R_{\text{Subjets}}$) a double b-jet was defined as a jet containing two b-quarks separated by ΔR_{Quarks} where ΔR_{Quarks} is smaller than the radius of the subjet.

5.8.7 Modelling of c-Production

The same process as for Section 5.8.6 was used but for c-jets instead of b-jets.

5.8.8 Fake Muons in b-Template

A fake muon is defined as a reconstructed muon not matched to a truth muon track. Since the flavour templates are built using muon-filtered JX_μ samples,

which have a 3 GeV generator level minimum p_T cut on the muons, the number of fake muons in these templates is likely to be lower than for data. As seen in Figure 5.11, muons from b-decays have a different p_T spectrum compared to fake muons and so mismodelling of the muon fakes can affect the final efficiency measurement. Figure 5.11(a) and Figure 5.11(b) show the different fake contributions in unfiltered and filtered Monte Carlo respectively. To evaluate the systematic uncertainty associated with this, the number of fake muons in the muon filtered templates was increased by a factor of 6 to bring the fake fraction in line with unfiltered Monte Carlo, and the fits re-performed. The difference between these fit results and the default ones was taken as the systematic uncertainty.

5.8.9 Scale Factor for Inclusive b-jets

The p_T^{Rel} method can only measure the b-tagging efficiency in data for b-jets with a semi-leptonic B-hadron decay. As these jets always contain a high-momentum and well-measured muon track, wheareas the hadronically decaying b-jets do not, the b-tagging efficiency may be different for these two types of b-jets. However the calibration results in this thesis are to first order insensitive to this effect as they are given in the form of data-to-simulation scale factors. Therefore as long as the simulation adequately models the relative differences in b-tagging efficiencies between semi-leptonically and hadronically decaying b-jets, the same data-to-simulation scale factor is valid for both types of jets. A study [96] was performed in the past with $t\bar{t}$ dilepton events and the ratio of scale factors between semi-leptonically and hadronically decaying b-jets was found to be consistent with unity for all b-tagging algorithms and operating points. The uncertainty in that measurement, $\pm 4\%$, is assigned in this analysis as a systematic uncertainty.

5.9 Results

The b-tagging efficiencies and data to Monte Carlo scale factors measured using the p_T^{Rel} method are shown below for the MV1 b-tagging algorithm at the 70% efficiency working point. The results for all of the b-tagging algorithms and working points listed in Table 5.2 are given in Appendix A.2. A table of systematic uncertainties is also provided for each measurement.

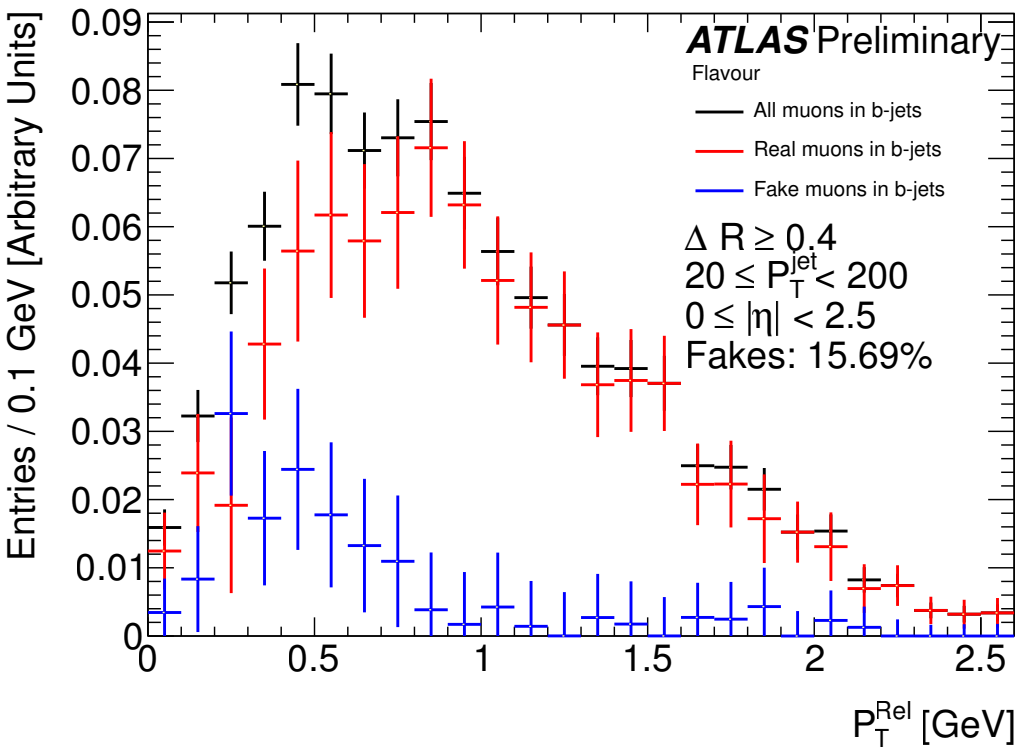

(a) Unfiltered Monte Carlo

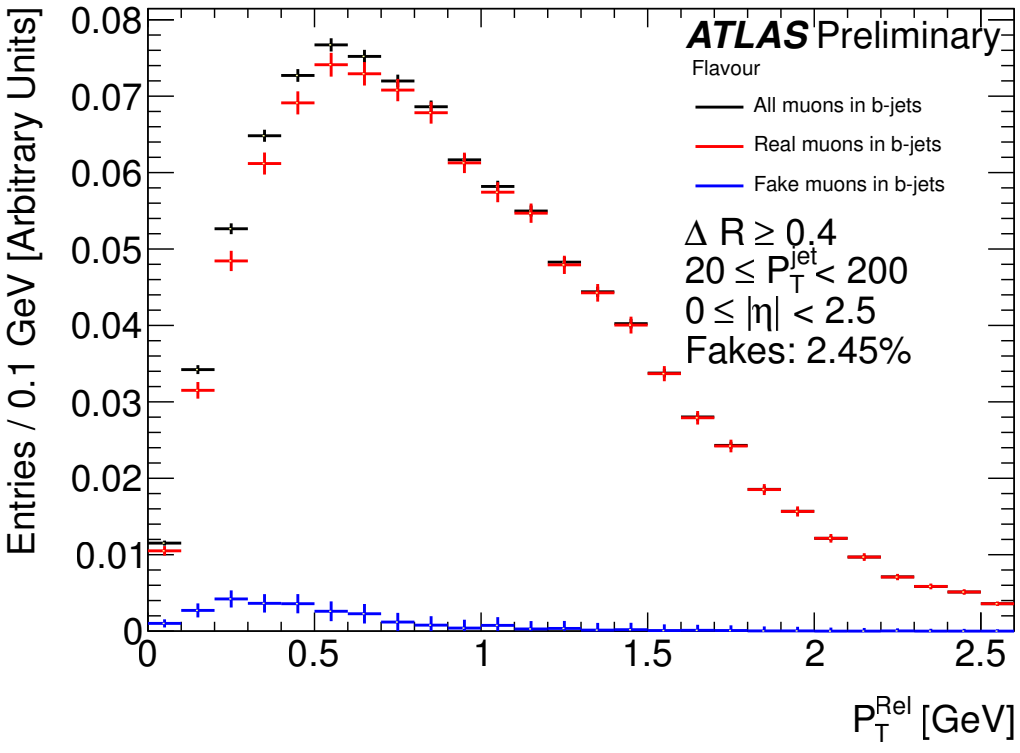

(b) Filtered Monte Carlo

Figure 5.11: Fake muons in b-template.

5.9.1 MV1 at 70%

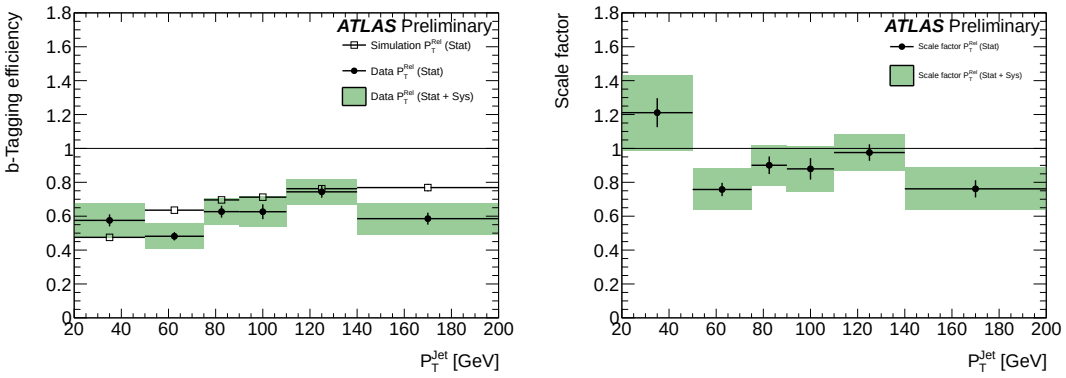

(a) Efficiency

(b) Data/MC scale factor

Figure 5.12: Efficiency and scale factors for MV1 tagger at 70% working point in $\Delta R_{\text{Subjets}} < 0.4$ bin.

Uncertainty	p_T^{jet} **bin [GeV]**					
	20-50	**50-75**	**75-90**	**90-110**	**110-140**	**> 140**
Statistical [%]						
Statistical (MC)	3.5	1.0	1.5	1.7	1.9	2.9
Statistical (Data)	6.1	5.1	5.6	7.0	4.6	6.0
Total Statistical	7.1	5.2	5.8	7.2	5.0	6.7
Systematic [%]						
MC stats	9.1	1.6	2.3	2.8	3.5	4.4
Pileup weight	0.2	1.8	2.0	1.0	1.1	1.0
Light charm ratio	0.2	1.0	0.6	0.0	1.8	4.1
Muon fakes	3.6	6.5	4.2	4.9	4.2	9.0
Model b prod.	9.2	13.0	9.4	11.3	4.1	9.6
Model c prod.	9.7	1.2	3.5	1.9	5.3	0.7
Light temp. con.	1.3	0.2	0.3	0.1	0.7	1.7
Inclusive *b*-jets	4.0	4.0	4.0	4.0	4.0	4.0
Jet energy scale	0.0	0.0	0.0	0.0	0.0	0.0
Total systematic	17.1	15.4	12.0	13.4	9.8	15.1

Table 5.8: Statistical and systematic errors (%) for the MV1 tagger at 70% working point in $\Delta R_{\text{Subjets}} < 0.4$ bin.

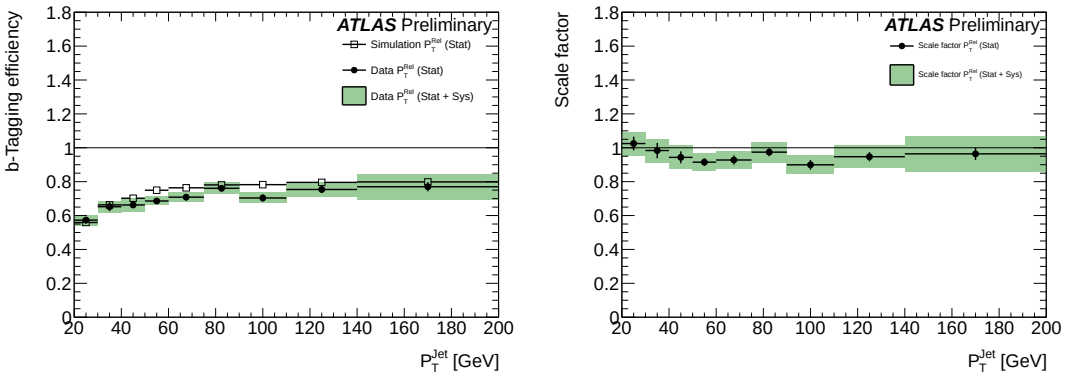

(a) Efficiency (b) Data/MC scale factor

Figure 5.13: Efficiency and scale factors for MV1 tagger at 70% working point in $\Delta R_{\text{Subjets}} \geq 0.4$ bin.

Uncertainty	p_T^{jet} **bin [GeV]**								
	20-30	**30-40**	**40-50**	**50-60**	**60-75**	**75-90**	**90-110**	**110-140**	**> 140**
Statistical [%]									
Statistical (MC)	1.9	2.1	2.4	1.0	0.9	1.0	1.1	1.1	1.3
Statistical (Data)	3.4	4.1	2.9	2.3	2.8	2.2	3.0	2.6	3.5
Total Statistical	4.0	4.6	3.7	2.5	2.9	2.5	3.2	2.8	3.7
Systematic [%]									
MC stats	2.9	2.8	3.8	1.3	1.2	1.7	1.6	2.5	2.4
Pileup weight	0.4	0.1	0.2	0.3	0.2	0.2	0.4	0.1	0.1
Light charm ratio	1.1	0.8	0.8	0.0	0.2	0.3	0.3	1.4	2.7
Muon fakes	0.4	0.4	1.1	1.8	0.3	0.8	0.3	0.8	6.6
Model b prod.	1.4	0.0	2.7	0.6	0.3	0.8	0.9	0.5	2.9
Model c prod.	0.9	0.8	0.8	1.6	2.1	3.3	2.3	3.8	4.4
Light temp. con.	1.7	1.4	1.2	1.3	0.6	0.6	0.5	1.1	0.5
Inclusive b-jets	4.0	4.0	4.0	4.0	4.0	4.0	4.0	4.0	4.0
Jet energy scale	0.0	0.0	0.0	0.0	0.0	0.0	0.0	0.0	0.0
Total systematic	5.6	5.3	6.5	5.0	4.8	5.6	5.0	6.4	10.1

Table 5.9: Statistical and systematic errors (%) for the MV1 tagger at 70% working point in $\Delta R_{\text{Subjets}} \geq 0.4$ bin.

5.10 Summary and Discussion

This chapter presented details of the analysis used to provide the first b-tagging calibration on Cambridge-Aachen subjets, and the first calibration with jet separations of less than 0.4 in ΔR. Both of which are necessary for use in boosted analyses, such as the one presented on boosted $H \to b\bar{b}$ in the next chapter.

This calibration is binned into two regions of $\Delta R_{\text{Subjets}}$, that above 0.4 and that below 0.4. In the $\Delta R_{\text{Subjets}} > 0.4$ region, a direct comparison can be made with the AntiK_T jet p_T^{Rel} calibration. There are two areas of possible difference, the first is the efficiency with which to b-tag a Cambridge-Aachen subjet, compared to that of an AntiK_T jet under the same kinematic conditions. The second is how well this efficiency is modelled in simulation compared to the efficiency measured in data. As the application of b-tagging algorithms to Cambridge-Aachen subjets is a relatively recent development on the ATLAS experiment, there was not an expectation of performance in comparison to AntiK_T jets.

In terms of the efficiency profiles, the performance was similar between the Cambridge-Aachen calibration and the AntiK_T one for all b-tagging algorithms calibrated. The same increase in efficiency with p_T^{jet} was observed, and the efficiency values obtained with Cambridge-Aachen jets and AntiK_T jets agree within experimental uncertainties, and within $\sim 5\%$. For several of the b-tagging algorithms, however, in the p_T^{jet} range $90 \leq p_T^{Subjet} < 110$ GeV, there is a notable drop in the efficiency measured on data, both compared to AntiK_T jets, and the efficiency modelled in simulation for Cambridge-Aachen subjets.

In terms of how well the b-tagging is modelled on Monte Carlo compared to that measured on data for Cambridge-Aachen subjets, it was found that it is generally well modelled in the $\Delta R_{\text{Subjets}} > 0.4$ region, with most scale factors being within experimental uncertainty of unity, or close to being so. For several of the b-tagging algorithms calibrated, however, the efficiency at low p_T^{Subjet} (approximately $20 \leq p_T^{Subjet} < 40$ GeV) is greater in data than modelled in simulation, although still in agreement within experimental uncertainties.

In the $\Delta R_{\text{Subjets}} < 0.4$ regime, it was found that agreement between the simulated efficiency and that measured in data was poorer. Similar levels of agreement and scale factor profiles were seen for all b-tagging algorithms, where in the low p_T^{Subjet} range the efficiency measured on data was greater than simulation, but within experimental uncertainty of it. In the high p_T^{Subjet} range,

the efficiency measured on data was significantly less than that of simulation, and the disagreement was greater than uncertainties.

The statistical and systematic uncertainties in the $\Delta R_{\text{Subjets}} > 0.4$ region are comparable to those of the AntiK_T jet p_T^{Rel} calibration, with the total systematic uncertainty being $\sim$ 5 - 7% over most of the p_T^{Subjet} range. However in the $\Delta R_{\text{Subjets}} < 0.4$ region, both the data statistical uncertinties and the Monte Carlo statistical uncertainties are increased by a factor of two, the latter of which affects the systematic uncertainties through the template shapes used to fit to data. This results in total systematic uncertainties on the scale factors in this region being of $\sim$ 10 - 20%.

Chapter 6

Search for the Higgs boson in the $H \to b\bar{b}$ decay channel

6.1 The Higgs boson

The Higgs boson was predicted by Peter Higgs in 1964 [2] as a consequence of applying theories of spontaneous symmetry breaking to explain the generation of the vector boson masses. The theoretical framework for the Higgs mechanism is laid out in detail in Section 2.2 of this thesis. Proof of its existence has been sought for many years, with the possible mass range in which it can exist being ever narrowed by consecutive experiments (at LEP and the Tevatron) ruling out regions of parameter space. Prior to the discovery of the Higgs boson in 2012, a most-likely Higgs boson mass was predicted from global fits to electroweak data of ~ 120 GeV [5]. This, coupled with results [6] from ATLAS and CMS experiments published in 2012, indicating a Higgs boson mass of 125 - 126 GeV, motivate a Higgs boson search in the "low-mass regime", defined here as $100 \leq M_H \leq 150$ GeV. At the time of starting this analysis, the Higgs boson had not been observed to decay to fermions, although this fermion coupling is vital to explain the mass generation in the fermion sector. At the time of writing, the Higgs boson has been observed to decay to $\tau^+\tau^-$ with a significance of 4.1 σ [114], although Higgs boson decays to $b\bar{b}$ have yet to be observed. These facts coupled with the high branching ratio in the low Higgs boson mass region, make the $H \to b\bar{b}$ decay channel a natural, albeit difficult, choice of search channel.

LEP was an electron-positron collider (maximum $\sqrt{s} = 209$ GeV), the

Tevatron was a proton-anti-proton collider ($\sqrt{s} = 1.8$ TeV) and the LHC is a proton-proton collider (currently $\sqrt{s} = 8$ TeV, design $\sqrt{s} = 14$ TeV). Each collider provides different dominant background processes and so different sensitivities to different production and decay channels. The ATLAS experiment searches for the Standard Model Higgs boson in a variety of channels, and in the low mass range the channels with the largest branching ratios are (from Figure 2.9) $H \to b\bar{b}$, $H \to WW$, $H \to gg$, $H \to \tau^+\tau^-$, and $H \to c\bar{c}$. The decays with jet final states are difficult to differentiate from the background processes coming from hadronic collisions, such as those of the LHC. Other information is required to be identified in the process, such as the presence of a vector boson that decays leptonically. In Figure 2.6, it can be seen that there exists a production mechanism where a Higgs boson is produced in association with a W-boson, known as associated vector boson production, and this is used in the search for $H \to b\bar{b}$.

6.2 The $H \to b\bar{b}$ decay channel

6.2.1 Signal process

The production of a Higgs boson in association with a leptonically decaying vector boson (W or Z) is the most promising production method for a discovery of a $H \to b\bar{b}$ decay. The isolated lepton resulting from the W or Z decay provides a clean signature to trigger on and a means to reject some hadronic-only backgrounds. The jets resulting from the $H \to b\bar{b}$ (or other) decays are analysed with jet-substructure techniques, b-tagging is applied, and they are then used to determine the invariant mass of the Higgs candidate particle, M_{bb}, which is used as the discriminating variable in the analysis. For this analysis, production in association with a W-boson has been chosen to investigate due to its higher cross-section, compared to associated production with a Z-boson. The full process for a hadronic collider like the LHC is then $q\,\bar{q} \to WH \to b\,\bar{b}\,l\,\bar{\nu}$, and is illustrated in Figure 6.1.

6.2.2 Background processes

The use of the associated vector boson production channel (WH in this case) already reduces a significant fraction of background that would be present in for

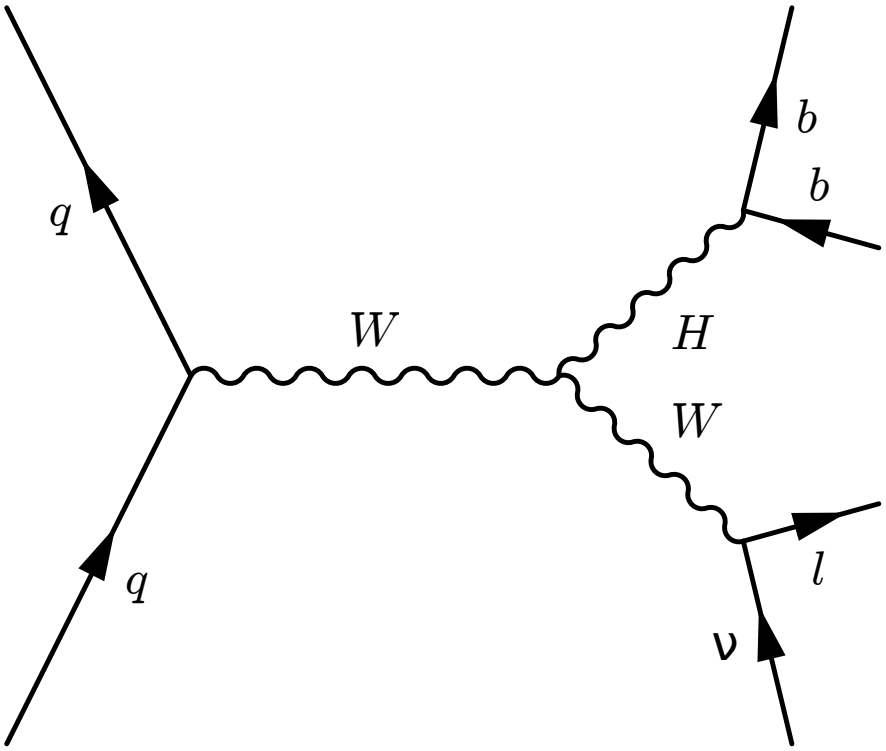

Figure 6.1: Feynman diagram showing the full physics process in the search for the Higgs boson decaying to a b-quark pair.

example the gluon-gluon fusion production channel. However events with a real or fake lepton provide background processes, and of course any processes also producing $b\bar{b}$. The main backgrounds in the analysis are listed below. Some background estimations are derived from direct Monte Carlo predictions, and some from data-driven techniques. These are explained in detail later in the chapter. A full list of background processes considered, with numbers of events and cross-sections can be found, sample by sample, in Appendix B, and also in summarised form in Table 6.2.

- $WZ \to l\bar{\nu}b\bar{b}$, which has a $b\bar{b}$ resonance at the Z-boson mass (91.2 GeV/c^2) and is a concern particularly for a low mass Higgs boson being searched for here.
- $Wb\bar{b} \to l\bar{\nu}b\bar{b}$
- W+non-b-jets (mis-tagged as b-jets)

- $t\bar{t} \to l\bar{\nu}\bar{l}\nu b\bar{b}$
- WW
- QCD multijet production
- single top production.

6.2.3 Considerations in the high-p_T regime

In the regime of Higgs boson $p_T > 200$ GeV, b-jets resulting from the Higgs boson decay are produced spatially close together, often with $\Delta R < 0.4$. Special techniques are required to perform analyses with these close jets, known collectively as "jet-substructure" techniques, as described in Section 5.2.1. It has been shown [94] that by considering only the high-p_T Higgs bosons, while a reduction in the number of signal events would occur as only $\sim 5\%$ of Higgs boson production has $p_T > 200$ GeV at $\sqrt{s} = 14$ TeV, a greater reduction in background processes such as $t\bar{t}$ can also be obtained. These estimations were performed for a centre-of-mass energy of 14 TeV whereby the cross-section for production of high-p_T Higgs bosons is higher than for the current centre-of-mass energy of 8 TeV. This chapter details the search for the Higgs boson with 8 TeV data in the high-p_T regime, using jet-substructure techniques and the results of the b-tagging calibration from Chapter 5

6.3 Data and simulated samples

6.3.1 Data samples

The analysis uses 20.4 fb^{-1} of 2012 proton-proton collision data taken by the ATLAS detector at a centre of mass energy $\sqrt{s} = 8$ TeV. The data are used only when all relevant elements (for the detection of electrons, muons and jets, performing b-tagging and measurement of E_T^{miss}) of the ATLAS detector were operational at the time. This selection of good data quality is done by use of a Good Runs List (GRL) prepared by the ATLAS data quality group [115].

6.3.2 Simulated samples

A simulation of the ATLAS detector (based on GEANT4) was used to provide Monte Carlo simulated samples for the signal and background processes under consideration for this analysis, although a parameterisation is used for simulation of the calorimetry.

The WH signal processes were generated with the Pythia8 [116] generator with the CTEQ6L1 [117] parton distribution functions (PDFs), in 5 GeV steps of Higgs mass from 100 GeV to 150 GeV. Pythia8 is tuned with the AU2 tune [118]. The production cross-sections are modelled at Next-to-Next-to-Leading-Order (NNLO) and the electroweak corrections applied at Next-to-Leading-Order (NLO). The decay branching ratios are calculated with HDECAY [119].

The main background processes are simulated with various generators, listed below. A full list of samples with numbers of events and cross-sections can be found in Appendix B.

- SHERPA [73] generator with CT10 [120] PDFs is used to simulate W and Z+jets events at leading order (LO).
- $t\bar{t}$ is simulated using the POWHEG [121] with CT10 PDFs. This is interfaced with Pythia6 [122] with the CTEQ6L1 PDFs and the Perugia2011C [118] tune.
- The single-top processes of t-channel and Wt production are also simulated with POWHEG.
- For s-channel single top production, the simulation is done with AcerMC [79], with the CTEQ6L1 PDFs and the Perugia2011C tune.
- Diboson processes are modelled with HERWIG [72] and the CTEQ6L1 PDFs with the AUET2 [118] tune.

6.4 Analysis procedure

Some of the following selection procedure is in common with the $H \to b\bar{b}$ search presented in [123, 115], covering all vector boson p_T ranges, hereafter referred to as the inclusive $H \to b\bar{b}$ analysis. The exception is in the jet selection

where the analysis presented in this chapter uses jet-substructure techniques with Cambridge-Aachen jets, rather than AntiK_T jets. In addition the inclusive analysis is split into five bins of p_T^V (p_T of the vector boson), whereas this analysis has a high-p_T requirement and therefore only makes use of the $p_T^V > 200$ GeV bin.

6.4.1 Trigger selection

The analysis begins with a trigger selection. Since both muon and electron channels ($W \to e\nu$, and $W \to \mu\nu$) are considered, different triggering requirements are needed for each channel. In both the electron and muon channels, various single lepton unprescaled triggers (minimum threshold in p_T of 24 GeV) are used depending on pileup conditions. These triggers have some track isolation requirements [115]. There are also higher threshold triggers at p_T above 36 GeV (for muon channel) and p_T above 60 GeV (for electron channel) without any isolation requirements. In addition the muon channel uses an E_T^{miss} trigger (threshold $E_T^{\text{miss}} > 80$ GeV) to deal with areas of reduced muon chamber coverage.

6.4.2 Lepton selection

Two categories of leptons are considered in this analysis, loose and tight.

Loose leptons are defined as having $E_T > 10$ GeV, and passing impact parameter and quality requirements [115]. Loose electrons are required to have $|\eta| < 2.47$ and loose muons are required to have $|\eta| < 0.1$, $0.1 < |\eta| < 2.5$, or $2.5 < |\eta| < 2.7$ depending whether they were reconstructed in the calorimeter with an inner detector track, muon spectrometer with an inner detector track, or muon spectrometer with no inner detector track respectively. Isolation requirements ensure the sum of the transverse momentum of all tracks within a cone of $R = 0.2$ around the lepton candidate track (excluding the candidate track), is less than 10% of the p_T of the lepton.

Tight leptons are required to satisfy all loose lepton criteria, but in addition $E_T > 25$ GeV. Electrons must pass additional quality requirements, and must have $|\eta| < 2.5$. It is also required that the sum of calorimeter energy deposits around a cone of $R = 0.3$ centred on the candidate lepton (excluding the energy

of the lepton) is less than 7% of the lepton energy. The track based isolation is tightened from 10% to 4%.

The analysis requires exactly one tight lepton, and zero loose leptons.

6.4.3 E_T^{miss} selection

The missing transverse energy, E_T^{miss}, is measured as the negative vector sum of the transverse momenta associated with energy clusters in the calorimeter with $|\eta| < 4.9$. Corrections are applied to the energies of the clusters associated to reconstructed objects (jets, electrons, τ-leptons and photons) and these are taken account of in the E_T^{miss} calculation. The p_T of the muons is added to the result with the energy deposited by those muons in the calorimeters accounted for. Also a track-based p_T^{miss} is calculated as the negative vector sum of the transverse momenta of tracks associated to the primary vertex.

6.4.4 W-boson selection

In order to reduce the contamination from $t\bar{t}$ background, a requirement on M_T^W is made such that $M_T^W < 120$ GeV, where M_T^W is defined as:

$$M_T^W = \sqrt{2p_T^l E_T^{\text{miss}} \left(1 - \cos\left(\phi^l - \phi^{\text{miss}}\right)\right)} \tag{6.1}$$

6.4.5 Boosted jet selection

In this boosted analysis, jets are reconstructed using the Cambridge-Aachen algorithm with a distance parameter of $R = 1.2$ from topological clusters in the calorimeters. The energies of the jets are corrected for the contribution of pileup interactions using a technique based on jet area [124]. Jet energy is calibrated using p_T and η dependent correction factors. The jets are then analysed with jet-substructure techniques discussed in detail in Section 5.2.1 to define two or three "subjets". The subjets both have to have $|\eta| < 2.5$. The highest p_T subjet must have $p_T > 70$ GeV, the second highest p_T subjet must have $p_T > 25$ GeV. In addition to this, the two leading p_T subjets must be b-tagged to form the Higgs boson candidate particle. The Higgs boson candidate fat-jet must have $|\eta| < 2.5$, and $p_T > 200$ GeV.

Unlike the inclusive analysis, which uses AntiK_T jets (with $R = 0.4$) and so has a minimum spatial separation, ΔR, between the jets of 0.4. In the boosted analysis, presented here, there is no minimum restriction on the spatial separation between the subjets, $\Delta R_{\text{Subjets}}$. The maximum spatial separation is $\Delta R_{\text{Subjets}} = 1.2$ (the radius of the fat-jet).

6.4.6 Additional AntiK_T jet veto

To further reduce the yields of background processes such as $t\bar{t}$, an additional jet veto is applied. If any AntiK_T jets (with $p_T > 30$ GeV and $|\eta| < 4.5$) are found outside of the spatial volume of the fat-jet, that is, not related to the Higgs boson candidate particle, then the event is removed from the analysis.

6.4.7 b-tagging selection

This analysis uses two types of tagging, "standard" b-tagging, and"truth-tagging".

Standard b-tagging is done via the MV1 b-tagging algorithm which uses a neural network approach based on information from other b-tagging algorithms, as described in Section 5.5.4. In this analysis, the b-tagging cut is chosen to provide a b-tagging efficiency of 70%, giving a rejection factor of 5 for c-quark jets, and 150 for light-quark jets. Two subjets are required to be b-tagged. This requirement causes problems with low statistics in some of the background samples, notably $V + c$, $V +$ light and WW samples, as the dijet invariant mass distribution shape becomes unreliable. Instead an alternative procedure, known as "truth-tagging" is used. This relies on a parameterisation of the probability to be b-tagged according to truth-flavour information, described in the next paragraph.

Truth tagging is used for some Monte Carlo samples, and relies on an association based on truth flavour information to spatially associate jets with truth hadrons, as follows. If a hadron containing a b-quark is found within $\min(0.4, \Delta R_{\text{Subjets}})$ in ΔR of a subjet, then that subjet is considered to be a b-jet; otherwise if a hadron containing a c-quark is found within $\min(0.4, \Delta R_{\text{Subjets}})$ of a subjet, then the subjet is considered to be a c-jet; the same applies for τ-leptons. If no match is found then the subjet is considered as a light-jet.

There are some discrepancies in the modelling of b-tagging efficiencies between

simulation and data. Scale factors are applied to correct for this and to obtain the systematic uncertainties associated with the efficiency measurements. For the inclusive analysis these scale factors were present (for AntiK_T jets, with $\Delta R > 0.4$), however for the boosted analysis (using Cambridge-Aachen subjets, with ΔR both > 0.4 and ≤ 0.4), they were obtained through a full b-tagging calibration. The results of the full b-tagging calibration on subjets are presented in Chapter 5.

6.4.8 $\Delta\phi_{W,H}$

In the boosted regime, the Higgs boson particle candidate will be produced approximately back-to-back with the vector boson, meaning a cut on $\Delta\phi_{W,H}$ (the angle in ϕ between the vector boson and the Higgs boson candidate) allows separation of boosted Higgs boson processes from other background processes. The cut is chosen as $\Delta\phi_{W,H} > 2.8$ in line with the inclusive analysis in their highest p_T^W bin.

6.4.9 Reconstructed object overlap

Reconstructed objects may overlap with each other, and so a special treatment is required. In the case of two overlapping objects (defined by $\Delta R < 0.4$), a decision is made on how to define the objects using the following criteria. If a loose electron (with $p_T > 15$ GeV) overlaps with a jet, then the object is considered as an electron. If the loose electron has $p_T < 15$ GeV, then the object is considered a jet. If a muon overlaps with a jet, then the object is considered as a jet that underwent a $q \to \mu\bar{\nu}$ decay. To account for occasional muon decays, any remaining loose electrons within $\Delta R < 0.2$ of a loose muon are removed.

6.4.10 Candidate selection

Table 6.1 summarises the whole selection process.

6.5 Results of event selection

Table 6.2 contains the number of events passing each cut for each process type combined for both muon and electron channels. Figures 6.2, 6.3 and 6.4 show the invariant mass distributions of the b-tagged subjets for both the electron, muon

Object	Selection
Leptons	1 tight lepton + 0 loose leptons
E_T^{miss}	$E_T^{\text{miss}} > 50$ GeV
M_T^W	$M_T^W < 120$ GeV
Fat-jets	1 fat-jet
Additional jet veto	No AntiK_T jets outwith fat-jet
Sub-jets	≥ 2 sub-jets, $\lvert\eta\rvert < 2.5$, $p_T^{\text{Subjet1}} > 70$ GeV, $p_T^{\text{Subjet2}} > 25$ GeV, $\Delta R_{\text{Subjets}} < 1.2$, 2 b-tags
Higgs-candidate	$\lvert\eta_H\rvert < 2.5$, $P_T^H > 200$ GeV
W-boson candidate	$P_T^W > 200$ GeV
$\Delta\phi_{W,H}$	$\Delta\phi_{W,H} > 2.8$

Table 6.1: Summary of analysis selection.

and combined channels. Figures 6.5-6.22 show the distributions of various other kinematic variables that are selected on, including E_T^{miss}, P_T^H, $|\eta_H|$, M_T^W, P_T^W and $\Delta\phi_{W,H}$.

6.5.1 Cut efficiencies

The raw cutflow results are shown in Table 6.2. The first row, "Preselection", represents the starting point of the cutflow for this analysis. At this stage some preselection has been applied on the samples, mainly requirements for one tight and zero loose leptons, a transverse mass cut, an E_T^{miss} cut, and the requirement for one good "fatjet" containing at least two good "subjets". All of these are listed in Table 6.1. An illustrative cut on the Higgs boson mass window ($80 \leq M_H \leq 150$ GeV) has been included in this table to give a measure of how much background is present in the signal mass region. This mass window cut is not actually used in the analysis, but allows the relative quantities of signal and background processes to be compared more informatively in the relevant region. In the analysis, each simulated event must be weighted such that it represents not only the quantity of simulated events passing a cutflow, but also the quantity of that process that would be observed under data conditions. Events are weighted

and scaled according to various parameters, dominantly the events are weighted by the cross-section of the process being modelled and the integrated luminosity of the data set. Additional re-weighting is also done event-by-event, for example re-weighting the Monte Carlo distributions to match the data pileup conditions, so in practice it is difficult to provide an accurate global scale factor for each process, only per-event scale factors.

However to permit a simple cross-check, Table 6.2 also provides a list of cross-section only scaling factors, i.e. not taking into account per-event effects such as pileup re-weighting. As such they can be erroneous by up to $\sim 30\%$. The scale factors are calculated using the cross-sections and numbers of simulated events listed sample by sample in Table B.1, summarised in Table 6.2, and the luminosity of the data set, 20.4 fb^{-1}. The scale factors are defined as in Equation 6.2. Since similar processes have been combined in Table 6.2 to save space, such as W+jets, these scale factors have been calculated as a weighted average of those of the sub-processes.

$$\mathrm{SF}_{\sigma} = \frac{N_{\mathrm{Expected}}}{N_{\mathrm{Simulated}}} = \frac{L\sigma}{N_{\mathrm{simulated}}} \tag{6.2}$$

For example for the signal process with cross-section $\sigma = 0.107$ pb, $N_{\mathrm{Simulated}} = 3 \times 10^6$ and $L = 20.4$ fb^{-1}, the scale factor is 0.728×10^{-3}.

Comparison with inclusive analysis

It is not possible to perform a direct, like for like, cut flow comparison with the inclusive analysis, even in the their highest p_T bin, as this format of result has not been presented by the inclusive analysis. However some indication of agreement can be obtained by comparison of the row containing the expected events in 2012 data from Table 6.2 with the results of the post-fit yields from the ATLAS internal note on the analysis [125]. However the inclusive analysis post-fit yields do not have a Higgs boson mass window cut, like Table 6.2 does, and the post-fit yields also include data from the $\sqrt{s} = 7$ TeV running. The number of events quoted here for the inclusive analysis, correspond to their top p_T bin and are scaled down to the number that would be found had a mass window cut been applied. For the W + jets background, this analysis observed 25 events, while the inclusive analysis observed ~ 12 events. For single top events, 10 events were observed in this analysis, while ~ 5 events were observed in the inclusive analysis. For $t\bar{t}$,

Process name:	Number of events (Efficiency [%])					
	Signal	$t\bar{t}$	Single Top	Diboson	W + jets	Data
N_{Events} or L:	3M	15M	30.2M	27.5M	318.39M	$L = 20.4$ fb^{-1}
$\sigma \times$ BR [pb]:	0.11	114.51	1.64 - 25.75	0.77 - 32.49	0.01 - 11363.37	
Scale factor:	0.728 $\times 10^{-3}$	0.154	0.026	0.017	0.012	
Cut name						
Preselection	70161	463591	309343	65702	1495627	318556
Jet veto	37211 (53.0)	59394 (12.8)	78199 (25.3)	35352 (53.8)	751510 (50.3)	95997 (30.1)
p_T^{Subjet1}	33099 (47.2)	51862 (11.2)	70165 (22.7)	31491 (47.9)	729995 (48.8)	82437 (25.9)
p_T^{Subjet2}	27195 (38.8)	45324 (9.78)	59756 (19.3)	27524 (41.9)	589835 (39.4)	68476 (21.5)
Higgs candidate $\lvert\eta\rvert$	25296 (36.1)	41138 (8.87)	54541 (17.6)	25301 (38.5)	588407 (39.3)	61628 (19.4)
Higgs candidate p_T	20702 (29.5)	30888 (6.66)	43361 (14.0)	20545 (31.3)	558973 (37.4)	44221 (13.9)
W-boson p_T	15425 (22.0)	13826 (2.98)	19875 (6.42)	12775 (19.4)	428585 (28.7)	18784 (5.90)
$\Delta\phi_{W,H}$	9616 (13.7)	8495 (1.83)	9813 (3.12)	7800 (11.9)	274865 (18.4)	10895 (3.42)
double b-tag	4578 (6.52)	458 (0.10)	574 (0.19)	408 (0.62)	4656 (0.31)	113 (0.04)
Higgs candidate mass	4262 (6.07)	371 (0.08)	380 (0.12)	327 (0.50)	2052 (0.14)	64 (0.02)
Expected events in 2012 data	3 ± 1	57 ± 17	10 ± 3	6 ± 2	25 ± 8	64 ± 8

Table 6.2: Monte Carlo and data cut flow table. Showing the number events passing each of the selection criteria. The top row shows sample type, the number of Monte Carlo events produced (or luminosity in the case of data) and the cross-section multiplied by the branching ratios for each process. Several of the columns are combinations of several sub-processes, in this case the range of cross-sections multiplied by the branching ratios are given. The numbers in this table are after a Higgs boson mass window restriction ($80 \leq M_H \leq 150$ GeV) has been applied. The final row shows the number events of this type expected to be found in data, and their uncertainty based on the uncertainty in the provided scale factor, and their statistical uncertainty. The statistical uncertainties on the Monte Carlo cut flow results are simply the square root of the values.

this analysis observed 57 events, while the inclusive analysis observed $\sim$ 17. For diboson, this analysis observed 6 events, while the inclusive analysis observed $\sim$ 2. For signal, this analysis observed 3 events, while the inclusive analysis observed $\sim$ 1.5. This approximate comparison suggests the inclusive analysis, in their top p_T bin, cuts $\sim$ 2-3 times the amount of background that the boosted analysis cuts, however the boosted analysis retains a factor of $\sim$ 2 times more signal. The results are similar in terms of $S/\sqrt{B}$, in the Higgs boson mass window, where the boosted analysis has $S/\sqrt{B} = 0.3$ and the inclusive analysis has $S/\sqrt{B} = 0.25$.

6.5.2 M_{bb} distributions

Figures 6.2, 6.3 and 6.4 show the electron, muon, and combined channel invariant mass distributions respectively. In the Data/MC plot, the Monte Carlo doesn't include the signal.

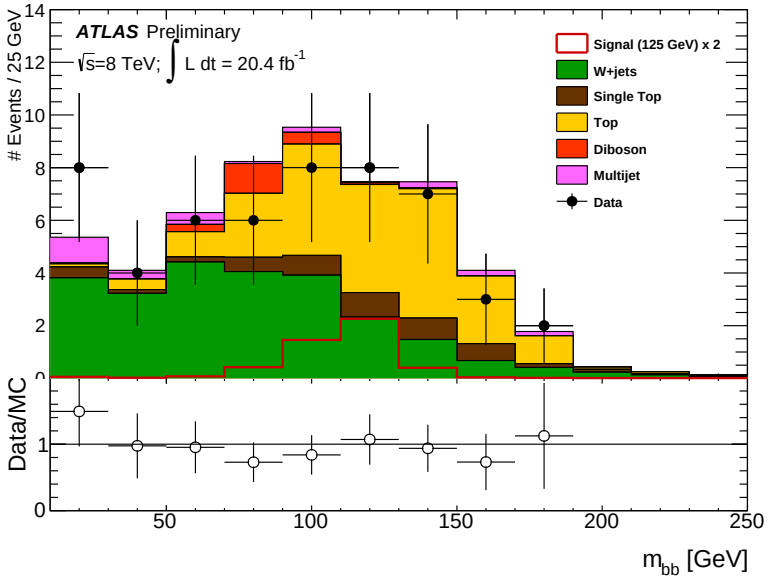

Figure 6.2: Invariant mass distribution of the two b-tagged subjets showing contributions from signal and backgrounds in the electron channel.

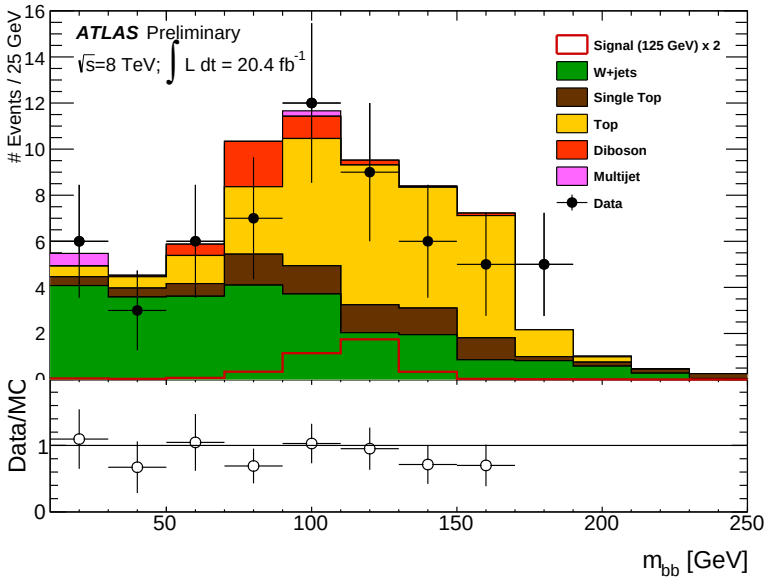

Figure 6.3: Invariant mass distribution of the two b-tagged subjets showing contributions from signal and backgrounds in the muon channel.

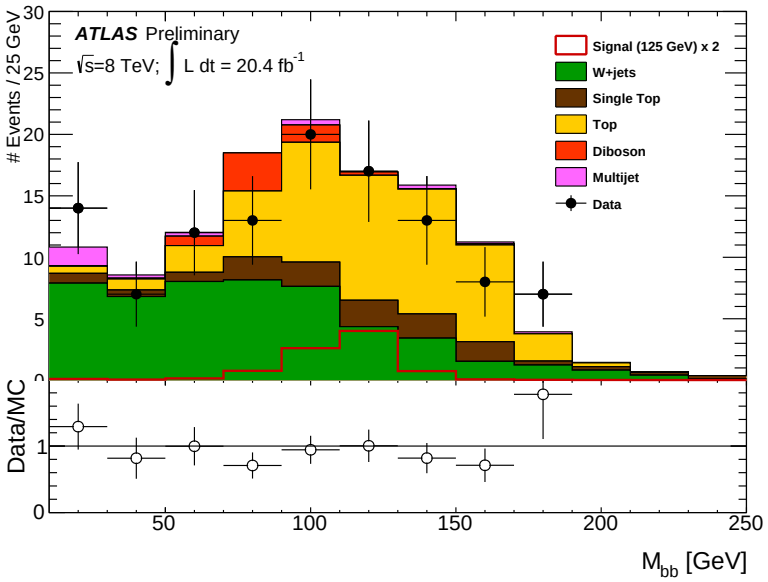

Figure 6.4: Invariant mass distribution of the two b-tagged subjets showing contributions from signal and backgrounds in the combined channel.

6.5.3 E_T^{miss} distributions

Figures 6.5, 6.6 and 6.7 show the electron, muon, and combined channel E_T^{miss} distributions respectively. In the Data/MC plot, the Monte Carlo doesn't include the signal.

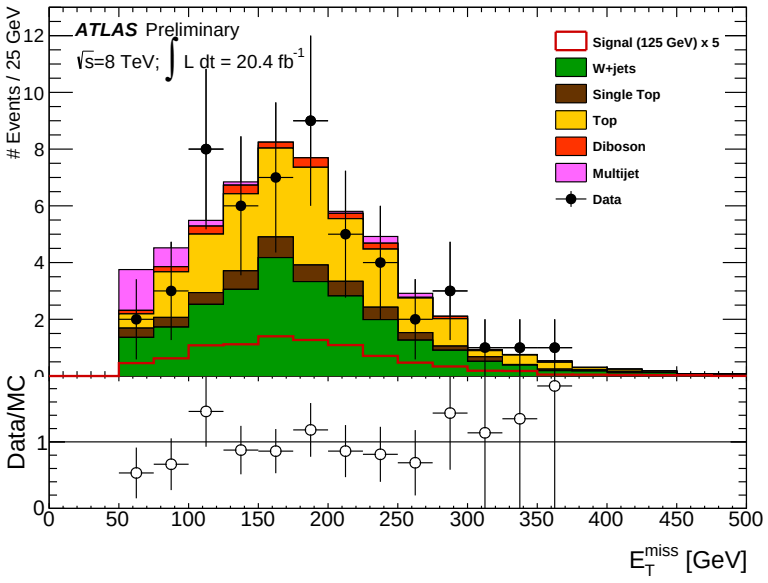

Figure 6.5: E_T^{miss} distribution showing contributions from signal and backgrounds in the electron channel.

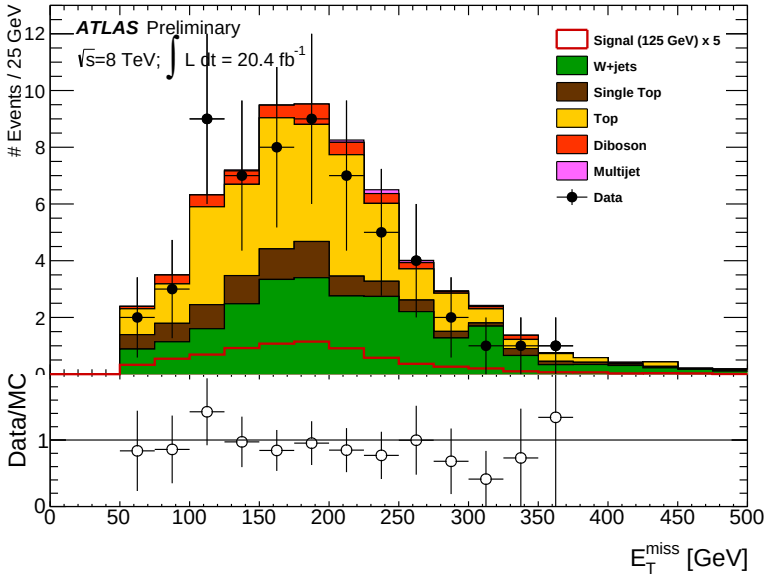

Figure 6.6: E_T^{miss} distribution showing contributions from signal and backgrounds in the muon channel.

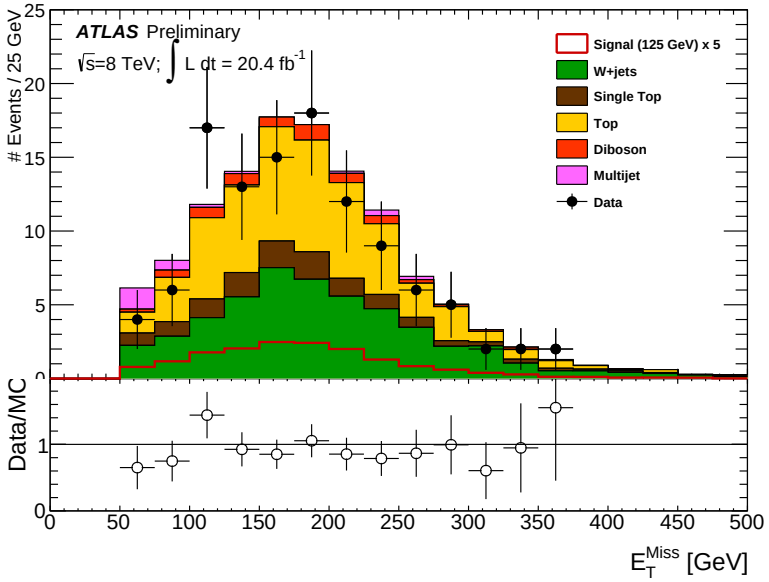

Figure 6.7: E_T^{miss} distribution showing contributions from signal and backgrounds in the combined channel.

6.5.4 P_T^H distributions

Figures 6.8, 6.9 and 6.10 show the electron, muon, and combined channel invariant mass distributions respectively. In the Data/MC plot, the Monte Carlo doesn't include the signal.

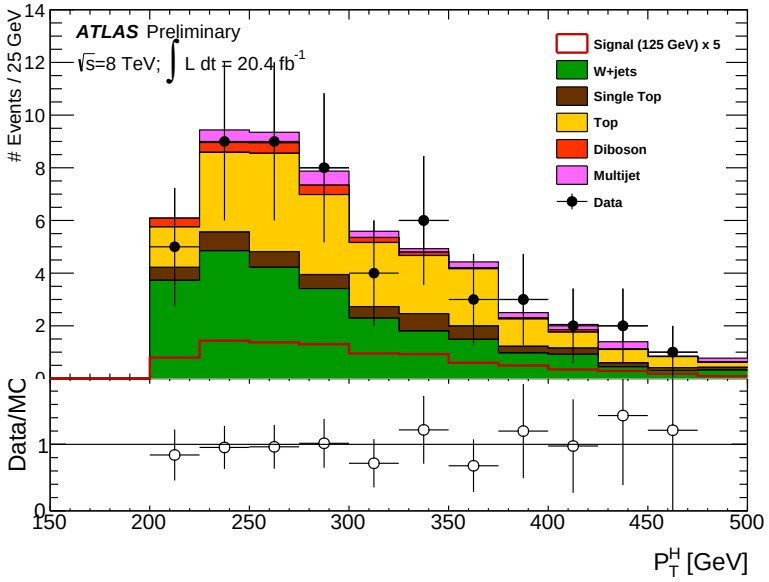

Figure 6.8: P_T^H distribution showing contributions from signal and backgrounds in the electron channel.

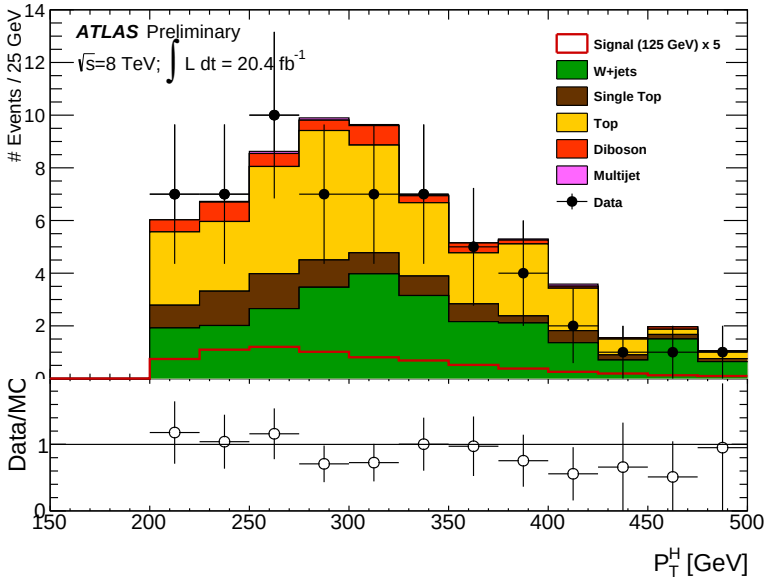

Figure 6.9: P_T^H distribution showing contributions from signal and backgrounds in the muon channel.

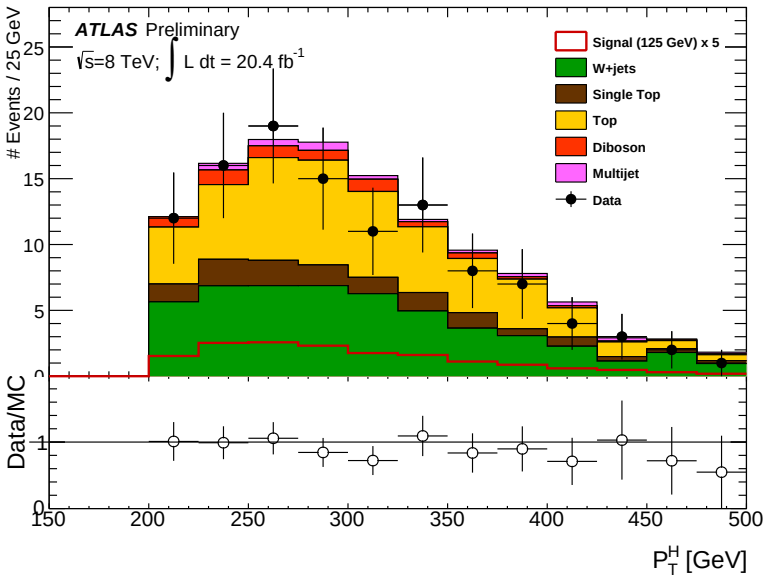

Figure 6.10: P_T^H distribution showing contributions from signal and backgrounds in the combined channel.

6.5.5 $|\eta_H|$ distributions

Figures 6.11, 6.12 and 6.13 show the electron, muon, and combined channel $|\eta_H|$ distributions respectively. In the Data/MC plot, the Monte Carlo doesn't include the signal.

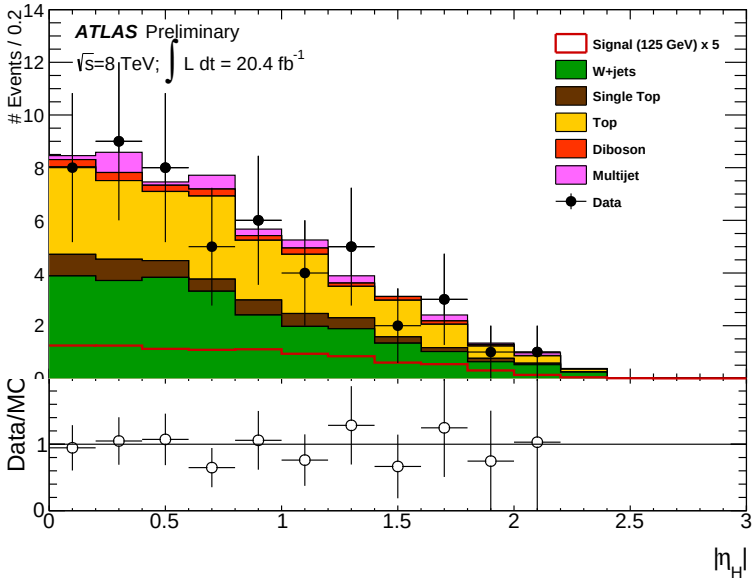

Figure 6.11: $|\eta_H|$ distribution showing contributions from signal and backgrounds in the electron channel.

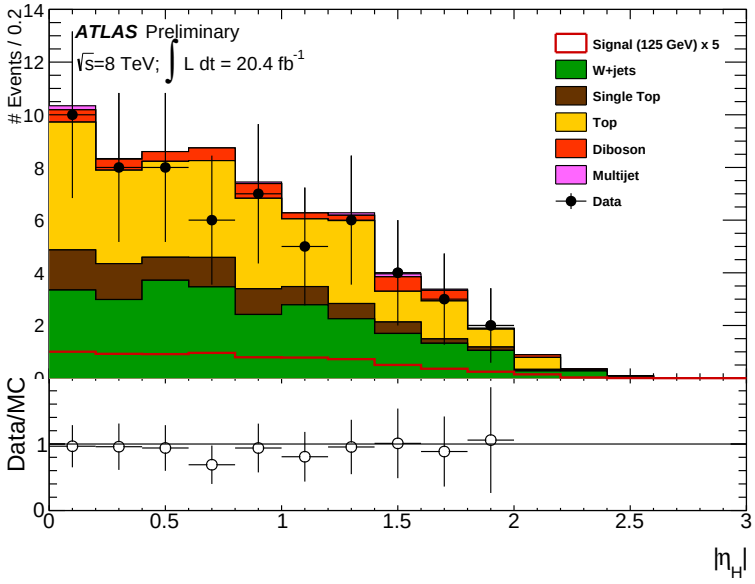

Figure 6.12: $|\eta_H|$ distribution showing contributions from signal and backgrounds in the muon channel.

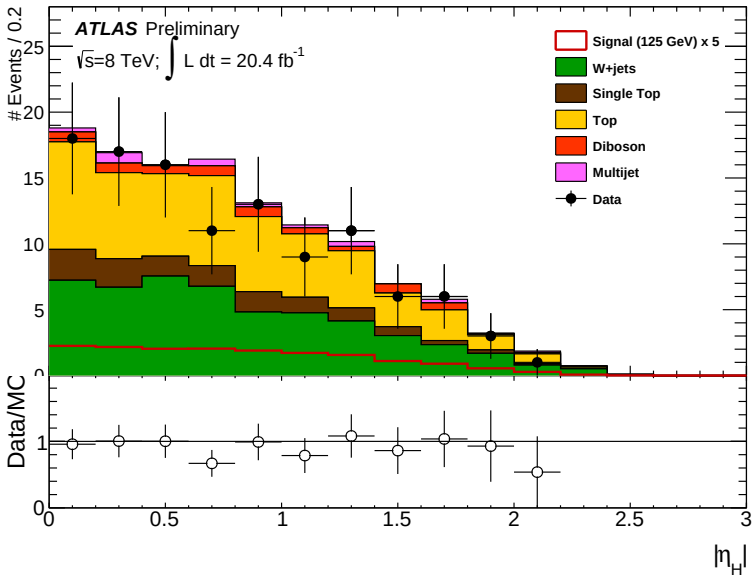

Figure 6.13: $|\eta_H|$ distribution showing contributions from signal and backgrounds in the combined channel.

6.5.6 M_T^W distributions

Figures 6.14, 6.15 and 6.16 show the electron, muon, and combined channel invariant mass distributions respectively. In the Data/MC plot, the Monte Carlo doesn't include the signal.

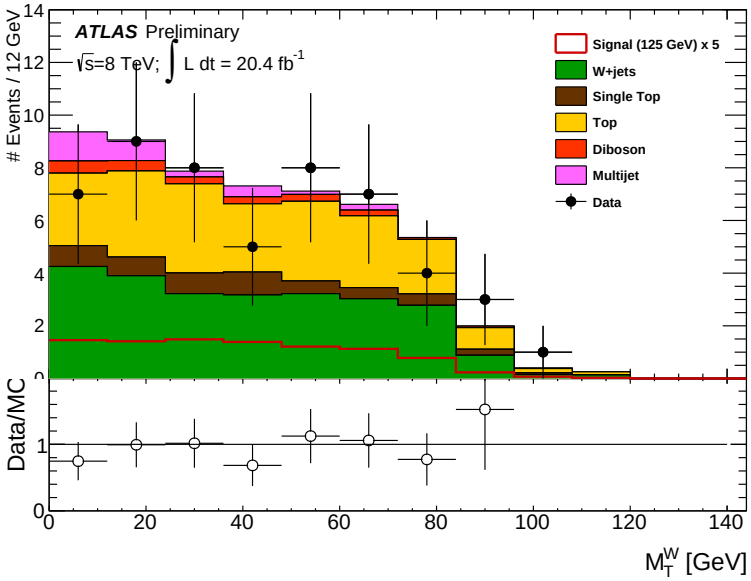

Figure 6.14: M_T^W distribution showing contributions from signal and backgrounds in the electron channel.

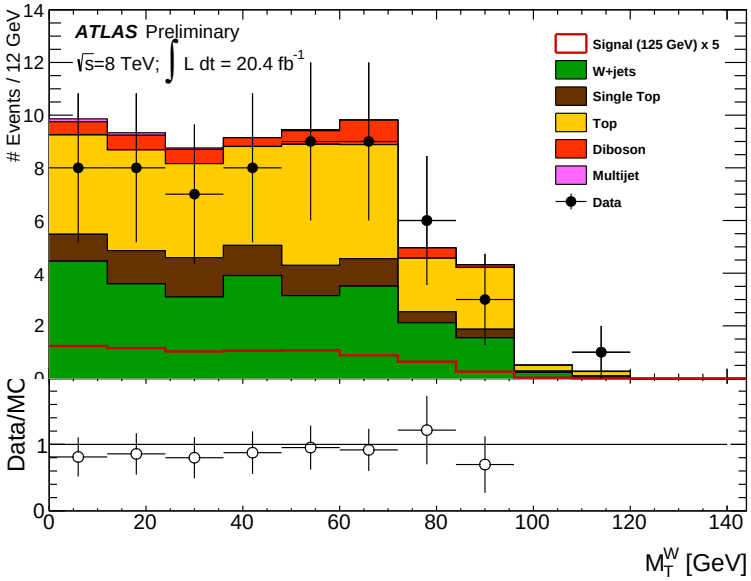

Figure 6.15: M_T^W distribution showing contributions from signal and backgrounds in the muon channel.

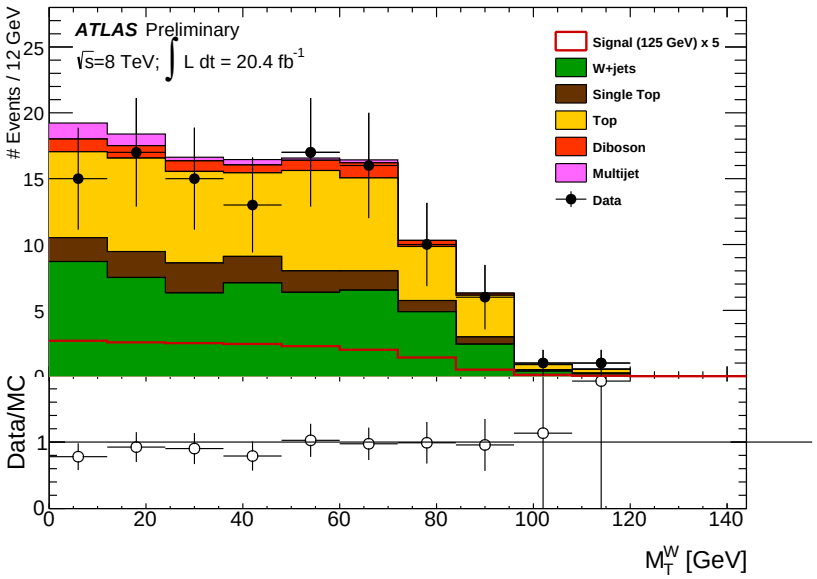

Figure 6.16: M_T^W distribution showing contributions from signal and backgrounds in the combined channel.

6.5.7 P_T^W distributions

Figures 6.17, 6.18 and 6.19 show the electron, muon, and combined channel P_T^W distributions respectively. In the Data/MC plot, the Monte Carlo doesn't include the signal.

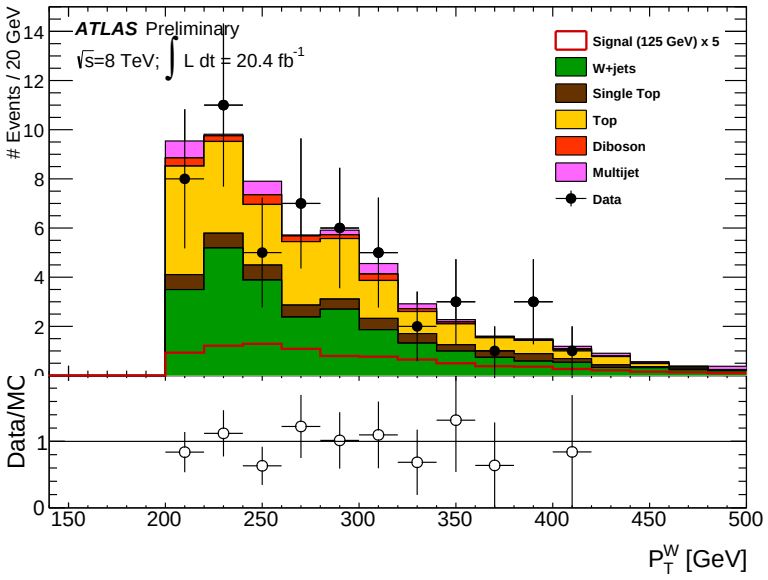

Figure 6.17: P_T^W distribution showing contributions from signal and backgrounds in the electron channel.

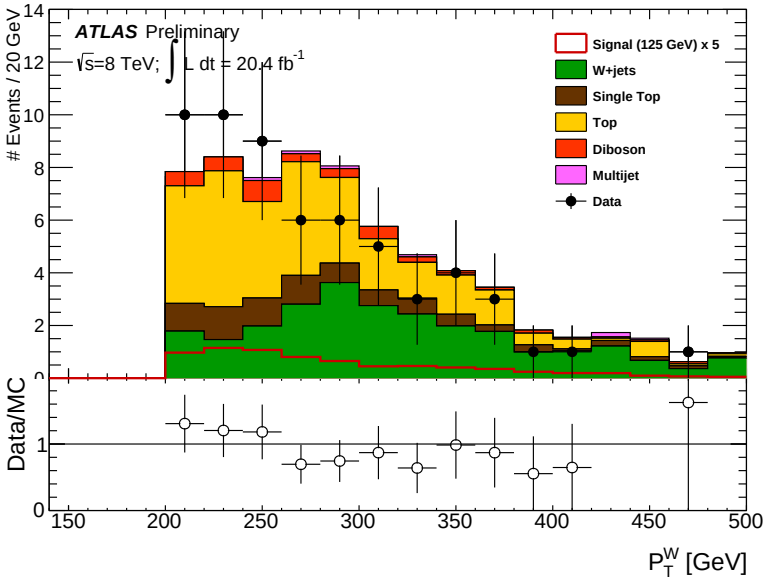

Figure 6.18: P_T^W distribution showing contributions from signal and backgrounds in the muon channel.

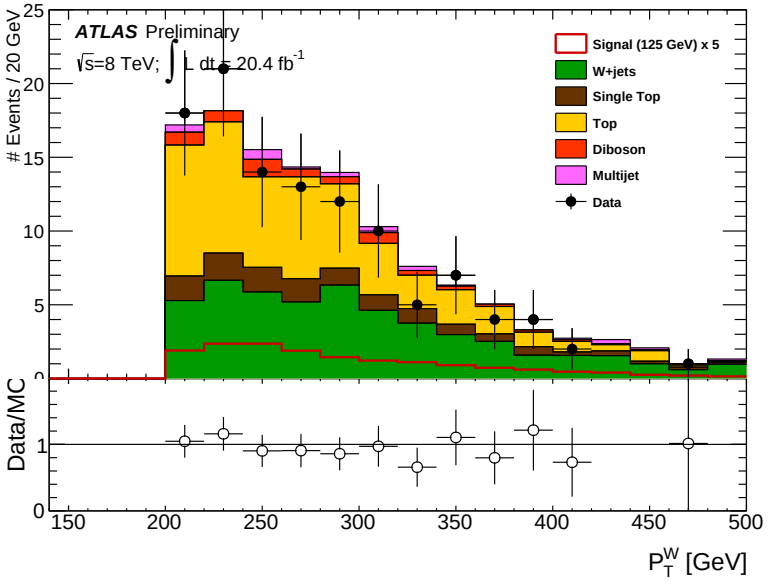

Figure 6.19: P_T^W distribution showing contributions from signal and backgrounds in the combined channel.

6.5.8 $\Delta\phi_{W,H}$ distributions

Figures 6.20, 6.21 and 6.22 show the electron, muon, and combined channel invariant mass distributions respectively. In the Data/MC plot, the Monte Carlo doesn't include the signal.

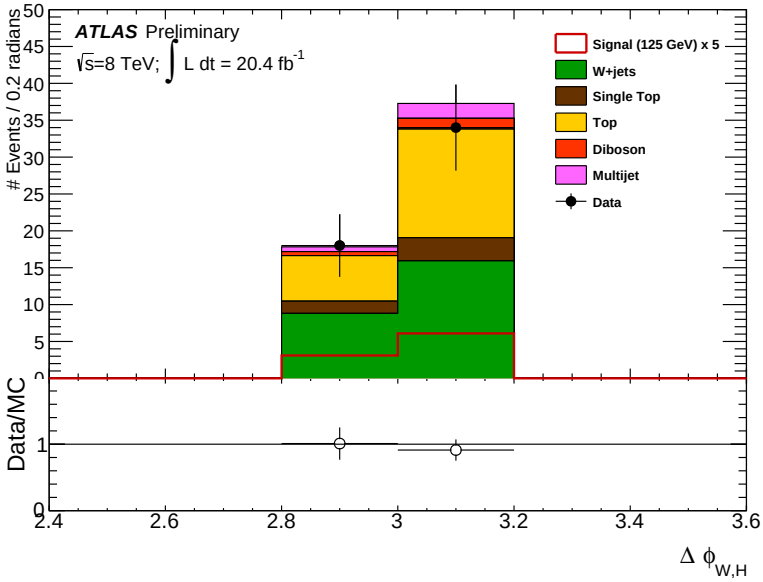

Figure 6.20: $\Delta\phi_{W,H}$ distribution showing contributions from signal and backgrounds in the electron channel.

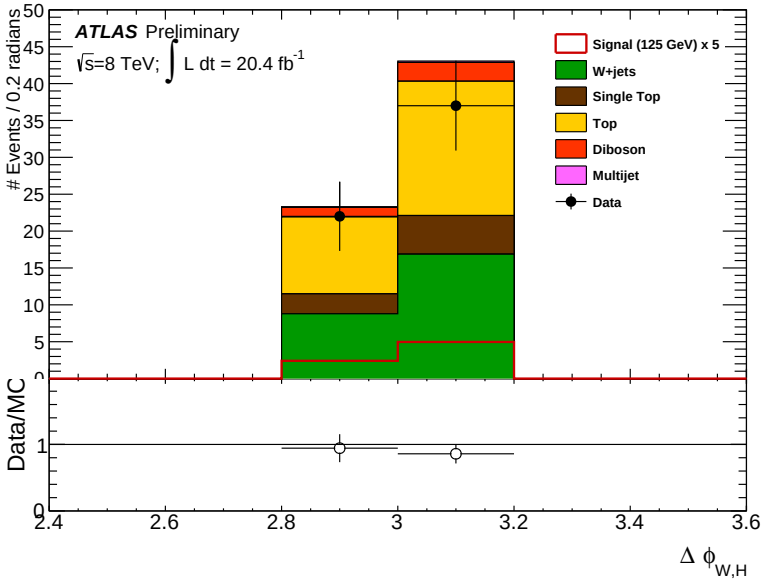

Figure 6.21: $\Delta\phi_{W,H}$ distribution showing contributions from signal and backgrounds in the muon channel.

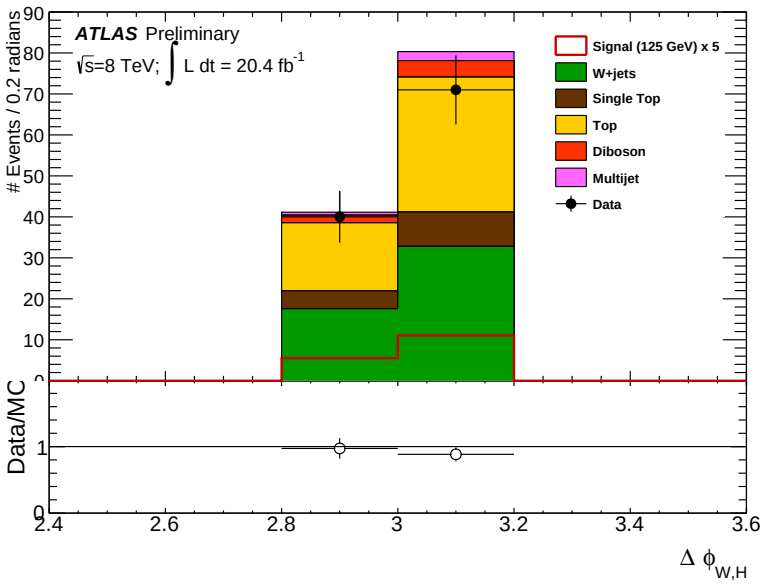

Figure 6.22: $\Delta\phi_{W,H}$ distribution showing contributions from signal and backgrounds in the combined channel.

6.6 Determination of background distributions

6.6.1 Multijet background

The modelling of the multijet background is done by reversing track isolation requirements on the leptons, see Section 6.4.2, such that instead of being $< 4\%$ the isolation requirement becomes $4\% \leq$ isolation $\leq 10\%$. Templates of M_T^W are obtained from this process, which are then fit along with the other backgrounds to the overall M_T^W distribution in data, using a χ^2 fit, to determine the normalisation of the multijet background. Once this normalisation is obtained, it is used to scale the multijet background templates for other variables, thereby allowing the multijet background values for all variables of interest to be determined.

6.6.2 W+jets background

The W+jets background is modelled using the SHERPA Monte Carlo generator. However SHERPA (and ALPGEN) are known to mis-model the $\Delta\phi$ between the dijets, and so corrections were implemented to account for this [125]. A correction factor is obtained by comparing the Monte Carlo predictions for W+jets with a measurement of W+jets obtained by subtracting other large backgrounds (top, diboson and multijet), which are considered to be well modelled, from data, leaving only W+jets. The ratio of these form the correction factors. The distributions are shown in Figure 6.23. There is an additional mis-modelling of the p_T^W in the higher p_T bins, which is compensated for by an inflation of the systematic uncertainty associated to it.

6.6.3 $t\bar{t}$ background

$t\bar{t}$ is modelled using the Monte Carlo generator POWHEG interfaced to PYTHIA. It is generally well modelled, although there is some mis-modelling at high-p_T, where there is some discrepancy in the lepton p_T and E_T^{miss} distributions between Monte Carlo generators and the $t\bar{t}$ control region (identified by selecting events with three jets rather than two jets). After conducting truth studies it was found [115] that by correcting the truth top p_T before running the showering model, the discrepancies could be reduced. The analysis makes use of these corrected samples.

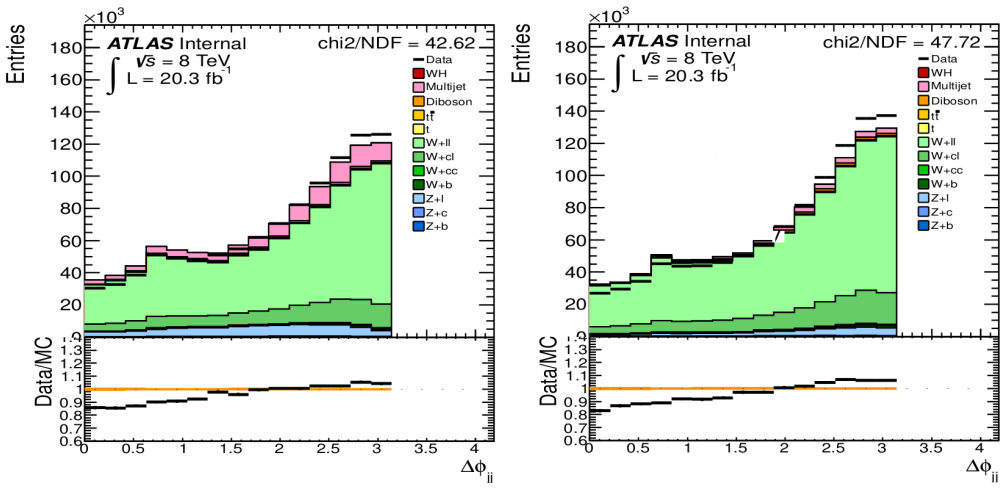

(a) Electron channel (b) Muon channel

Figure 6.23: W+jets $\Delta\phi_{jj}$ mismodelling in the electron and muon channels [125].

6.7 Description of systematic uncertainties

As this "boosted" $H \to b\bar{b}$ analysis shares much in common with the "inclusive" $H \to b\bar{b}$ analysis [115], aside from the jets, many of the systematic uncertainties are shared. For the non-jet related systematic effects, the systematic uncertainties obtained in the inclusive analysis are used. The effects of the jet related systematic uncertainties, such as the b-tagging efficiency scale factors and jet-energy scale, are evaluated explicitly in this analysis.

Some uncertainties involve only the normalisation of the distributions, while others involve the shapes of the distributions. As mentioned for the "boosted" analysis, the jet uncertainties are explicitly determined meaning that both normalisation and shape effects are accounted for. For the other systematic uncertainties, where the value obtained in the "inclusive" analysis is used, they are treated as normalisation only systematic uncertainties. Additionally, most systematic uncertainties are relevant for all signal and background processes, but there are some specific uncertainties for certain processes. For example the single top and $t\bar{t}$ uncertainties apply only to those processes. Likewise the theoretical uncertainty on the Higgs boson production cross-section is only relevant for the signal processes.

Detailed below are the systematic uncertainties associated with the analysis. In the statistical analysis presented in Section 6.8, each systematic uncertainty is treated as a nuisance parameter.

6.7.1 Data taking uncertainties

The uncertainty on the luminosity of the full 2012 data set is ±2.8%. The uncertainty on the modelling of additional pileup interactions is ±2%.

6.7.2 Trigger uncertainties

The systematic uncertainties on the efficiencies of the electron and muon triggers are less than ±1%, and for the E_T^{miss} trigger is ±5%.

6.7.3 Identification uncertainties

The systematic uncertainties on the identification efficiencies of the electron and muon are less than ±1%, and their isolation efficiencies also have uncertainties ±1%.

6.7.4 E_T^{miss} uncertainties

The systematic uncertainty on the E_T^{miss} measurement is contributed to by the systematic uncertainties on the measurements of all the associated objects that contribute to it, and is applied as a normalisation uncertainty of ±5%.

6.7.5 Jet energy scale uncertainty

The Jet Energy Scale (JES) uncertainties are evaluated using different Monte Carlo generators and simulations, and evaluating the differences in γ-jet balance, Z-jet balance, and multi-jet balance between the generators [126]. There are also contributions from mis-modelling of the detector description, pileup effects, b-jet energy scale effects, and effects from overlapping or close-by jets. The evaluation of the JES for "jet-substructure" regimes is preliminary and on advice from the relevant ATLAS working group experts [127] a figure of ±5% has been applied as the JES uncertainty. The JES was varied within this uncertainty and M_{bb}

distributions for each extreme were obtained so that the fitting procedure could take account of the shape and normalisation effects of these uncertainties.

6.7.6 b-tagging uncertainties

A mis-modelling of the b-tagging efficiencies between Monte Carlo and data is present, which is mitigated somewhat by the provision of b-tagging scale factors obtained from a full b-tagging calibration. These scale factors are used to correct the Monte Carlo modelling of the efficiency, to that of the data. The scale factors have their own uncertainties associated with them, and are p_T dependent. For the inclusive analysis, many calibration techniques are combined to provide these scale factors and uncertainties. When performing a boosted analysis, these calibrations are not directly relevant since the jet reconstruction algorithms are different (AntiK_T, vs Cambridge-Aachen), and the spatial separation of the jets is provided in the inclusive calibration only in the region $\Delta R \geq 0.4$.

For this reason part of the work I have done has been to provide a full, bespoke b-tagging calibration for the Cambridge-Aachen subjets (using the p_T^{Rel} method), parameterised not only in p_T, but also over the full $\Delta R_{\text{Subjets}}$ range to provide scale factors and associated systematic uncertainties relevant for boosted analyses. As discussed in Chapter 5.

The b-tagging scale factors were varied within their systematic uncertainties to provide M_{bb} distributions at both extremes of the uncertainty. The normalisation and shape effects were taken into account in the fitting procedure.

6.7.7 $t\bar{t}$ modelling uncertainties

The uncertainty on the modelling of $t\bar{t}$ background was evaluated by comparing the M_{bb} and p_T^W distributions between POWHEG (the default generator for $t\bar{t}$) and both MC@NLO and Alpgen generators. Additionally the effects of initial and final state radiation were investigated with AcerMC and the effects of different parton shower models were considered also. The result was a normalisation uncertainty of $\pm 5\%$ on the $t\bar{t}$ background. There is, in addition, a shape uncertainty in the M_{bb} distribution for $t\bar{t}$, found by comparing the M_{bb} shapes between generators. The shape difference is $\sim \pm 5\%$ and leads to a less than 5% uncertainty on the fit results [125]. This was evaluated in the inclusive

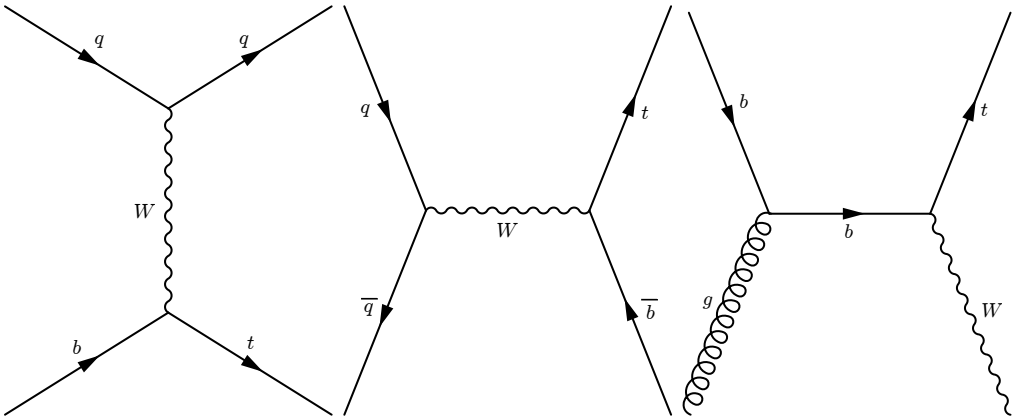

(a) t-channel (b) s-channel (c) Wt-channel

Figure 6.24: Feynman diagrams for single-top production.

analysis, but this wasn't evaluated fully as part of the boosted analysis. A full treatment would require the $t\bar{t}$ M_{bb} mismodelling study be repeated with Cambridge-Aachen subjets, and the shapes included in the fit. It is expected that this would have a similarly small effect on the boosted analysis, especially compared to the magnitude of other uncertainties.

6.7.8 V+jets modelling uncertainties

As mentioned in Section 6.6.2, a mis-modelling of the $\Delta\phi$ distributions is present in Monte Carlo for W+jets samples, and re-scaling is done to account for this. A systematic uncertainty is present on this re-scaling and is evaluated by modifying the re-scaling factor by 50% up and down and and comparing the M_{bb} distributions between the re-scaled case and the nominal case. The resulting difference was quantified as a normalisation uncertainty of ±10%.

6.7.9 Single-t modelling uncertainties

Uncertainties on the next-to-next-to-leading-order cross-sections for single top processes in t-channel, s-channel and in association with a W-boson (Wt) have been evaluated to be ±4%, ±4% and ±7% respectively. The Feynman diagrams for these processes are shown in Figure 6.24.

6.7.10 Diboson (WW and WZ) uncertainties

A diboson modelling uncertainty is introduced due to the use of a single Monte Carlo generator for diboson processes across all p_T^W bins, and analyses having only neutrinos, one charged lepton and one neutrino, and two charged leptons in the final state. In the past various different combinations of generators had been used for the different regions, but the recent approach in the "inclusive" analysis was to use a single generator and assign a systematic uncertainty on the normalisation in each region. This was evaluated as ±5% for WW and ±7% for WZ backgrounds.

6.7.11 Theory uncertainties

Theoretical uncertainty on the calculation of the Higgs boson branching ratio has been evaluated between ±2.5% and ±4.3% depending on the Higgs boson mass point. For the 125 GeV mass point the uncertainty is ±3.3%. There are also uncertainties on the WH production cross-section, of a further ±4% [125].

6.8 Fitting and limit setting procedure

The discriminant of the fit is on the invariant mass of the two b-tagged jets, M_{bb}. The distributions for signal, data and the background processes are used as inputs to the fit, as are the relevant systematic variations on these.

The objective of the fitting procedure and statistical testing, is to evaluate the compatibility of any observation with an expectation. This is done by defining a hypothesis whereby no signal is present, only background, often called the background-only hypothesis, or null hypothesis. Signal is defined depending on the process under study, in this case the signal is the observation of Higgs boson decays. Any measurement is then tested for compatibility with the null hypothesis. A measurement compatible with the null hypothesis indicates no signal is present, an observation incompatible with the null hypothesis could indicate the presence of signal events.

The fitting procedure uses a binned maximum likelihood function $\mathcal{L}(\mu, \theta)$ which is the product of Poisson probability terms, defined in Equation 6.3. μ is the signal strength parameter, which is the factor that multiplies the

expected signal yield in each bin. This parameter defines how "signal-like" any measurement is, i.e. $\mu = 0$ indicates no signal present (null hypothesis) and $\mu = 1$ indicates the signal plus background hypothesis (assuming a Standard Model Higgs boson). θ are nuisance parameters representing the dependence of the signal and background predictions on the systematic uncertainties. θ are parameterised either by a Gaussian or log-normal priors, or they are left to float in the fit.

A test statistic is used to evaluate the compatibility between the null hypothesis and the observed data and for exclusion intervals obtained using the CLs method [128]. The test statistic, q_μ, is defined in Equation 6.6.

$$\mathcal{L}(\mu, \theta) = \prod_{i=1}^{N_{\text{bins}}} \frac{(\mu s_i + b_i)^{n_i}}{n_i!} e^{-(\mu s_i + b_i)} \tag{6.3}$$

where s_i and b_i are given by:

$$s_i = s_{tot} \int_i f_s(x; \theta) dx \tag{6.4}$$

$$b_i = b_{tot} \int_i f_b(x; \theta) dx \tag{6.5}$$

$$q_\mu = -2\, ln \left(\frac{\mathcal{L}(\mu, \hat{\hat{\theta}}_\mu)}{\mathcal{L}(\hat{\mu}, \hat{\theta})} \right) \tag{6.6}$$

where $\hat{\mu}$ and $\hat{\theta}$ are the values of μ and θ respectively that maximise the likelihood, where $0 \leq \hat{\mu} \leq \mu$. $\hat{\hat{\theta}}_\mu$ is the nuisance parameter value that maximises the likelihood for a given μ value.

The test statistic q_μ is evaluated three times, as explained below and shown in Figure 6.25.

1. For the background hypothesis (with $\mu = 0$), where the n_i are background events only, resulting in a null hypothesis distribution of q_μ

2. For the signal + background hypothesis (with $\mu = 1$), where the n_i are the sum of signal and background events, resulting in a signal + background hypothesis of q_μ.

3. For the observed data, where the n_i are the observed events, resulting in one value of q_μ.

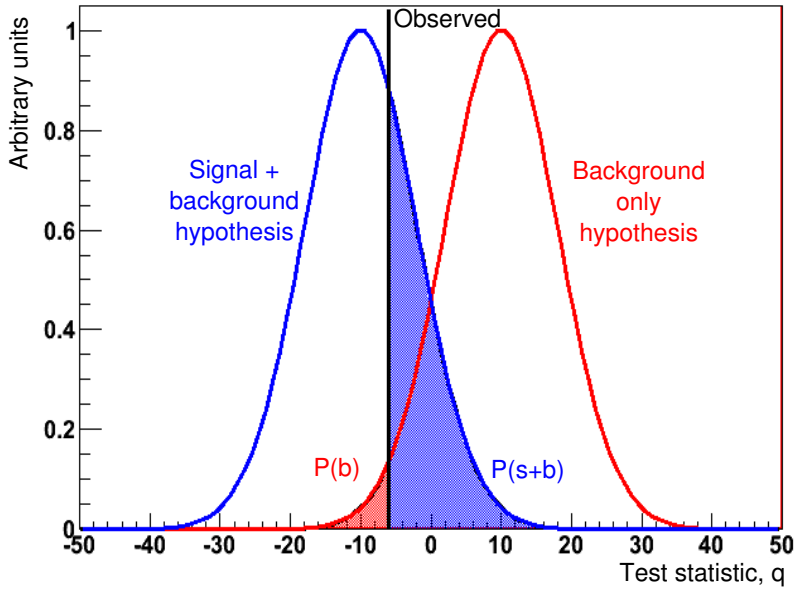

Figure 6.25: Examples of test statistics for the signal + background and background only hypotheses, and the observed data. Also shown are the p-values, P(b) or p_{B} is the probability that the background-only hypothesis yields a result that is more signal-like than the observation, and P(s+b) or $p_{\mathrm{S+B}}$ is the probability that the signal + background hypothesis yields a result that is more background-like than the observation. Modified from [129].

In Figure 6.25 $p_{\mathrm{S+B}}$ is the probability that the signal + background hypothesis yields a result that is more background-like than the observation. Likewise the p_{B} is the probability that the background-only hypothesis yields a result that is more signal-like than the observation. These are collectively known as "p-values".

6.8.1 Exclusion with the CLs method

Given the three values of the test statistic for the signal + background hypothesis, the background-only hypothesis and the observation, defined in the previous section, exclusion is performed using the CLs (Confidence Levels) method. This method allows the signal + background hypothesis to be rejected at a given confidence level, usually 95%. The results of the CLs method are used to set a limit on a variable related to the signal + background hypothesis, for example,

the Higgs boson production cross-section.

The CLs method works as follows. Firstly the CLs value is defined in Equation 6.7, where CL is the desired confidence level satisfying ($0 \leq \mathrm{CL} \leq 1$), typically $\mathrm{CL} = 0.95$.

$$\mathrm{CLs} = \frac{\mathcal{P}(q_\mu \geq \mathrm{Obs}|H_{\mathrm{Sig+Bkg}})}{\mathcal{P}(q_\mu \geq \mathrm{Obs}|H_{\mathrm{Null}})} = 1 - \mathrm{CL} \tag{6.7}$$

where $H_{\mathrm{Sig+Bkg}}$ is the signal + background hypothesis, and H_{Null} is the background-only hypothesis. This equation is equivalent, in terms of p-values, to Equation 6.8.

$$\mathrm{CLs} = \frac{p_{\mathrm{S+B}}}{1 - p_{\mathrm{B}}} = 1 - \mathrm{CL} \tag{6.8}$$

The CLs value can be calculated with respect to the observed test statistic (as in Equation 6.7), or alternatively with respect to the expected value of the null hypothesis test statistic. Thereby giving values of CLs for "observed" and "expected" cases. The threshold value of the CLs is fixed, depending on the given CL value. CL is typically desired to be 0.95, thereby enforcing 0.05 as the threshold value. An exclusion is obtained (at 95% confidence level) when the calculated CLs value drops below 0.05, as this rejects the signal + background hypothesis at the 95% confidence level. Since p_{B} is fixed, but $p_{\mathrm{S+B}}$ is dependent on the μ parameter from Equation 6.3, a limit can be set by adjusting μ until the ratio satisfies the desired CLs threshold. This is illustrated in Figure 6.26.

6.8.2 Discovery and significance

In order to claim a discovery, a certain level of significance in the measurement is required. The p_0-value is defined as the probability that the null hypothesis could result in an observation at least as extreme as the one observed. This is illustrated in Figure 6.27. Significance can be quantified in terms of the p_0-value or alternatively it can be quantified in terms of the number of standard deviations, σ, of the observation from the median of the null hypothesis. For LHC experiments, a significance of 5σ (equivalent to a p_0-value less than 3×10^{-7}) is required to claim a discovery.

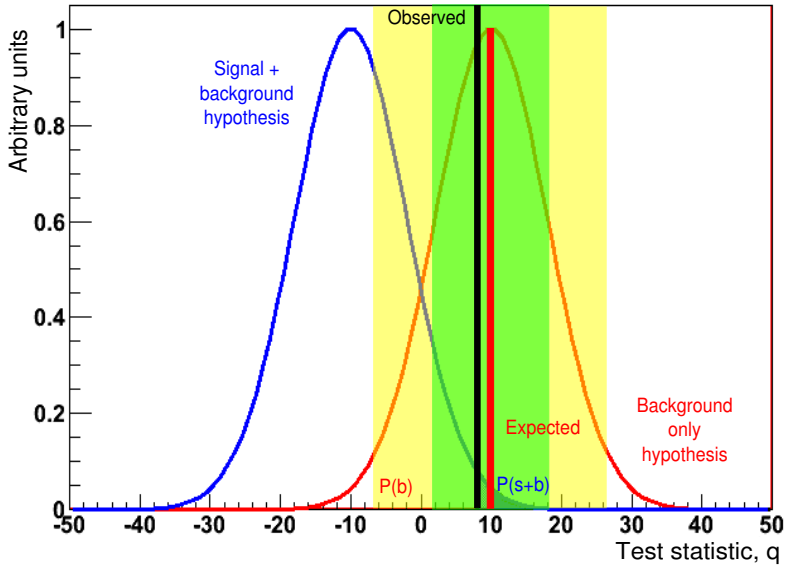

Figure 6.26: The CLs method, defined as in Equations 6.7 & 6.8. The green and yellow bands are $\pm 1\sigma$ and $\pm 2\sigma$ bands around the expected value of the background-only hypothesis test statistic, respectively. Modified from [129].

6.9 $H \to b\bar{b}$ results

The results of the analysis, are presented in Table 6.3, and include the value of the signal strength (μ) parameter, the observation significance, and the expected and observed exclusion limits for a Higgs boson mass of 125 GeV. These are presented for the electron-only, muon-only and combined channels. At Higgs boson mass of 125 GeV, in the combined channel the observed and expected limits on the Standard Model Higgs boson production cross-section are $6.12 \times \sigma_{\mathrm{SM}}$ and $5.52 \times \sigma_{\mathrm{SM}}$ respectively, where σ_{SM} is the Standard Model cross-section in the absence of Higgs boson production. Meaning that Higgs boson production with cross-section greater than $6.12 \times \sigma_{\mathrm{SM}}$ can been excluded at the 95% confidence level. μ has been found to be 0.93 ± 2.63 and the observation significance is 0.38 σ.

The exclusion limits found for the combined channel for this analysis over the entire Higgs boson mass range under consideration are shown in Figure 6.28.

The uncertainties on the evaluation for the signal strength for the combined

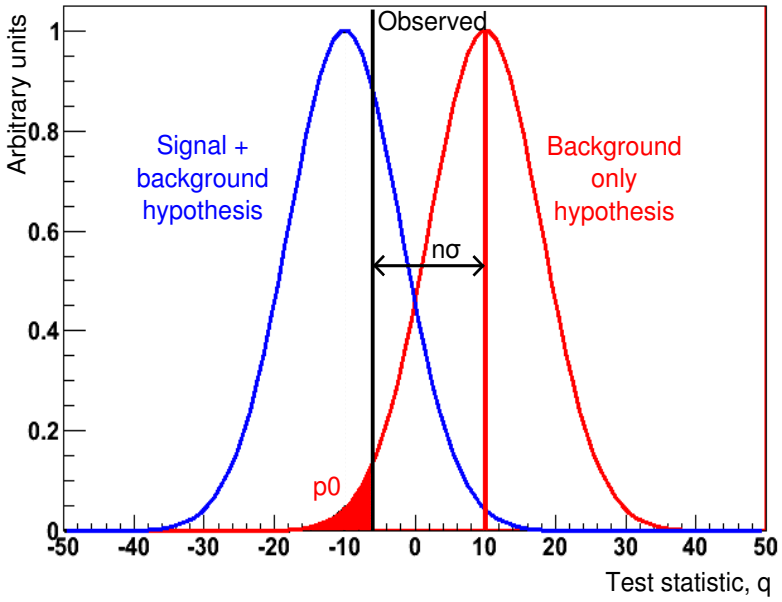

Figure 6.27: Example test statistic distributions showing the significance and p_0-value. The significance is defined as the number of standard deviations, σ, of the observation from the median of the background-only hypothesis. While the p_0-value is defined as the probability that the null hypothesis could result in an observation at least as extreme as the one observed. Modified from [129].

Parameter	e **channel**	μ **channel**	**Combined channel**
Signal strength, μ	0.58 ± 3.06	0.44 ± 4.52	0.93 ± 2.63
Observed limit $[\frac{\sigma}{\sigma_{\mathrm{SM}}}]$	6.92	9.97	6.12
Expected limit $[\frac{\sigma}{\sigma_{\mathrm{SM}}}]$	6.63	9.74	5.52
Observation significance $[\sigma]$	0.18	0.11	0.38

Table 6.3: Summary of results for Higgs boson mass of 125 GeV.

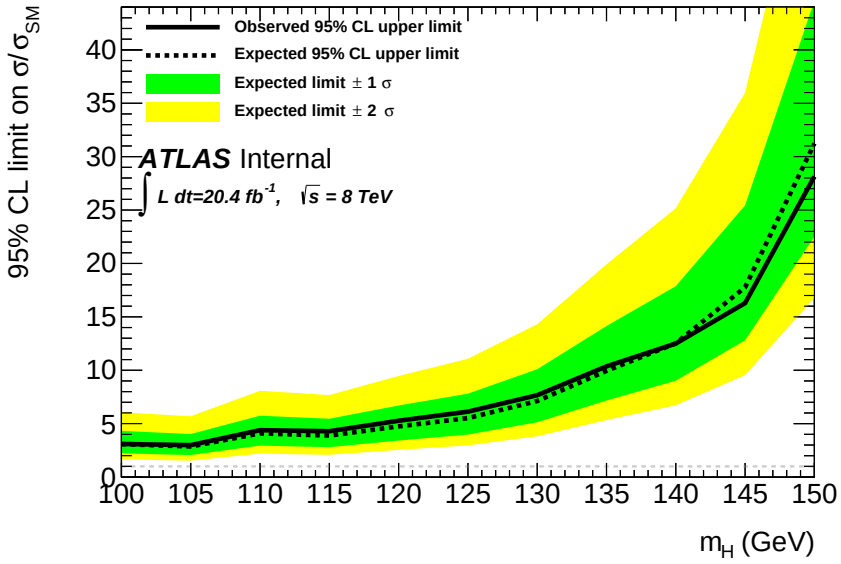

Figure 6.28: CLs results in the $H \to b\bar{b}$ search.

channel are listed in Table 6.4.

6.10 Discussion of results

The $H \to b\bar{b}$ decay channel is a particularly difficult search channel due to the large amounts of hadronic activity causing large background yields. An approach was adopted in this analysis to consider only Higgs boson candidates accompanied by a recoiling W-boson with large p_T, so called "boosted" events. This requirement was imposed with the expectation of reducing the number of signal events passing selection cuts, but reducing the number of background events even more so. The uncertainties are therefore dominated by the statistical uncertainty on the measured data, and the performance of the analysis is therefore limited by this factor.

The result of the analysis, an observed limit of $6.12 \times \sigma_{\mathrm{SM}}$, was found for a Higgs boson mass of 125 GeV, with a corresponding expected limit of $5.52 \times \sigma_{\mathrm{SM}}$. The entire Higgs boson mass range considered in this analysis ($100 \leq M_{\mathrm{H}} \leq 150$ GeV) has a limit in excess of $1 \times \sigma_{\mathrm{SM}}$, therefore no mass in this range can be excluded by this analysis alone. The value of signal strength obtained at Higgs

Uncertainty name	Absolute uncertainty	Percentage uncertainty [%]
Data statistics	± 2.234	± 240.215
Floating normalisation	± 0.744	± 80.000
Luminosity	± 0.300	± 32.258
Pileup modelling	± 0.207	± 22.258
Trigger efficiency	± 0.121	± 13.011
E_T^{miss}	± 0.522	± 56.129
Jet energy scale	± 0.561	± 60.323
b-tagging efficiency	± 0.351	± 37.742
$t\bar{t}$ modelling	± 0.252	± 27.079
W+jets modelling	± 0.078	± 8.387
Single top modelling	± 0.063	± 6.774
Diboson modelling	± 0.022	± 2.366
Theory	± 0.107	± 11.505
Total	± 2.632	± 283.011

Table 6.4: Uncertainties on the determination of the signal strength, μ. Theory uncertainties are on Higgs boson branching fraction and production cross-section.

boson mass of 125 GeV, 0.93 ± 2.63, is consistent with both 0 (no signal) and 1 (Standard Model Higgs boson signal), and the uncertainty is dominated by the statistical uncertainty on the data.

Direct comparison of the performance of the analysis with that of the inclusive analysis is difficult because the inclusive analysis is conducted over a much larger Higgs boson p_T range, and over all three possible associated production decay modes, $WH \to l\nu b\bar{b}$, $ZH \to \nu\bar{\nu}b\bar{b}$ and $ZH \to l^+l^-b\bar{b}$. The results quoted by the inclusive analysis generally are for the combined p_T ranges, and decay channels. However there is some information available about the signal and background yields after all selections on a channel-by-channel basis, and per Higgs boson p_T range, and these were compared in Section 6.5.1. These show that the $S/\sqrt{B}$ for both analyses is similar. Considering the observation significance, $\sim 1\sigma$ [130] over all three channels and the full Higgs boson p_T range in the inclusive analysis, compared to $\sim 0.38\sigma$ for the boosted analysis in the $WH \to l\nu b\bar{b}$ channel, it is unlikely that adding the two additional decay channels in the boosted analysis would the increase the significance above 1σ at this point. The inclusive analysis, by making use of all Higgs boson p_T ranges, has a factor of 100 more data passing all selections, but the greatest significance is in the Higgs boson $p_T > 200$ GeV

range.

Analysis [131] performed by the CMS experiment, in comparison, achieved a 2.1σ observation for a Higgs boson mass of 125 GeV, in the associated vector boson production channel. This analysis contains all the decay channels of the ATLAS inclusive analysis, but in addition it includes $WH \to \tau\nu_\tau b\bar{b}$. The CMS analysis only examines the region with Higgs boson candidate $p_T > 100$ GeV. The CDF and D0 collaborations at the Tevatron have also conducted searches [132] for the Higgs boson decaying to bottom quarks, which was produced in association with a vector boson. Like the ATLAS inclusive analysis the $WH \to \tau\nu_\tau b\bar{b}$ channel is not included. The Tevatron analyses, with 9.7 fb^{-1} of data at $\sqrt{s} = 1.96$ TeV, have obtained a significance for an excess at Higgs boson mass of 125 GeV, of $\sim 2.8\sigma$. A larger excess was observed, of 3.3σ, at a Higgs boson mass of 135 GeV.

There is a possibility to optimise the selections in the boosted analysis, both in terms of kinematic subjet selection and optimisation of the algorithms which define the subjets, neither of which were fully explored in the analysis presented in this chapter. In addition to this, there would be an improvement gained by combining both the boosted and inclusive analyses in the Higgs boson $p_T > 200$ GeV range. At least 25% of the events with Higgs boson $p_T > 200$ GeV in the boosted analysis are inaccessible to the inclusive analysis as the two b-tagged jets which decay from the Higgs boson are separated by $\Delta R < 0.4$, where the inclusive analysis cannot resolve the jets.

Chapter 7

Summary and Conclusions

The discovery of the Higgs boson is one of the major goals of the LHC physics programme. It was discovered [6, 7] in 2012 with a mass $\sim$ 126 GeV and a significance in excess of 5σ, however, this discovery gave no information about its coupling to fermions. Since then a $H \to \tau^+\tau^-$ decay as been observed [114] with a significance $\sim 4\sigma$, but a $H \to b\bar{b}$ decay hasn't yet been conclusively observed. This thesis presented an overview of the theory behind the Standard Model and the Higgs boson, and a description of the detector equipment that was used in the search for the Higgs boson decay to b-quarks.

The remainder of this thesis presented the efforts in the search for the Higgs boson via the $H \to b\bar{b}$ decay channel, where the Higgs boson had been produced in association with a W-boson. At hadron colliders such as the LHC, this is a notoriously difficult channel due to large background yields, therefore a novel technique was adopted. By requiring that the Higgs boson and the W-boson were both produced with high transverse momentum, and exploiting the "back-to-back" topology of the process, a reduction in the background yield was obtained, with a lesser reduction in the signal yield. This technique was originally proposed to be used at LHC design energy of $\sqrt{s} = 14$ TeV, but was applied here with 2012 run conditions ($\sqrt{s} = 8$ TeV). The jet structure was also affected by this high transverse momentum requirement. Specifically jets would often be initally reconstructed as one single object while they contained, for example, both b-jets from the Higgs boson decay. Novel jet identification techniques were made use of to extract this "jet-substructure" and recover the relevant information.

In order to make use of these jet-substructure techniques with b-tagging

algorithms, a full b-tagging calibration was performed to measure the b-tagging efficiencies in both data and simulation and their associated systematic uncertainties for these novel jet-substructure definitions, which had never been measured before. The result was a bespoke measurement on the jet-substructure definitions used in the analysis. In addition the calibration was able to provide measurements with very small distances between the subjets, which had not been possible with previous calibrations. This allowed an extra $\sim 25\%$ of events to be analysed that would not have been possible with "conventional" jets.

The $H \to b\bar{b}$ analysis itself made use of 20.4 fb^{-1} of 2012 proton proton collision data taken with the ATLAS experiment at $\sqrt{s} = 8$ TeV, and set exclusion limits, at the 95% confidence level, between 3 and 28 times the Standard Model production cross-section, in the Higgs boson mass range $100 \leq H_H \leq 150$ GeV. For a Higgs boson mass of 125 GeV, this exclusion limit is $6.12 \times \sigma_{\text{SM}}$.

This analysis was a first full analysis using "boosted" techniques in the search for $H \to b\bar{b}$. The analysis performance was limited by the low quantities of data that have been collected where the Higgs boson has p_T above 200 GeV and W-boson p_T above 200 GeV.

LHC Run II is forecast to increase the centre-of-mass energy from $\sqrt{s} = 8$ TeV to $\sqrt{s} = 14$ TeV. This alone will result in a 70% increase in the $q\bar{q} \to WH$ production cross-section, and an increase in the fraction of Higgs bosons produced with $p_T > 200$ GeV. In addition, at present $\sim 25\%$ of Higgs bosons produced in this high p_T regime decay to subjets separated by $\Delta R_{\text{Subjets}} < 0.4$. This fraction is dependent on Higgs boson p_T, so an increase in the fraction of Higgs bosons produced with higher transverse momentum will also lead to an increase in the fraction whose decay products have separations below 0.4 in ΔR. With a higher fraction of events in this regime, jet-substructure techniques will become more critical.

Run II is also forecast to double the current dataset in its first year of running, and collect 100 fb^{-1} of data over 4 years, leading to a factor of 5 increase on the current dataset. This alone will more than half the data statistical uncertainties in the boosted and inclusive analyses. This, when coupled with the increase in production of Higgs bosons in the high p_T regime and the related increase in close-by jets, will most benefit the boosted analysis where the data statistical uncertainties will be reduced by more than a factor of three.

However the increased luminosity is not only positive. The main method by which the luminosity will be increased is by reducing the bunch spacing from 50 ns, to 25 ns. This will lead to an increase in the out-of-time pileup. The mass resolution in the $H \to b\bar{b}$ channel is already poorer than other Higgs search channels and additional out-of-time pileup interactions could further broaden the mass distributions. Although no such significant changes are expected from in-time pileup.

Recent studies [133] have predicted that combined analyses in the $WH \to l\nu b\bar{b}$, and $ZH \to l^+l^-b\bar{b}$ channels could reach a significance of 3.9σ with 300 fb^{-1} of integrated luminosity, at $\sqrt{s} = 14$ TeV. To achieve a 5σ observation more data than this would have to be collected. This study did not include the use of jet-substructure techniques, nor did it include the $ZH \to \nu\bar{\nu}b\bar{b}$ decay channel.

Future LHC runs at higher energies, coupled with the increase in integrated luminosity, and the optimisation of jet-substructure techniques are promising for improving the performance of this analysis. As a result of the efforts in this thesis, the framework is now in place for both boosted b-tagging calibrations, and boosted Higgs analyses for future LHC running.

Appendix A

Additional b-tagging calibration information and all results

A.1 Good runs list used

`data12_8TeV.periodAllYear_DetStatus-v54-pro13-04_DQDefects-00-00-33_PHYS_StandardGRL_All_Good.xml`

A.2 All b-tagging calibration results

The b-tagging efficiencies and data to Monte Carlo scale factors measured using the p_T^{Rel} method are shown below for each of the b-tagging algorithms and working points listed in Table 5.2. A table of systematic uncertainties is also provided for each measurement.

A.2.1 SV0 at 50%

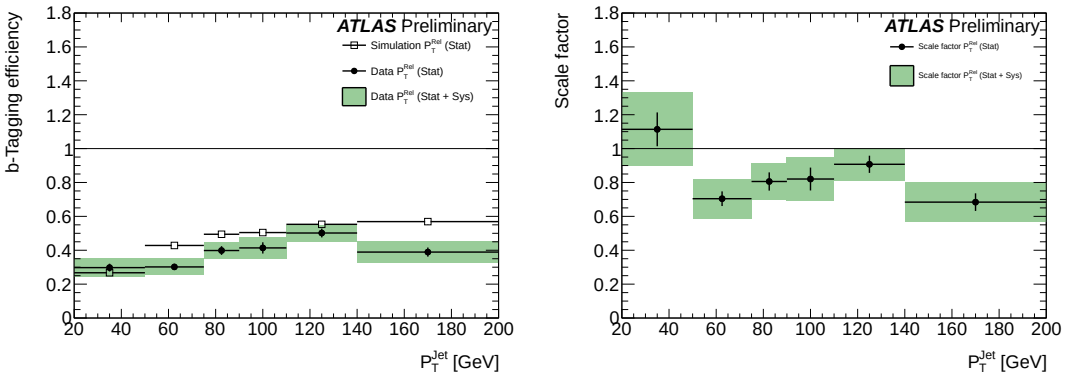

(a) Efficiency (b) Data/MC scale factor

Figure A.1: Efficiency and scale factors for SV0 tagger at 50% working point in $\Delta R_{\text{Subjets}} < 0.4$ bin.

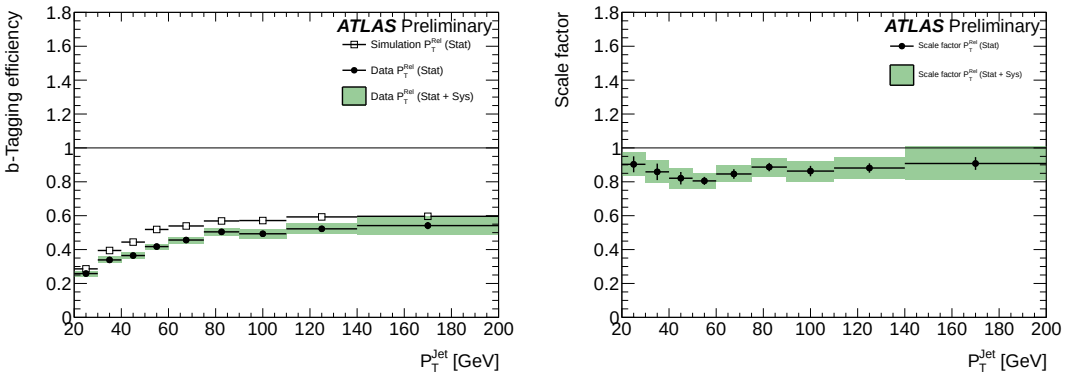

(a) Efficiency (b) Data/MC scale factor

Figure A.2: Efficiency and scale factors for SV0 tagger at 50% working point in $\Delta R_{\text{Subjets}} \geq 0.4$ bin.

Uncertainty	p_T^{jet} **bin [GeV]**					
	20-50	**50-75**	**75-90**	**90-110**	**110-140**	**> 140**
Statistical [%]						
Statistical (MC)	4.5	1.1	1.7	1.9	2.1	3.2
Statistical (Data)	7.7	6.0	6.5	8.0	5.2	6.9
Total Statistical	9.0	6.1	6.7	8.2	5.6	7.6
Systematic [%]						
MC stats	9.8	1.6	2.3	2.8	3.9	4.4
Pileup weight	1.8	1.8	2.0	1.0	0.8	1.0
Light charm ratio	0.5	1.0	0.6	0.0	1.0	4.1
Muon fakes	5.1	6.5	4.2	4.9	2.0	8.9
Model b prod.	7.7	13.0	8.7	11.2	2.7	9.6
Model c prod.	9.7	1.2	3.5	1.9	5.9	0.7
Light temp. con.	1.2	0.2	0.3	0.1	0.7	1.7
Inclusive *b*-jets	4.0	4.0	4.0	4.0	4.0	4.0
Jet energy scale	0.0	0.0	0.0	0.0	0.0	0.0
Total systematic	17.2	15.4	11.4	13.4	9.0	15.1

Table A.1: Statistical and systematic errors (%) for the SV0 tagger at 50% working point in $\Delta R_{\text{Subjets}} < 0.4$ bin.

Uncertainty	p_T^{jet} **bin [GeV]**								
	20-30	**30-40**	**40-50**	**50-60**	**60-75**	**75-90**	**90-110**	**110-140**	**> 140**
Statistical [%]									
Statistical (MC)	2.5	2.5	2.8	1.1	1.0	1.1	1.2	1.2	1.4
Statistical (Data)	4.6	5.1	3.5	2.7	3.2	2.5	3.4	2.9	3.9
Total Statistical	5.2	5.7	4.5	2.9	3.4	2.8	3.6	3.2	4.1
Systematic [%]									
MC stats	2.9	2.8	3.7	1.4	1.2	1.8	1.5	2.4	2.4
Pileup weight	0.6	0.2	0.4	0.1	0.1	0.2	0.4	0.3	0.1
Light charm ratio	0.9	0.7	0.8	0.0	0.2	0.2	0.3	1.4	3.0
Muon fakes	0.2	0.5	0.4	0.2	0.2	0.1	1.7	0.7	6.5
Model b prod.	1.5	0.4	1.1	0.4	0.3	0.0	2.3	0.3	3.1
Model c prod.	1.3	0.6	0.7	1.5	2.1	3.1	2.9	4.0	4.1
Light temp. con.	1.7	1.4	1.2	1.3	0.6	0.6	0.5	1.0	0.5
Inclusive b-jets	4.0	4.0	4.0	4.0	4.0	4.0	4.0	4.0	4.0
Jet energy scale	0.0	0.0	0.0	0.0	0.0	0.0	0.0	0.0	0.0
Total systematic	5.7	5.2	5.8	4.7	4.7	5.4	6.0	6.5	10.0

Table A.2: Statistical and systematic errors (%) for the SV0 tagger at 50% working point in $\Delta R_{\text{Subjets}} \geq 0.4$ bin.

A.2.2 JetFitterCOMBNN at 57%

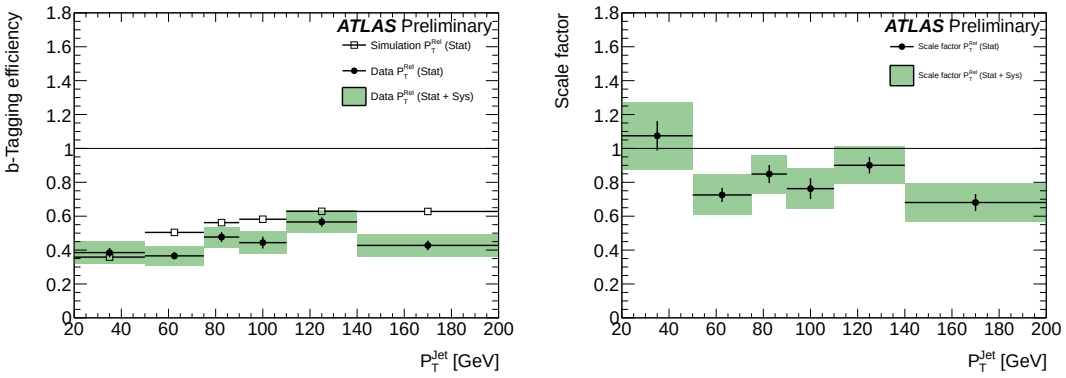

(a) Efficiency (b) Data/MC scale factor

Figure A.3: Efficiency and scale factors for JetFitterCOMBNN tagger at 57% working point in $\Delta R_{\text{Subjets}} < 0.4$ bin.

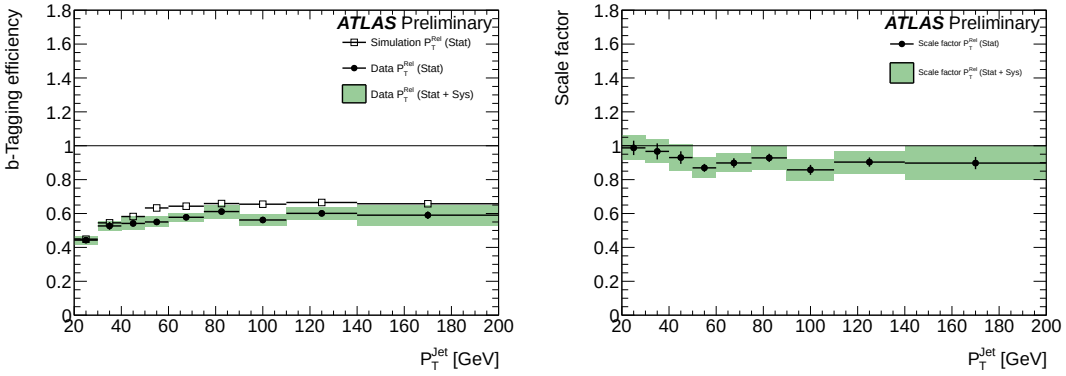

(a) Efficiency (b) Data/MC scale factor

Figure A.4: Efficiency and scale factors for JetFitterCOMBNN tagger at 57% working point in $\Delta R_{\text{Subjets}} \geq 0.4$ bin.

Uncertainty	p_T^{jet} **bin [GeV]**					
	20-50	**50-75**	**75-90**	**90-110**	**110-140**	**> 140**
Statistical [%]						
Statistical (MC)	3.9	1.0	1.6	1.8	2.0	3.0
Statistical (Data)	7.0	5.6	6.1	7.8	5.0	6.7
Total Statistical	8.1	5.7	6.3	8.0	5.4	7.3
Systematic [%]						
MC stats	9.7	1.6	2.3	2.8	3.1	4.8
Pileup weight	0.3	1.8	2.0	1.0	1.1	1.0
Light charm ratio	0.9	1.0	0.6	0.0	1.8	4.1
Muon fakes	6.5	6.5	4.2	4.9	5.6	8.3
Model b prod.	8.4	13.0	9.4	11.2	6.1	9.6
Model c prod.	7.0	1.2	3.5	2.0	5.2	0.7
Light temp. con.	1.3	0.2	0.3	0.1	0.7	1.7
Inclusive b-jets	4.0	4.0	4.0	4.0	4.0	4.0
Jet energy scale	0.0	0.0	0.0	0.0	0.0	0.0
Total systematic	16.6	15.4	12.0	13.4	11.2	14.9

Table A.3: Statistical and systematic errors (%) for the JetFitterCOMBNN tagger at 57% working point in $\Delta R_{\text{Subjets}} < 0.4$ bin.

Uncertainty	p_T^{jet} **bin [GeV]**								
	20-30	**30-40**	**40-50**	**50-60**	**60-75**	**75-90**	**90-110**	**110-140**	**> 140**
Statistical [%]									
Statistical (MC)	2.1	2.3	2.5	1.0	1.0	1.1	1.1	1.2	1.3
Statistical (Data)	3.8	4.4	3.1	2.5	3.0	2.4	3.2	2.8	3.8
Total Statistical	4.3	4.9	4.0	2.7	3.1	2.6	3.4	3.0	4.0
Systematic [%]									
MC stats	3.0	2.8	3.7	1.0	1.1	1.5	1.3	2.4	2.4
Pileup weight	0.1	0.2	0.1	0.8	0.1	0.7	0.3	0.2	0.2
Light charm ratio	1.0	0.7	0.8	0.0	0.2	0.3	0.3	1.3	2.8
Muon fakes	0.6	0.2	0.6	4.0	2.0	3.6	2.8	1.2	6.7
Model b prod.	1.9	0.2	4.8	2.3	1.2	2.4	3.2	0.7	2.9
Model c prod.	0.9	0.9	1.3	1.6	2.2	3.5	2.6	4.4	4.4
Light temp. con.	1.8	1.5	1.2	1.3	0.6	0.6	0.5	1.1	0.5
Inclusive b-jets	4.0	4.0	4.0	4.0	4.0	4.0	4.0	4.0	4.0
Jet energy scale	0.0	0.0	0.0	0.0	0.0	0.0	0.0	0.0	0.0
Total systematic	5.8	5.2	7.5	6.6	5.3	7.1	6.5	6.8	10.2

Table A.4: Statistical and systematic errors (%) for the JetFitterCOMBNN tagger at 57% working point in $\Delta R_{\text{Subjets}} \geq 0.4$ bin.

A.2.3 JetFitterCOMBNN at 60%

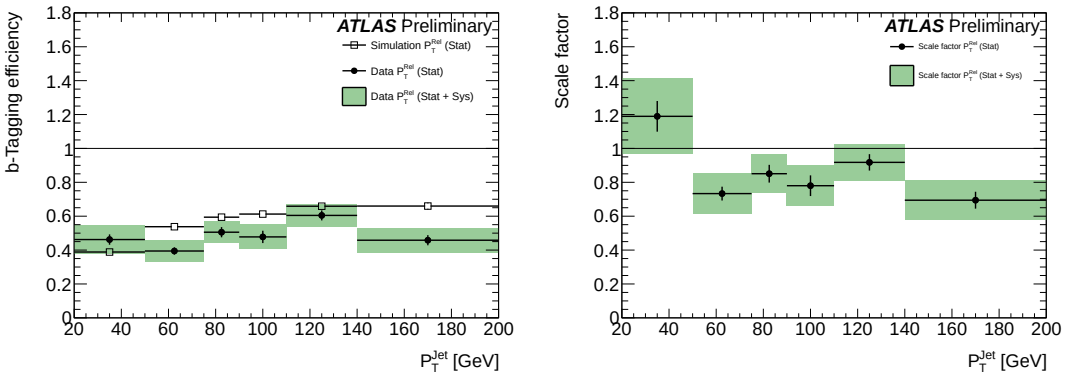

(a) Efficiency (b) Data/MC scale factor

Figure A.5: Efficiency and scale factors for JetFitterCOMBNN tagger at 60% working point in $\Delta R_{\text{Subjets}} < 0.4$ bin.

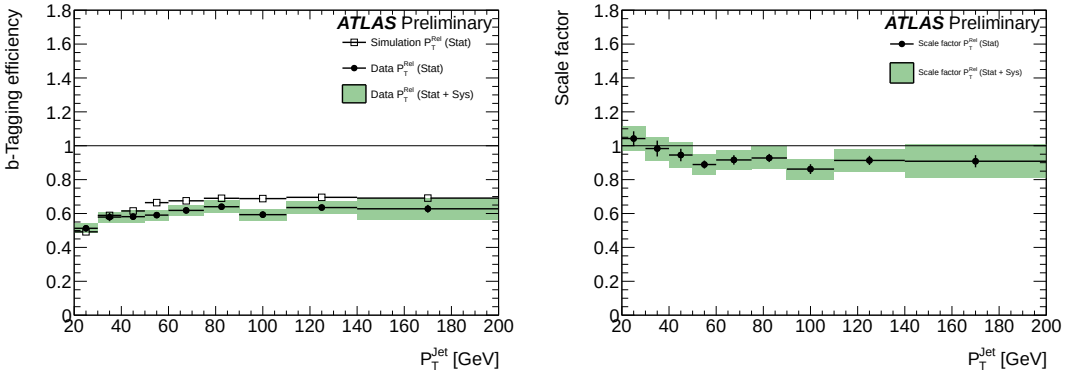

(a) Efficiency (b) Data/MC scale factor

Figure A.6: Efficiency and scale factors for JetFitterCOMBNN tagger at 60% working point in $\Delta R_{\text{Subjets}} \geq 0.4$ bin.

Uncertainty	p_T^{jet} **bin [GeV]**					
	20-50	**50-75**	**75-90**	**90-110**	**110-140**	**> 140**
Statistical [%]						
Statistical (MC)	3.8	1.0	1.6	1.8	2.0	3.0
Statistical (Data)	6.6	5.5	6.0	7.6	4.9	6.5
Total Statistical	7.6	5.6	6.2	7.8	5.3	7.2
Systematic [%]						
MC stats	8.8	1.6	2.3	2.8	3.3	4.4
Pileup weight	1.6	1.8	2.0	1.0	1.1	1.0
Light charm ratio	0.8	1.0	0.6	0.0	1.8	4.1
Muon fakes	1.0	6.5	4.2	4.9	5.1	8.9
Model b prod.	11.6	13.0	9.3	11.2	5.1	9.6
Model c prod.	7.7	1.2	3.5	2.0	5.2	0.7
Light temp. con.	1.3	0.2	0.3	0.1	0.7	1.7
Inclusive b-jets	4.0	4.0	4.0	4.0	4.0	4.0
Jet energy scale	0.0	0.0	0.0	0.0	0.0	0.0
Total systematic	17.2	15.4	11.9	13.4	10.5	15.1

Table A.5: Statistical and systematic errors (%) for the JetFitterCOMBNN tagger at 60% working point in $\Delta R_{\text{Subjets}} < 0.4$ bin.

Uncertainty	p_T^{jet} **bin [GeV]**								
	20-30	**30-40**	**40-50**	**50-60**	**60-75**	**75-90**	**90-110**	**110-140**	**> 140**
Statistical [%]									
Statistical (MC)	2.0	2.2	2.5	1.0	0.9	1.1	1.1	1.2	1.3
Statistical (Data)	3.6	4.2	3.0	2.4	2.9	2.4	3.2	2.7	3.7
Total Statistical	4.1	4.8	3.9	2.6	3.0	2.6	3.4	3.0	4.0
Systematic [%]									
MC stats	2.8	2.8	3.7	1.1	1.0	1.6	1.4	2.4	2.4
Pileup weight	0.7	0.1	0.2	0.8	0.7	0.4	0.3	0.2	0.2
Light charm ratio	1.0	0.8	0.6	0.0	0.2	0.2	0.3	1.4	2.8
Muon fakes	0.3	0.3	0.1	3.7	2.3	2.7	2.3	0.9	6.8
Model b prod.	1.7	0.1	4.2	1.5	1.8	1.8	2.7	0.6	2.9
Model c prod.	0.5	0.8	1.1	1.6	2.2	3.8	2.7	4.2	4.4
Light temp. con.	1.8	1.5	1.2	1.3	0.6	0.6	0.5	1.1	0.5
Inclusive b-jets	4.0	4.0	4.0	4.0	4.0	4.0	4.0	4.0	4.0
Jet energy scale	0.0	0.0	0.0	0.0	0.0	0.0	0.0	0.0	0.0
Total systematic	5.6	5.2	7.1	6.1	5.6	6.6	6.2	6.6	10.2

Table A.6: Statistical and systematic errors (%) for the JetFitterCOMBNN tagger at 60% working point in $\Delta R_{\text{Subjets}} \geq 0.4$ bin.

A.2.4 JetFitterCOMBNN at 70%

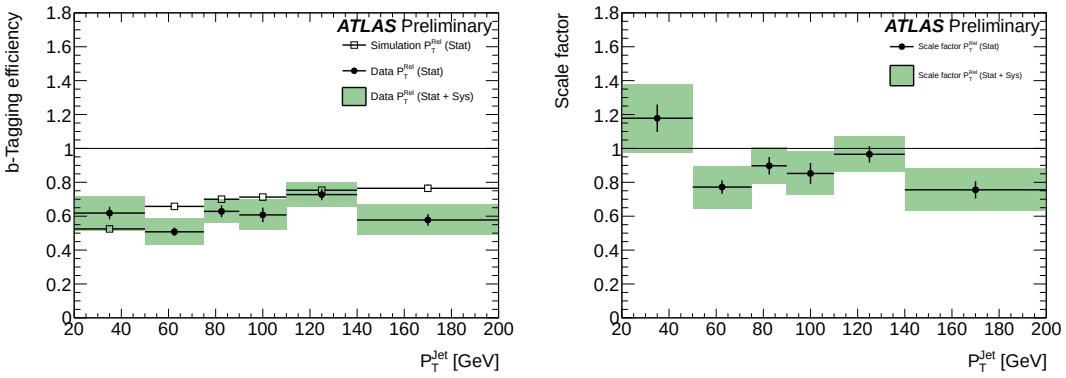

(a) Efficiency (b) Data/MC scale factor

Figure A.7: Efficiency and scale factors for JetFitterCOMBNN tagger at 70% working point in $\Delta R_{\text{Subjets}} < 0.4$ bin.

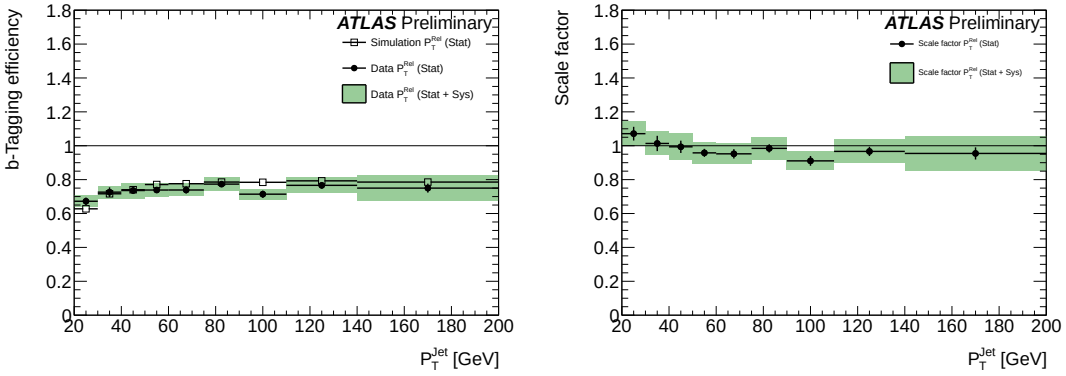

(a) Efficiency (b) Data/MC scale factor

Figure A.8: Efficiency and scale factors for JetFitterCOMBNN tagger at 70% working point in $\Delta R_{\text{Subjets}} \geq 0.4$ bin.

Uncertainty	p_T^{jet} **bin [GeV]**					
	20-50	**50-75**	**75-90**	**90-110**	**110-140**	**> 140**
Statistical [%]						
Statistical (MC)	3.4	1.0	1.5	1.7	1.9	2.9
Statistical (Data)	6.0	5.0	5.6	7.1	4.6	6.0
Total Statistical	6.9	5.1	5.8	7.3	5.0	6.7
Systematic [%]						
MC stats	9.3	1.6	2.3	2.8	3.7	4.3
Pileup weight	0.6	1.8	2.0	1.0	1.2	1.0
Light charm ratio	0.1	1.0	0.6	0.0	2.4	4.1
Muon fakes	4.8	6.5	4.1	4.9	3.4	9.0
Model b prod.	7.3	13.0	7.5	11.3	3.5	9.6
Model c prod.	8.2	1.2	3.5	1.9	5.5	0.7
Light temp. con.	1.3	0.2	0.3	0.1	0.7	1.7
Inclusive b-jets	4.0	4.0	4.0	4.0	4.0	4.0
Jet energy scale	0.0	0.0	0.0	0.0	0.0	0.0
Total systematic	15.8	15.4	10.6	13.4	9.6	15.2

Table A.7: Statistical and systematic errors (%) for the JetFitterCOMBNN tagger at 70% working point in $\Delta R_{\text{Subjets}} < 0.4$ bin.

Uncertainty	p_T^{jet} **bin [GeV]**								
	20-30	**30-40**	**40-50**	**50-60**	**60-75**	**75-90**	**90-110**	**110-140**	**> 140**
Statistical [%]									
Statistical (MC)	1.9	2.1	2.3	1.0	0.9	1.0	1.1	1.1	1.3
Statistical (Data)	3.3	3.9	2.8	2.3	2.7	2.2	3.0	2.6	3.5
Total Statistical	3.8	4.5	3.7	2.5	2.9	2.5	3.2	2.8	3.8
Systematic [%]									
MC stats	3.0	2.8	3.8	1.1	1.0	1.7	1.6	2.4	2.4
Pileup weight	0.3	0.2	0.1	0.8	0.8	0.3	0.4	0.2	0.2
Light charm ratio	0.9	0.8	0.8	0.0	0.2	0.3	0.3	1.3	2.7
Muon fakes	0.3	0.3	0.5	3.7	2.3	2.1	0.2	0.9	6.7
Model b prod.	1.6	0.2	3.9	1.5	1.9	1.4	1.0	0.5	2.9
Model c prod.	0.5	0.7	0.9	1.6	2.2	3.5	2.4	4.1	4.4
Light temp. con.	1.7	1.4	1.2	1.3	0.6	0.6	0.5	1.1	0.5
Inclusive b-jets	4.0	4.0	4.0	4.0	4.0	4.0	4.0	4.0	4.0
Jet energy scale	0.0	0.0	0.0	0.0	0.0	0.0	0.0	0.0	0.0
Total systematic	5.7	5.2	6.9	6.2	5.6	6.1	5.1	6.6	10.1

Table A.8: Statistical and systematic errors (%) for the JetFitterCOMBNN tagger at 70% working point in $\Delta R_{\text{Subjets}} \geq 0.4$ bin.

A.2.5 JetFitterCOMBNN at 80%

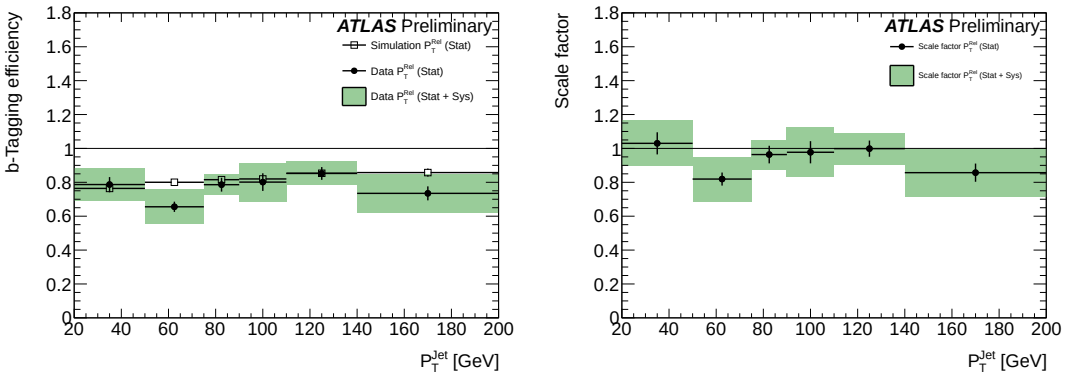

(a) Efficiency (b) Data/MC scale factor

Figure A.9: Efficiency and scale factors for JetFitterCOMBNN tagger at 80% working point in $\Delta R_{\text{Subjets}} < 0.4$ bin.

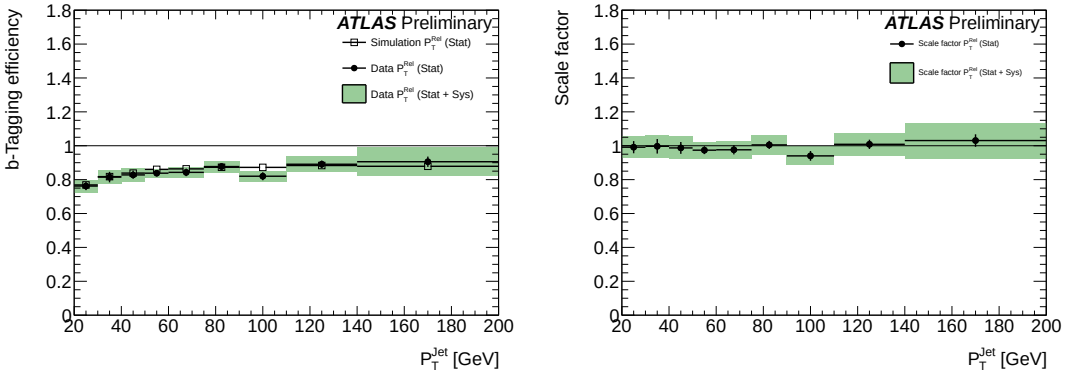

(a) Efficiency (b) Data/MC scale factor

Figure A.10: Efficiency and scale factors for JetFitterCOMBNN tagger at 80% working point in $\Delta R_{\text{Subjets}} \geq 0.4$ bin.

Uncertainty	p_T^{jet} **bin [GeV]**					
	20-50	**50-75**	**75-90**	**90-110**	**110-140**	**> 140**
Statistical [%]						
Statistical (MC)	3.0	0.9	1.4	1.6	1.8	2.8
Statistical (Data)	5.6	4.6	5.2	6.5	4.4	5.6
Total Statistical	6.3	4.7	5.4	6.7	4.8	6.3
Systematic [%]						
MC stats	8.7	1.6	3.0	2.8	4.2	4.3
Pileup weight	0.2	1.8	0.8	0.9	0.8	1.0
Light charm ratio	0.3	1.0	0.8	0.0	1.9	4.1
Muon fakes	2.2	6.5	0.3	4.9	1.9	9.0
Model b prod.	3.1	13.0	4.0	11.2	0.4	9.6
Model c prod.	4.8	1.2	2.8	1.9	4.5	0.7
Light temp. con.	1.0	0.2	0.3	0.1	0.7	1.7
Inclusive b-jets	4.0	4.0	4.0	4.0	4.0	4.0
Jet energy scale	0.0	0.0	0.0	0.0	0.0	0.0
Total systematic	11.4	15.4	7.1	13.4	7.9	15.1

Table A.9: Statistical and systematic errors (%) for the JetFitterCOMBNN tagger at 80% working point in $\Delta R_{\text{Subjets}} < 0.4$ bin.

Uncertainty	p_T^{jet} **bin [GeV]**								
	20-30	**30-40**	**40-50**	**50-60**	**60-75**	**75-90**	**90-110**	**110-140**	**> 140**
Statistical [%]									
Statistical (MC)	1.8	2.0	2.3	0.9	0.9	1.0	1.0	1.1	1.2
Statistical (Data)	3.2	3.8	2.7	2.2	2.6	2.2	2.9	2.5	3.4
Total Statistical	3.6	4.3	3.5	2.4	2.8	2.4	3.1	2.7	3.6
Systematic [%]									
MC stats	3.0	2.8	3.6	1.3	1.4	1.8	1.7	2.5	3.1
Pileup weight	0.1	0.1	0.3	0.2	0.1	0.2	0.3	0.1	0.4
Light charm ratio	0.6	0.7	0.7	0.1	0.3	0.2	0.2	1.3	3.0
Muon fakes	0.2	0.2	0.4	0.1	0.1	0.2	0.4	0.7	5.7
Model b prod.	0.8	0.1	0.2	0.1	0.5	0.1	0.2	0.4	2.3
Model c prod.	0.2	0.4	0.6	1.2	1.8	2.6	1.9	3.4	4.0
Light temp. con.	1.4	1.3	1.1	1.2	0.5	0.6	0.5	1.0	0.5
Inclusive b-jets	4.0	4.0	4.0	4.0	4.0	4.0	4.0	4.0	4.0
Jet energy scale	0.0	0.0	0.0	0.0	0.0	0.0	0.0	0.0	0.0
Total systematic	5.3	5.2	5.6	4.6	4.6	5.1	4.8	6.1	9.4

Table A.10: Statistical and systematic errors (%) for the JetFitterCOMBNN tagger at 80% working point in $\Delta R_{\text{Subjets}} \geq 0.4$ bin.

A.2.6 MV1 at 60%

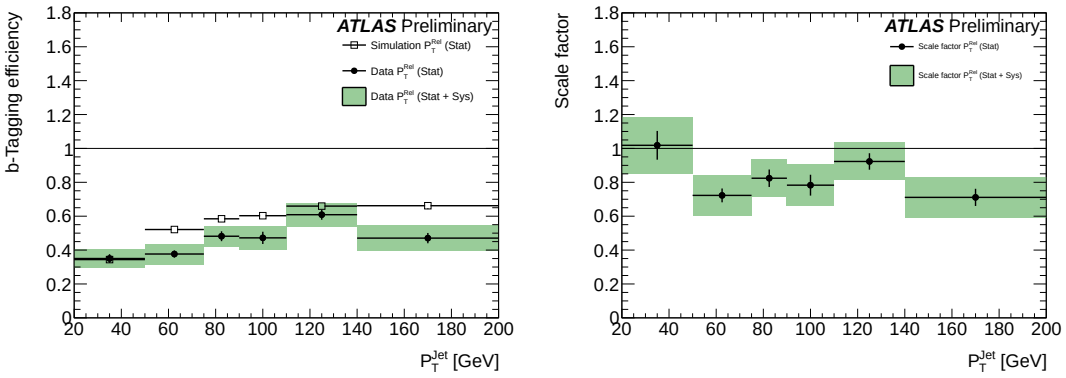

(a) Efficiency (b) Data/MC scale factor

Figure A.11: Efficiency and scale factors for MV1 tagger at 60% working point in $\Delta R_{\text{Subjets}} < 0.4$ bin.

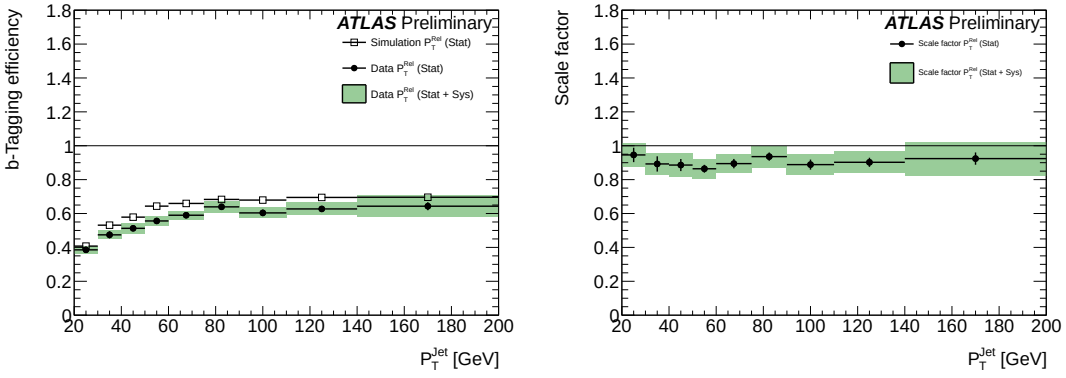

(a) Efficiency (b) Data/MC scale factor

Figure A.12: Efficiency and scale factors for MV1 tagger at 60% working point in $\Delta R_{\text{Subjets}} \geq 0.4$ bin.

Uncertainty	p_T^{jet} **bin [GeV]**					
	20-50	**50-75**	**75-90**	**90-110**	**110-140**	**> 140**
Statistical [%]						
Statistical (MC)	4.0	1.0	1.6	1.8	2.0	3.0
Statistical (Data)	7.3	5.6	6.0	7.7	4.9	6.5
Total Statistical	8.3	5.6	6.3	7.9	5.3	7.1
Systematic [%]						
MC stats	9.6	1.6	2.3	2.8	3.2	4.3
Pileup weight	0.4	1.8	2.0	1.0	1.1	1.0
Light charm ratio	0.7	1.0	0.6	0.0	1.8	4.1
Muon fakes	3.3	6.5	4.2	4.9	5.3	9.2
Model b prod.	4.1	13.0	9.3	11.3	5.6	9.6
Model c prod.	7.9	1.2	3.5	2.0	5.2	0.7
Light temp. con.	1.1	0.2	0.3	0.1	0.7	1.7
Inclusive *b*-jets	4.0	4.0	4.0	4.0	4.0	4.0
Jet energy scale	0.0	0.0	0.0	0.0	0.0	0.0
Total systematic	14.1	15.4	11.9	13.4	10.9	15.2

Table A.11: Statistical and systematic errors (%) for the MV1 tagger at 60% working point in $\Delta R_{\text{Subjets}} < 0.4$ bin.

Uncertainty	p_T^{jet} **bin [GeV]**								
	20-30	**30-40**	**40-50**	**50-60**	**60-75**	**75-90**	**90-110**	**110-140**	**> 140**
Statistical [%]									
Statistical (MC)	2.2	2.3	2.5	1.0	0.9	1.1	1.1	1.2	1.3
Statistical (Data)	3.9	4.5	3.1	2.5	2.9	2.4	3.2	2.7	3.7
Total Statistical	4.5	5.0	4.0	2.7	3.1	2.6	3.3	3.0	3.9
Systematic [%]									
MC stats	3.0	2.8	3.8	1.2	1.2	1.7	1.5	2.5	2.4
Pileup weight	0.4	0.1	0.5	0.0	0.0	0.3	0.3	0.0	0.2
Light charm ratio	0.9	0.8	0.8	0.0	0.2	0.3	0.3	1.4	2.7
Muon fakes	0.0	0.3	0.5	3.3	1.8	2.2	1.9	0.8	6.7
Model b prod.	1.5	0.1	3.3	1.5	1.2	1.5	2.5	0.6	2.9
Model c prod.	1.2	0.7	0.7	1.8	2.1	3.5	2.5	4.0	4.4
Light temp. con.	1.8	1.4	1.2	1.3	0.6	0.6	0.5	1.1	0.5
Inclusive b-jets	4.0	4.0	4.0	4.0	4.0	4.0	4.0	4.0	4.0
Jet energy scale	0.0	0.0	0.0	0.0	0.0	0.0	0.0	0.0	0.0
Total systematic	5.7	5.2	6.7	5.9	5.2	6.2	5.9	6.5	10.1

Table A.12: Statistical and systematic errors (%) for the MV1 tagger at 60% working point in $\Delta R_{\text{Subjets}} \geq 0.4$ bin.

A.2.7 MV1 at 70%

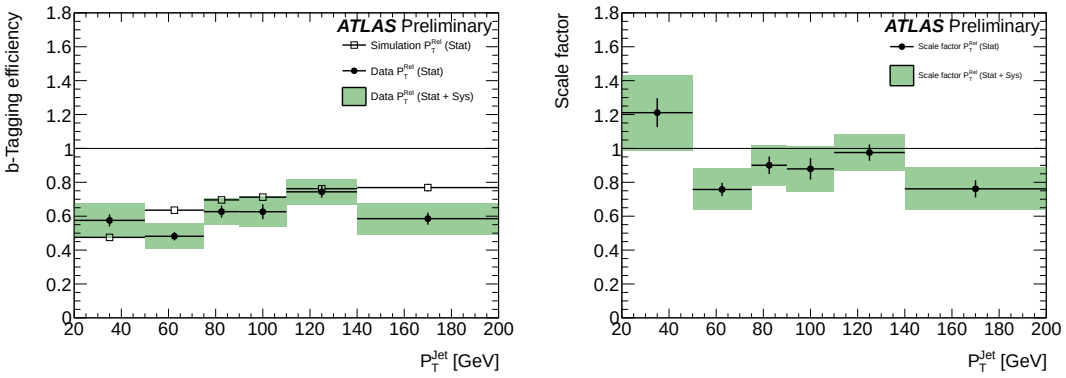

(a) Efficiency (b) Data/MC scale factor

Figure A.13: Efficiency and scale factors for MV1 tagger at 70% working point in $\Delta R_{\text{Subjets}} < 0.4$ bin.

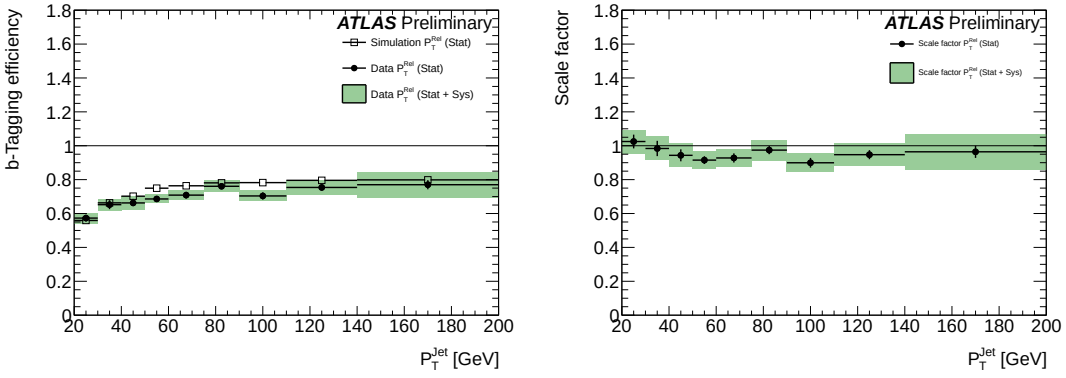

(a) Efficiency (b) Data/MC scale factor

Figure A.14: Efficiency and scale factors for MV1 tagger at 70% working point in $\Delta R_{\text{Subjets}} \geq 0.4$ bin.

Uncertainty	p_T^{jet} **bin [GeV]**					
	20-50	**50-75**	**75-90**	**90-110**	**110-140**	**> 140**
Statistical [%]						
Statistical (MC)	3.5	1.0	1.5	1.7	1.9	2.9
Statistical (Data)	6.1	5.1	5.6	7.0	4.6	6.0
Total Statistical	7.1	5.2	5.8	7.2	5.0	6.7
Systematic [%]						
MC stats	9.1	1.6	2.3	2.8	3.5	4.4
Pileup weight	0.2	1.8	2.0	1.0	1.1	1.0
Light charm ratio	0.2	1.0	0.6	0.0	1.8	4.1
Muon fakes	3.6	6.5	4.2	4.9	4.2	9.0
Model b prod.	9.2	13.0	9.4	11.3	4.1	9.6
Model c prod.	9.7	1.2	3.5	1.9	5.3	0.7
Light temp. con.	1.3	0.2	0.3	0.1	0.7	1.7
Inclusive b-jets	4.0	4.0	4.0	4.0	4.0	4.0
Jet energy scale	0.0	0.0	0.0	0.0	0.0	0.0
Total systematic	17.1	15.4	12.0	13.4	9.8	15.1

Table A.13: Statistical and systematic errors (%) for the MV1 tagger at 70% working point in $\Delta R_{\text{Subjets}} < 0.4$ bin.

Uncertainty	p_T^{jet} **bin [GeV]**								
	20-30	**30-40**	**40-50**	**50-60**	**60-75**	**75-90**	**90-110**	**110-140**	**> 140**
Statistical [%]									
Statistical (MC)	1.9	2.1	2.4	1.0	0.9	1.0	1.1	1.1	1.3
Statistical (Data)	3.4	4.1	2.9	2.3	2.8	2.2	3.0	2.6	3.5
Total Statistical	4.0	4.6	3.7	2.5	2.9	2.5	3.2	2.8	3.7
Systematic [%]									
MC stats	2.9	2.8	3.8	1.3	1.2	1.7	1.6	2.5	2.4
Pileup weight	0.4	0.1	0.2	0.3	0.2	0.2	0.4	0.1	0.1
Light charm ratio	1.1	0.8	0.8	0.0	0.2	0.3	0.3	1.4	2.7
Muon fakes	0.4	0.4	1.1	1.8	0.3	0.8	0.3	0.8	6.6
Model b prod.	1.4	0.0	2.7	0.6	0.3	0.8	0.9	0.5	2.9
Model c prod.	0.9	0.8	0.8	1.6	2.1	3.3	2.3	3.8	4.4
Light temp. con.	1.7	1.4	1.2	1.3	0.6	0.6	0.5	1.1	0.5
Inclusive b-jets	4.0	4.0	4.0	4.0	4.0	4.0	4.0	4.0	4.0
Jet energy scale	0.0	0.0	0.0	0.0	0.0	0.0	0.0	0.0	0.0
Total systematic	5.6	5.3	6.5	5.0	4.8	5.6	5.0	6.4	10.1

Table A.14: Statistical and systematic errors (%) for the MV1 tagger at 70% working point in $\Delta R_{\text{Subjets}} \geq 0.4$ bin.

A.2.8 MV1 at 75%

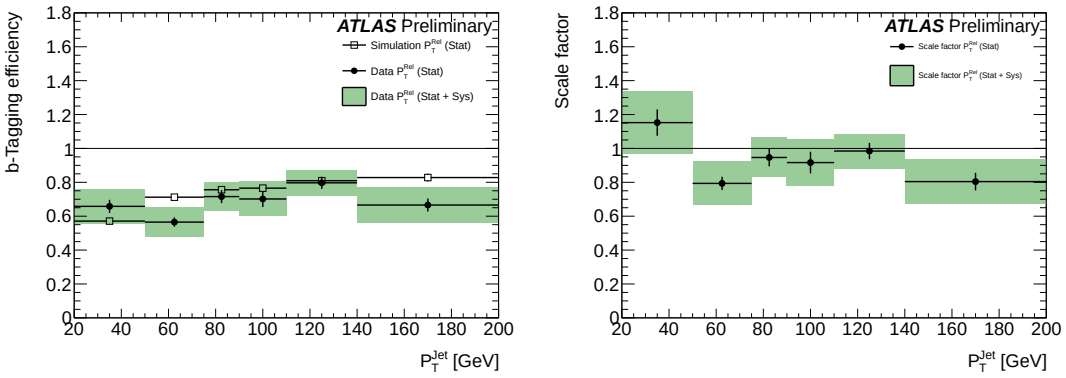

(a) Efficiency (b) Data/MC scale factor

Figure A.15: Efficiency and scale factors for MV1 tagger at 75% working point in $\Delta R_{\text{Subjets}} < 0.4$ bin.

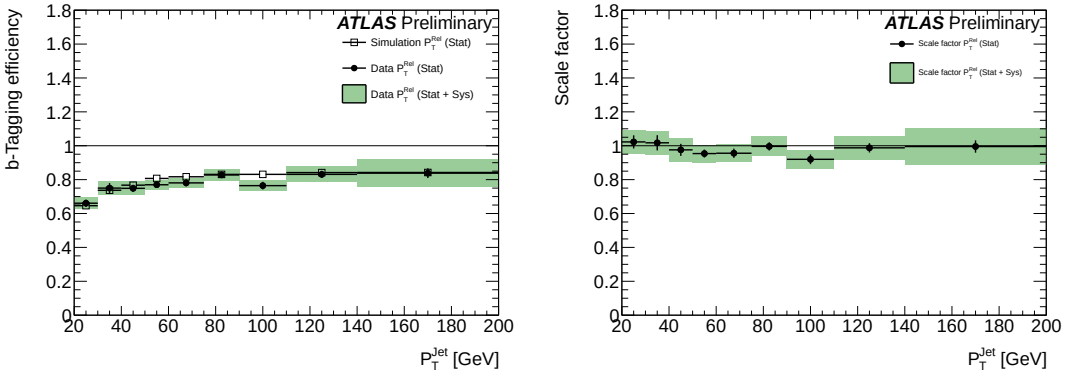

(a) Efficiency (b) Data/MC scale factor

Figure A.16: Efficiency and scale factors for MV1 tagger at 75% working point in $\Delta R_{\text{Subjets}} \geq 0.4$ bin.

Uncertainty	p_T^{jet} **bin [GeV]**					
	20-50	**50-75**	**75-90**	**90-110**	**110-140**	**> 140**
Statistical [%]						
Statistical (MC)	3.3	0.9	1.5	1.6	1.9	2.8
Statistical (Data)	5.9	4.8	5.3	6.8	4.5	5.8
Total Statistical	6.7	4.9	5.5	7.0	4.9	6.4
Systematic [%]						
MC stats	9.3	1.6	2.3	2.8	4.1	4.5
Pileup weight	0.6	1.8	2.0	1.0	0.7	1.0
Light charm ratio	0.2	1.0	0.6	0.0	2.0	4.1
Muon fakes	4.6	6.5	4.2	4.9	1.3	8.7
Model b prod.	4.9	13.0	8.3	11.3	2.0	9.6
Model c prod.	8.0	1.2	3.5	1.9	6.4	0.7
Light temp. con.	1.2	0.2	0.3	0.1	0.7	1.7
Inclusive *b*-jets	4.0	4.0	4.0	4.0	4.0	4.0
Jet energy scale	0.0	0.0	0.0	0.0	0.0	0.0
Total systematic	14.6	15.4	11.2	13.4	9.1	15.0

Table A.15: Statistical and systematic errors (%) for the MV1 tagger at 75% working point in $\Delta R_{\text{Subjets}} < 0.4$ bin.

Uncertainty	p_T^{jet} **bin [GeV]**								
	20-30	**30-40**	**40-50**	**50-60**	**60-75**	**75-90**	**90-110**	**110-140**	**> 140**
Statistical [%]									
Statistical (MC)	1.9	2.1	2.3	1.0	0.9	1.0	1.0	1.1	1.2
Statistical (Data)	3.3	3.9	2.8	2.2	2.7	2.2	2.9	2.5	3.4
Total Statistical	3.8	4.4	3.6	2.4	2.8	2.4	3.1	2.8	3.6
Systematic [%]									
MC stats	3.0	2.8	3.8	1.4	1.2	1.8	1.7	2.5	2.4
Pileup weight	0.2	0.1	0.4	0.1	0.1	0.2	0.3	0.1	0.1
Light charm ratio	0.9	0.8	0.8	0.1	0.2	0.3	0.3	1.3	2.7
Muon fakes	0.4	0.3	0.6	1.3	0.4	0.2	0.4	0.8	6.6
Model b prod.	1.5	0.1	2.1	0.3	0.4	0.0	0.0	0.5	2.9
Model c prod.	0.2	0.9	0.7	1.5	1.9	3.1	2.2	4.0	4.4
Light temp. con.	1.7	1.4	1.2	1.2	0.6	0.6	0.5	1.0	0.5
Inclusive b-jets	4.0	4.0	4.0	4.0	4.0	4.0	4.0	4.0	4.0
Jet energy scale	0.0	0.0	0.0	0.0	0.0	0.0	0.0	0.0	0.0
Total systematic	5.6	5.2	6.2	4.9	4.6	5.4	4.9	6.4	10.1

Table A.16: Statistical and systematic errors (%) for the MV1 tagger at 75% working point in $\Delta R_{\text{Subjets}} \geq 0.4$ bin.

A.2.9 MV1 at 80%

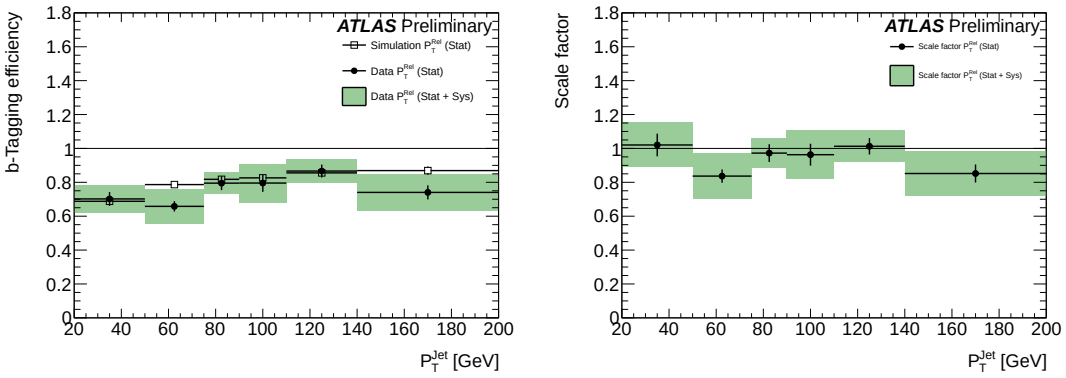

(a) Efficiency (b) Data/MC scale factor

Figure A.17: Efficiency and scale factors for MV1 tagger at 80% working point in $\Delta R_{\text{Subjets}} < 0.4$ bin.

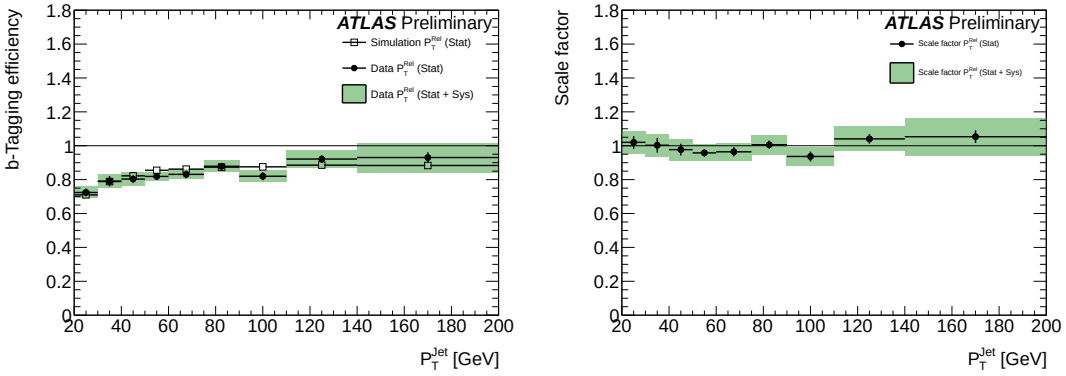

(a) Efficiency (b) Data/MC scale factor

Figure A.18: Efficiency and scale factors for MV1 tagger at 80% working point in $\Delta R_{\text{Subjets}} \geq 0.4$ bin.

Uncertainty	p_T^{jet} **bin [GeV]**					
	20-50	**50-75**	**75-90**	**90-110**	**110-140**	**> 140**
Statistical [%]						
Statistical (MC)	3.1	0.9	1.4	1.6	1.8	2.8
Statistical (Data)	5.8	4.6	5.2	6.5	4.4	5.6
Total Statistical	6.6	4.7	5.4	6.7	4.8	6.3
Systematic [%]						
MC stats	8.8	1.6	3.1	2.8	4.2	4.7
Pileup weight	0.4	1.8	0.9	1.0	0.9	1.0
Light charm ratio	0.2	1.0	0.9	0.0	1.8	4.1
Muon fakes	1.9	6.5	0.3	4.9	2.6	8.0
Model b prod.	0.2	13.0	4.1	11.2	0.4	8.8
Model c prod.	4.6	1.2	2.9	2.0	4.3	0.7
Light temp. con.	1.0	0.2	0.3	0.1	0.7	1.7
Inclusive b-jets	4.0	4.0	4.0	4.0	4.0	4.0
Jet energy scale	0.0	0.0	0.0	0.0	0.0	0.0
Total systematic	10.9	15.3	7.2	13.4	8.0	14.2

Table A.17: Statistical and systematic errors (%) for the MV1 tagger at 80% working point in $\Delta R_{\text{Subjets}} < 0.4$ bin.

Uncertainty	p_T^{jet} **bin [GeV]**								
	20-30	**30-40**	**40-50**	**50-60**	**60-75**	**75-90**	**90-110**	**110-140**	**> 140**
Statistical [%]									
Statistical (MC)	1.8	2.0	2.3	0.9	0.9	1.0	1.0	1.1	1.2
Statistical (Data)	3.2	3.8	2.7	2.2	2.7	2.2	2.9	2.5	3.3
Total Statistical	3.7	4.3	3.6	2.4	2.8	2.4	3.1	2.7	3.6
Systematic [%]									
MC stats	2.8	2.8	3.6	1.3	1.4	1.8	1.7	2.5	2.9
Pileup weight	0.3	0.1	0.3	0.0	0.1	0.2	0.3	0.1	0.2
Light charm ratio	0.8	0.7	0.7	0.1	0.2	0.2	0.3	1.3	3.1
Muon fakes	0.1	0.1	0.4	0.1	0.1	0.2	0.4	0.7	5.9
Model b prod.	1.2	0.3	0.3	0.1	0.2	0.2	0.2	0.4	3.0
Model c prod.	0.5	0.5	0.5	1.2	1.7	2.6	2.1	3.9	4.1
Light temp. con.	1.5	1.3	1.1	1.2	0.5	0.6	0.5	1.0	0.5
Inclusive b-jets	4.0	4.0	4.0	4.0	4.0	4.0	4.0	4.0	4.0
Jet energy scale	0.0	0.0	0.0	0.0	0.0	0.0	0.0	0.0	0.0
Total systematic	5.4	5.2	5.6	4.6	4.6	5.2	4.9	6.4	9.8

Table A.18: Statistical and systematic errors (%) for the MV1 tagger at 80% working point in $\Delta R_{\text{Subjets}} \geq 0.4$ bin.

Appendix B

Additional $H \to b\bar{b}$ analysis information

B.1 Simulated samples used

Table B.1: Summary of samples used in analysis.

Run no.	**Sample name**	$\sigma\times$ **BR [pb]**	N_{Events}
161800	Pythia8_AU2CTEQ6L1_WH100_lnubb	0.293	300k
161801	Pythia8_AU2CTEQ6L1_WH105_lnubb	0.248	300k
161802	Pythia8_AU2CTEQ6L1_WH110_lnubb	0.207	300k
161803	Pythia8_AU2CTEQ6L1_WH115_lnubb	0.171	300k
161804	Pythia8_AU2CTEQ6L1_WH120_lnubb	0.137	300k
161805	Pythia8_AU2CTEQ6L1_WH125_lnubb	0.107	3M
161806	Pythia8_AU2CTEQ6L1_WH130_lnubb	0.080	300k
161807	Pythia8_AU2CTEQ6L1_WH135_lnubb	0.058	300k
161808	Pythia8_AU2CTEQ6L1_WH140_lnubb	0.040	300k
161809	Pythia8_AU2CTEQ6L1_WH145_lnubb	0.026	300k
161810	Pythia8_AU2CTEQ6L1_WH150_lnubb	0.015	300k
167740	Sherpa_CT10_WenuMassiveCBPt0_BFilter	154.394	15M
167741	Sherpa_CT10_WenuMassiveCBPt0_CJetFilterBVeto	553.945	10M
167742	Sherpa_CT10_WenuMassiveCBPt0_CJetVetoBVeto	11363.371	50M
167743	Sherpa_CT10_WmunuMassiveCBPt0_BFilter	154.394	15M
167744	Sherpa_CT10_WmunuMassiveCBPt0_CJetFilterBVeto	553.945	10M
167745	Sherpa_CT10_WmunuMassiveCBPt0_CJetVetoBVeto	11363.371	50M
167746	Sherpa_CT10_WtaunuMassiveCBPt0_BFilter	154.394	15M

Continued on Next Page...

Table B.1 – Continued

Run no.	**Sample name**	$\sigma\times$ **BR [pb]**	N_{Events}
167747	Sherpa_CT10_WtaunuMassiveCBPt0_CJetFilterBVeto	553.945	10M
167748	Sherpa_CT10_WtaunuMassiveCBPt0_CJetVetoBVeto	11363.371	50M
167761	Sherpa_CT10_WenuMassiveCBPt40_70_BFilter	24.800	2M
167762	Sherpa_CT10_WenuMassiveCBPt40_70_CJetFilterBVeto	121.297	3M
167763	Sherpa_CT10_WenuMassiveCBPt40_70_CJetVetoBVeto	572.149	5M
167764	Sherpa_CT10_WmunuMassiveCBPt40_70_BFilter	24.800	2M
167765	Sherpa_CT10_WmunuMassiveCBPt40_70_CJetFilterBVeto	121.297	3M
167766	Sherpa_CT10_WmunuMassiveCBPt40_70_CJetVetoBVeto	572.149	5M
167767	Sherpa_CT10_WtaunuMassiveCBPt40_70_BFilter	24.800	1.1M
167768	Sherpa_CT10_WtaunuMassiveCBPt40_70_CJetFilterBVeto	121.297	3M
167769	Sherpa_CT10_WtaunuMassiveCBPt40_70_CJetVetoBVeto	572.149	5M
167761	Sherpa_CT10_WenuMassiveCBPt70_140_BFilter	12.659	2M
167762	Sherpa_CT10_WenuMassiveCBPt70_140_CJetFilterBVeto	54.674	3M
167763	Sherpa_CT10_WenuMassiveCBPt70_140_CJetVetoBVeto	208.250	5M
167764	Sherpa_CT10_WmunuMassiveCBPt70_140_BFilter	12.660	2M
167765	Sherpa_CT10_WmunuMassiveCBPt70_140_CJetFilterBVeto	54.674	3M
167766	Sherpa_CT10_WmunuMassiveCBPt70_140_CJetVetoBVeto	208.250	5M
167767	Sherpa_CT10_WtaunuMassiveCBPt70_140_BFilter	12.659	1.1M
167768	Sherpa_CT10_WtaunuMassiveCBPt70_140_CJetFilterBVeto	54.674	3M

Continued on Next Page...

Table B.1 – Continued

Run no.	**Sample name**	$\sigma\times$ **BR [pb]**	N_{Events}
167769	Sherpa_CT10_WtaunuMassiveCBPt70_140_CJetVetoBVeto	208.250	5M
167770	Sherpa_CT10_WenuMassiveCBPt140_280_BFilter	2.163	5M
167771	Sherpa_CT10_WenuMassiveCBPt140_280_CJetFilterBVeto	7.527	2M
167772	Sherpa_CT10_WenuMassiveCBPt140_280_CJetVetoBVeto	24.575	2M
167773	Sherpa_CT10_WmunuMassiveCBPt140_280_BFilter	2.163	5M
167774	Sherpa_CT10_WmunuMassiveCBPt140_280_CJetFilterBVeto	7.527	2M
167775	Sherpa_CT10_WmunuMassiveCBPt140_280_CJetVetoBVeto	24.575	1.7M
167776	Sherpa_CT10_WtaunuMassiveCBPt140_280_BFilter	2.163	1M
167777	Sherpa_CT10_WtaunuMassiveCBPt140_280_CJetFilterBVeto	7.527	2M
167778	Sherpa_CT10_WtaunuMassiveCBPt140_280_CJetVetoBVeto	24.575	2M
167779	Sherpa_CT10_WenuMassiveCBPt280_500_BFilter	0.168	100k
167780	Sherpa_CT10_WenuMassiveCBPt280_500_CJetFilterBVeto	0.469	200k
167781	Sherpa_CT10_WenuMassiveCBPt280_500_CJetVetoBVeto	1.386	500k
167782	Sherpa_CT10_WmunuMassiveCBPt280_500_BFilter	0.168	100k
167783	Sherpa_CT10_WmunuMassiveCBPt280_500_CJetFilterBVeto	0.469	30k
167784	Sherpa_CT10_WmunuMassiveCBPt280_500_CJetVetoBVeto	1.386	500k
167785	Sherpa_CT10_WtaunuMassiveCBPt280_500_BFilter	0.168	100k
167786	Sherpa_CT10_WtaunuMassiveCBPt280_500_CJetFilterBVeto	0.469	200k
167787	Sherpa_CT10_WtaunuMassiveCBPt280_500_CJetVetoBVeto	1.386	500k

Continued on Next Page...

Table B.1 – Continued

Run no.	**Sample name**	$\sigma\times$ **BR [pb]**	N_{Events}
167788	Sherpa_CT10_WenuMassiveCBPt500_BFilter	0.011	100k
167789	Sherpa_CT10_WenuMassiveCBPt500_CJetFilterBVeto	0.027	10k
167790	Sherpa_CT10_WenuMassiveCBPt500_CJetVetoBVeto	0.074	10k
167791	Sherpa_CT10_WmunuMassiveCBPt500_BFilter	0.011	10k
167792	Sherpa_CT10_WmunuMassiveCBPt500_CJetFilterBVeto	0.027	10k
167793	Sherpa_CT10_WmunuMassiveCBPt500_CJetVetoBVeto	0.074	50k
167794	Sherpa_CT10_WtaunuMassiveCBPt500_BFilter	0.011	10k
167795	Sherpa_CT10_WtaunuMassiveCBPt500_CJetFilterBVeto	0.027	10k
167796	Sherpa_CT10_WtaunuMassiveCBPt500_CJetVetoBVeto	0.074	50k
117050	PowhegPythia_P2011C_ttbar	114.505	15M
110101	AcerMCPythia_P2011CCTEQ6L1_singletop_tchan_l	25.75	9M
110119	PowhegPythia_P2011C_st_schan_lep	1.642	1.2M
110140	PowhegPythia_P2011C_st_Wtchan_incl_DR	20.461	20M
161995	Herwig_AUET2CTEQ6L1_WW_NoLeptonFilter	32.488	10M
161996	Herwig_AUET2CTEQ6L1_WZ_NoLeptonFilter	12.010	20M
169492	Herwig_AUET2CTEQ6L1_ZZ_LepEF_METVeto	0.773	2.5M
169493	Herwig_AUET2CTEQ6L1_ZZ_METEF_LepVeto	1.075	5M

Bibliography

[1] A. Bettini. *Introduction to Elementary Particle Physics.* Cambridge University Press, Cambridge, 2008.

[2] P. W. Higgs. Broken Symmetries and the Masses of Gauge Bosons. *Phys. Rev. Lett.*, 13:508–509, Oct 1964.

[3] F. Englert and R. Brout. Broken Symmetry and the Mass of Gauge Vector Mesons. *Phys. Rev. Lett.*, 13:321 – 323, Aug 1964.

[4] G. S. Guralnik, C. R. Hagen, and T. W. B. Kibble. Global Conservation Laws and Massless Particles. *Phys. Rev. Lett.*, 13:585 – 587, Nov 1964.

[5] M. Baak, M. Goebel, et al. Updated status of the global electroweak fit and constraints on new physics. *The European Physical Journal C*, 72(5):1–35, 2012.

[6] G. Aad, T. Abajyan, et al. Observation of a new particle in the search for the Standard Model Higgs boson with the ATLAS detector at the LHC. *Physics Letters B*, 716:1–29, 2012.

[7] S. Chatrchyan et al. Observation of a new boson at a mass of 125 GeV with the CMS experiment at the LHC. *Physics Letters B*, 716:30–61, 2012.

[8] P. Jenni, M. Nessi, et al. ATLAS high-level trigger, data-acquisition and controls: Technical Design Report. Technical report, CERN, Geneva, 2003.

[9] Cush. Standard Model of Elementary Particles. . http://en.wikipedia.org/wiki/Standard_Model, August 2013.

[10] E. Fermi. Zur Quantelung des idealen einatomigen Gases. *Zeitschrift für Physik*, 36(11-12):902–912, 1926.

[11] N. Bose. Plancks Gesetz und Lichtquantenhypothese. *Zeitschrift für Physik*, 26(1):178–181, 1924.

[12] I. Mrsi. Elementary Particle Interactions. . http://en.wikipedia.org/wiki/Standard_Model, March 2013.

[13] D.. Griffiths. *Introduction to Elementary Particles.* WILEY-VCH Verlag GbmH & Co., Weinheim, 2008.

[14] A. Proca. Sur la théorie ondulatoire des électrons positifs et négatifs. *J. Phys. Radium*, 7:347–353, Aug 1936.

[15] M. Gell-Mann. Symmetries of Baryons and Mesons. *Phys. Rev.*, 125:1067–1084, Feb 1962.

[16] S.L. Glashow. Partial-symmetries of weak interactions. *Nuclear Physics*, 22(4):579–588, 1961.

[17] S. Weinberg. A Model of Leptons. *Phys. Rev. Lett.*, 19:1264–1266, Nov 1967.

[18] A. Salam. Weak and Electromagnetic Interactions. *Conf.Proc.*, C680519:367–377, 1968.

[19] T. Barszczxak, E. Blaufuss, et al. Evidence for Oscillation of Atmospheric Neutrinos. *Phys. Rev. Lett.*, 81:1562 – 1567, Aug 1998.

[20] N. Cabibbo. Unitary Symmetry and Leptonic Decays. *Phys. Rev. Lett.*, 10:531–533, Jun 1963.

[21] S. L. Glashow, J. Iliopoulos, and L. Maiani. Weak Interactions with Lepton-Hadron Symmetry. *Phys. Rev. D*, 2:1285–1292, Oct 1970.

[22] M. Kobayashi and T. Maskawa. CP Violation in the Renormalizable Theory of Weak Interaction. *Prog.Theor.Phys.*, 49:652–657, 1973.

[23] J. F. Arguin, R. M. Barnett, et al. Review of Particle Physics. *Phys. Rev. D*, 86:010001, Jul 2012.

[24] L. Alvarez-Gaume and J. Ellis. Eyes on a prize particle. *Nat Phys*, 7(1):2–3, 2011.

[25] S Heinemeyer et al. Higgs boson production cross sections at 8 TeV. https://twiki.cern.ch/twiki/bin/view/LHCPhysics/CrossSections#Latest_plots, 2012.

[26] S Heinemeyer et al. Handbook of LHC Higgs Cross Sections: 3. Higgs Properties. *arXiv*, (arXiv:1307.1347), 2013.

[27] The LEP Collaboration. LEP design report. Technical report, CERN, Geneva, 1984. Copies shelved as reports in LEP, PS and SPS libraries. Accessible via http://cds.cern.ch/record/102083.

[28] F. T. Cole, E. L. Goldwasser, and R. R. Wilson. National Accelerator Laboratory design report January 1968. Technical report, Fermilab, 1968. Accessible via http://inspirehep.net/record/53213/.

[29] J. Baglio, A. Djouadi, et al. The Tevatron Higgs exclusion limits and theoretical uncertainties: A critical appraisal. *Physics Letters B*, 699(5):368–371, 2011.

[30] P. Teixeira-Dias. Higgs boson searches at LEP. *J.Phys.Conf.Ser.*, 110:042030, 2008.

[31] P. Bryant and L. Evans. LHC Machine. *Journal of Instrumentation*, 3(08):S08001, 2008.

[32] The ALICE Collaboration. The ALICE experiment at the CERN LHC. *Journal of Instrumentation*, 3(08):S08002, 2008.

[33] The ATLAS Collaboration. The ATLAS Experiment at the CERN Large Hadron Collider. *Journal of Instrumentation*, 3(08):S08003, 2008.

[34] The CMS Collaboration. The CMS experiment at the CERN LHC. *Journal of Instrumentation*, 3(08):S08004, 2008.

[35] The LHCb Collaboration. The LHCb Detector at the LHC. *Journal of Instrumentation*, 3(08):S08005, 2008.

[36] C. Lefévre. The CERN accelerator complex, Dec 2008. Accessible via http://cds.cern.ch/record/1260465.

[37] F. Zimmerman. LHC: The Machine. In *SLAC Summer Institute*. SLAC, 2012. Accessible via http://www-conf.slac.stanford.edu/ssi/2012/lectures.asp.

[38] CERN Bulletin: What is β^*. http://cds.cern.ch/journal/CERNBulletin/2010/23/News%20Articles/1269066?ln=en, June 2010.

[39] S. Fartoukh and M. Giovannozzi. Dynamic aperture computation for the as-built CERN Large Hadron Collider and impact of main dipoles sorting. *Nuclear Instruments and Methods in Physics Research Section A: Accelerators, Spectrometers, Detectors and Associated Equipment*, 671(0):10–23, 2012.

[40] O. S. Brüning, P. Collier, et al. *LHC Design Report*. CERN, Geneva, 2004. Accessible via http://cds.cern.ch/record/782076.

[41] J. P. Blewett. 200-GeV intersecting storage accelerators. In *Proceedings of The 8th International Conference on High-energy Accelerators*, Geneva, 1971. CERN. Accessible via http://lss.fnal.gov/conf/C710920/.

[42] Layout of a FODO Cell. http://www.lhc-closer.es/1/3/4/0.

[43] The CERN Accelerator Team. Diagram of an LHC dipole magnet, Jun 1999. Accessible via http://cds.cern.ch/record/40524.

[44] Lyndon Evans. The Large Hadron Collider. *New Journal of Physics*, 9(9):335, 2007.

[45] N. Andari, K. Assamagan, et al. Higgs Production Cross Sections and Decay Branching Ratios. Technical Report ATL-PHYS-INT-2010-030. ATL-COM-PHYS-2010-046, CERN, Geneva, Mar 2010.

[46] U. Baur. Measuring the W boson mass at hadron colliders. pages 47–59, 2003. Accessible via http://arxiv.org/abs/hep-ph/0304266.

[47] J. Pequenao. Computer generated image of the whole ATLAS detector, Mar 2008. Accessible via https://cds.cern.ch/record/1095924.

[48] G. Kane and A. Pierce (Editors). *Perspectives on LHC physics*. World Scientific Publishing Company, London, 2008.

[49] The ATLAS Collaboration. ATLAS: technical proposal for a general-purpose *pp* experiment at the Large Hadron Collider at CERN. Technical report, CERN, Geneva, 1994. Accessible via http://inspirehep.net/record/386786.

[50] G. Aad, M. Ackers, et al. ATLAS pixel detector electronics and sensors. *Journal of Instrumentation*, 3(07):P07007, 2008.

[51] J. Pequenao. Computer generated image of the ATLAS inner detector, Mar 2008. Accessible via http://cds.cern.ch/record/1095926.

[52] M. Karagoz Unel. Alignment of the ATLAS Inner Detector Tracking System. In *ICHEP/08*, Oct 2008.

[53] V. A. Mitsou. The ATLAS Transition Radiation Tracker. Technical Report ATL-CONF-2003-012. hep-ex/0311058, CERN, Geneva, Nov 2003.

[54] D. Froidevaux and M. A. Parker. The Performance Specifications of the ATLAS Inner Detector. Technical Report ATL-INDET-94-046. ATL-I-PN-46, CERN, Geneva, May 1994.

[55] H. Gordon, M. Leltchouk, et al. A Review of the Expected Performance of the ATLAS Barrel EM Calorimeter. Technical Report ATL-CAL-94-038. ATL-AC-PN-38, CERN, Geneva, Apr 1994.

[56] K. Oe. Measurement of Missing ET in ATLAS. In *DFS/JPS-06*, 2006. Accessible via http://atlas.kek.jp/sub/documents/hawaii200610/oe.pdf.

[57] J Beringer, J.F. Arguin, et al. Review of Particle Physics, 2012-2013. Review of Particle Properties. *Phys. Rev. D*, 86(1):010001, 2012.

[58] C. W. Fabjan and F. Gianotti. Calorimetry for particle physics. *Rev. Mod. Phys.*, 75:1243–1286, Oct 2003.

[59] Z. Meng. Performance of the ATLAS liquid argon calorimeter. In *Physics at the LHC*. DESY, Hamburg, 2010. Accessible via http://cds.cern.ch/record/1270158/.

[60] The ATLAS Collaboration. Expected Performance of the ATLAS Experiment - Detector, Trigger and Physics. 2009. Accessible via http://arxiv.org/abs/0901.0512.

[61] B. A. Petersen. ATLAS Trigger System. In *ICHEP/12*, Jul 2012. Accessible via http://cds.cern.ch/record/1459646.

[62] J. Pequenao. Event Cross Section in a computer generated image of the ATLAS detector, Mar 2008. Accessible via http://cds.cern.ch/record/1096081.

[63] Collaboration ATLAS. 2D event display of a $H \to e^+e^-e^+e^-$ decay in the ATLAS detector. General Photo. Accessible via http://www.atlas.ch/photos/events-collision-proton.html, May 2012.

[64] Collaboration ATLAS. 3D event display of a $H \to e^+e^-e^+e^-$ decay in the ATLAS detector. General Photo. Accessible via http://www.atlas.ch/photos/events-collision-proton.html, May 2012.

[65] The ATLAS Collaboration. The ATLAS Simulation Infrastructure. *The European Physical Journal C - Particles and Fields*, 70:823–874, 2010. 10.1140/epjc/s10052-010-1429-9.

[66] The ATLAS Collaboration. ATLAS Computing: technical design report. Technical report, CERN, Geneva, 2005. Accessible via http://cds.cern.ch/record/837738.

[67] G. Barrand, I. Belyaev, et al. GAUDI - The Software Architecture and Framework for building LHCb Data Processing Applications. In *Computing in High Energy and Nuclear Physics*, Padova, Italy, 2000. Accessible via http://lhcb-comp.web.cern.ch/lhcb-comp/general/publications/pap-a152.pdf.

[68] L. Lönnblad. CLHEP - a project for designing a C++ class library for high energy physics. *Computer Physics Communications*, 84(1-3):307–316, 1994.

[69] M. Dobbs and J.B. Hansen. The HepMC C++ Monte Carlo event record for High Energy Physics. *Computer Physics Communications*, 134(1):41–46, 2001.

[70] The Geant4 Collaboration. *Geant4 User's Guide for Application Developers*, Dec 2009. http://geant4.cern.ch.

[71] S. Mrenna, T. Sjöstrand, et al. PYTHIA 6.4 physics and manual. *Journal of High Energy Physics*, 2006(05):026, 2006.

[72] G. Abbiendi, I.G. Knowles, et al. HERWIG 5.1 - a Monte Carlo event generator for simulating hadron emission reactions with interfering gluons. *Computer Physics Communications*, 67(3):465–508, 1992.

[73] T. Gleisberg, S. Höche, et al. SHERPA 1., a proof-of-concept version. *Journal of High Energy Physics*, 2004(02):056, 2004.

[74] S P Baranov, J Hrivnc, et al. Overview of Monte Carlo simulations for ATLAS B-physics in the period 1996-1999. Technical Report ATL-PHYS-2000-025. ATL-COM-PHYS-99-042, CERN, Geneva, 2000. revised version number 1 submitted on 2000-09-29 16:58:34.

[75] M. Gyulassy, X. Wang, et al. HIJING 1.0: A Monte Carlo program for parton and particle production in high energy hadronic and nuclear collisions. *Computer Physics Communications*, 83(2-3):307–331, 1994.

[76] M.L. Mangano, M. Moretti, et al. ALPGEN, a generator for hard multiparton processes in hadronic collisions. *Journal of High Energy Physics*, 2003(07):001, 2003.

[77] S. Frixione, P. Nason, et al. Matching NLO QCD and parton showers in heavy flavour production. *Journal of High Energy Physics*, 2003(08):007, 2003.

[78] Carlo Oleari. The POWHEG-BOX. *Nucl.Phys.Proc.Suppl.*, 205-206:36–41, 2010. Accessible via http://inspirehep.net/record/862229/.

[79] B.P. Kersevan and E. Richter-Was. The Monte Carlo event generator AcerMC version 2.0 with interfaces to PYTHIA 6.2 and HERWIG 6.5. (arXiv:hep-ph/0405247), 2004.

[80] F.E. Paige, S.D. Protopopescu, et al. ISAJET 7.69: A Monte Carlo event generator for pp, $\bar{p}p$, and e^+e^- reactions. *arXiv*, 2003.

[81] T. Stelzer and W.F. Long. Automatic generation of tree level helicity amplitudes. *Computer Physics Communications*, 81(3):357–371, 1994.

[82] R. Field et al. PYTHIA tune A, HERWIG, and JIMMY in Run 2 at CDF", collaboration = "cdf collaboration", year = "2005", eprint = "hep-ph/0510198", archiveprefix = "arxiv", primaryclass = "hep-ph", reportnumber = "cdf-anal-cdf-public-7822", slaccitation = "

[83] C.M. Harris, P. Richardson, et al. CHARYBDIS: a black hole event generator. *Journal of High Energy Physics*, 2003(08):033, 2003.

[84] E. Boos, V. Bunichev, et al. CompHEP 4.4 - automatic computations from Lagrangians to events. *Nuclear Instruments and Methods in Physics Research Section A: Accelerators, Spectrometers, Detectors and Associated Equipment*, 534(1-2):250–259, 2004.

[85] S. Jadach, J.H. Kuhn, et al. TAUOLA - a library of Monte Carlo programs to simulate decays of polarized τ leptons. *Computer Physics Communications*, 64(2):275–299, 1991.

[86] E. Barberio, B. van Eijk, et al. Photos - a universal Monte Carlo for QED radiative corrections in decays. *Computer Physics Communications*, 66(1):115–128, 1991.

[87] D.J. Lange. The EvtGen particle decay simulation package. *Nuclear Instruments and Methods in Physics Research Section A: Accelerators, Spectrometers, Detectors and Associated Equipment*, 462(1-2):152–155, 2001.

[88] Description of calorimeters. http://www.atlas.ch/photos.

[89] W. Seligman. Geant4 simulation of the ATLAS liquid-argon calorimeters. In *ATLAS Software Conference*. Brookhaven National Laboratory, 2003. Accessible via http://www.usatlas.bnl.gov/computing/Jackie/200308-BNL.sxi.pdf.

[90] J. Apostolakis, A. Buckley, et al. Final Report of the ATLAS Detector Simulation Performance Assessment Group. Technical Report CERN-LCGAPP-2010-01, CERN, Geneva, 2010.

[91] MORTRAN. http://www.slac.stanford.edu/exp/e871/documentation/offline/mortran.html.

[92] M. Cacciari, G. P. Salam, and G. Soyez. The Anti-k(t) jet clustering algorithm. *JHEP*, 0804:063, 2008.

[93] A Cambridge-Aachen (C-A) based Jet Algorithm for boosted top-jet tagging. Technical Report CMS-PAS-JME-09-001, CERN, 2009. Geneva, Jul 2009.

[94] J. M. Butterworth, A. R. Davison, et al. Jet Substructure as a New Higgs-Search Channel at the Large Hadron Collider. *Phys. Rev. Lett.*, 100:242001, Jun 2008.

[95] G. Salam. Jet substructure as a new Higgs search channel at the LHC. In *SUSY/08*, Jun 2008.

[96] The ATLAS Collaboration. Measurement of the b-tag Efficiency in a Sample of Jets Containing Muons with 5 fb^1 of Data from the ATLAS Detector. Technical Report ATLAS-CONF-2012-043, CERN, Geneva, Mar 2012.

[97] A. Rizzi, F. Palla, et al. Track impact parameter based b-tagging with cms. Technical Report CMS-NOTE-2006-019, CERN, Geneva, Jan 2006.

[98] The ATLAS Collaboration. Calibrating the b-Tag and Mistag Efficiencies of the SV0 b-Tagging Algorithm in 3 pb^{-1} of Data with the ATLAS Detector. Technical Report ATLAS-CONF-2010-099, CERN, Geneva, Dec 2010.

[99] The ATLAS Collaboration. Commissioning of the ATLAS high-performance b-tagging algorithms in the 7 TeV collision data. Technical Report ATLAS-CONF-2011-102, CERN, Geneva, Jul 2011.

[100] The ATLAS Collaboration. b-jet tagging calibration on c-jets containing D^{*+} mesons. Technical Report ATLAS-CONF-2012-039, CERN, Geneva, Mar 2012.

[101] Impact parameter-based b-tagging algorithms in the 7 TeV collision data with the ATLAS detector: the TrackCounting and JetProb algorithms. Technical Report ATLAS-CONF-2010-041, CERN, 2010.

[102] M. Lehmacher. b-Tagging Algorithms and their Performance on ATLAS. In *ICHEP/08*, Nov 2008. Accessible via http://arxiv.org/abs/0809.4896.

[103] The ATLAS Collaboration. Performance of the ATLAS Secondary Vertex b-tagging Algorithm in 7 TeV Collision Data. Technical Report ATLAS-CONF-2010-042, CERN, Geneva, Jul 2010.

[104] G. Piacquadio and C Weiser. A new inclusive secondary vertex algorithm for b-jet tagging in ATLAS. *Journal of Physics: Conference Series*, 119(3):032032, 2008.

[105] R. Fruhwirth. Application of Kalman filtering to track and vertex fitting. *Nucl.Instrum.Meth.*, A262:444–450, 1987.

[106] The ATLAS Collaboration. Identification and Tagging of Double b-hadron jets with the ATLAS Detector. Technical Report ATLAS-CONF-2012-100, CERN, Geneva, Jul 2012.

[107] ATLAS Flavour Tagging Working Group. *b*-tagging benchmarks. https://twiki.cern.ch/twiki/bin/view/AtlasProtected/BTaggingBenchmarks, Dec 2012.

[108] The ATLAS Collaboration. Calibrating the *b*-Tag Efficiency and Mistag Rate in 35 pb^{-1} of Data with the ATLAS Detector. Technical Report ATLAS-CONF-2011-089, CERN, Geneva, Jun 2011.

[109] J. Delemontex, T. Wang. *b*-Tagging Efficiency and Mistag Rate Measurement in ATLAS. In *3rd France China Particle Physics Laboratory Workshop*. Institute of Nuclear Physics in Lyon, 2010. Accessible via https://indico.in2p3.fr/conferenceOtherViews.py?confId=2368.

[110] S. Agostinelli et al. GEANT4 a simulation toolkit. *Nuclear Instruments and Methods in Physics Research Section A: Accelerators, Spectrometers, Detectors and Associated Equipment*, 506(3):250–303, 2003.

[111] G. Piacquadio et al. Primary vertex reconstruction in the ATLAS experiment at LHC. *J. Phys: Conf. Ser.*, 119:032033, 2008.

[112] M. Limper. *Track and vertex reconstruction in the ATLAS inner detector*. PhD thesis, Universiteit van Amsterdam, 2009.

[113] ATLAS Luminosity Public Results. https://twiki.cern.ch/twiki/bin/view/AtlasPublic/LuminosityPublicResults.

[114] The ATLAS Collaboration. Evidence for Higgs Boson Decays to the $\tau^+\tau^-$ Final State with the ATLAS Detector. Technical Report ATLAS-CONF-2013-108, CERN, Geneva, Nov 2013.

[115] The ATLAS Collaboration. Search for the bb decay of the Standard Model Higgs boson in associated W/ZH production with the ATLAS detector. Technical Report ATLAS-CONF-2013-079, CERN, Geneva, Jul 2013.

[116] S. Mrenna, T. Sjöstrand, et al. A brief introduction to PYTHIA 8.1. *Computer Physics Communications*, 178(11):852–867, 2008.

[117] J. Huston, H.L. Lai, et al. New generation of parton distributions with uncertainties from global QCD analysis. *JHEP*, 0207:012, 2002.

[118] The ATLAS Collaboration. ATLAS tunes of PYTHIA 6 and Pythia 8 for MC11. Technical Report ATL-PHYS-PUB-2011-009, CERN, Geneva, Jul 2011.

[119] A. Djouadi, J. Kalinowski, et al. HDECAY: a program for Higgs boson decays in the Standard Model and its supersymmetric extension. *Computer Physics Communications*, 108(1):56–74, 1998.

[120] M. Guzzi, J. Huston, et al. New parton distributions for collider physics. *Phys. Rev. D*, 82:074024, Oct 2010.

[121] S. Alioli, P. Nason, et al. NLO Higgs boson production via gluon fusion matched with shower in POWHEG. *JHEP*, 0904:002, 2009.

[122] S. Mrenna, T. Sjostrand, et al. PYTHIA 6.4 Physics and Manual. *JHEP*, 0605:026, 2006.

[123] G. Aad et al. Search for the Standard Model Higgs boson produced in association with a vector boson and decaying to a b-quark pair with the ATLAS detector. *Physics Letters B*, 718(2):369 – 390, 2012.

[124] M. Cacciari and G.P. Salam. Pileup subtraction using jet areas. *Physics Letters B*, 659(1-2):119–126, 2008.

[125] G. Aad, B. Allbrooke, et al. Search for the Standard Model Higgs boson in associated production with a vector boson and decaying to bottom quarks with the ATLAS detector. Technical Report ATL-COM-PHYS-2013-465, CERN, Geneva, Aug 2013.

[126] Jet energy scale and its systematic uncertainty in proton-proton collisions at $\sqrt{s}$ = 7 TeV with ATLAS 2011 data. Technical Report ATLAS-CONF-2013-004, CERN, Geneva, Jan 2013.

[127] A.R. Davison and D. Miller. Private Communication: JES uncertainty figure of merit for C/A subjets in ptrel analysis, June 2012.

[128] A L Read. Presentation of search results: the CL s technique. *Journal of Physics G: Nuclear and Particle Physics*, 28(10):2693, 2002.

[129] C. Debenedetti. W/Z production associated with a H or a Z boson decaying to a $b\bar{b}$ pair. In *IOP High Energy and Astro Particle Physics*, Liverpool, Apr 2013. Accessible via http://indico.cern.ch/event/214998/.

[130] D. Lopez Mateos. Search for the Higgs Boson in VH(bb) Channel using the ATLAS Detector. In *EPS-HEP/13*, Sep 2013. Accessible via http://indico.cern.ch/event/218030/.

[131] S. Chatrchyan et al. Search for the standard model Higgs boson produced in association with a W or a Z boson and decaying to bottom quarks. *Phys.Rev.*, D89:012003, 2014.

[132] T. Aaltonen et al. Evidence for a particle produced in association with weak bosons and decaying to a bottom-antibottom quark pair in Higgs boson searches at the Tevatron. *Phys.Rev.Lett.*, 109:071804, 2012.

[133] Prospects for the study of the Higgs boson in the VH(bb) channel at HL-LHC. Technical Report ATL-PHYS-PUB-2014-011, CERN, Geneva, Jul 2014. Accessible via http://cds.cern.ch/record/1740962/.

Publications

The ATLAS Collaboration. Measurement of the cross section for the production of a W boson in association with b-jets in pp collisions at $\sqrt{s} = 7$ TeV with the ATLAS detector. In *Physics Letters B, 707(5):418 - 437*, 2012.